What doctors have learned from a year of COVID-19 p. 1195

Managing data in smart cities p. 1200

Bushfire smoke in the stratosphere p. 1269

Science

$15
19 MARCH 2021
sciencemag.org

AAAS

PLANKTIVOROUS SHARKS

Cretaceous convergence with modern filter-feeding rays p. 1253

NOMIS & Science
YOUNG EXPLORER AWARD

Research at the intersection of the social and life sciences

Unconventional. Interdisciplinary. Bold.

The newly launched **NOMIS & *Science* Young Explorer Award** recognizes bold, early-career researchers with an M.D., Ph.D., or M.D./Ph.D. who ask fundamental questions at the intersection of the social and life sciences. It is awarded to scientists who conduct research with an enthusiasm that catalyzes cross-disciplinary collaboration and who take risks to creatively address relevant and exciting questions.

Award winners will receive a cash prize of up to $15,000, and their essay submissions will be published in *Science*. They will also be invited to share their ideas with leading scientists in their respective fields at an award ceremony and to present their research to the NOMIS Board of Directors for potential future funding.

Apply by May 15, 2021
at www.sciencemag.org/nomis

Science
AAAS

NOMIS
FOUNDATION
Creating the Spark

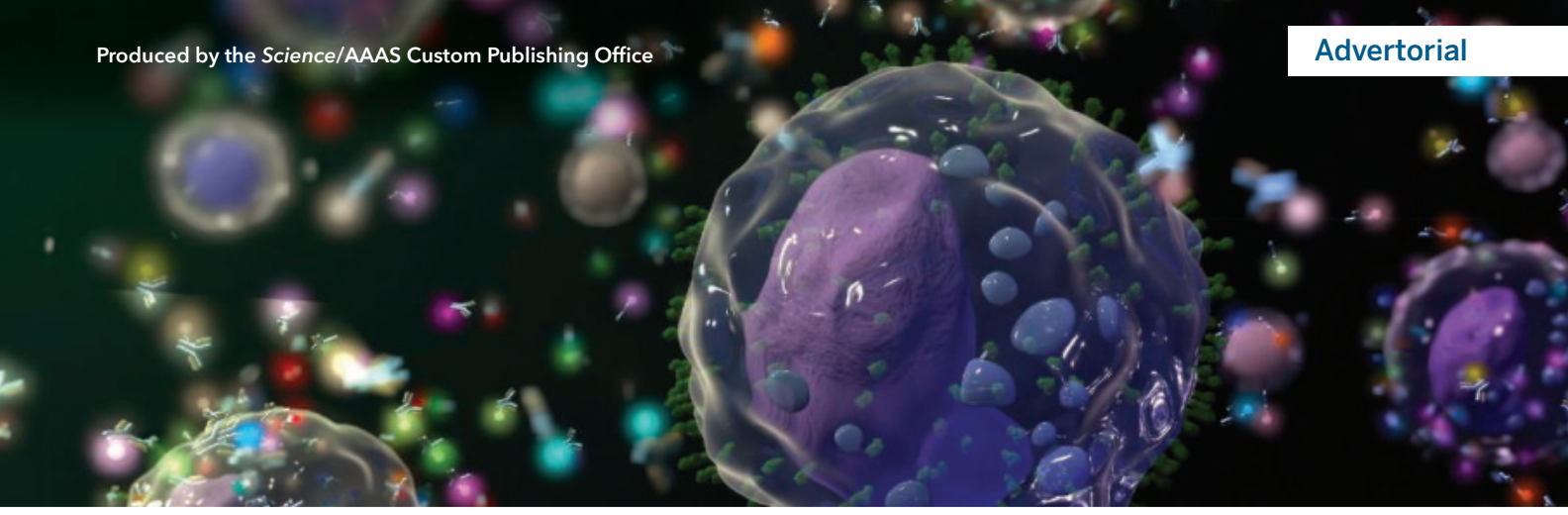

Exploring immunity with brilliance

Expanding the spectral range of flow cytometry provides more information on single immune cells. With BD Horizon Brilliant™ Ultraviolet (BUV) and BD Horizon Brilliant Violet™ (BV) Reagents, scientists find extensive diversity in populations of immune cells, are better able to study diseases in depth, and further boost their drug discovery research.*

Learning more about the immune system with flow cytometry helps scientists detect and defeat diseases of all kinds. Using this technology to study the molecular features of individual immune cells gets even more powerful as scientists add more fluorochromes, which allows more markers to be tracked simultaneously. Here, two researchers explain how they use and benefit from innovative dyes.

At CIMA LAB Diagnostics of the University of Navarra in Pamplona, Spain, flow cytometry core director Bruno Paiva uses flow cytometry in various research applications, including monitoring of circulating tumor cells, measuring residual disease, and profiling immune cells, all of which "could help us to identify patients with hematological cancer who might enjoy long-term survival or those at risk of disease progression," he says. During the COVID-19 pandemic, Paiva's team is also using flow cytometry in research to better understand the severity of the infection in patients with blood cancer and to see if immune status had an association with serious symptoms caused by the SARS-CoV-2 virus.

Flow cytometry can also be used to explore the development of immune cells. Working as a postdoctoral researcher at Sunnybrook Research Institute, which is affiliated with the University of Toronto, Joanne Leung uses flow cytometry to characterize subsets of these cells. She says, "Immune subsets have more diversity than we imagined– which is dependent on the surface markers or transcription factors that flow cytometry can also look at." In particular, Leung studies transient populations of T cells with the potential to become effector or memory cells.

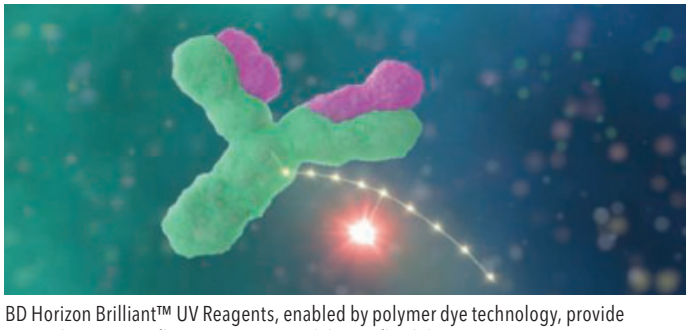

BD Horizon Brilliant™ UV Reagents, enabled by polymer dye technology, provide researchers greater flow cytometry panel design flexibility.

Dissecting cell features with flow cytometry depends on dyes that can be distinguished from one another, requiring many fluorochrome options across the spectrum.

Unleashing Experimental Potential

Despite using flow cytometry in somewhat different ways, both Paiva and Leung find that this technology benefits from more colors, especially the right ones. The line of BUV and BV dyes "yielded new opportunities to increase the number of parameters simultaneously measured at the single-cell level," Paiva says. "These reagents, together with new instruments, facilitate the design of high-parameter panels, which are enabling immunology research with unprecedented resolution. These fluorochromes facilitate the detection of more than 15 to 20 targets in research applications."

Leung agrees on the benefits of more dyes. "Specifically, the line of BUV reagents allow for better resolution, and I don't have to spend as much time worrying about panel design as markers are spread over more lasers," she says. That results in a better separation of cell populations. Leung continues, "I can see which cells are positive or negative for a specific marker with better resolution, because these dyes are specifically excited by the UV laser and there's not much interference with other fluorochromes."

Regarding her work on transient T cells, Leung explains, "Using BUV dyes to identify these rare populations allows me to visually see a better separation of them and trust that they are real and not artifacts."

Describing flow cytometry as "the bread and butter" of immunology research, Leung says that she and fellow scientists ask a lot of this technology and the associated reagents. With the BD Horizon Brilliant™ UV Reagents, she says that she gets the "credibility" and assurance she needs to publish her research with confidence.

As the field of flow cytometry expands and experiments grow in complexity, the need for innovative fluorochromes will only increase. Advanced fluorochromes such as BD Horizon Brilliant™ UV Dyes offer researchers the ability to reach for deeper insights and go beyond their current research paradigm to propel their science.

*For Research Use Only. Not for use in diagnostic or therapeutic procedures.

Sponsored by

BD

IMAGES: PROVIDED BY BD BIOSCIENCES; BD, THE BD LOGO, HORIZON BRILLIANT, AND HORIZON BRILLIANT VIOLET ARE TRADEMARKS OF BECTON, DICKINSON AND COMPANY OR ITS AFFILIATES. ALL OTHER TRADEMARKS ARE THE PROPERTY OF THEIR RESPECTIVE OWNERS. © 2021 BD. ALL RIGHTS RESERVED. BD-26915(v1.0) 0221

Waseda professor Haruko Noguchi dancing with local children in the Kibera district of Nairobi, Kenya

How economic research can impact health care in Japan

"Only a few universities in Japan provide courses in health economics—the study of how a nation uses its resources to promote health and care for the sick," says Haruko Noguchi, a professor in Waseda University's Faculty of Political Science and Economics in Tokyo. Using empirical evidence, Noguchi wants to show how health economics can help the government form effective policies to improve access to health care and enhance quality of life.

Collecting data for better health care

Noguchi's initiation into health economics came in a roundabout way when she was working as a researcher at a university hospital in New York City. There, she was shocked to find that some walk-in patients were turned away because they lacked insurance. "I couldn't believe it. In Japan, anyone can be treated under the national insurance scheme." The experience made her appreciate just how much government policies and health care systems could affect citizen's lives.

After obtaining her Ph.D. from the City University of New York in 1997, Noguchi went on to conduct postdoctoral research at Stanford University, where she helped perform big data analyses to understand the factors behind increases and decreases in medical costs and to investigate how the development and dissemination of new drugs and technology affected rehospitalization and mortality rates due to clinical complications. In 2000, she returned to Japan after almost 10 years abroad, with the goal of using her knowledge to improve evidence-based health care policy decision-making, given that the country was far behind the United States at the time.

"I was shocked by the lack of available data here. Things needed to change because universal health care in Japan is open to moral hazard—people can overuse it, and you also get physician-induced demand."

Together with the late professor Shigekoto Kaihara—then-director of the Department of Central Medical Information at the University of Tokyo Hospital and chair of the government-appointed investigative commission on the use of medical claims data to improve the quality of medical care—Noguchi pushed for the administration to collect and organize the data and make it available to researchers, which they did in 2013. She hopes this will prompt the government to continue using scientific evidence to optimize the cost-effective, efficient delivery of health care in Japan.

As a member of the Health Sciences Council (Subcommittee on Immunization and Vaccination, Research and Development, Production and Distribution Section) at the Ministry of Health, Labour and Welfare, Noguchi currently advises the government on effective distribution of the COVID-19 vaccine.

She says that analysis of health data can help researchers to better deal with the pandemic. For instance, some countries decided to go into lockdown as infection and death rates from the virus rose, but their economies suffered as a result. This brought its own set of problems. In Japan, suicides increased among part-time working women in their 40s and 50s when they lost their jobs.

On the other hand, some research in the United States found that premature deaths due to air pollution decreased when air quality improved because of reduced vehicle travel and electricity usage during lockdown (*1*). Also, Noguchi's

PHOTO: PROVIDED BY WASEDA UNIVERSITY

PHOTO: © TIMOFEY ZADVORNOV/SHUTTERSTOCK.COM

team discovered that the state of emergency instituted in April 2020 under the Abe administration led to a decline in property and violent crime rates (*2*). Similar declines were seen in Los Angeles and Indianapolis in the United States.

"[Showing us] how to mitigate the trade-offs between socioeconomic activities and health caused by COVID-19 is an important role of policy," she says.

Hybrid payment system in health care

The construction of an efficient payment system for health care is a common research theme, but it remains an urgent and unresolved issue in countries where national finances are being squeezed by increasing social safety net costs, such as medical care for an aging population.

Countries seeking to move away from a purely fee-for-service (FFS) system may consider a hybrid approach whereby only some procedures are paid by FFS, while others are paid prospectively (based on predetermined amounts). However, little evidence exists as to whether such a hybrid payment system produces overall cost savings without adversely affecting health outcomes.

In 2003, Japan shifted from FFS to a hybrid payment system in which certain inpatient procedures were paid prospectively. Noguchi took advantage of this reform to test how such a hybrid system impacts overall costs and health outcomes.

Her research team found that health care providers responded opportunistically to the reform, moving some procedures out of the bundled inpatient setting to FFS services. This resulted in no overall reduction in cost. There was some evidence of a moderate deterioration in health outcomes, in terms of a decline in the probability of symptoms being cured by the time of discharge. This suggested that a hybrid payment system may not be superior to either FFS or a prospective payment system (*3*).

Internationalization at Waseda

In 2012, Noguchi was appointed professor at her alma mater Waseda, where she received her undergraduate and Master's degrees.

"When I returned to Waseda to do research and teach health economics, I was delighted to find that there had been a dramatic increase in overseas students and researchers," says Noguchi. "In fact, Waseda had nearly 8,000 foreign students in the 2018 academic year, the highest among universities in Japan."

This is important for a number of reasons. To counteract the effect of Japan's declining and aging population and to become more globally competitive, Japanese universities are welcoming more international students and researchers. "When I was in America," notes Noguchi, "I was readily accepted and learned first-hand the benefits of having a diverse society. I want Waseda to become a leader in helping Japanese people understand such an idea."

In September 2020, she was appointed head of the Center for Positive/Empirical Analysis of Political Economy. The center is the first in Japan to conduct empirical studies of the political economy based on theory and evidence. Researchers affiliated with the center include experts in carbon pricing, social media and suicide prevention, and development economics.

The center is one of seven units comprising the Waseda Goes Global Plan, an ambitious, 10-year project started in 2014 and part of the Japanese government's multibillion-dollar Top Global University scheme to internationalize the country's leading universities. The other model research units are in the fields of global Japanese studies; health promotion; information and communications technology (ICT) and robotics; energy and nanomaterials; multiscale analysis, modelling and simulation; and global Asia studies.

Regarding internationalization at Waseda, Noguchi says, "In terms of education, we need to do our utmost to teach students how to lead a valuable life and contribute to society. In terms of research, we must spare no effort to support healthy competition among researchers so their achievements can be internationally recognized. These philosophies were established at the time of Waseda's founding, and we must return to them once again. This will set us on the right path to take on new challenges."

References

1. S. Cicala, S. P. Holland, E. T. Mansur, N. Z. Muller, A. J. Yates, "Expected Health Effects of Reduced Air Pollution from COVID-19 Social Distancing," NBER Working Paper Series, https://www.nber.org/system/files/working_papers/w27135/w27135.pdf.
2. https://www.jcer.or.jp/jcer_download_log.php?f=eyJwb3N0X2lkIjo2NjQwNiwiZmlsZV9wb3N0X2lkIjoiNzA4MTkifQ==&post_id=66406&file_post_id=70819
3. F. Rong, Y. Shen, H. Noguchi, *Health Econ.* **30**, 505–524 (2021).

Sponsored by

WASEDA University
早稲田大学

CONTENTS

19 MARCH 2021 • VOLUME 371 • ISSUE 6535

1195

NEWS

IN BRIEF

1186 News at a glance

IN DEPTH

1188 Ebola virus may lurk in survivors for many years
Genomic analyses of Guinea patients points to "new paradigm" for how outbreaks start
By K. Kupferschmidt

1189 Key human embryo stage mimicked in the lab
Four research teams report growing cellular clusters that resemble human blastocysts
By M. Leslie

1190 Genome reveals giraffe's recipe for standing tall
Transgenic mice with giraffe's mutations may suggest high blood pressure treatments *By S. Moutinho*
SCIENCE ADVANCES RESEARCH ARTICLE
BY C. LIU *ET AL*. 10.1126/SCIADV.ABE9459

1191 Studies chase clues to immune syndrome in kids
Causes and simple diagnostics for MIS-C have been elusive *By J. Couzin-Frankel*

1192 Biologists revel in pinpointing active genes in tissue samples
Spatial transcriptomics is a "total game changer" for cellular biology, revealing how location affects gene activity *By E. Pennisi*

1194 Europe may bar neighbors from key research
Quantum and space grant rules would exclude U.K., Swiss, and Israeli researchers *By N. Wallace*

FEATURES

1195 Medicine's longest year
Physicians sift through a torrent of research to find what works to treat COVID-19 *By K. Servick* et al.
PODCAST

INSIGHTS

PERSPECTIVES

1200 Smart cities built with smart materials
Sensors and actuators that respond locally avoid overburdening data analysis networks *By R. Napolitano* et al.
PODCAST

1202 Immune cell control of nutrient absorption
Intestinal γδ T cells regulate a gut epithelial cell program for dietary sugar uptake
By J. Talbot and D. R. Littman
RESEARCH ARTICLE p. 1223

1203 Tandem catalysis at nanoscale
Porous overcoatings help mediate coupled reactions *By C. Pei and J. Gong*
REPORT p. 1257

1204 DNA sensor in standby mode during mitosis
Distinct control mechanisms restrict innate DNA sensor activity on mitotic chromosomes *By A. Ablasser*
RESEARCH ARTICLE p. 1221

1206 SARS-CoV-2 transmission without symptoms
Symptomless transmission silently drives viral spread and is key to ending the pandemic
By A. L. Rasmussen and S. V. Popescu

1208 Lewis Wolpert (1929–2021)
Pioneering developmental biologist
By C. Tickle and J. Slack

POLICY FORUM

1209 Justice, diversity, and research ethics review
It is time for institutional review boards and research ethics committees to address the ethics of inclusion
By D. H. Strauss et al.

BOOKS *ET AL.*

1212 Doubling down on our earthly interventions
Can we engineer our way out of the planetary problems we've engineered our way into? *By K. Caldeira*

1213 Profiling the gene editor
A new biography traces CRISPR's origins and embraces scientist-led oversight of its future *By G. J. Annas*
EDITORIAL p. 1185

PHOTO: DANIELE FREDIANI/ARCHIVIO DANIELE FREDIANI/MONDADORI PORTFOLIO/GETTY IMAGES

LETTERS

1214 Seize China's momentum to protect pangolins
By C. Xia et al.

1214 Minimize collateral damage in locust control
By A. Hochkirch and D. Bhaskar

1215 Appropriate names for COVID-19 variants
By S. S. Abdool Karim et al.

RESEARCH

IN BRIEF

1216 From *Science* and other journals

REVIEW

1219 Sustainability
Using satellite imagery to understand and promote sustainable development
M. Burke et al.
REVIEW SUMMARY; FOR FULL TEXT: DOI.ORG/10.1126/SCIENCE.ABE8628

RESEARCH ARTICLES

1220 Spliceosome
Structure of the activated human minor spliceosome *R. Bai* et al.
RESEARCH ARTICLE SUMMARY; FOR FULL TEXT: DOI.ORG/10.1126/SCIENCE.ABG0879

1221 Innate immunity
Phosphorylation and chromatin tethering prevent cGAS activation during mitosis
T. Li et al.
RESEARCH ARTICLE SUMMARY; FOR FULL TEXT: DOI.ORG/10.1126/SCIENCE.ABC5386
PERSPECTIVE p. 1204

1222 Immunology
Structure-based decoupling of the pro- and anti-inflammatory functions of interleukin-10
R. A. Saxton et al.
RESEARCH ARTICLE SUMMARY; FOR FULL TEXT: DOI.ORG/10.1126/SCIENCE.ABC8433

1223 Immunometabolism
γδ T cells regulate the intestinal response to nutrient sensing *Z. A. Sullivan* et al.
RESEARCH ARTICLE SUMMARY; FOR FULL TEXT: DOI.ORG/10.1126/SCIENCE.ABA8310
PERSPECTIVE p. 1202

1224 Innate immunity
CARD8 is an inflammasome sensor for HIV-1 protease activity
Q. Wang et al.
RESEARCH ARTICLE SUMMARY; FOR FULL TEXT: DOI.ORG/10.1126/SCIENCE.ABE1707

1225 Ribozymes
Processive RNA polymerization and promoter recognition in an RNA World
R. Cojocaru and P. J. Unrau

1232 Organic chemistry
Sequential C–F bond functionalizations of trifluoroacetamides and acetates via spin-center shifts *Y.-J. Yu* et al.

REPORTS

1240 Topological optics
Generating arbitrary topological windings of a non-Hermitian band *K. Wang* et al.

Development

1245 Early developmental asymmetries in cell lineage trees in living individuals
L. Fasching et al.

1249 Landmarks of human embryonic development inscribed in somatic mutations *S. Bizzotto* et al.

1253 Paleontology
Manta-like planktivorous sharks in Late Cretaceous oceans *R. Vullo* et al.

1257 Catalysis
Tandem In_2O_3-Pt/Al_2O_3 catalyst for coupling of propane dehydrogenation to selective H_2 combustion *H. Yan* et al.
PERSPECTIVE p. 1203

1261 2D materials
Tuning electron correlation in magic-angle twisted bilayer graphene using Coulomb screening *X. Liu* et al.

1265 Astrochemistry
Detection of two interstellar polycyclic aromatic hydrocarbons via spectral matched filtering *B. A. McGuire* et al.

1269 Atmospheric aerosols
Record-breaking aerosol levels explained by smoke injection into the stratosphere
E. Hirsch and I. Koren

DEPARTMENTS

1184 Editorial
COVID-19 vaccination passports
By Christopher Dye and Melinda C. Mills

1185 Editorial
Behind the scenes of the CRISPR story
By H. Holden Thorp
BOOKS *ET AL.* p. 1213

1278 Working Life
What sparks joy *By Taylor Wright*

ON THE COVER

1203 & 1257

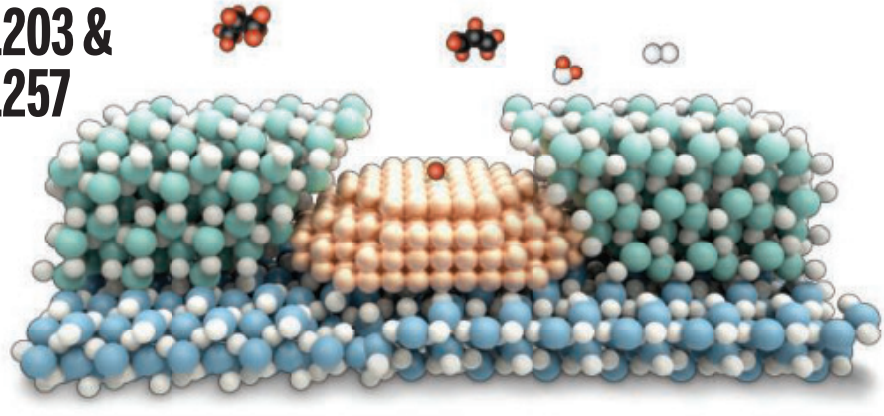

GRAPHIC: V. ALTOUNIAN/*SCIENCE*, BASED ON C. PEI AND J. GONG

Artist's view of three eagle sharks (*Aquilolamna milarcae*) feeding on plankton in the Gulf of Mexico 93 million years ago. This newly described group of Late Cretaceous sharks (Aquilolamnidae) occupied the same ecological niche as Cenozoic devil and manta rays (Mobulidae), indicating that "winged" suspension feeders evolved independently in two distinct lineages of cartilaginous fishes before and after the end-Cretaceous crisis. See page 1253. *Illustration: Oscar Sanisidro*

Science Careers 1275

SCIENCE (ISSN 0036-8075) is published weekly on Friday, except last week in December, by the American Association for the Advancement of Science, 1200 New York Avenue, NW, Washington, DC 20005. Periodicals mail postage (publication No. 484460) paid at Washington, DC, and additional mailing offices. Copyright © 2021 by the American Association for the Advancement of Science. The title SCIENCE is a registered trademark of the AAAS. Domestic individual membership, including subscription (12 months): $165 ($74 allocated to subscription). Domestic institutional subscription (51 issues): $2148; Foreign postage extra: Air assist delivery: $98. First class, airmail, student, and emeritus rates on request. Canadian rates with GST available upon request, GST #125488122. Publications Mail Agreement Number 1069624. **Printed in the U.S.A.**
Change of address: Allow 4 weeks, giving old and new addresses and 8-digit account number. **Postmaster:** Send change of address to AAAS, P.O. Box 96178, Washington, DC 20090–6178. **Single-copy sales:** $15 each plus shipping and handling available from backissues.sciencemag.org; bulk rate on request. **Authorization to reproduce** material for internal or personal use under circumstances not falling within the fair use provisions of the Copyright Act can be obtained through the Copyright Clearance Center (CCC), www.copyright.com. The identification code for *Science* is 0036-8075. *Science* is indexed in the *Reader's Guide to Periodical Literature* and in several specialized indexes.

EDITORIAL

COVID-19 vaccination passports

Christopher Dye is a professor of epidemiology in the Department of Zoology at the University of Oxford, Oxford, UK. christopher.dye@zoo.ox.ac.uk

Melinda C. Mills is director of the Leverhulme Centre for Demographic Science and a professor of sociology at the University of Oxford, Oxford, UK. melinda.mills@nuffield.ox.ac.uk

As countries grow eager to reignite their economies and people increasingly yearn for mobility and normalcy in life, pressure is mounting for some form of COVID-19 health status certificate that would support these desires. There has already been an explosion of COVID-19 passport initiatives for domestic use and international travel. But scientific, legal, and ethical concerns abound with such documentation. Given the high stakes, what is the path forward?

From doctors' examinations to ship inspections, clean bills of health have secured passage through centuries of human plagues. Today's best-known health passport is the International Certificate of Vaccination or Prophylaxis, created by the World Health Organization (WHO). WHO's Yellow Card has certified vaccinations for cholera, plague, and typhoid, among other infections. There is certainly precedent for a COVID-19 vaccination passport certifying that the holder can travel, study, play, and work without compromising personal or public health. Among newly proposed COVID-19 passport schemes are the WHO's Smart Vaccination Certificate, Israel's "green passport," the European Union's proposed Digital Green Pass, and the Africa Centres for Disease Control and Prevention's "My COVID Pass."

> "Many issues surround the fair use of vaccination passports."

Given the momentum, what are the main principles that COVID-19 passports should follow to ensure their appropriate use?

A COVID-19 passport should be scientifically valid. Passport holders must be protected from illness so that they can carry out the activities for which the passport has been issued and to avoid burdening health services. A passport would ideally certify that holders are not, and cannot become, a source of infection for others. Vaccines have high efficacy in preventing symptomatic COVID-19, and there is growing evidence that they can prevent transmission too. No vaccine is perfect, and it remains to be determined whether vaccines meet minimum requirements for preventing infection and illness. The duration of protection conferred by vaccines should be tied to passport expiry dates, perhaps with options to revoke passports if new coronavirus variants compromise efficacy. These passports should also be judged for their comparative advantage. They may be preferable to viral RNA and antigen tests, which aim to certify that individuals are temporarily free of infection, and to antibody tests, which do not guarantee immunity to infection or disease.

The vaccination certificate should be portable, affordable, and linked safely and securely to the identity of the holder. Ideally, it will be internationally standardized with verifiable credentials and based on interoperable technologies. Forgery and personal data security are dominant concerns, but such problems are routinely solved for financial and other sensitive transactions.

Many issues surround the fair use of vaccination passports. The widely held view is that documents must avoid discrimination and inequity. Ideally, a passport would be exclusive only with respect to its primary purpose, which is to protect the health of individuals and others with whom they come into contact. But such exclusions inevitably raise barriers elsewhere. Some, such as restrictions on nonessential leisure activities, should be relatively easy to manage. The greatest risk is that people for whom vaccination is unacceptable, untested, inaccessible, or impossible are denied access to essential goods and services. This could happen where there is vaccine hesitancy or refusal among certain ethnic minorities; where there are no data on vaccine efficacy for people at risk, such as children and pregnant women; where migrants are undocumented and unreachable; where passports are exclusively digital, barring people without smartphones; and where people are not yet eligible for vaccination. These examples signal the need for alternatives and exemptions.

Some decisions about how to use passports will be made by public debate and consent, drawing on social and ethical norms. Others will be determined by domestic and international law. Some employers have already announced "no jab, no job" policies. In such cases, the freedom of choice for individual employees, set against a firm's duty and preference for the care of all staff, might be tested in court.

COVID-19 is a new human disease. The challenges presented by vaccination passports are also new in detail, but mostly familiar in kind. Adding to current, imperfect certification procedures by diagnostic tests, vaccination passports are likely to be widely adopted during the pandemic and its probable sequel, endemic and episodic disease. The choice about how passports are used should be guided by exemplary science, appropriate technologies, and fair use for all.

–Christopher Dye and Melinda C. Mills

10.1126/science.abi5245

Open-Design Upright Microscope

- Optional motorized or fixed XY stage, or motorized translator
- Open-design microscope with motorized focus
- Quickly configurable based on experimental needs
- Optimized *In vivo* and *In vitro* experimentation on one setup
- Uses standard Olympus objectives
- Free Multi-Link™ software coordinates movement with MPC-200 controller
- OCC or DIC transmitted light (LED)
- Epi-fluorescent imaging

BOB™

SUTTER INSTRUMENT

PHONE: +1.415.883.0128
FAX: +1.415.883.0572
EMAIL: INFO@SUTTER.COM
WWW.SUTTER.COM

Share
Your Robotics Research with the **World**.

Shaping the future of robotics with high impact research!

As a multidisciplinary online-only journal, *Science Robotics* publishes original, peer-reviewed, research articles that advance the field of robotics. The journal provides a central forum for communication of new ideas, general principles, and original developments in research and applications of robotics for all environments.

Submit your research today.
Learn more at: **robotics.sciencemag.org**

Twitter: @SciRobotics
Facebook: @ScienceRobotics

Science Robotics
AAAS

Behind the scenes of the CRISPR story

H. Holden Thorp
Editor-in-Chief, *Science* journals.
hthorp@aaas.org;
@hholdenthorp

Walter Isaacson, one of America's foremost biographers, recently told me that he sees three fundamental units as the cornerstones of 20th-century innovation: the bit, the atom, and the gene. Having written about Steve Jobs and Albert Einstein—embodiments of the first two—in previous works, in his latest book, *The Code Breaker*, reviewed in this issue of *Science* (see page 1213), Isaacson's focus turns to the gene. His story centers on the life of biochemist Jennifer Doudna, who, together with Emmanuelle Charpentier, won the 2020 Nobel Prize in Chemistry for their pioneering work on the gene editing technology known as CRISPR-Cas9. The book is an extraordinarily detailed and revealing account of scientific progress and competition that grants readers behind-the-scenes access to the scientific process, which the COVID-19 pandemic has taught us remains opaque to the wider public. It also provides lessons in science communication that go beyond the story itself.

Doudna granted Isaacson numerous interviews for the book, as well as total access to her lab meetings and to her team's Slack channel. In contrast to many of his previous biographies, which relied heavily on archival documents and focused on individuals whose lives and legacies were fully realized at the time of writing, this allowed Isaacson to "see history being made." This also meant that Doudna would be around to read the finished product. Yet he reports that "she never asked for any control of the book, nor for the right to change anything."

This struck me as a bold and important decision. Society is starved for compelling stories about scientists, and by allowing Isaacson to study her life closely, Doudna opened the door for a much-needed narrative about the mechanisms of modern science.

When I asked her about the decision to allow Isaacson full access to her work, Doudna told me she was struck by his desire to fully comprehend how CRISPR came to be and by his efforts to understand the broader biomedical research landscape in which it arose. "I was impressed that he wanted to learn all about the way experimental science is conducted as well as about the personalities involved in the story of CRISPR. Walter is a great reporter and storyteller," she explained. "I wanted him to be able to write this story with as much first-hand knowledge as possible." I suspect many folks wouldn't have the courage to do this, but I hope others will follow her lead so that the public can gain a better appreciation for the excitement of scientific discovery and the self-correcting nature of science.

The Code Breaker is a story about discovery, collaboration, and competition. Doudna's collaborator Emmanuelle Charpentier and her competitor biochemist Feng Zhang gave Isaacson extensive interviews, as did other luminaries of science, including geneticists Eric Lander and George Church. This allowed Isaacson to document the arguments that lead researchers to change their hypotheses, the competition they engage in for credit and patents, and the conferences where—in nonpandemic times—ideas are exchanged and collaborations are often formed.

> **"*The Code Breaker* is a story about discovery, collaboration, and competition."**

The book also includes a great deal of detail about scientific publishing. Isaacson illustrates how scientists argue over reviewers and about what format their research manuscripts should take. He describes how publications can be expedited when there is competition and manages to infuse drama into the experience of uploading a submission to a journal website. Doudna and Charpentier's 2012 *Science* paper, which described the CRISPR-Cas9 system and suggested that it might be used for gene editing, even gets its own chapter.

I asked Isaacson if he had known these details about scientific publishing before he embarked on this project and if he had learned anything along the way. Despite having written about scientists in the past, he told me he knew relatively little about the drama and importance of scientific publishing, and that he found it inspiring: "I learned that the rigor and honesty of the review process are so crucial to the progress of science. In an era that has become loose with facts and truth—and skeptical about science—it's useful to have bulwarks that believe that evidence matters and intellectual honesty is our true north compass point." I couldn't agree more with this sentiment and hope that we will continue to see more inspiring scientific stories made accessible in this way.

–H. Holden Thorp

Published online 11 March 2021; 10.1126/science.abh4256

PHOTO: CAMERON DAVIDSON

NEWS

> "I simply do not have the mental bandwidth to be a full time homeschooling mom, housekeeper, and researcher."
>
> **An unnamed engineer and associate professor,** in a report by U.S. science academies about the stress and trauma that the COVID-19 pandemic has caused female scientists.

IN BRIEF

Edited by **Jeffrey Brainard**

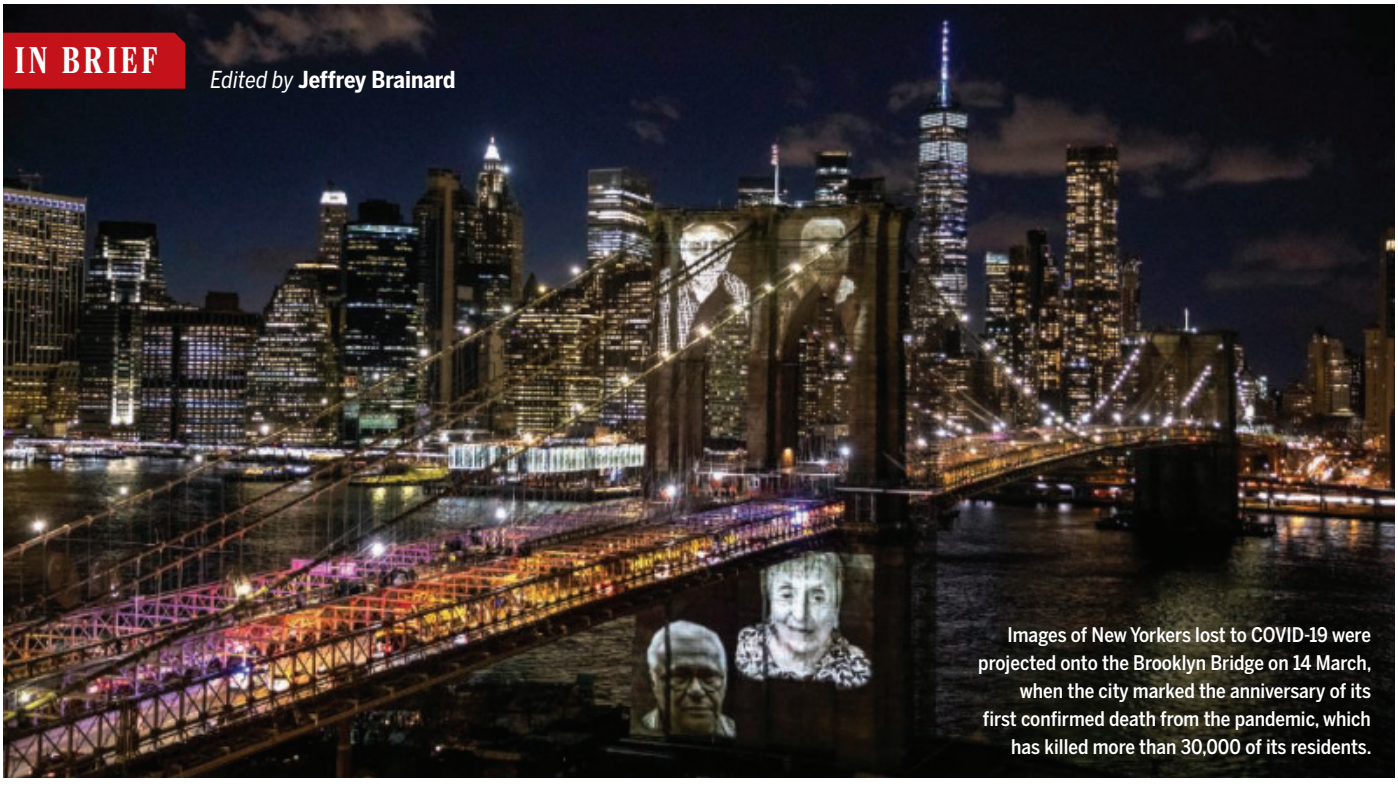

Images of New Yorkers lost to COVID-19 were projected onto the Brooklyn Bridge on 14 March, when the city marked the anniversary of its first confirmed death from the pandemic, which has killed more than 30,000 of its residents.

PHOTO: MICHAEL NAGLE/XINHUA/GETTY IMAGES

COVID-19

European countries pause AstraZeneca vaccine over side effects

More than 20 European countries this week temporarily halted use of the AstraZeneca vaccine against COVID-19 after reports of serious and unusual bleeding and clotting disorders in more than a dozen people who had received the vaccine. At least seven of the cases were fatal. Most of the affected patients were younger than age 50 and had no previous health issues, according to health authorities in Austria, Germany, and Norway, all of which reported similar incidents. The European Medicines Agency, which authorized the vaccine in January, said it is investigating; interim findings were expected to be announced after *Science* went to press. The pause threatened to further hamper already sluggish vaccination campaigns across the continent, just as many countries are facing sharply increasing infection rates driven by the more transmissible B.1.1.7 variant of the pandemic coronavirus.

Countries to boost vaccine supply

PUBLIC HEALTH | To increase global access to COVID-19 vaccines, Australia, India, Japan, and the United States have partnered to invest in expanded manufacturing of the still-scarce shots. At a summit last week, the so-called Quad group pledged to fund Biological E, a pharmaceutical company in India, to make 1 billion more doses of the Johnson & Johnson vaccine it already produces and potentially other COVID-19 vaccines by 2022. Quad's overall financial commitment was not specified, but some of the money may come from mechanisms such as the U.S. government's International Development Finance Corporation and Japan's International Cooperation Agency. Although the aim is to boost vaccine supply in Indo-Pacific countries that have secured few doses, products could also go to other regions. Separately, Pfizer and BioNTech announced a manufacturing alliance with 13 companies to increase production of their COVID-19 vaccine.

Group to speed future vaccines

VIROLOGY | Multiple COVID-19 vaccines were developed with remarkable speed in 2020, but a nonprofit that has backed several of them wants the world to move even faster for the next pandemic. Last week, the Coalition for Epidemic Preparedness Innovations (CEPI) unveiled a $3.5 billion plan to develop, test, and seek authorization for vaccines against future emerging pathogens within 100 days. CEPI wants to create a standing "library of vaccines" for critical virus families and conduct initial safety tests of them in humans so that when "disease X" surfaces, vaccine developers could quickly fine-tune a candidate for efficacy trials. About 20% of the money would go toward making vaccines that protect against a wide range of beta coronaviruses, the genus that includes SARS-CoV-2, the cause of COVID-19. The plan also calls for accelerating development of vaccines against other known threats, including the chikungunya, Lassa fever, Nipah, and Middle East respiratory syndrome viruses. CEPI has raised $2.2 billion from governments, philanthropies, and industry since its inception in 2017, but this plan would require a new infusion of cash.

Graduate students can unionize

UNIVERSITIES | Graduate students employed as teaching and research assistants by private universities in the United States will retain their right to unionize under a decision by the U.S. National Labor Relations Board (NLRB) last week. In 2019, NLRB had proposed a rule establishing that students were not employees and so were ineligible to form labor unions. Last week, the board withdrew that proposal, which never went into effect. Eight private U.S. universities have negotiated contracts with student workers, and students at additional institutions have voted to form unions. Republicans, who now hold a three-to-one majority on the NLRB, had voted for the 2019 proposal, but the board attributed last week's about-face to changing priorities.

JAMA withdraws racism podcast

RACIAL JUSTICE | A deputy editor at *JAMA* resigned, and the journal apologized, in the wake of a February podcast in which the editor questioned the existence of structural racism in health care. The podcast and an associated tweet on *JAMA*'s official Twitter account contradicted the official position of the American Medical Association, which publishes *JAMA*, acknowledging such racism. More than 3800 people signed an online petition criticizing the podcast, which has been taken offline. Last week, James Madara, the association's CEO, announced the resignation of Edward Livingston, the editor who hosted and offered the comments in the podcast. Madara also said *JAMA* is examining its editorial processes and will hire an associate editor with expertise in structural racism in health care.

The Atacama Large Millimeter/submillimeter Array on the Chajnantor Plateau has lain dormant during the pandemic.

PHOTO: © ALMA; ESO/NAOJ/NRAO

ASTRONOMY

Chilean telescope reopens after pandemic shutdown

The Atacama Large Millimeter/submillimeter Array (ALMA), a set of 66 radio astronomy dishes perched high in the Chilean Andes, shut down on 22 March 2020 because of the pandemic and has remained inactive ever since—far longer than most scientific facilities. The long lull reflected the complicated logistics required to support 200 staff members at its remote location, 5000 meters high. Managers announced this week that ALMA will resume observations in March following a 6-month campaign of restorations and repairs. Technicians are rushing to get as many dishes as possible working and hope more than 40 will be ready for the restart. Users say they are itching to get back to work.

Marine scientists see harassment

WORKPLACE | A startling 78% of female marine scientists reported in a survey that they had been sexually harassed, Women in Ocean Science said last week—a larger percentage than revealed by surveys of other scientific disciplines. The new report drew responses from 980 self-selected professional researchers, graduate students, and undergraduates. They reported that sexual harassment is common during fieldwork, which often takes place in isolated, confined spaces on ships and other research sites. The most common forms of harassment were verbal remarks, staring, and unwanted touching. More than one-third of women who experienced or witnessed misconduct did not report it because of the harasser's position of power, their fear for the target's career, or because they thought no action would result. The group asked colleges to revise policies to protect women.

Mice grown longer outside womb

DEVELOPMENTAL BIOLOGY | Researchers in Israel have found a way to grow mouse embryos outside the uterus for longer than ever before—until halfway through the animals' 20-day gestation—opening up new avenues for studying mammalian development. A rotating system of jars keeps the embryos bathed in nutrients and provides levels of oxygen, carbon dioxide, and atmospheric pressure necessary for growth. Five-day-old embryos, which would normally implant in the wall of the mother's uterus, grew in the jars up to day 11, when most internal organs and limbs have formed, the researchers reported online on 17 March in *Nature*. The method could help answer questions about how organs form and certain developmental disorders arise.

IN DEPTH

Government health workers prepare to vaccinate staff at the Regional Hospital of Nzérékoré in Guinea, where the first cases of a new Ebola outbreak were found in January.

INFECTIOUS DISEASES

Ebola virus may lurk in survivors for many years

Genomic analyses of Guinea patients points to "new paradigm" for how outbreaks start

By **Kai Kupferschmidt**

Virus that lay dormant in a survivor of the devastating Ebola epidemic in West Africa between 2013 and 2016 apparently triggered a new outbreak in Guinea in January, genomic analyses show. Sequencing the virus from the Guinea outbreak, which has so far sickened at least 18 people and killed nine, found it was virtually identical to the strain that ravaged Guinea, Sierra Leone, and Liberia more than 5 years ago.

Researchers knew the Ebola virus can linger in the human body and ignite fresh outbreaks for well over a year—but not 5 years. "This is pretty shocking," says virologist Angela Rasmussen of Georgetown University. The finding raises tricky questions about how to prevent such outbreaks without further stigmatizing Ebola survivors.

Until recently, scientists assumed new Ebola outbreaks start when the virus makes the leap from wildlife to people. But some of the more than 15,000 survivors of the West African epidemic were found to harbor the virus in places where the immune system can't reach, such as the eyes, testes, and cerebrospinal fluid. How it survives there, apparently hardly replicating, is unclear. But a resurgence in Guinea in 2016 originated from a survivor who shed the virus in his semen more than 500 days after his recovery and infected a sexual partner. The ongoing Ebola outbreak in North Kivu, in the Democratic Republic of the Congo, was started by sexual transmission from a survivor of the 2020 outbreak there.

Guinea's new outbreak was detected after several people who attended the January funeral of a nurse fell ill and died. The country officially declared an Ebola outbreak on 14 February. Since then, the Guinea Center for Research and Training in Infectious Diseases (CERFIG), the country's National Hemorrhagic Fever Laboratory, and the Pasteur Institute in Dakar, Senegal, have all sequenced virus samples. On 12 March on the website virological.org, the three groups agreed the outbreak was caused by the Makona strain of the *Zaire ebolavirus* species, just like the West African epidemic; the genome of the new virus differs at only 12 locations from that of the earlier one. Given that similarity, the virus can't be a new introduction from wildlife, says infectious disease physician Eric Delaporte of the University of Montpellier, a member of one of the three teams.

The nurse, who was diagnosed with typhoid and malaria before she died, was not known to be an Ebola survivor, but she could have had contact with a survivor privately or through her job, or she might have been infected herself years ago and had few symptoms. "Figuring out what exactly happened is one of the biggest questions now," says Dan Bausch, a veteran of several Ebola outbreaks who leads the United Kingdom's Public Health Rapid Support Team.

With three outbreaks now apparently caused by survivors, humans seem just as likely as wildlife to be the source of new Ebola outbreaks, Delaporte says: "This is clearly a new paradigm for how these outbreaks start." The question now is how to prevent these resurgences—perhaps, Bausch suggests, with new therapeutics that can clear the virus from survivors' bodies.

The findings raise another question: What will it mean for Ebola survivors, who already face serious stigmatization? "Will they be highlighted as a source of danger?" asks Frederic Le Marcis, a social anthropologist at the École Normale Supérieure of Lyon and the French Research Institute for Development, who is working in Guinea. "Will they be chased out of their own families and communities?"

Bausch calls for an educational campaign in Ebola-affected countries explaining that unprotected sex with a survivor may pose a risk, but more casual contacts do not. Another important message should be that some people infected with Ebola show few symptoms, says CERFIG virologist Alpha Keita, meaning people may be survivors without knowing it. "So don't stigmatize Ebola survivors—you don't know that you are not a survivor yourself." ■

PHOTO: CAROL VALADE/AFP/GETTY IMAGES

DEVELOPMENTAL BIOLOGY

Key human embryo stage mimicked in the lab

Four research teams report growing cellular clusters that resemble human blastocysts

By **Mitch Leslie**

A human embryo at the blastocyst stage is smaller than the tip of a ballpoint pen and may contain fewer than 100 cells, but this developmental waypoint has long puzzled and vexed biologists and physicians. Many miscarriages occur during this stage, for example, and a blastocyst can also split to create twins. Now, multiple research groups have found ways to mimic blastocysts, coaxing lab-grown human cells to form clusters that closely resemble the true thing.

The feat, described in two *Nature* papers this week and two recent preprints, could enable researchers to tackle important questions about human fertility, such as why in vitro fertilization (IVF) often fails. Moreover, the ersatz blastocysts "will be windows into this stage of human development," says stem cell biologist Aryeh Warmflash of Rice University, who wasn't connected to the work. "They will allow us to study it in ways we could not do before."

We were all blastocysts once. This phase, which in humans starts about 5 days after fertilization and lasts only a couple of days, is a watershed. "The blastocyst is the first stage in which we have specialized cell types developing," says developmental biologist Janet Rossant of the Hospital for Sick Children and the University of Toronto. The stage also initiates another momentous event: implantation, in which the blastocyst nestles into the uterine lining and begins to interact with the mother's cells to build the placenta.

But answering questions such as which genes orchestrate blastocyst development and why implantation is so often unsuccessful has been difficult. The only source for human blastocysts is donated embryos originally generated for IVF treatments, which are scarce and carry hefty ethical baggage. In the United States, for instance, researchers cannot use funding from the National Institutes of Health to study these blastocysts. Seeking an alternative, several groups of scientists have induced mouse stem cells to form blastocystlike clumps dubbed blastoids, but they don't perfectly re-enact what happens in a human embryo.

To create a human blastoid, cell biologist Jun Wu of the University of Texas Southwestern Medical Center and colleagues initially harnessed embryonic stem (ES) cells, which can be isolated from human blastocysts and give rise to all the cell types in our bodies. Under certain culture conditions, the cells can form each of the three cell types in the blastocyst, researchers previously found. Wu and his team took that discovery a step further and showed that when they stimulated cultured human ES cells with two molecular mixtures, the cells congregated into dead ringers for blastocysts.

Because ES cells come from human blastocysts, they share many of the same ethical and practical limitations. But with the right molecular prodding, researchers can convert mature cells, such as fibroblasts from the skin, into induced pluripotent stem (iPS) cells, which have the same tissue-generating capabilities as ES cells but don't require the destruction of embryos. Nudging human iPS cells with the same two molecular mixtures also yields blastocystlike cell clusters, Wu's team now reports in *Nature*.

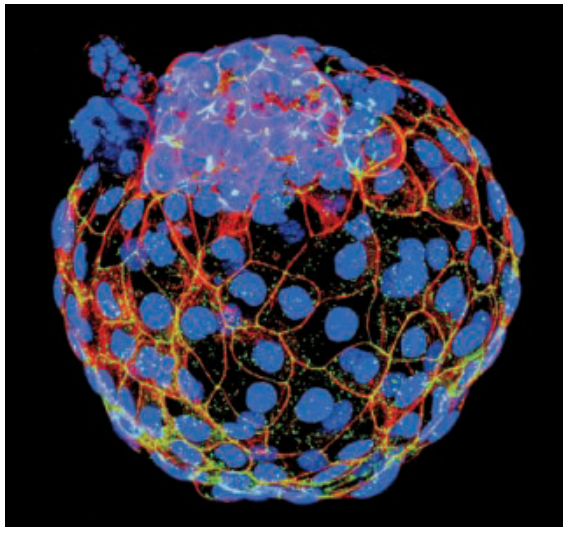

This lab-grown ball of human cells shares many similarities with 5-day-old human embryos.

IMAGE: UNIVERSITY OF TEXAS SOUTHWESTERN MEDICAL CENTER

The second group publishing in *Nature*, led by stem cell biologist Jose Polo of Monash University in Australia, chanced on a different recipe for making human blastoids while studying how skin cells morph into iPS cells. The group noticed that intermediate cells, which hadn't fully converted into iPS cells, could spawn all three types of blastocyst cells. On standard culture plates the cells couldn't display their full potential. But in roomier quarters, they converged into spheres that closely resembled blastocysts. In preprints posted last week two independent groups, led by developmental biologists Magdalena Zernicka-Goetz of the California Institute of Technology and by Yang Yu of Peking University Third Hospital, reported also making blastocystlike clusters from "extended" human stem cells.

Polo's and Wu's groups demonstrated that their blastoids recapitulated many characteristics of human blastocysts. They contained about the same number of cells, for example, and switched on many of the same genes. And at least in the culture dish, blastoids re-create some early steps of implantation.

Making the clusters was inefficient, and those that did form showed several key differences from IVF-derived blastocysts. "There's a lot going on that we don't understand," says reproductive and developmental biologist Susan Fisher of the University of California, San Francisco. Still, she stresses, "As a first step it's extremely exciting, and a huge amount can be learned."

Although the new techniques are inefficient, Polo notes they can still produce blastoids in large numbers. That could enable researchers to use blastoids to test whether certain chemicals disrupt embryonic development, trace how mutations lead to birth defects, and refine IVF.

The blastoids are not embryos, Wu cautions, but are "a collection of cells that undergoes the early stages of embryogenesis." A human blastoid could not develop into a fetus, he adds. A widely accepted research guideline, codified into law in some countries, forbids growing blastocysts for more than 14 days—and all four groups abided by that limit with their blastoids. New recommendations from the International Society for Stem Cell Research, due to be published later this year, may provide further guidance about working with embryolike structures such as blastoids.

But the public's reaction to these new creations is uncertain, Fisher says. "It's a test case for how scientists and lay people feel about a collection of cells." ■

GENETICS

Genome reveals giraffe's recipe for standing tall

Transgenic mice with giraffe's mutations may suggest high blood pressure treatments

Researchers are uncovering the mutations that give giraffes like this pair from Uganda their unique physique.

By **Sofia Moutinho**

To biologists, the giraffe's long neck is a prime example of evolution's handiwork, cited by both Charles Darwin and Jean-Baptiste Lamarck as support for their evolutionary theories. But it is also an engineering problem. In order get oxygen up its 2-meter neck to its brain, a giraffe's heart constantly pumps blood at a pressure roughly 2.5 times higher than is normal in humans. Now, a new giraffe genome is revealing genetic alterations that allow these animals to live happily with hypertension—along with other genes linked to giraffes' unusual physique.

The findings illuminate "the fascinating evolution of the giraffe form," says wildlife biologist Monica Bond at the Wild Nature Institute. The researchers also expressed a giraffe gene in mice and showed it protected them from hypertension, perhaps laying the groundwork for new therapies for humans. "It is a beautiful validation of the notion that you can try to assess differences in species by making gene substitutions in mice models," says molecular biologist Douglas Cavener of Pennsylvania State University, University Park, who published the first giraffe genome 5 years ago.

For the new study, researchers from China, Norway, and Denmark compared the genes of a male Rothschild's giraffe (*Giraffa camelopardalis rothschildi*) with those of 50 other mammals, including the giraffe's closest relative, the short-necked, zebra-size okapi; the animals diverged about 11.5 million years ago. The new study provides detailed data on about 97% of the giraffe's DNA, compared with two-thirds of the genome in the earlier sequence. Published in *Science Advances* this week, the study identifies 490 genes with unique adaptations in the giraffe.

Most of the mutations are in genes linked to cardiovascular features, bone growth, and the sensory system. The team zeroed in on the gene *FGFRL1*, in which Cavener and his colleagues had found seven unique mutations. In humans and mice, mutations in this gene are linked to cardiovascular and skeletal defects. To find out more, the team used the powerful DNA editor called CRISPR to insert the giraffe mutations into the *FGFRL1* gene of mice.

The mutant mice did not grow long necks or show any obvious change in their cardiovascular system. So the team decided to see how the animals would respond to high blood pressure, the normal condition of the giraffe. They gave five of 10 modified mice a drug to induce high blood pressure, and also injected the drug into five normal mice. The normal mice developed hypertension and associated kidney and heart damage. But all the mutant rodents, including those given the drug, stayed healthy, and their blood pressure rose only slightly.

"The *FGFRL1* giraffe gene does something to the cardiovascular system that counteracts the effects of hypertension," says co-author Rasmus Heller, an evolutionary geneticist at the University of Copenhagen. "But we don't know what yet."

Further studies on *FGFRL1* might point to treatments for hypertension, Heller says. But many genes cause hypertension, and there's no evidence so far that *FGFRL1* plays an important role in the disease in humans, cautions hypertension and precision medicine specialist Bina Joe at the University of Toledo. "If indeed this is a major gene protecting humans from hypertension, it should have come up as a candidate in genomewide association studies," which scan thousands of people for gene variants linked to a disease. "Talking about therapeutic approaches at this point would be premature," agrees University of Tennessee Health Science Center nephrologist L. Darryl Quarles, who notes that researchers don't yet understand how the mutations affect blood pressure.

The study highlights other unique mutations, including those in genes related to eye development and vision. Previous studies have shown that giraffes have the best vision of all hoofed mammals, which together with their stature allows them to scan the horizon effectively. On the other hand, the giraffe has lost at least 53 olfactory genes compared with the okapi. Heller says this could indicate that giraffes have a lousy sense of smell—a sense that is less important when your nose is 6 meters above the ground. "The giraffe … has traded off the sense of smell for improved eyesight," he notes. "When you upgrade one feature, you often downgrade another."

The team also found mutations in genes that regulate sleep patterns, which could explain why giraffes in the wild only sleep 40 minutes per day and about 3 to 5 minutes at a time.

Bond notes that giraffes are endangered and in the past 30 years, their population has declined 40%, to 68,000 in the wild. She says knowing more about the animal's genome can help shape effective conservation strategies based on genes related to fitness, health, and immunity. "Genetics is one more piece of the puzzle in understanding an organism," she says. "The more we can understand them, the better we can help protect them." ■

PHOTO: JAN VERMEER/MINDEN PICTURES

COVID-19

Studies chase clues to immune syndrome in kids

Causes and simple diagnostics for MIS-C have been elusive

By **Jennifer Couzin-Frankel**

In March 2020, Audrey Odom John was certain her teenage patient had a new disease. As chief of pediatric infectious diseases at the Children's Hospital of Philadelphia (CHOP), John is accustomed to mystery cases and rare diagnoses. But within weeks, two more children were admitted with parallel symptoms: fever, rash, inflammation, and shock. Two of those first three patients had relatives who had recently tested positive for COVID-19, and just as John began to wonder about a connection, a late-April alert from the United Kingdom made the link explicit.

The notice described an uptick in cases that mirrored those at CHOP, with some affected children also testing positive for COVID-19. In the months since, John and pediatric specialists worldwide have raced to understand what's now called multisystem inflammatory syndrome in children, or MIS-C. They've learned that—contrary to some early suspicions—it appears distinct from Kawasaki disease, a rare inflammatory reaction thought to strike young children after unknown infections (*Science*, 29 May 2020, p. 923).

They've also come to recognize its unique profile of immune system overactivity and have identified effective treatments. Now, they are hunting for clues to why it develops, 4 to 6 weeks after infection with the pandemic coronavirus, and how to spot it early.

Careful tracking of cases has shown that MIS-C is rare, though still frightening to parents: As of early March, the U.S. Centers for Disease Control and Prevention had logged more than 2600 MIS-C cases, including 33 deaths. But most youngsters recover after about a week in the hospital.

To explore its relation to COVID-19, researchers compared blood samples from 14 children with MIS-C against those of 16 children and more than 100 adults hospitalized for acute COVID-19. From an immune perspective, "There is a decent bit of overlap" in the different cohorts, says Laura Vella, a pediatric infectious disease physician at CHOP who led the work along with E. John Wherry at the University of Pennsylvania.

Both adults and children with acute COVID-19 had high levels of inflammation and immune activation, in which immune cells get revved up to target potential harms—but in MIS-C patients, the degree of activation sometimes exceeded that of the sickest adult patients, the researchers reported this month in *Science Immunology*. One subgroup of immune cells stood out: the so-called "vascular patrolling" T cells. Their high activation, suggesting they were targeting blood vessels, could explain the cardiac inflammation and aneurysms in some patients.

Vella and her colleagues also noted that despite the rampant inflammation in the MIS-C patients, it abated quickly with treatment. "They can turn this around with therapy," Vella says, whereas people with COVID-19 experienced longer lasting inflammation.

Science's COVID-19 reporting is supported by the Heising-Simons Foundation.

The immunologic findings dovetail with what doctors have seen: Most children with MIS-C improve rapidly with therapies that suppress the immune system. U.S. MIS-C patients are routinely treated with intravenous immunoglobulin. But this treatment often isn't available in underresourced countries. In September 2020, a large U.K. clinical trial called Recovery, which has been testing therapies on thousands of adults, began to recruit children for a study of other approaches. "Across the globe, people have adopted different strategies" for treating MIS-C, says Elizabeth Whittaker, a pediatric infectious disease specialist at Imperial College London, who's involved in the trial. Trial leaders want to know whether children can be treated with steroids alone or even just supportive care, for example drugs to stabilize blood pressure.

Ironically, powerful treatments for MIS-C also make it harder to study: Blood samples to probe the immune system are often collected after therapy has started. Treatment "changes a tremendous number of cell types," says Virginia Pascual, a pediatric rheumatologist and director of the Gale and Ira Drukier Institute for Children's Health at Weill Cornell Medicine. Her work is part of a large study called the Pediatric Research Immune Network on SARS-CoV-2 and MIS-C (PRISM), which aims to decipher the causes and long-term outcomes of the syndrome.

Sponsored by the National Institutes of Health, PRISM has enrolled more than 100 patients since November, and hopes to include at least 250 overall. Over 1 year, researchers will repeatedly collect a raft of samples including blood, saliva, and urine

PHOTO: ISTOCK.COM/MARIJA STEPANOVIC

Weeks after infection, COVID-19 can cause inflammation, shock, and other symptoms in children.

from patients with symptoms of MIS-C or who have COVID-19. "All of our efforts ... now are to try to capture these samples before [children] start to be treated with these very potent medications," Pascual says. That's not easy, says Steven Webber, pediatrician-in-chief at Vanderbilt University, who is leading the study. For parents whose child has fallen suddenly, critically, ill, "It's hard to think straight," he says. "And then someone comes along and says, 'We would really love for you to be in this important study.'"

Theories for what's driving MIS-C are emerging. Many children test negative for SARS-CoV-2 on a nasal swab, but the virus may hide elsewhere in the body; stool samples may provide clues. Some wonder whether antibodies produced after infection react to the body's own tissues. Pascual is exploring whether SARS-CoV-2 causes a subtle immune system abnormality, perhaps in immune system precursor cells, and subsequent exposure to another virus—a "second hit"—sends the immune system into overdrive. The good news, Pascual says, is "all these hypotheses are testable."

Clarity could help physicians quickly diagnose MIS-C; right now, that requires sophisticated blood testing and specialists that not all health centers have access to. Early diagnosis and treatment could improve outcomes. Although most children have recovered, "I don't think the low mortality is inherent to the disease," Webber says.

A paper published last week in *The Lancet Child & Adolescent Health* identified factors linked to more severe disease in 1080 young people with MIS-C. High c-reactive protein, a marker of inflammation, increased risk, as did older age. Children who were Black were more likely to end up in the intensive care unit, and some 77% of children in the paper were Black or Hispanic—the groups hit hardest by COVID-19, John notes.

A deeper mystery to her is age. Teenagers can be severely affected by MIS-C, but people in their 20s almost never are, even though immunologically, the two groups are nearly identical. John wonders whether differences in hormones or exposure to other viruses might be at work.

Ultimately, she hopes ongoing studies will bring speedy, accurate diagnostics and more targeted treatment. "Our current approach is a hammer" to squash the entire immune system, she says, and it can have side effects like fluid buildup in the lungs. "There's definitely room to take a precision immunology approach," she says. One year after the mystery of MIS-C emerged, she's eager for answers. ■

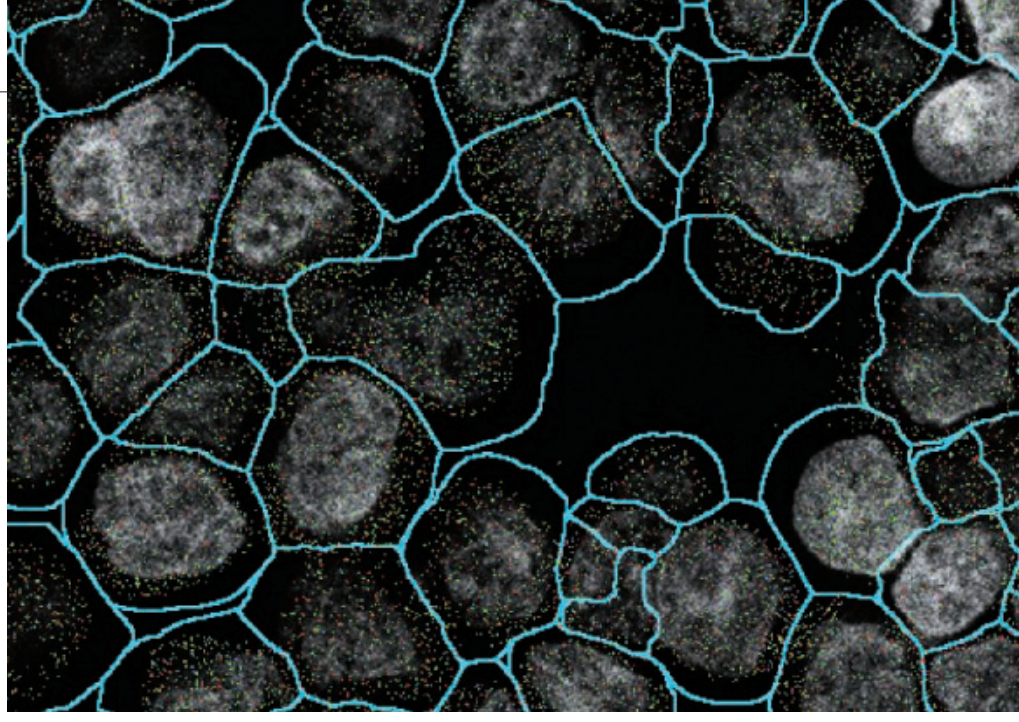

New methods can map the activity of myriad genes (colored dots) in cells (blue outlines) across a tissue.

CELL BIOLOGY

Biologists revel in pinpointing active genes in tissue samples

Spatial transcriptomics is a "total game changer" for cellular biology, revealing how location affects gene activity

By **Elizabeth Pennisi**

As with real estate, location matters greatly for cells. Douglas Strand confirmed that truth last year when he used a new technique to map gene activity in bladder cancers. Until recently, scientists wanting to know all the genes at work in a tissue could analyze single cells without knowing their position, or they could measure average activity levels of genes across thousands of cells. Now, an emerging technology called spatial transcriptomics combines precision and breadth, mapping the work of thousands of genes in individual cells at pinpoint locations in tissue. That, Strand says, has been a "total game changer" for his research.

The virtual Advances in Genome Biology and Technology (AGBT) meeting this month was a big coming-out party for the technique, which is revealing whole new landscapes of gene expression. Strand, for example, reported finding that cells surrounding bladder tumors, though outwardly normal, display many of the same gene activity changes as the cancer. "They looked more like tumor than normal tissue," says Strand, who works at the University of Texas Southwestern Medical Center. He found surprises within the tumors, too: hidden patterns of gene activity suggesting some of the cells are more likely than others to spread beyond the bladder.

Other biologists at the meeting reported using the technique to study Alzheimer's disease, track the dynamics of different types of T cells, and study lung, heart, and other tissues in COVID-19 patients. "The field is developing very, very fast," says Aparna Bhaduri of the University of California, Los Angeles, who uses it to examine developing human brains.

Scientists studying cells have long been able to examine the activity of a few, select genes in intact tissue—for example, by engineering a gene to tack on a fluorescent tag to the protein it encodes. By 2010, traditional transcriptomics, which examines cellular activity of many, if not all, known genes by probing for the messenger RNA (mRNA) transcripts they encode, took off. But those studies require tissues to be ground up first, so the data represent the average activity of genes in millions of cells.

More recently, biologists have begun to monitor all the genes of single cells, uncovering vast differences in gene activity between

IMAGE: JOSEPH BEECHAM/NANOSTRING

different cell types and variation even within types. But because those cells are extracted from tissue with enzymes or teased out with lasers, microscopic tweezers, or other methods, the influence of their precise location and neighbor cells is lost. "We could see the individual parts, but we didn't know how the parts fit together," explains Joseph Beechem, a biophysicist at NanoString Technologies, a leading company for spatial transcriptomics and related methods.

Then in 2016, Swedish researchers described in *Science* how they managed to keep track of cells' locations while assessing the activity of about 200 of their genes (*Science*, 1 July 2016, p. 78). The group put thin slices of a tissue onto slides precoated with short, known sequences of DNA, meant to act like identifiable barcodes, attached to other DNA designed to latch nonspecifically onto any mRNA nearby. The team treated the tissue with detergent to make cells leak their mRNA, which linked to the anchored, barcoded DNA, marking which cell the mRNA came from. Then, they added enzymes and DNA bases to the slice to translate each mRNA into a complementary DNA strand. Sequencing that strand along with its position-identifying barcode revealed the active parent gene and its position. Those data enabled computer programs to reconstruct the tissue locations of all the active genes.

Multiple companies have begun to sell expensive machines that conduct such spatial transcriptomics analyses, making it possible to study thousands of genes in hundreds of cells in their proper places. That "can tell you a lot about how cell communication might break down in disease," says Aviv Regev, a computation and systems biologist who heads the Genentech Research and Early Development unit of Roche.

Christopher Mason, a geneticist at Weill Cornell Medicine (WCM), and colleagues have performed spatial transcriptomics on fresh or preserved tissue samples from autopsied COVID-19 patients, comparing them with lung tissue of healthy adults and people who died of other acute respiratory infections or flu. The commercial devices they used, one based on the Swedish approach, can assess lots of genes but can't completely pinpoint their activity to single cells. (Other methods are limited to far fewer genes, but specify locations better.) The team, including WCM's Robert Schwartz and Alain Borczuk and others, mapped the activity of the gene for angiotensin-converting enzyme 2, the cell-surface receptor targeted by SARS-CoV-2, and other identifying immune cells called macrophages and neutrophils.

In normal lung tissue, macrophages make up less than 4% of the cells; in COVID-19 lungs, they sometimes topped 50%, Mason reported at the AGBT meeting. The lung itself changes as well, he and his colleagues discovered by looking at gene activity in these lung samples. Late in the disease, the organ's normal cellular architecture was disrupted, and cells adjacent to blood vessels had changed.

The WCM group and others have done spatial analyses of gene activity for other parts of the COVID-19–ravaged body. The coronavirus seems to turn off genes in nasal cells that sense smells and causes a reorganization of the cells in the lining of the nose; those changes may contribute to the loss of smell and taste infected people often experience. The hearts of COVID-19 patients also betrayed an impact. Under the microscope they appear to have a normal number of muscle cells, Mason says, "but if you look at gene expression, it seems the cells have forgotten what they are supposed to be doing."

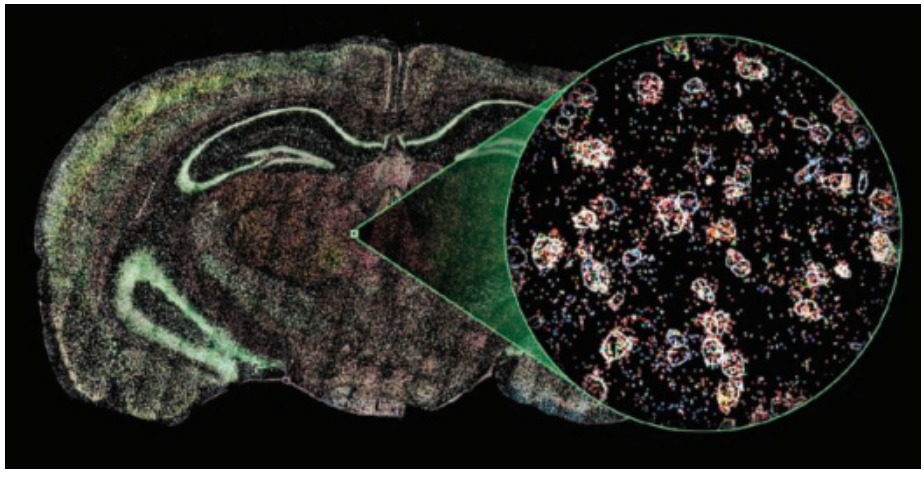

A magnified view (inset) of a slice of mouse brain reveals genes active in cells (marked by white nuclei).

IMAGE: REBUS BIOSYSTEMS, INC.

Stanford University neuroscientist Andrew Yang has done a similar gene activity comparison of preserved human brain tissue to understand why some people with protein deposits called amyloid plaques don't develop Alzheimer's disease and others do. In tissue from Alzheimer's patients, nonneuronal cells close to these plaques show increased activity of genes whose proteins mark nerve cell connections called synapses for destruction. Other revved up genes suggest increased action by scavenger cells called microglia, which prune synapses and cause potentially harmful inflammation. "We're beginning to understand what makes for a good or bad response to these aggregates," Yang says.

These early results only begin to address the potential of spatial transcriptomics. The current methods don't yet work robustly in all types of tissues, and analyses can take days to complete. Companies continue to upgrade their instruments, but so far, none can really quantify all the active genes in a tissue at the single-cell level.

At about $300,000 each, some of the machines are also prohibitively expensive for many labs. The Broad Institute has come up with a cheaper DIY version. Called "Slide-seq," the technique uses a layer of tiny beads, coated with pieces of barcoded DNA, on a slide to help mark the positions of mRNA from thousands of genes (*Science*, 29 March 2019, p. 1463). At the AGBT meeting, Broad genomicist Robert Stickels described version 2.0, which crams much more DNA onto each bead and can put up to 1 million beads on a slide, making the gene-activity mapping more precise by an order of magnitude.

The entire protocol is public, Stickels says. "It really empowers other labs to do it." For example, Abhishek Sampath Kumar, a graduate student at the Max Planck Institute for Molecular Genetics, now gets slides from Broad. "This technique is easy to apply," says Kumar, who is studying mammalian heart development. "You don't need any special instruments compared to other methods."

Both industrial and academic labs are racing to improve spatial transcriptomics and to extend cell-by-cell mapping to other key indicators. "Soon there will be technologies that give you more and more types of data all together at the same time, spatial information, RNA, DNA, chromatin, protein, temporal information about cellular histories, metabolite profiling, you name it, at single-cell resolution," Stickels predicts.

Many biologists are thrilled at the prospects. "I think we will be rewriting the textbook on how organisms develop, and we are going to understand how the body responds to drugs in a way that nobody has been able to do before," Beechem says. "Spatial biology is providing the next revolution in biology." ■

RESEARCH FUNDING

Europe may bar neighbors from key research

Quantum and space grant rules would exclude U.K., Swiss, and Israeli researchers

By **Nicholas Wallace**

In a sign of growing national tensions over the control of strategic research, the European Commission is trying to block countries outside the European Union from participating in quantum computing and space projects under Horizon Europe, its new research funding program.

The proposed rules, which must still be approved by delegates from the 27 EU member states in the coming weeks, would shut out researchers in nations accustomed to access to European research programs, including Switzerland, the United Kingdom, and Israel. European Economic Area (EEA) countries Norway, Lichtenstein, and Iceland would be barred from space projects while remaining eligible for quantum computing funding.

Research advocates see the proposed restrictions as self-defeating for all parties, including the European Union. "It would be a classic lose-lose, with researchers in all countries having to work harder, and spend more, to make progress in these fields," says Vivienne Stern, director of UK Universities International. The unexpected news has upset leaders of collaborations and left them scrambling to find out whether they will need to exclude partners—or even drop out themselves—if they want their projects to be eligible for further funding. "It is really a pity because we have a tight and fruitful relationship with our partners in the U.K.," says Sandro Mengali, director of the Italian research nonprofit Consorzio C.R.E.O. and coordinator of an EU-funded project developing heat shields for spacecraft.

In 2018, when the European Commission first announced plans for the €85 billion, 7-year Horizon Europe program, it said it would be "open to the world." Switzerland, Israel, the EEA nations, and other countries have long paid to "associate" with EU funding programs like Horizon Europe—giving their researchers the right to apply for grants, just like those in EU member states. After leaving the European Union, the United Kingdom struck a deal in December 2020 to join Horizon Europe, which put out its first grant calls last month through the European Research Council. (Switzerland and Israel are currently seeking membership in the program.)

But more recently, "strategic autonomy" and "technological sovereignty" have become watchwords among policymakers in Brussels, who argue the European Union should domestically produce components in key areas like quantum computing and space technology. Those views influenced the Commission's research policy department, overseen by EU research commissioner Mariya Gabriel, which drafted the calls and their eligibility rules, first revealed by the news website Science|Business. The draft says the restrictions are necessary to "safeguard the Union's strategic assets, interests, autonomy, or security."

EU research chief Mariya Gabriel has called for strategic autonomy.

PHOTO: FRANCISCO SECO/AP IMAGES

"It's a bit of a contradiction," says a Swiss government official who asked to remain anonymous because of the sensitivity of forthcoming discussions. "You want to open the program to the world and work with the best. But the core group of associated countries with whom you're used to working, suddenly you exclude them and force them to work with the competitors." The official says the Commission gave no warnings the proposal was coming but believes the combination of Brexit and the COVID-19 crisis, in which Europe has struggled to secure access to vaccines, masks, and other equipment, may have further spurred Europe to guard its technologies.

The restrictions affect €170 million in funding that could be available in the next few months. The affected areas include quantum computing, quantum communications, satellite communications, space transport, launchers, and "space technologies for European non-dependence and competitiveness." Projects relating to the Copernicus Earth-observation system and the Galileo satellite-navigation programs would remain largely open to associated countries.

Shutting out the associated countries would be a "lost opportunity" and could slow progress in quantum computing, says Lieven Vandersypen, a quantum nanoscientist at the Delft University of Technology in the Netherlands. "To me, it doesn't make sense." Vandersypen contributes to an EU-funded project that is investigating how to create the basic bits of a quantum computer from cheap and readily available silicon. The project includes U.K. and Swiss researchers at University College London and the University of Basel. "They are in there for a good reason," Vandersypen says. "They bring in really valuable expertise." With a few years left on the grant, the project isn't in any immediate danger. But the exclusions would be bad for long-term planning, Vandersypen says.

Non-EU researchers working on a €150 million European quantum "flagship" initiative set up in 2018 are also upset by the sudden reversal and wonder about their future status. "We discuss with our partners in Europe, they ask us, 'Can you join?' And we don't know—that's probably the worst thing," says Hugo Zbinden, a quantum physicist at the University of Geneva and coordinator of one of these flagship projects, QRANGE, which is investigating how a quantum random number generator can improve encryption.

Following outrage over the exclusions, the Commission was expected to send revised rules to delegates this week, ahead of a virtual meeting on 25 March. As *Science* went to press, it was not known whether the new draft would keep the exclusions. "Of course, you hope that we will be in," Zbinden says. "For the time being, we are waiting for some news." ■

Nicholas Wallace is a journalist in Brussels.

A nurse dons a face mask at Houston Methodist Hospital on 4 July 2020.

PHOTO: ERIN SCHAFF/THE NEW YORK TIMES/REDUX

MEDICINE'S LONGEST YEAR

Physicians sift through a torrent of research to find what works to treat COVID-19

By **Kelly Servick**, **Jennifer Couzin-Frankel**, *and* **Catherine Matacic**

Ready or not, the patients were coming. This time last year, physicians around the world prepared, most for the first time in their careers, to treat a new disease—over and over and over again.

"There was a terrible sense of foreboding, like in a movie when the minor key music starts playing," says Robert Arntfield, a critical care physician at Western University in London, Canada.

In Wuhan, China, the doctors who first encountered the pandemic coronavirus raced to share surprising symptoms and possible treatments with far-flung colleagues.

Science's COVID-19 reporting is supported by the Heising-Simons Foundation.

In Tokyo, ill cruise ship patrons from the *Diamond Princess* were wheeled into the hospital of the National Center for Global Health and Medicine. Infectious disease physician Norio Ohmagari dusted off the best treatment plan he had: one for the related coronavirus that causes Middle East respiratory syndrome. "Honestly," he says, "we were not quite sure what we could do."

Cornerstones of care

Doctors have few treatments for the early stages of COVID-19, but have developed a small arsenal of therapies to employ as symptoms become more severe. Research continues on how and when to administer drugs, oxygen, and other treatments.

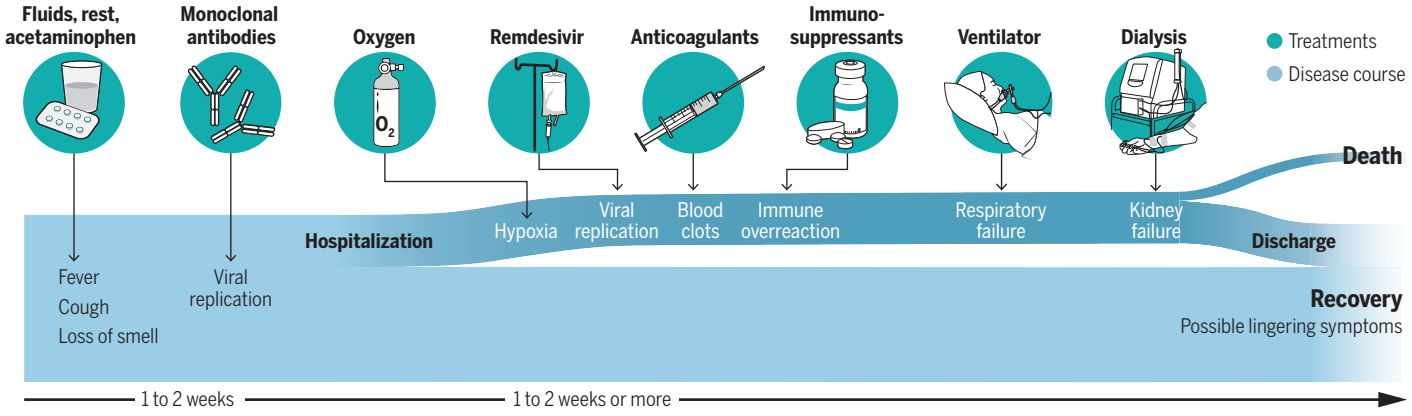

Monoclonal antibodies appear to reduce risk of hospitalization in outpatients at high risk of severe disease—provided patients can access them.

Oxygen, delivered through nasal prongs, a mask, or an invasive breathing tube, is crucial to COVID-19 care. But how it's administered varies among hospitals.

The antiviral remdesivir is widely used in hospitalized patients, but evidence is mixed on whether it shortens hospital stays. It hasn't been shown to improve survival.

Anticoagulants can prevent blood clots that are common in COVID-19 patients, but physicians must weigh the risk of bleeding when deciding the right dose.

The immunosuppressant drugs dexamethasone and tocilizumab have both reduced mortality in large clinical trials of hospitalized patients, showing it's possible to tame the potentially deadly inflammation that characterizes severe disease.

In the United Kingdom's Cynon Valley, a man arrived at a clinic for routine bloodwork, then announced he had a high fever and cough. Shouts went out for a doctor. As primary care physician Chris Butler prepared to assess the patient, "I was dropping my gloves," he says. "I was pretty nervous."

Over the harrowing year that followed, clinical evidence on how to treat the pandemic coronavirus poured in—a muddy torrent of hundreds of thousands of papers, preprints, and press releases. Many physicians were torn between waiting for results from large clinical trials, the gold standard of evidence, and offering something, anything, to the gravely ill patients in front of them. "These are smart physicians who are watching people get very sick, watching people die, feeling helpless, and wanting to do whatever they can," says Lisa Moores, a pulmonary and critical care physician at the Uniformed Services University of the Health Sciences in Bethesda, Maryland.

Unproven drugs became first-line treatments. "Tens or hundreds of thousands of patients got ineffective or harmful therapies," says Matthew Semler, a critical care physician at Vanderbilt University, citing widespread use of the antimalarial drug hydroxychloroquine, now known to prevent neither disease nor death.

Physicians memorized treatment guidelines one day only to learn they'd changed the next. "When you have the whole world working on something at the same time … the evidence evolves fast," says Meghan Lane-Fall, a critical care physician who studies health care delivery at the University of Pennsylvania (UPenn). "Every time I take care of a COVID patient … I have to sit down and go, 'OK, what are we doing now?'" Even today, she says, "There is no single standard of care."

Yet 12 months after the World Health Organization (WHO) declared a pandemic, physicians have gleaned a rough understanding of COVID-19's pathology and an aspirational strategy for treating it: Early in the illness, the goal is to stave off severe disease by stopping the virus from replicating. As infection progresses, the primary enemy becomes a hyperactive immune response that wreaks havoc on the body's organs (*Science*, 24 April 2020, p. 356).

A few therapies—mostly repurposed drugs—have risen to the top. Dexamethasone, a cheap and common steroid, surprised doctors by slicing mortality in the sickest patients in a randomized trial; another anti-inflammatory, tocilizumab, also helped patients survive. The antiviral drug remdesivir, which appeared to speed recovery in some studies but not in others, is widely used in hospitalized patients. Monoclonal antibodies, meanwhile, are playing catch-up: Given early, they may help avert severe disease, but they can be tough to deliver to outpatients, and some appear less potent against new viral variants. Beyond drugs, physicians have honed their intensive care unit (ICU) practices to support patients' failing organs.

COVID-19 remains enigmatic—and deadly—but shifts in care appear to have helped. An analysis published this month of nearly 200,000 patients in 555 U.S. hospitals found mortality rates dropped from 22.1% in March 2020 to 6.5% in August, although factors beyond new treatments, such as reduced crowding in hospitals, may have also played a role. After a traumatic year, doctors describe scientific progress they couldn't have imagined—and a crisis that brought into stark relief the challenges of applying research to the art of medicine.

"I'M SORRY TO SAY that your COVID test came back positive."

More than 120 million people have heard some version of those words, setting them on an uncertain path. About 10% to 15% will veer into serious illness, and others will face enduring, sometimes disabling symptoms. Gamely pumping the brakes are primary care doctors, trained to handle everything from warts to stomach bugs. "My patients are my family," says Ada Stewart, a physician in South Carolina and president of the American Academy of Family Physicians (AAFP), who is haunted by the loss of about 10 of her patients to the virus.

Family physician Ada Stewart watches her COVID-19 outpatients for signs of worsening disease.

CREDITS: (GRAPHIC) N. DESAI/*SCIENCE*; (PHOTO) AAFP

Newly diagnosed patients "come into the clinic asking, 'What can you give me right now that can prevent me from going down this pathway … [of becoming] very, very sick?'" says Jacqueline Chu, a physician in primary care and infectious disease who serves a working-class population in Chelsea, Massachusetts, that has been hit hard by COVID-19; her clinic is affiliated with nearby Massachusetts General Hospital.

Outpatient care is often basic, and Chu offers the same advice she does for riding out any virus at home: fluids, rest, and acetaminophen for pain and fever. But doctors now know which patients are more likely to develop serious disease; they keep closer tabs on the elderly and those with heart disease, diabetes, or obesity. When scientists at the Cleveland Clinic crunched data on everyone receiving a positive COVID-19 test through their health system, they identified another risk factor for severe illness: living in some of the poorest ZIP codes. Those patients now get 2 weeks of daily checkins to spot symptoms quickly.

Doctors also know that even robust young people who appear to be recovering one day can deteriorate the next. To spot falling blood oxygen levels, pulse oximeters have become the new thermometers, widely recommended for home use.

Testing experimental treatments for newly diagnosed people has proved difficult. Some clinical trials struggle to find participants because community clinics are disconnected from trial infrastructure, says Butler, who runs the PRINCIPLE trial, among the largest studying high-risk people with COVID-19 at home, out of the University of Oxford's Nuffield Department of Primary Care Health Sciences.

PRINCIPLE's chief successes thus far have been in identifying what doesn't work: In late January, it announced that the antibiotics azithromycin and doxycycline—tried because they have some anti-inflammatory and antiviral properties and because bacterial infections may set in after the virus takes hold—failed to speed recovery in outpatients.

Other trials have racked up failures, too. After months of urging COVID-19 survivors to donate antibody-rich plasma for infusion into infected people, the U.S. National Institutes of Health (NIH) this month halted a trial of convalescent plasma in patients with mild and moderate illness, finding it wasn't improving outcomes. Last week, a preprint on a large U.K. trial reported no survival benefit in hospitalized patients, either. Trials in outpatients are ongoing.

Such failures can guide care and help doctors dissuade patients from embracing dubious treatments. "I had patients buying COVID 'treatment packs' from Mexico" that claimed to include antibiotics, steroids, and vitamins, says Andrew Carroll, a family physician in Chandler, Arizona. "None of this has any basis in research."

Sarah Coles, who practices family medicine in nearby Phoenix, chairs the AAFP commission that issues treatment guidelines to its 136,000 members. These days she's tracking data on a promising therapy: monoclonal antibodies. These labmade proteins mimic the body's own immune response and are designed to block the virus from attaching to cells. In November 2020, after interim trial data suggested they could cut the risk of hospitalization by two-thirds and prevent deaths, the U.S. Food and Drug Administration (FDA) gave emergency use authorization to monoclonal antibodies made by the drug companies Regeneron and Eli Lilly and Co.

But the antibodies have to be infused at a hospital or specialized site within days of the first symptoms—a logistical challenge. "We have not created the on-ramps" to ease access, says David Wohl, an infectious disease doctor at the University of North Carolina (UNC), Chapel Hill, who's working to widen the entry points. The 1800 doses administered at UNC are a fraction of what patients needed, he suspects. And in South Carolina, Stewart has rural patients without transportation for whom the therapy is literally out of reach. Meanwhile, supplies of the drugs have fluctuated, and at least some monoclonals seem to falter when facing new viral variants.

What's more, official guidance is equivocal on antibodies. With clinical trials ongoing, NIH treatment guidelines say there are "currently insufficient data to recommend either for or against" most monoclonal antibodies, although on 2 March the agency suggested an Eli Lilly cocktail be offered to those at high risk of severe disease days after symptoms appear. The guidelines strike some physicians as too conservative. But Coles wants to see outcomes from more trial participants before fully embracing monoclonals. "We've been burned before," she says.

With a meager arsenal, physicians like Coles and Stewart listen carefully, coach patients on symptoms to watch for, and make judgment calls. One day not long ago, a patient of Stewart's 1 week out from diagnosis

In Milan, a team of intensive care unit doctors and nurses gathers information to coordinate care for COVID-19 patients.

PHOTO: DANIELE FREDIANI/ARCHIVIO DANIELE FREDIANI/MONDADORI PORTFOLIO/GETTY IMAGES

described intense fatigue and chest pain. Stewart felt her own worries rising. "Get to the hospital," she advised. Once there, the patient turned out to have blood clots in both lungs and was quickly admitted—passing into the hands of a new medical team trying to shield her from the worst.

COVID-19 PATIENTS who arrive at the hospital doors have reached a precarious point. Most have endured at least a week of fever, coughing, and fatigue as viral particles multiplied throughout their bodies. Now, they're on the cusp of a more perilous stage, in which a misfiring immune system can wreak havoc on their organs.

Elevated levels of immune signaling molecules in the blood are a marker of danger. But one of the clearest signs of trouble is a blood oxygen level below 94%, says Varidhi Nauriyal, an infectious disease specialist at the University of Pittsburgh. So the first treatment for people hospitalized with COVID-19 is oxygen, typically delivered through a mask or nasal prongs.

Most patients also get remdesivir, the lone COVID-19 treatment that's been formally approved by FDA. The antiviral caught researchers' attention early last year for its ability to inhibit SARS-CoV-2 in a lab dish. In April, an international NIH-sponsored trial reported that the drug shortened hospital stays by several days. But in October, WHO's much larger trial, Solidarity, found no improvement in recovery time or mortality (*Science*, 23 October 2020, p. 388). NIH's treatment guidelines recommend remdesivir, but WHO's do not.

"It doesn't seem to be the miracle drug that we would like it to be," says Mangala Narasimhan, a pulmonary and critical care physician at New York's Northwell Health system. But because remdesivir has few side effects and became entrenched in many treatment plans early in the pandemic, it remains standard therapy in most hospital wards and some ICUs, says Leora Horwitz, a hospitalist and health care systems researcher at New York University's Langone Health. "I don't think it's going to do people any harm, I just don't think it's going to do them very much good," she says.

Patients are also routinely treated for a common complication of COVID-19: blood clots, which develop in the veins of an estimated 17% of hospitalized patients and nearly 30% of ICU patients. Those clots can travel to the lungs, cutting off blood flow to the heart, or to the brain, where they can cause a stroke. Many guidelines call for giving most people a low, prophylactic dose of anticoagulants on admission.

But as patients worsen, physicians struggle over whether to up the anticoagulant dose, which boosts the risk of gastrointestinal and intracranial bleeding. Three trials—the United Kingdom's REMAP-CAP, the NIH-led ACTIV-4, and Canada's ATTACC—are rushing to clarify the risks and benefits.

In December 2020, all three trials stopped enrolling ICU patients, citing concerns about bleeding; preliminary results posted in a preprint this month found no survival benefit in the ICU. But in January, interim results from more than 1000 non-ICU patients looked promising: Compared with a prophylactic dose, full-dose blood thinners reduce the need for organ support and may also reduce mortality, NIH announced.

If those data hold up, they are "pretty profound," says Todd Hecht, a hospitalist and director of the anticoagulation management program at the Hospital of the University of Pennsylvania (HUP). Perhaps ICU patients were simply so sick that high-dose anticoagulants had no effect, he says.

Large, randomized trials are the best way to disentangle the complex realities of COVID-19 care. But doctors sometimes sought faster ways to help the patients in front of them. At Henry Ford Hospital in Detroit, the flood of deteriorating patients in March 2020 prompted doctors to consider a then-unproven therapy: corticosteroids, drugs used for decades to reduce inflammation in conditions from asthma to allergies. Infectious disease specialist Mayur Ramesh and his team reviewed emerging evidence from China and decided to run what they called a "quasiexperiment." Starting in late March, they gave all COVID-19 patients on oxygen a 3-day course of the corticosteroid methylprednisolone and compared their outcomes with those of patients admitted earlier.

The team debated doing a full clinical trial, says Nauriyal, who was then helping supervise Henry Ford's ICU. But many had high hopes for the therapy and didn't want to withhold it from a control group.

By early April, they saw a signal in their data: Of 81 patients admitted before steroids were added to treatment, 44% moved to the ICU and 26% died; for 132 patients admitted later, those numbers were 27% and 14%. Convinced the treatment was saving lives, Ramesh called colleagues at dozens of other institutions to spread the word. But without the rigor of a randomized trial or peer-reviewed data, few hospitals were willing to change their practice.

The Henry Ford team continued to dose patients with steroids, other medications, and oxygen, and many got better. But as everywhere, some patients deteriorated. As their lungs or other organs failed, they were transferred to a new space full of hissing and beeping equipment: the ICU.

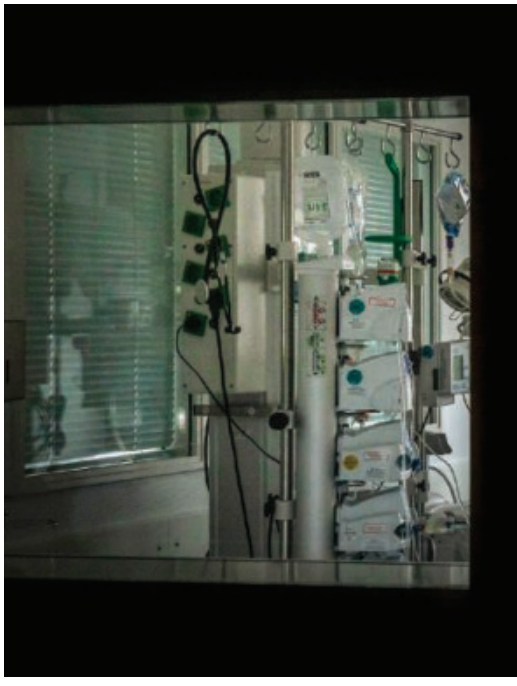

PHOTO: ALEXANDER ROSSBACH/VISUM/REDUX

"THEY'RE ALL THE SAME." That was the impression Lane-Fall had when the first seven COVID-19 patients arrived in her ICU at HUP in March 2020. "And they're all super-sick."

U.S. records suggest nearly 30% of COVID-19 patients admitted to the hospital move to the ICU. Those critically ill patients face an inflammatory assault on their lungs and other organs. Many have multiple blood clots, and some require dialysis to support faltering kidneys.

When patients with lung failure began to fill ICUs 1 year ago, many physicians fell back on years of experience with acute respiratory distress syndrome (ARDS), a life-threatening buildup of fluid in lungs damaged by trauma or infection. "If someone had told me, 'You're going to be hearing a lot of stuff, but this is ARDS. Treat ARDS,' that would have gone a huge way" toward reassuring physicians, says UPenn critical care physician George Anesi. In COVID-19 treatment, "Some of the foundational principles of critical care medicine really emerged [as] true," he says. Those include proning—periodically flipping patients onto their stomachs to make full use of their lungs—and management of mechanical ventilators.

Choosing the right ventilator settings presents judgment calls. Forcing too much air into the lungs can further damage them. But delivering smaller, rationed breaths can distress patients; sedation to reduce that discomfort brings its own problems. Striking the right balance "is not drug development or anything fancy," Semler says, "but this is what you're actually doing all day, every day."

A nurse adjusts the oxygen supply—crucial to COVID-19 care—of an ICU patient in Nuremburg, Germany.

An even bigger dilemma was who to put on ventilators in the first place. Because COVID-19 patients' oxygen levels can crash abruptly, early wisdom was to insert a breathing tube at the first sign of trouble. Compared with noninvasive methods, mechanical ventilation was also suspected to better contain viral particles and carry less risk of infection for hospital staff. But patients who spend long periods on a ventilator generally face a long recovery. Gradually, physicians started to use ventilators more sparingly. A preprint released in mid-April suggesting less aggressive oxygen therapy did not increase airborne viral particles reassured some doctors about their own risk.

Instead of moving declining patients to a ventilator, some hospitals have tried a 6- to 24-hour "trial period" with a high-flow oxygen mask and careful monitoring, says critical care physician Massimiliano Greco of the Humanitas Research Hospital in Milan. "What we learned is that some of these patients can actually do well," he says. Although a clinical trial might pinpoint the right time to intubate, Lane-Fall says the risks of intubating too early are already clear enough that a randomized trial wouldn't be ethical.

But randomized trials have brought welcome clarity about one drug, the corticosteroid dexamethasone. Recovery, an Oxford-led effort with tens of thousands of hospitalized participants across the United Kingdom, included dexamethasone in trials of a lineup of potential therapies.

The results for the sickest patients were dramatic: In the subset of about 1000 Recovery participants on invasive mechanical ventilation, mortality 28 days after admission was 29%, versus 41% for those getting usual care. Given how many drugs fail in trials for critically ill patients, that effect size "was far in excess of anything that any grant reviewer would have said is even plausible," says Kenneth Baillie, a critical care physician at the University of Edinburgh and one of the trial investigators. "I'm going to devote my whole career to medical research, and that one paper on steroids is probably going to be [my] most important."

At Henry Ford, Ramesh's team was ecstatic when Recovery announced results in June, a month after Ramesh and colleagues had published their methylprednisolone findings. Both drugs are steroids with similar methods of action, suggesting Henry Ford's gamble hadn't been far off base.

Yet for patients on oxygen but not ventilators, Recovery's results were less dramatic: 23% mortality, versus 26% in patients who got usual care. Oxygen needs and severity of illness vary widely in that group, leaving some uncertainty about which patients benefited, notes UPenn critical care physician Nuala Meyer. That's a cost of Recovery's simple design, she says. The trial "needed to not be burdensome to providers," she says, "but you sacrifice some level of detail."

In Recovery participants who didn't need supplemental oxygen at enrollment, dexamethasone was actually linked to increased mortality. That may be because early in disease, steroids can prevent the immune system from clearing the virus, Ramesh says. He worries that some emergency room and urgent care doctors are giving dexamethasone too soon. "If you don't understand the timing, you are just throwing things at people," he says. "You may be hurting them."

Last month, another arm of the Recovery trial found mortality reductions with tocilizumab, a newer, more expensive anti-inflammatory drug approved to treat rheumatoid arthritis that blocks inflammatory signaling by the molecule interleukin-6. Those results echoed positive findings from the U.K. REMAP-CAP trial, first released in a January preprint.

Earlier trials had failed to find benefits. But most patients in the Recovery and REMAP-CAP trials were also getting dexamethasone, which may have tamed inflammation enough for tocilizumab to have an effect, says Roy Gulick, an infectious disease doctor at Weill Cornell Medicine who co-chairs the NIH COVID-19 treatment guidelines panel.

As with monoclonal antibodies, converting studies into treatment recommendations isn't straightforward. With tocilizumab, "The big question from the data we have today is, which group benefits?" Gulick says. After weeks of deliberation, the NIH panel on 5 March recommended tocilizumab alongside dexamethasone for patients who resemble Recovery or REMAP-CAP participants in oxygen needs, inflammatory markers, and other factors.

Doctors may lack clarity about how best to use dexamethasone and tocilizumab, but having two proven drugs available against a brand-new virus is remarkable, says intensive care physician Antoine Vieillard-Baron of the Ambroise Paré University Hospital, outside of Paris. "It's big, big news."

One year into the pandemic, however, exhausted doctors long for much more: treatments that can stop patients from reaching the ICU, or even the hospital, in the first place. "The amount of death that we've seen this year is just terrible," Narasimhan says. Vaccines are starting to curb infections in some parts of the world, but many people will get sick in the coming months. They need a treatment to stop viral replication before the inflammatory cascade begins.

"The real therapeutic approach would be a direct antiviral," Anthony Fauci, director of the National Institute of Allergy and Infectious Diseases, told *Science* earlier this year. Also needed are drugs that can silence the precise cellular signals driving inflammation, Baillie says. "How do we stop people dying of COVID?" he asks. "I think in the future, that must be achievable." ■

INSIGHTS

PERSPECTIVES

Light and heat sensors on a building at the University of Southern Denmark adjust shutters to optimize indoor conditions.

ENGINEERING

Smart cities built with smart materials

Sensors and actuators that respond locally avoid overburdening data analysis networks

By **Rebecca Napolitano[1], Wesley Reinhart[2], Juan Pablo Gevaudan[1]**

The Smart City Index (*1*) defines a smart city as "an urban setting that applies technology to enhance the benefits and diminish the shortcomings of urbanization for its citizens." The top-ranked city, Singapore, has addressed urban challenges with information technology since 2014 through its Smart Nation Initiative (*2*). The influence of technology is reflected in the city's open platform for sharing energy data, crowdsourced location data for smart navigation, and even online forums for citizen participation in policy-making (*2*). The smart city concept requires the acquisition of massive amounts of data in real time, and large networks of smart devices must spread the burden of communication and processing evenly across the network to prevent information overload at its center. Opportunities to solve this challenge have recently emerged through the development of increasingly "smart materials" that can sense, process, and respond to environmental stimuli without centralized resources.

A recent market analysis predicted that the number of connected devices, sensors, and actuators that constitute the Internet of Things (IoT) will reach more than 46 billion in 2021, driven largely by reduction in hardware costs to as little as $1 per device (*3*). Inexpensive connected sensing devices measuring strain, temperature, and humidity (*4*), as well as the enhancement of indirect sensing methods that use computer vision and crowd-sourcing (*5*), provide vast amounts of data to quantify the built environment (*6*). The ability to continuously monitor the physical state of infrastructure with high resolution in time and space has exciting implications for sustainability and equity. Quantitative, data-driven decision-making can enable predictive maintenance in place of conventional intuition-based workflow, although such automated systems can also learn to replicate human biases (*7*).

However, efficient decision-making based on these data streams becomes limited by the burden of transmitting and processing the raw, unprioritized data. As the number of connected devices rises, smart cities have shifted from a hierarchical network architecture based on cloud computing to a more decentralized information ecosystem.

[1]Department of Architectural Engineering, Pennsylvania State University, University Park, PA 16802, USA. [2]Department of Materials Science and Engineering, Pennsylvania State University, University Park, PA 16802, USA. Email: napolitano@psu.edu

PHOTO: HUFTON+CROW/VIEW PICTURES/UNIVERSAL IMAGES GROUP/GETTY IMAGES

Managing structural data

Infrastructure decision-making can benefit from distributed sensor data if data can be processed efficiently. Data management can benefit from "need-to-know" processing strategies, as illustrated for the construction of a subway system, where tunneling can create ground-surface subsidence that can undermine an overlying building. At the city scale, analysis of these data can lead to decisions to mitigate subsidence impact, such as stopping tunneling or adding underlying support.

Macroscale networks
The data from the mesoscale network are processed through fog computing within the building and passed to city-wide networks.

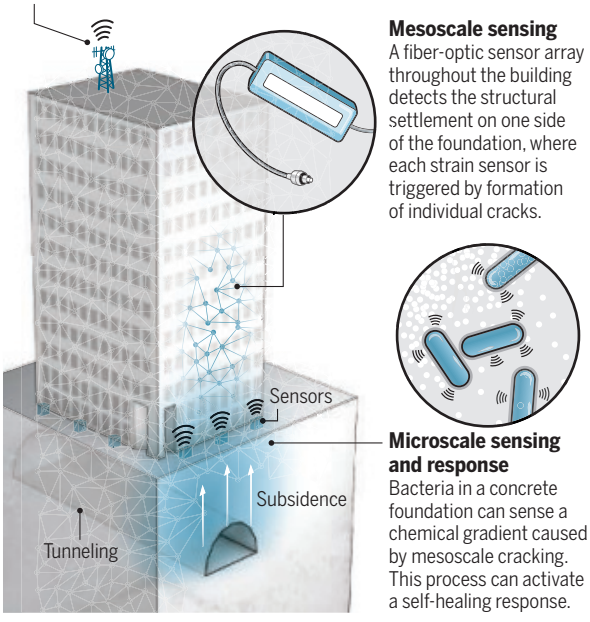

Mesoscale sensing
A fiber-optic sensor array throughout the building detects the structural settlement on one side of the foundation, where each strain sensor is triggered by formation of individual cracks.

Microscale sensing and response
Bacteria in a concrete foundation can sense a chemical gradient caused by mesoscale cracking. This process can activate a self-healing response.

GRAPHIC: V. ALTOUNIAN/*SCIENCE*

In this so-called "fog computing" model, data processing is performed at the edge of the network to avoid costly communication with a central cloud server (*8*). Alternatively, "mist computing" represents an even more extreme paradigm in which data processing is handled by microprocessors attached directly to the sensors and actuators. One advantage of mist computing is a reduced burden on communications systems by constraining information to a "need-to-know basis." This approach has an added sustainability benefit because communication among IoT devices accounts for as much as five times the power consumption necessary for the computation itself (*9*).

Orthogonal to these advances in IoT technology, multifunctional and responsive materials have been designed to substantially alter their shape or properties in response to external stimuli. When taken to the extreme, this concept results in "living materials," which use biological organisms (*10*) as highly efficient chemical machines for sensing and responding to their environment. Such materials are engineered to sense and regulate their state at the microscopic scale to effect macroscopic structural or functional changes. A common function of smart or living materials is self-healing to improve the service life of a larger structure in support of its sustainability. For example, bacteria-triggered self-healing represents one of the most popularized concepts in living cementitious materials. Extensive research has been conducted on the use of extremophiles and engineered bacteria to imbue materials with the self-sensing capacity needed to trigger these self-healing properties (*10*).

In effect, these smart and living materials participate in an extreme version of the mist-computing model for structural health monitoring. Chemical gradients in the cement are detected, interpreted, and acted upon by means of incredibly low-power sensing and response mechanisms without increasing the communication and processing burden on the built environment. This latter point is critical because the electronic sensing and transmission of millimeter-scale chemical gradients across an entire smart city would absolutely overwhelm digital data processing systems. Information at this small scale is also irrelevant to decisions being made for an entire city block, so restricting it to an appropriate level reduces the cognitive load on stakeholders such as building managers and government policymakers (see the figure). This approach is analogous to how the human nervous system coordinates the contraction of many millions of cells through a hierarchy of control structures, rather than by consciously addressing individual muscle fibers.

Smart materials can also process data without the assistance of active biological matter. A fascinating example of computation in material substrates is the recent demonstration of photonic "metamaterials" (internally structured materials) that can solve complex mathematical equations (*11*). These devices exploit diffractive optics to leverage material microstructure into passive, all-optical transformations. A complementary idea is that of "mechanologic," in which a mechanical metamaterial deforms in a preprogrammed way to combine computation and actuation (*12*). Given the rapid advancements in design and fabrication of these extraordinary materials, a next generation of smart materials may emerge with programmed thermal, optical, and mechanical responses acting as a self-sensing, self-actuating smart façade, or as a solar tracker to improve the efficiency of photovoltaic energy harvesting (*13*).

With connected sensors being deployed to provide real-time structural health monitoring of critical infrastructure [e.g., bridges, dams, residential and commercial buildings, and even temporary structures (*14*)], managing the flood of data is more important than ever to prevent smart cities from suffering "analysis paralysis." Smart and living materials may push data processing to previously unimagined extremes, with the literal foundations of the built environment acting as analog-computing substrates. This approach should offer pronounced advantages for sustainability, including increased longevity of infrastructure, reduced waste from the proliferation of electronic sensors, and reduced power consumption from communications. Moreover, the current challenge to implementation of mist-computing infrastructures is tied to their complexity and size, which are too great to manage by centralized systems (*15*). Thus, autonomous smart materials present a compelling tool in achieving robust and sustainable structural health monitoring in smart cities of the future. ■

REFERENCES AND NOTES

1. IMD, *Smart City Index 2020—A Tool for Action, an Instrument for Better Lives for All Citizens* (2020), p. 123.
2. J. J. Woo, *Technology and Governance in Singapore's Smart Nation Initiative* (Harvard Kennedy School, 2018).
3. S. Barker, M. Rothmuller, "The Internet of Things: Consumer, Industrial & Public Services 2020–2024" (Juniper Research, 2020).
4. V. Moustaka, A. Vakali, L. G. Anthopoulos, *ACM Comput. Surv.* **51**, 103 (2018).
5. C. Z. Dong, F. N. Catbas, *Struct. Health Monit.* 10.1177/1475921720935585 (2020).
6. A. Salazar Miranda, Z. Fan, F. Duarte, C. Ratti, *Comput. Environ. Urban Syst.* **86**, 101563 (2021).
7. F. Duarte, P. deSouza, *Harvard Data Sci. Rev.* 10.1162/99608f92.b3fc5cc8 (2020).
8. J. Santos, T. Wauters, B. Volckaert, F. De Turck, *Entropy* **20**, 4 (2018).
9. E. M. Dogo, A. F. Salami, C. O. Aigbavboa, T. Nkonyana, in *Edge Computing: From Hype to Reality* (Springer, 2019), pp. 107–132.
10. P. Q. Nguyen, N. M. D. Courchesne, A. Duraj-Thatte, P. Praveschotinunt, N. S. Joshi, *Adv. Mater.* **30**, 1 (2018).
11. N. M. Estakhri, B. Edwards, N. Engheta, *Science* **363**, 1333 (2019).
12. B. Treml, A. Gillman, P. Buskohl, R. Vaia, *Proc. Natl. Acad. Sci. U.S.A.* **115**, 6916 (2018).
13. F. M. Hoffmann, R. F. Molz, J. V. Kothe, E. O. B. Nara, L. P. C. Tedesco, *Renew. Energy* **115**, 750 (2018).
14. M. Flah, I. Nunez, W. Ben Chaabene, M. L. Nehdi, *Arch. Comput. Methods Eng.* 10.1007/s11831-020-09471-9 (2020).
15. J. S. Preden *et al.*, *Computer* **48**, 37 (2015).

ACKNOWLEDGMENTS

We thank Z. Ounaies for inspiring our research collaborations.

10.1126/science.abg4254

METABOLISM

Immune cell control of nutrient absorption

Intestinal γδ T cells regulate a gut epithelial cell program for dietary sugar uptake

By **Jhimmy Talbot**[1] *and* **Dan R. Littman**[1,2]

The gastrointestinal tract performs the critical function of nutrient acquisition, supplying the energetic and metabolic demands of most metazoan organisms. This process is subject to extensive regulation because of changes in nutrient availability and perturbations of the microbiota, as well as alterations in internal states such as depletion in nutrient stores, reproductive cues (*1*), and immune responses (*2*). The gastrointestinal system must thus have adaptive features that provide plasticity for its diverse functions. On page 1223 of this issue, Sullivan *et al.* (*3*) provide evidence that γδ T lymphocytes, immune cells that reside inside the intestine, are integral to a regulatory circuit that promotes local adaptation to increased abundance of sugars in the diet. This study could contribute to better insights into the association of alterated immune responses with metabolic disorders such as obesity and malabsorption syndromes.

The transcriptional programs associated with absorptive and metabolic functions of the intestine can be altered by food intake and composition of the diet (*4*, *5*). In the duodenum of mice fed with a sugar-rich diet, there is increased expression of genes associated with carbohydrate digestion and absorption (*5*). However, it was unclear how the increase in sugar content promotes changes in intestinal transcriptional programs that are associated with sugar metabolism [called the carbohydrate transcriptional program (CarbTP)].

Because of the extensive experimental evidence for a link between diet, the commensal microbiota, and host metabolism, Sullivan *et al.* examined the role of the host microbiome in controlling diet-dependent plasticity in CarbTP. However, a sugar-rich diet promoted up-regulation of the CarbTP in a microbiota-independent manner, providing evidence that not all intestinal metabolic alterations induced by dietary changes are controlled by the microbiota. The transport of nutrients from the intestinal lumen into the host is promoted by absorptive intestinal epithelial cells that, with their secreted mucins and other specialized epithelial cells, provide a physical barrier and are in direct contact with the ingested diet. The inability to recapitulate in vitro CarbTP increases through direct exposure of these epithelial cells to high amounts of sugar prompted Sullivan *et al.* to postulate that local adaptations to changes in diet composition may require more complex cellular interactions in the mouse intestine. They found that immune cells, and specifically γδ T lymphocytes, were important for up-regulation of the CarbTP in intestinal epithelial cells of mice fed a sugar-rich diet, compared with an isocaloric protein-rich diet. This places an immune cell at the center of a circuit that controls intestinal adaptation to the amount of macronutrients in the diet.

γδ T lymphocytes have distinct abilities to quickly respond to environmental perturbations and orchestrate immune responses. They straddle innate and adaptive immune functions and contribute not only to host antimicrobial defense but also to other physiological functions (*6*). Recent reports have revealed that γδ T lymphocytes can modulate neuronal functions and behavior (*7*), thermogenesis (*8*), and intestinal metabolism (*9*). γδ T lymphocytes in the intestine can modulate host glucose homeostasis through the regulation of metabolic hormone bioavailability (*9*). Sullivan *et al.* describe a mechanism by which γδ T lymphocytes control intestinal metabolic transcription programs. They find that in response to sugar-rich diets, γδ T lymphocytes promote CarbTP up-regulation in epithelial cells through inhibition of another population of resident intestinal immune cells, type 3 innate lymphoid cells (ILC3) (see the figure).

ILC3 control intestinal host-microbiota interactions through the production of secreted factors, particularly interleukin-22 (IL-22), which instructs epithelial cells to increase barrier defense functions. IL-22 production by ILC3 is regulated by signals derived from multiple gut-resident cell types, including enteric glia (*10*), gut neurons (*4*), and other immune cells, such as macrophages (*11*). An inability to down-regulate IL-22 production by ILC3 results in reduced transcriptional programs associated with lipid metabolism in the intestine, as well as altered concentrations of circulating triglycerides and fatty acids (*2*, *4*). Therefore, in mice, ILC3 inhibit metabolic programs associated with lipid absorption while promoting innate immune responses.

Sullivan *et al.* describe a previously unknown role for ILC3 in intestinal metabolism, showing that γδ T lymphocytes can inhibit their production of IL-22. This inhibition is an essential step in intestinal epithelial cell adaptation to sugar-rich diets and up-regulation of CarbTP. It is still unclear how γδ T lymphocytes communicate with ILC3 to instruct down-regulation of cytokine production. Understanding this may help to identify strategies to rectify defects in nutrient absorption through the modulation of innate immune pathways. Moreover, it could also clarify whether immune-mediated alterations in intestinal absorptive functions can explain the association between an altered gut microbiota and malabsorptive dysfunctions in infants (*12*).

Trade-off circuits that coordinate nutrition and immune defense have been described

Immune-mediated intestinal adaptation to dietary alterations

A sugar-rich diet causes relocation of γδ T cells to the intestinal crypt, possibly through prostaglandin E2 (PGE2) signaling, where they inhibit interleukin-22 (IL-22) production by type 3 innate lymphoid cells (ILC3s). This leads to remodeling of epithelial cells and a transcriptional program associated with carbohydrate digestion and absorption (CarbTP).

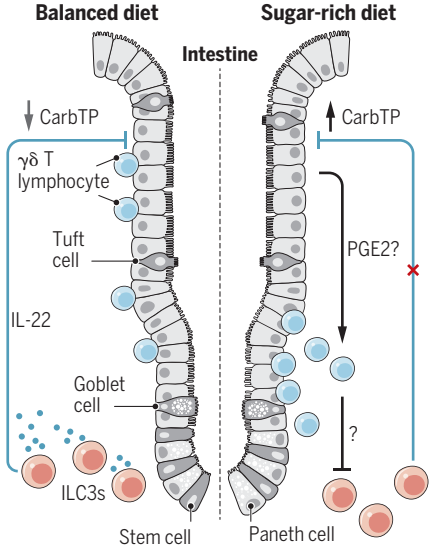

GRAPHIC: JOSHUA BIRD/*SCIENCE*

[1]Molecular Pathogenesis Program, The Kimmel Center for Biology and Medicine of the Skirball Institute, New York University School of Medicine, New York, NY, USA. [2]Howard Hughes Medical Institute, New York, NY, USA. Email: dan.littman@med.nyu.edu; jhimmy.talbot@nyulangone.org

in other organisms. In some plants, a transcription factor that up-regulates responses for increasing nutrient uptake also represses immune defense genes (*13*). It was suggested that negative regulation of plant immune systems is relevant for the assembly of a root-associated microbiota that augments organism growth (*13*). If the same concept can be translated to animals, it will be important to determine whether down-regulation of ILC3-mediated immune responses by γδ T lymphocytes influences the commensal microbiota composition. Such adapted microbiota could have a major role in helping the host handle luminal increases in carbohydrates or could protect the host against intestinal colonization by some enteropathogens through niche-competition (*14*). Conversely, a newly assembled microbiota could also have deleterious effects, such as participating in the progression of host metabolic dysfunctions. Moreover, pathogens can exploit systems that coordinate nutritional and immune responses (*4*, *15*). Therefore, it will be important to determine whether enteropathogens can modulate γδ T lymphocytes, which could lead to inhibition of ILC3-mediated host resistance to some infections.

It is still unknown whether γδ T lymphocytes directly sense luminal signals (increase in sugar content) or if another cellular relay participates in transducing dietary information to γδ T lymphocytes. Sullivan *et al*. provide some evidence suggesting that tuft cells, specialized intestinal epithelial cells, might play a role in the up-regulation of CarbTP on a sugar-rich diet, but more studies are needed to dissect the mechanisms of interaction between epithelial cells, γδ T lymphocytes, and ILC3 in the control of metabolism. It will also be important to learn whether the on-demand regulation of CarbTP by γδ T lymphocytes contributes to overall sugar digestion and absorption. The identification of γδ T lymphocytes as decoders of nutritional input adds to our understanding of how organisms adapt to changes in nutrient availability. ■

REFERENCES AND NOTES

1. D. Hadjieconomou *et al*., *Nature* **587**, 455 (2020).
2. K. Mao *et al*., *Nature* **554**, 255 (2018).
3. Z. A. Sullivan *et al*., *Science* **371**, aba8310 (2021).
4. J. Talbot *et al*., *Nature* **579**, 575 (2020).
5. T. Goda, *Br. J. Nutr*. **84** (Suppl 2), S245 (2000).
6. A. C. Hayday, *J. Immunol*. **203**, 311 (2019).
7. K. Alves de Lima *et al*., *Nat. Immunol*. **21**, 1421 (2020).
8. A. C. Kohlgruber *et al*., *Nat. Immunol*. **19**, 464 (2018).
9. S. He *et al*., *Nature* **566**, 115 (2019).
10. S. Ibiza *et al*., *Nature* **535**, 440 (2016).
11. A. K. Savage, H.-E. Liang, R. M. Locksley, *J. Immunol*. **199**, 1912 (2017).
12. R. Y. Chen *et al*., *N. Engl. J. Med*. **383**, 321 (2020).
13. G. Castrillo *et al*., *Nature* **543**, 513 (2017).
14. J. Behnsen *et al*., *Immunity* **40**, 262 (2014).
15. Y. T. Lu *et al*., *Plant Physiol*. **164**, 1456 (2014).

10.1126/science.abg6455

GRAPHIC: V. ALTOUNIAN/*SCIENCE* BASED ON C. PEI AND J. GONG

CHEMICAL ENGINEERING

Tandem catalysis at nanoscale

Porous overcoatings help mediate coupled reactions

By **Chunlei Pei**[1] *and* **Jinlong Gong**[1,2]

Chemical engineering processes are typically governed by multiple unit operations. To minimize the energy consumption and economic cost, researchers face the challenge of integrating multiple steps of reactions and separations. A tandem reaction involves sequential reactions within one condition, presenting an effective scheme for emerging chemical industries (*1*). On page 1257 of this issue, Yan *et al*. (*2*) present a tandem catalyst with porous overcoating structures, In_2O_3-Pt/Al_2O_3, for coupling catalytic propane dehydrogenation with selective H_2 combustion.

To control the reaction sequence and selectivity under the coexistence of reactants, intermediates, and products, the design of tandem catalysts plays a crucial role in mediating the multiple reactions under the same condition (*3*). In principle, a tandem catalyst is composed of different types of catalytic sites, and a predetermined sequence of reactions occurs at each corresponding catalytic site. The key to manipulating the process of tandem catalysis is to coordinate the transport of reactive intermediates among catalytic sites (*4*, *5*). Random physical mixtures of catalysts cannot effectively mediate the reaction sequence. Therefore, the proximity (*6*, *7*) and hierarchy (*8*) of catalytic sites within the tandem catalyst must be carefully constructed to regulate the transport of key intermediates.

The research on the tandem coupling of catalytic propane dehydrogenation to selective H_2 combustion bridges the fundamental philosophy to the industrial application. The on-purpose production of propylene directly from propane is a highly desired process to fill the supply-demand gap in the alkene market (*9*, *10*). The catalytic propane dehydrogenation process as an endothermic reaction is restricted by the thermodynamic equilibrium, as well as sintering and coking under high temperatures (*11*, *12*). Instant removal of H_2 through selective combustion could force the catalytic dehydrogenation to move for-

[1]Key Laboratory for Green Chemical Technology of Ministry of Education, School of Chemical Engineering and Technology, Tianjin University, Tianjin 300072, China. [2]Joint School of National University of Singapore and Tianjin University, International Campus of Tianjin University, Binhai New City, Fuzhou 350207, China. Email: jlgong@tju.edu.cn

Tandem catalysis with porous overcoating structure

Propane dehydrogenation makes propylene, which is an important feedstock for polymers. The porous overcoating structure regulates the transport of hydrogen species and promotes the selective H_2 combustion, which consequently drives catalytic propane dehydrogenation forward. The relative location of the alumina-supported platinum and the indium oxide ceramic is important for tandem catalysis.

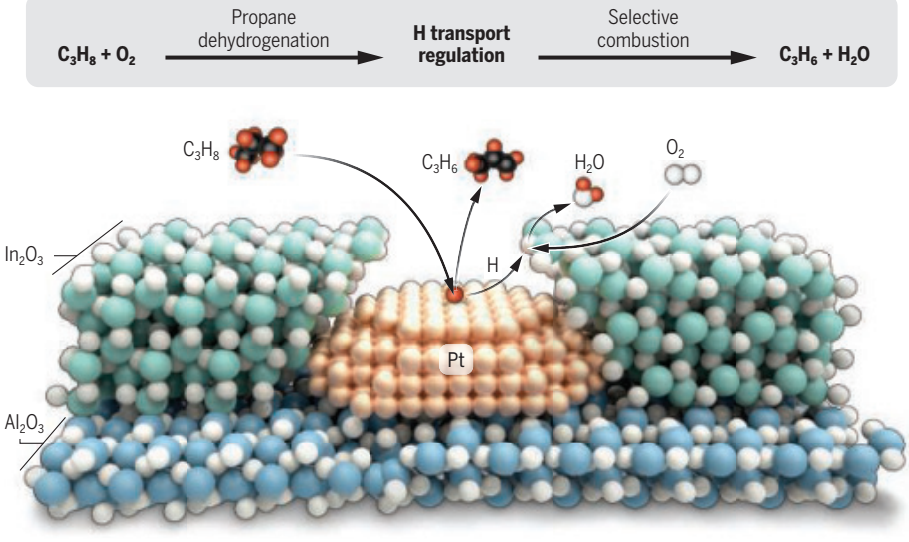

ward and break the thermodynamic limitation of the nonoxidative catalytic reaction (*13*). However, to avoid the combustion of carbon species, the catalytic dehydrogenation and selective H_2 combustion must be properly regulated in sequence by the tandem catalyst.

Yan *et al*. report a catalytic system comprising alumina-supported Pt nanoclusters (Pt/Al_2O_3) for propane dehydrogenation and In_2O_3 for selective H_2 combustion (see the figure). To rationally coordinate sequential reactions, Pt/Al_2O_3 is overcoated by In_2O_3 films by using an atomic layer deposition (ALD) process. The coating becomes porous, with the pore size of about 1.4 nm, upon thermal treatment. This leads to the exposure of approximately half of the surface Pt atoms for the access of gaseous molecules. A bonus of this structure is that the porous In_2O_3 films could prevent the aggregation of Pt particles at high temperatures.

"The methodology exemplifies the strategy of mediating the transport of key intermediates across various catalytic sites and integrating multiple reactions sequentially."

The deliberate design of this porous overcoating structure is to enable H atoms generated by propane dehydrogenation on Pt surfaces to rapidly diffuse across the interface and react with O_2 on In_2O_3. Yan *et al*. simply vary the number of ALD cycles in the range of 2 to 55 to control the film thickness. The In_2O_3 film with a thickness of ~2 nm achieves the optimal propane conversion and propylene selectivity. These resuts confirm that the dedicated architecture of the tandem catalyst facilitates the coupled reaction. An appropriate proximity could minimize the oxidization of propylene into CO_x and promote the propylene selectivity even at high values of propane conversion.

The authors demonstrate that this porous overcoating topology is essential by comparing it with a physical mixture of Pt-based and In_2O_3-based catalysts and a conventional Pt/In_2O_3-supported structure. The characterization of H_2 temperature-programmed reduction reveals that the partially reduced indium species (In_2O_{3-x}) can only be formed with the porous tandem structure under H_2 reduction. The authors argue that the intimate contact between Pt and In_2O_3 over the tandem catalyst eases the diffusion of hydrogen species from Pt to the $Pt\text{-}In_2O_3$ interface and subsequently reacting with In_2O_3. The coordinated transport of H_2 bridges the propane dehydrogenation to selective H_2 combustion and drives the propylene production forward.

The tandem catalyst achieves 75% propylene selectivity at 40% propane conversion and leads to a stable 30% propylene yield at 450°C. The study on reaction kinetics proves that the O_2-enhanced dehydrogenation and H_2 combustion progress much faster on the tandem structure, further implying more intensive transport of H atoms. The tandem catalyst outperforms state-of-the-art catalysts of oxidative propane dehydrogenation. Further, this performance also exceeds the thermodynamic equilibrium conversion of about 24% for nonoxidative propane dehydrogenation. The tandem coupling at nanoscale performs comparably with or better than macroscale engineering strategies, such as membrane, staged, or chemical looping reactors.

The authors' findings should inspire further developments both in academic and industrial areas. The methodology exemplifies the strategy of mediating the transport of key intermediates across various catalytic sites and integrating multiple reactions sequentially. The mechanistic understanding on the diffusion of reactive intermediates between tandem catalytic sites remains challenging, which relies on the advance of time- and spatially resolved spectroscopy and microscopy technologies. Furthermore, the industrial manufacture of tandem catalysts with atomic-level control of overcoating films needs substantial development to provide this revolutionary technology for the olefin industry. ■

REFERENCES AND NOTES

1. L. F. Tietze, U. Beifuss, *Angew. Chem. Int. Ed.* **32**, 131 (1993).
2. H. Yan *et al*., *Science* **371**, 1257 (2021).
3. Y. Yamada *et al*., *Nat. Chem.* **3**, 372 (2011).
4. F. Jiao *et al*., *Science* **351**, 1065 (2016).
5. P. Gao *et al*., *Nat. Chem.* **9**, 1019 (2017).
6. J. Zečević, G. Vanbutsele, K. P. de Jong, J. A. Martens, *Nature* **528**, 245 (2015).
7. Z. Li *et al*., *Joule* **3**, 570 (2019).
8. J. Bao, J. He, Y. Zhang, Y. Yoneyama, N. Tsubaki, *Angew. Chem. Int. Ed.* **47**, 353 (2008).
9. J. J. H. B. Sattler, J. Ruiz-Martinez, E. Santillan-Jimenez, B. M. Weckhuysen, *Chem. Rev.* **114**, 10613 (2014).
10. S. Chen *et al*., *Chem. Soc. Rev.* (2021). 10.1039/d0cs00814a
11. S. Chen *et al*., *J. Am. Chem. Soc.* **141**, 18653 (2019).
12. J. T. Grant *et al*., *Science* **354**, 1570 (2016).
13. T. Waku, J. A. Biscardi, E. Iglesia, *J. Catal.* **222**, 481 (2004).

ACKNOWLEDGMENTS

The authors are supported by the National Natural Science Foundation of China (U1862207 and 21525626) and the Program of Introducing Talents of Discipline to Universities (BP0618007).

10.1126/science.abh0424

IMMUNOLOGY

DNA sensor in standby mode during mitosis

Distinct control mechanisms restrict innate DNA sensor activity on mitotic chromosomes

By **Andrea Ablasser**

Pathogen sensing in innate immunity relies on receptors that must be efficient and precise. To achieve this, cells express various signaling receptors that bind microbial structures, which are absent in the host. In addition, a fascinating mechanism of pathogen sensing is based on the recognition of double-stranded DNA (dsDNA). Coupling such a universal signal to the execution of immune defense not only enables protection against a broad spectrum of pathogens but also allows for the identification of damaged host cells. However, activating immunity to self-DNA can have fatal consequences for the host. What mechanisms guide the critical decision about whether to respond to a DNA molecule? On page 1221 of this issue, Li *et al*. (*1*) report that cyclic guanosine monophosphate (GMP)–adenosine monophosphate (AMP) synthase (cGAS)—a major host sensor for dsDNA—exploits phosphorylation and chromatin tethering during mitosis, which abolishes its activity on host genomic DNA.

The sensing of dsDNA from the interior of a cell through cGAS can be activated by both foreign and self-DNA (*2*). Upon binding to dsDNA, cGAS synthesizes the second messenger cyclic GMP-AMP (cGAMP), which then activates the endoplasmic reticulum–localized protein stimulator of interferon genes (STING). Activation of STING triggers de novo synthesis of type I interferon genes and multiple proinflammatory mediators, which collectively elicit a potent innate immune response. In addition to detecting infection with pathogens containing dsDNA, the pathway also responds to diverse "sterile" insults, such as the emergence of malignant cells or dis-

Global Health Institute, Swiss Federal Institute of Technology Lausanne (EPFL), Lausanne, Switzerland. Email: andrea.ablasser@epfl.ch

ruption of tissue homeostasis, and thereby contributes in critical ways to both organismal health and disease.

The seemingly indiscriminate sensing capability of cGAS demands auxiliary mechanisms that prevent the enzyme from engaging with self-DNA in healthy cells. Within the cytoplasm, this task is mediated by both DNA-degrading enzymes and the compartmentalization of DNA inside mitochondria. By contrast, within the cell nucleus, cGAS is restricted by tethering to nucleosomes, and chromatin architectural proteins shield genomic DNA from cGAS binding (*3*, *4*). However, as cells progress through mitosis, the entire cGAS pool is exposed to the whole nuclear DNA content, with cGAS rapidly associating with mitotic chromosomes (*5*, *6*). Whether this particular cell cycle stage afforded additional safeguards complementing the inhibitory role of nucleosomes remained unclear.

Li *et al*. tracked cGAS activity throughout the cell cycle and observed that when isolated from mitotic cells, but not from any other cell cycle stage, the enzyme's capability to synthesize cGAMP was considerably reduced in vitro. This finding was indicative of a specific modification of the cGAS protein itself that could alter its functional properties. Indeed, to properly orchestrate cellular division, many mitotic processes are regulated by rapid and reversible post-translational modifications, one of the most prominent being phosphorylation. That cGAS could be subject to a similar mode of regulation appears an intuitive and appealing solution. Indeed, by monitoring its phosphorylation status, Li *et al*. showed that cGAS underwent phosphorylation for exactly as long as cells remained in mitosis. Using mass spectrometry analysis, they further revealed multiple mitosis-specific phosphorylation sites, some of which were reliant on the activity of Aurora kinase B, a serine and threonine kinase that is crucially involved in orchestrating mitotic processes. Intriguingly, all phosphorylated residues mapped to the amino-terminal region of cGAS, which is highly disordered and contains multiple positively charged residues known to strengthen its interaction with DNA and thereby promote cGAS phase separation—a process that has been linked to the enzyme's activity (*7*, *8*).

Could the weakening of ionic interactions between cGAS and DNA through hyperphosphorylation contribute to cGAS silencing during mitosis? Li *et al*. show that substituting all serine and threonine residues of the cGAS amino terminus with phosphomimetic amino acids severely compromised cGAS phase separation and enzyme activity in vitro. However, a cGAS mutant that could not be phosphorylated at its amino terminus was still suppressed in living mitotic cells. To explain the missing part of regulation, the authors considered the inhibitory effect of nucleosomes, which sequester cGAS primarily through an inhibitory protein-protein interaction contributed by the "acidic patch" of the histone octamer (*9*–*14*). It was predicted that in the nucleosome-bound state, cGAS could neither engage DNA nor oligomerize—two essential steps for enzymatic activation. Consistently, Li *et al*. demonstrate that defective acidic patch anchoring combined with preventing amino-terminal phosphorylation triggered cGAMP production from mitotic cells. Moreover, the authors showed that cGAS does not oligomerize on mitotic chromosomes in living cells.

Together, this emphasizes the importance of both phosphorylation and inhibitory nucleosome interactions for cGAS inactivation during mitosis (see the figure). Whereas the phosphorylation safeguard negatively affects cGAS DNA interactions and phase separation, nucleosome binding locks cGAS in a monomeric conformation that is unable to bind to DNA. By contrast, upon mitotic exit, the dephosphorylation pattern of cGAS indicates that inhibition inside the nucleus is sufficiently controlled. Yet, in this location, other mechanisms likely take over to enhance the inhibition imparted by nucleosome tethering, including architectural chromatin binding proteins, such as barrier-to-autointegration factor 1 (BAF) and histone H1, which can efficiently suppress the immunogenicity of self-DNA (*4*, *15*).

With this new insight on the mechanistic basis of cGAS regulation on chromatin, new questions about the interrelationship between DNA sensing and immunity are emerging. For example, could cGAS phosphorylation present yet another immune evasion strategy hijacked by pathogens to propagate infection? Intriguingly, Li *et al*. report that the amino terminus of cGAS is selectively responsible for chromatin binding but not absolutely necessary to respond to (mitochondrial) DNA. On the basis of this observation, it is tempting to speculate that chromatin recognition by cGAS during mitosis and the attendant nuclear enrichment may serve a beneficial purpose for the host—the nature of which remains to be uncovered. Could disruption of chromatin safeguards also underpin certain pathological processes? Mutations in genes regulating histone de novo synthesis were identified as a cause of the severe autoimmune syndrome Aicardi-Goutières syndrome (*15*). Whether this or another disease can be explained by defects in inhibition of cGAS in response to mitotic or nuclear DNA could ultimately be of medical relevance. Insight into the basics of cGAS-STING pathway regulation may also open possibilities for immunotherapies aimed at boosting immune activation. ■

Regulating DNA binding in mitosis

In mitotic cells, cGAS associates with chromatin but is inactivated by amino-terminal phosphorylation and nucleosome tethering. In nonmitotic cells, cGAS can be activated by dsDNA in the cytosol, but nucleosome binding and chromatin architectural proteins, such as histone H1 and BAF, restrict cGAS activation in the nucleus.

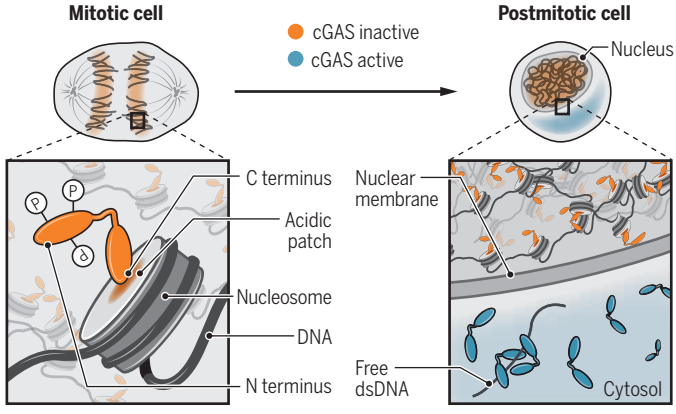

BAF, barrier-to-autointegration factor 1; cGAS, cyclic guanosine monophosphate–adenosine monophosphate synthase; dsDNA, double-stranded DNA; P, phosphorylation.

GRAPHIC: C. BICKEL/*SCIENCE*

REFERENCES AND NOTES

1. T. Li *et al*., *Science* **371**, eabc5386 (2021).
2. A. Ablasser, Z. J. Chen, *Science* **363**, eaat8657 (2019).
3. H. E. Volkman, S. Cambier, E. E. Gray, D. B. Stetson, *eLife* **8**, 47491 (2019).
4. B. Guey *et al*., *Science* **369**, 823 (2020).
5. H. Yang, H. Wang, J. Ren, Q. Chen, Z. J. Chen, *Proc. Natl. Acad. Sci. U.S.A.* **114**, E4612 (2017).
6. K. J. Mackenzie *et al*., *Nature* **548**, 461 (2017).
7. M. Du, Z. J. Chen, *Science* **361**, 704 (2018).
8. J. Tao *et al*., *J. Immunol.* **198**, 3627 (2017).
9. C. Zierhut *et al*., *Cell* **178**, 302 (2019).
10. T. Kujirai *et al*., *Science* **370**, 455 (2020).
11. J. A. Boyer *et al*., *Science* **370**, 450 (2020).
12. G. R. Pathare *et al*., *Nature* **587**, 668 (2020).
13. S. Michalski *et al*., *Nature* **587**, 678 (2020).
14. B. Zhao *et al*., *Nature* **587**, 673 (2020).
15. C. Uggenti *et al*., *Nat. Genet.* **52**, 1364 (2020).

ACKNOWLEDGMENTS

A.A. is a member of the scientific advisory board of IFM Therapeutics and a scientific co-founder of IFM Due.

10.1126/science.abg7422

VIEWPOINT: COVID-19

SARS-CoV-2 transmission without symptoms

Symptomless transmission silently drives viral spread and is key to ending the pandemic

By **Angela L. Rasmussen**[1] and **Saskia V. Popescu**[1,2]

Severe acute respiratory syndrome coronavirus 2 (SARS-CoV-2) has a potentially long incubation period and spreads opportunistically among those who are unaware they are infected. Asymptomatic COVID-19 cases are those that do not develop symptoms for the duration of infection, whereas presymptomatic cases develop symptoms later in the course of infection, but both are crucial drivers of transmission (*1*). Transmission without symptoms poses specific challenges for determining the infectious timeline and potential exposures. Early in the pandemic, most transmission was from undocumented cases, suggesting that spread was driven by people who were either asymptomatic or experiencing such mild disease that it was not recognized as COVID-19 (*2*). Contagious people without observable signs of illness make infection prevention efforts vulnerable to compliance with masking, distancing, hand hygiene, symptom screening, and ultimately, people staying home when possible. The lack of widespread testing in asymptomatic individuals further complicates COVID-19 mitigation and control efforts.

The true occurrence and transmission capacity of asymptomatic and presymptomatic infections are difficult to evaluate. Owing to insufficient surveillance testing (testing regardless of symptoms), presymptomatic cases lost to follow up, and unrecognized mild symptoms, symptomless cases are often undercounted or misclassified. It is virtually impossible to detect such cases without continuous community surveillance screening, which has not been widely implemented, or without effective contact tracing and testing. Beyond implementing general and often vague control measures, public health efforts have struggled to truly address symptomless transmission. Surveillance testing has predominantly been carried out in targeted populations such as long-term care facilities. Only certain industries, such as professional sports and entertainment, have implemented asymptomatic testing, but such data are not publicly available and these groups are not representative of the broader community. It is important to understand infectiousness and viral shedding, as well as the overall contribution of asymptomatic or presymptomatic cases to secondary cases.

The prevalence of symptomless cases is not precisely established. Early studies reported that asymptomatic cases accounted for 30 to 80% of infections (*3*), but more recent data point to a rate of asymptomatic cases between 17 and 30% (*4*). A recent systematic review of studies reporting SARS-CoV-2 diagnoses by quantitative reverse transcriptase polymerase chain reaction (qRT-PCR, the standard molecular diagnostic test) and follow-up of symptoms found that the proportion of asymptomatic infections was 20% and that the rate of presymptomatic individuals could not be determined because of heterogeneity across studies (*4*). A limitation of such studies is measurement of asymptomatic status and selection bias. Often, large outbreaks driven by asymptomatic or presymptomatic transmission are restricted to specific populations or circumstances, such as in skilled nursing or long-term care facilities, where surveillance testing takes place (*5*). Because these are high-risk clinical environments, it is not surprising that symptomless transmission has been detected more frequently than in nonclinical settings, such as restaurants or offices, which lack access to testing or medically trained staff. The unknown prevalence of asymptomatic SARS-CoV-2 infections makes disease control and mitigation strategies inherently challenging.

Beyond assessing the prevalence of symptomless infections, it is vital to determine their risk for secondary transmission. Contact tracing is reliant on case identification, which generally involves testing of people with symptoms. This reliance on symptom-based testing, especially early in the pandemic, was also complicated by limited understanding of the full range of COVID-19 symptoms. The lack of surveillance testing makes analysis of secondary attack rates (the percentage of cases that result from one infected person within a defined group) for asymptomatic cases exceedingly difficult. In symptomatic COVID-19, infectiousness begins 2 days prior to symptom onset and for several days after, with reduced or undetectable viral shedding within the first week of symptom onset (*5*, *6*). Viral shedding kinetics for asymptomatic COVID-19 is not well understood. Early in infection, individuals have similar viral loads regardless of eventual symptom severity, but asymptomatic cases have lower titers at peak replication, faster viral clearance, and thus a shorter infectious period (*6*).

Measuring the true impact of symptomless infections on transmission can be extremely confounding. Data on asymptomatic and presymptomatic cases who had close contacts but did not result in transmission are limited. Some studies found that asymptomatic cases were 42% less likely to transmit the virus, and observed lower secondary attack rates, whereas others have noted that regardless of a shorter infectious period, there is similar transmissibility for those with presymptomatic or asymptomatic COVID-19 in the first days of infection (*6*). Studies of presymptomatic transmission suggest that higher secondary attack rates are likely compared with asymptomatic cases (*7*). Moreover, analyses of contact tracing data indicated that at least 65% of transmission occurs prior to symptom onset (*8*). Another study found that only 12.6% of cases resulted from symptomless transmission (*9*). These discrepancies can be explained by several factors, including the misclassification of cases that were not followed up (*4*), but also that many are identified as a result of specific settings, such as superspreading events on cruise ships or in choir practice that result in rigorous investigations, and may not be representative of typical transmission events.

Determining the true transmission capability of asymptomatic and presymptomatic cases is inherently complex, but knowledge gaps should not detract from acknowledging their role in the spread of SARS-CoV-2. Those with symptoms appear to have higher secondary attack rates, but these cases are also more likely to present for testing and practice isolation because of obvious illness (*10*). The public health and infection prevention challenges rely on those without symptoms to self-quarantine and implement a suite of interventions, such as masking, social distancing, ventilation, and hand hygiene. However, emphasis on the degree of contagiousness rather than the knowledge that people without symptoms are generally contagious detracts from the public health threat that

[1]Georgetown Center for Global Health Science and Security, Georgetown University, Washington, DC, USA. [2]Schar School of Policy and Government, George Mason University, Fairfax, VA, USA.
Email: ar1692@georgetown.edu; spopesc2@gmu.edu

asymptomatic and presymptomatic infections pose and the need for continuous community-based surveillance and interventions.

The 2003 outbreak of the related SARS-CoV was eventually contained by using standard epidemiological approaches of isolating cases and tracing and quarantining contacts. This was effective because contagious patients could be easily identified through temperature and symptom screening. A major distinction from SARS-CoV is viral shedding of SARS-CoV-2 in the absence of observable clinical symptoms. Unlike SARS-CoV, SARS-CoV-2 viral loads are highest at symptom onset and up to a week after (*6*), which suggests substantial presymptomatic shedding. Therefore, people are likely contagious for a relatively long period and when they are unaware they have been infected or exposed. The minimum infectious dose required for transmission is also not known and likely varies depending on individual exposure and susceptibility. Although viral loads decline over the course of infection, the exact point at which someone stops being contagious is unclear, but probably occurs within 10 days of infection in most cases, provided symptoms are resolving.

Testing provides limited clarity on whether a person is likely to be contagious on the basis of estimated viral loads. Although people who have fully recovered from COVID-19 can continue to shed viral RNA and test positive by qRT-PCR in the absence of recoverable infectious SARS-CoV-2, as assessed by culture (*1, 5, 6, 11–14*), these cases have not been associated with new clusters of transmission (*12*, *13*). qRT-PCR detects viral RNA but not infectious virus particles. PCR cycle thresholds can be used to estimate viral load in nasal swabs, but do not always directly correlate with the quantity of infectious virus shed in respiratory particles. These particles are highly heterogeneous depending on various factors, including where in the respiratory tract cells are secreting infectious virus, breathing rate, and symptoms such as coughing (*15*). Not all exhaled particles contain infectious virus, and the amount of time that virus remains infectious after exhalation in respiratory particles can vary substantially depending on environmental conditions such as temperature and humidity, as well as the quantity of infectious particles being shed. Assays that measure infectious titer must be performed in biosafety level 3 (BSL-3) containment, so this cannot be routinely measured in clinical settings. Furthermore, qRT-PCR and rapid antigen tests can be performed in hours or minutes, compared to several days for determining infectious titer. Viral loads determined by qRT-PCR are, at best, a crude measure of actual infectious virus shedding, so further research is needed to establish viral loads in asymptomatic and presymptomatic cases (see the figure).

The biological basis for transmission without symptoms is poorly understood, even though it is common for respiratory viruses, including "common cold" pathogens such as rhinoviruses and other coronaviruses, to be spread by both contact and inhalation. Symptomless transmission is influenced by the timing and magnitude of the host response to infection, which is a major determinant of pathogenicity. Delayed or reduced host antiviral immune responses are closely linked to COVID-19 severity, suggesting a relationship between host response and symptom onset. This includes suppressed interferon-induced cytokine expression, which is linked to symptoms. As a gateway between the body and the environment, the upper respiratory tract is regularly exposed to external antigens. Thus, the nasal mucosa is a niche immune site in which antiviral responses are modulated by external factors (such as temperature or humidity) and host susceptibility (mucus, receptor distribution, and host response to infection) and may explain why symptomless spread is common for respiratory viruses.

With many contagious people experiencing no symptoms and in the absence of robust surveillance testing for asymptomatic or presymptomatic infections, it is critical to maximize efforts to reduce transmission risk in the community. Academic debates about the frequency of different transmission routes reframe exposure risk reduction as a dichotomy rather than a spectrum, confusing rather than informing guidance. Rather than targeting transmission by either inhalation or contact, infection prevention efforts should focus instead on the additive nature of risk reduction and the need for continued vigilance in community-based infection prevention measures, including masks, distancing, avoiding enclosed spaces, ventilation, hand hygiene, and disinfection.

Transmission without symptoms critically contributes to the unabated spread of SARS-CoV-2 and presents a considerable infection prevention challenge. Although asymptomatic individuals appear to be contagious for a shorter period of time and may pose a lower transmission risk, they still pose a substantial public health risk as they are more likely to be out in the community. It is unclear how vaccination will affect the number of asymptomatic cases, although preliminary data suggest that mass immunization will reduce infection overall, thus reducing transmission. For presymptomatic cases, research has shown that viral shedding is highest just before and for a few days after symptoms begin, which is a critical time to ensure that individuals who may not realize they have been exposed stay home when possible and practice risk reduction efforts when in the community. Until there is widespread implementation of robust surveillance and epidemiological measures that allow us to put out these smokeless fires, the COVID-19 pandemic cannot be fully extinguished. ■

Viral replication and symptom onset

The titer of infectious severe acute respiratory syndrome coronavirus 2 (SARS-CoV-2) and the amount of viral RNA are generally lower in asymptomatic (A) than presymptomatic (Pre) COVID-19. There is likely to be a threshold at which a person becomes contagious, but this is not known. In presymptomatic patients, symptoms usually begin when viral load peaks, so there is a period of infectiousness when a person has no symptoms.

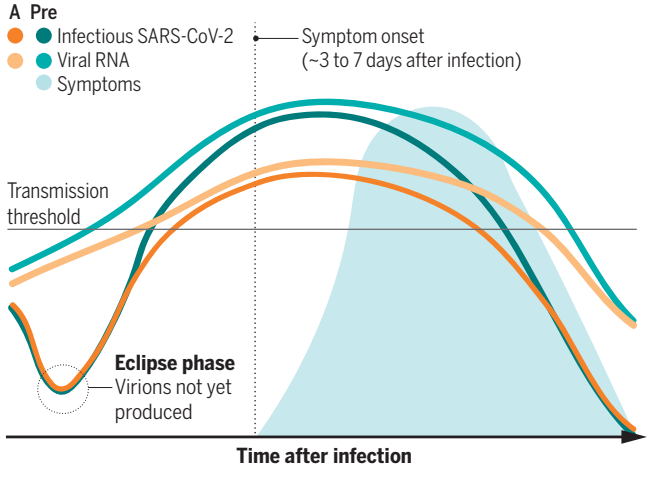

GRAPHIC: N. CARY/*SCIENCE*

REFERENCES AND NOTES

1. D. P. Oran, E. J. Topol, *Ann. Intern. Med.* **173**, 362 (2020).
2. R. Li *et al.*, *Science* **368**, 489 (2020).
3. W. Zhang *et al.*, *Emerg. Infect. Dis.* **26**, 1924 (2020).
4. D. Buitrago-Garcia *et al.*, *PLOS Med.* **17**, e1003346 (2020).
5. R. Wölfel *et al.*, *Nature* **581**, 465 (2020).
6. M. Cevik *et al.*, *Lancet Microbe* **2**, e13 (2021).
7. J. Y. Chun, G. Baek, Y. Kim, *Int. J. Infect. Dis.* **99**, 403 (2020).
8. L. C. Tindale *et al.*, *eLife* **9**, e57149 (2020).
9. Z. Du *et al.*, *Emerg. Infect. Dis.* **26**, 1341 (2020).
10. X. Qiu *et al.*, *medRxiv* 2020.09.01.20135194 (2020).
11. M. M. Arons *et al.*, *N. Engl. J. Med.* **382**, 2081 (2020).
12. Korean Disease Control and Prevention Agency; www.kdca.go.kr/board/board.es?mid=a30402000000 (2020).
13. J. Lu *et al.*, *EBioMedicine* **59**, 102960 (2020).
14. J. Bullard *et al.*, *Clin. Infect. Dis.* **71**, 2663 (2020).
15. P. Z. Chen *et al.*, *medRxiv* 2020.10.13.20212233 (2020).

10.1126/science.abf9569

RETROSPECTIVE

Lewis Wolpert (1929–2021)

Pioneering developmental biologist

By **Cheryll Tickle** and **Jonathan Slack**

Lewis Wolpert, a towering figure in developmental biology, died on 28 January. He was 91. A charismatic advocate of his science, Lewis originated the concept of positional information to explain the formation of pattern in the development of an embryo. His work played a central role in building the field.

Lewis was born on 19 October 1929 in Johannesburg, South Africa. He studied civil engineering at the University of Witwatersrand and, after graduating in 1950 with his bachelor's of science degree, worked in Pretoria as a soil mechanic. He protested apartheid by attending demonstrations and distributing newspapers for Nelson Mandela. In 1953, he left South Africa for Israel and then moved to London, England, in 1954. There, he began with a postgraduate diploma in soil mechanics at Imperial College London and then did his PhD at King's College London with biologist James Danielli, studying the mechanics of cell division in sea urchin embryos. At the marine station in Kristineberg, Sweden, Lewis met the embryologist Trygve Gustafson and became fascinated by sea urchin embryo development. Together, they showed how complicated changes in embryo shape could be explained by a small number of cellular properties. Lewis was appointed, in 1960, as a lecturer at King's College London and, in 1966, to a chair at the Middlesex Hospital Medical School, which later merged with University College London, where he remained until he retired in 2004.

In the early 1960s, Lewis worked on regeneration of hydra, a small freshwater animal. Both hydra and sea urchin embryos can regulate their proportions—if a part is removed, the whole pattern reforms itself at a smaller scale in the remaining tissue. Applying his engineering background, Lewis proposed a model in which position within the organism is specified by a linear gradient between two fixed boundary regions. He drew an analogy between the pattern of the body plan of an organism—e.g., an animal with a head, trunk, and tail—and the pattern of the French flag's blue, white, and red. He first presented the idea in 1966 at a Theoretical Biology Symposium and published it in expanded form in 1969 in the *Journal of Theoretical Biology*. One of us (J.S.), enthralled by a lecture Lewis gave on this topic, later joined his research group. Lewis's ideas initially met with considerable hostility, but he was encouraged to stick with them by founders of the field of molecular biology, Sydney Brenner and Francis Crick.

Pattern formation is the process that controls the spatial organization of the embryo, leading to precisely ordered arrays of differentiated cells. Lewis proposed that this process occurs in two distinct steps. First, cells are informed of their position in the embryo, for example, by a French flag–like mechanism. Second, they "interpret" this positional value according to their genetic constitution and developmental history, differentiating to form a specific cell or tissue type. The theory of positional information brought together various ideas of previous researchers in a new and predictive way. It was truly revolutionary in an era when developmental biologists were mostly focused on mechanisms of gene transcription. The theory is widely applicable and has illuminated many aspects of development, including specification of body plan in both vertebrate and invertebrate embryos.

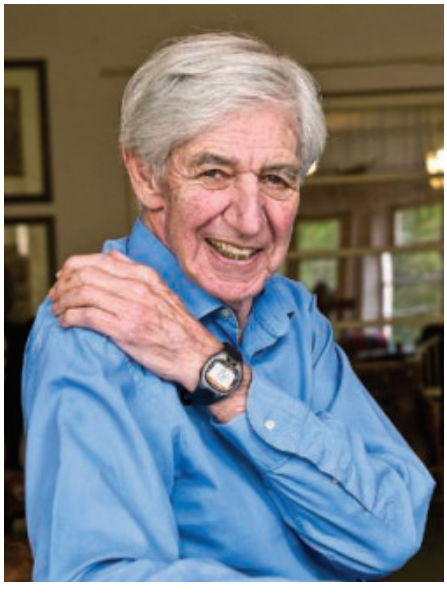

PHOTO: FRANCESCO GUIDICINI/CAMERA PRESS/REDUX

After arriving at the Middlesex Hospital Medical School, Lewis took up the problem of chick embryo limb development. He applied his concepts of positional information to this problem, and over many years, with several collaborators, including one of us (C.T.), he laid the basis for today's detailed understanding of limb development. This knowledge has helped elucidate general principles about how organs form and provided insights into clinical conditions in which limb development is affected.

Both of us were lucky and privileged to be postdocs in Lewis's lab in the 1970s. The atmosphere was exhilarating, largely thanks to Lewis's infectious enthusiasm. We were working on deep biological problems that nobody else had recognized; his lab was "the" place to do science and the venue for some memorable parties. Lewis relished coming up with experiments to test his models, although he did not carry them out himself. (He was the first to admit that his practical skills were limited.) Seminars in his lab were very informal but always interesting. Because he was not particularly interested in details, Lewis allowed speakers to show only one slide of a gel. Our work became even more thrilling as the experiments on the chick limb began to flesh out Lewis's concepts, providing evidence for a combination of graded signals and timing mechanisms specifying positional values. Lewis later proposed that positional information interacts with a repetitive prepattern to give limb digits their individual character.

In the 1990s, Lewis wrote the textbook *Principles of Development*, with the aim of presenting concepts and avoiding too much detail. He was excited by identification of developmentally important genes involved in limb development, studying Hox genes with biologist Denis Duboule. But his main interest was elaborating his models, for example, with theoretician Michel Kerszberg, querying whether diffusion is sufficiently robust to specify position.

Lewis's interests and influence extended far beyond developmental biology. He enjoyed biking and playing tennis. He was very active in promoting science to nonscientists in the UK through radio and television and wrote several popular science books. The best known of these is *Malignant Sadness*, which is based on his own personal experience with depression. In *The Unnatural Nature of Science*, Lewis argued that science is completely different from art in that science is about the way in which the world works, whereas art is a personal creation. But we wonder whether developmental biologists would ever have thought about French flags if it had not been for him. ■

Department of Biology and Biochemistry, University of Bath, Bath, UK. Email: cat24@bath.ac.uk

10.1126/science.abh0231

POLICY FORUM

ETHICS AND DIVERSITY

Justice, diversity, and research ethics review

It is time for institutional review boards and research ethics committees to address the ethics of inclusion

By **David H. Strauss[1,2], Sarah A. White[1,3], Barbara E. Bierer[1,3,4]**

The disproportionate impact of COVID-19 on certain populations, such as Black, Latinx, and Indigenous populations in the United States, has focused attention on inequalities in health and on the need to increase enrollment of racial and ethnic minorities and other underrepresented groups in biomedical research (*1*). Yet too often, in the United States and globally, participant enrollment in research has not reflected the demographic composition of the general population, those affected by the health conditions being studied, or those for whom the investigational product is intended (*2*), with racial and ethnic minorities and the young and the elderly, among others, being consistently underrepresented (*3*). Underlying causes for this underrepresentation have been described (*4*, *5*), but change has been slow. Notwithstanding the roles of other stakeholders in addressing this issue, we maintain that the specific value of institutional review boards (IRBs) and research ethics committees (RECs) in promoting diversity has been underrecognized and their authority underutilized. Here, we substantiate the role of and outline practical steps for the IRB and REC (hereafter "IRB") to help achieve greater diversity in clinical research.

The appropriate inclusion of diverse populations in clinical research is necessary if we are to understand how biological variability and social determinants of health contribute to disease prevalence, transmission, course, experience of illness, and treatment outcome. The inclusion of understudied and underserved groups informs clinical decision-making and health policy and can serve efforts to address mistrust of research and health care (*6*, *7*). Responsibility to the goals of diversity lies with all stakeholders in the clinical research enterprise (*6*), and a commitment to diversity, individually and collaboratively, by research sponsors, funders, academic institutions, contract research organizations, study sites, investigators, and IRBs is necessary.

[1]Multi-Regional Clinical Trials Center of Brigham and Women's Hospital and Harvard University, Cambridge, MA, USA. [2]Vagelos College of Physicians and Surgeons, Columbia University, New York, NY, USA. [3]Brigham and Women's Hospital, Boston, MA, USA. [4]Harvard Medical School, Boston, MA, USA. Email: bbierer@bwh.harvard.edu

RESPECT, BENEFICENCE, JUSTICE

Most regulated clinical research undergoes obligate review and approval by an IRB. IRBs are charged with safeguarding the rights and well-being of human participants in accordance with the foundational tenets of respect for persons, beneficence, and justice, as described in the Belmont Report (*8*). An IRB's ethical responsibilities with regard to diversity derive from these and other principles, guidelines, and standards (*9*, *10*).

The discussion of justice in Belmont cites "moral requirements that there be fair procedures and outcomes in the selection of research subjects." As Belmont and other codes of ethics emerged from a historical backdrop of abuse and injustice in research, "fair procedures" have been applied by IRBs largely (and, we believe, too narrowly) to ensure that subjects are not exploited and enrolled as a matter of convenience. The idea of justice within the Belmont Report also includes the notion of access to the benefits of research (i.e., knowledge gained); this has direct implications for populations that have been understudied, whether incidentally or systematically. Subject selection cannot be equitable, and the requirements of justice cannot be met, when there is de facto exclusion of understudied populations.

This notion of justice is supported by the World Health Organization's International Ethical Guidelines for Health-related Research Involving Humans, Guideline 3, which states, "In cases where the underrepresentation of particular groups results in or perpetuates health disparities, equity may require special efforts to include members of those populations in research" (*9*), and by the World Medical Association Declaration of Helsinki, which states, "Groups that are underrepresented in medical research should be provided appropriate access to participation in research" (*10*). Therefore, consideration of diversity is essential to the question of fairness in subject selection and to IRB review.

Diversity in clinical research is responsive to the principle of beneficence, which places priority on the welfare of research participants and creates the obligation that research presents a favorable balance of benefit to risk, after risks and burdens have been minimized. In calling for "maximization of benefits" in the research, Belmont directs attention to both individual benefit and to the broader value of research to society. A clinical research enterprise that is not inclusive does not adequately address the health needs of a diverse society. Group differences in susceptibility to disease and in treatment outcome can only be identified when those groups are studied. It is the obligation of an IRB to maximize benefits through the inclusion of understudied groups in a manner that is consistent with the study aims and does not introduce unacceptable harm or burden.

Belmont describes two ethical convictions in relation to respect for persons, self-determination, and decision-making: the obligations to treat individuals as autonomous agents and to protect those with diminished autonomy. IRBs provide additional safeguards for research involving participants with compromised voluntariness (e.g., prisoners) or impaired comprehension. With regard to the inclusion of diverse populations, respect for persons demands efforts to foster informed and autonomous decision-making and, therefore, to address common barriers posed by age, language, culture, and educational disadvantage. Respect for persons requires the identification of opportunities and resources to engage understudied populations and to enhance awareness, access, and inclusion in research (*4*, *6*). It also demands modification of those aspects of research and of consent that inadvertently limit the participation of understudied populations. For example, although inclusion of non-English speakers in a study may involve additional expenses of translation and/or interpreters, it strengthens the commitment to autonomy and justice.

The ethical positions presented above compel attention to inclusion of diverse populations in clinical research and define a specific duty for the IRB. In a 2019 survey (*11*), a majority of IRB chairs, IRB ad-

ministrators, and investigators agreed that "IRBs should play a key role in ensuring diversity among participants in terms of gender, ethnicity, and language." Despite this, there has been scant regulatory consideration, and little formal discussion within the field, as to whether diversity falls within the IRB's remit. There are also little data as to whether and when IRBs exercise this authority, but the observed underrepresentation in completed studies suggests that IRBs do not consistently attend to this responsibility. Further questions relate to recent U.S. regulation and policy requiring a single, designated IRB to serve as the IRB of record for multicenter research and whether this will offer benefit in consistency and reach with regard to diversity and inclusion.

INCLUSION AND PROTECTION

In the face of the persistent problem of underrepresentation in clinical research, institutions should establish policies and provide necessary resources at all institutional levels to ensure that reviewing IRBs fulfill this obligation. The specific approaches we outline here will serve to help incorporate the ethical oversight of diversity in IRB procedures, deliberations, and expectations (see the box).

An IRB has authority to require that a research protocol details study elements relevant to considerations of diversity. A description and justification by the investigator of the demographics of the intended study sample (e.g., by age, sex, race, ethnicity, social determinants of health) and a description of either the demographics of the condition or those using or intended to use the product in the general population permit the IRB to make an assessment of the appropriateness of the recruitment plan. When the makeup of the proposed sample deviates substantially from that of the demographics of the condition being studied in the general population or for whom the intervention is intended, and no valid scientific justification is offered, the IRB can require modification of the study to recruit a more representative sample. Such requirements are tailored to the nature and phase of the study, the study's specific aims, and the study location, as discussed further below.

Note that inclusion of a demographically diverse study population does not imply that statistical conclusions regarding heterogeneity of treatment outcome will be possible, but it may allow directional assessments of efficacy and safety that can then be further investigated. Inclusion will, at a minimum, address the equitable selection of participants and the principle of justice in research.

Institutional review board oversight: Points to consider by reviewers

INITIAL REVIEW

Study aims and subject selection

- Do the demographics of the proposed sample reflect those of the population affected by the condition or for whom the intervention is intended?
  - When they do not, is the deviation adequately justified?
  - Is planned under- or overrepresentation by age, race, ethnicity, sex, gender, or social determinants of health in the sample scientifically justified?
  - Is there a statistical plan for examining heterogeneity in outcome or across subgroups?

Criteria for inclusion and exclusion

- Will inclusion and exclusion criteria inadvertently or unnecessarily result in under- or overrepresentation of understudied subgroups?
- Have alternative approaches to minimizing risk that do not rely on exclusion been considered?

Recruitment

- Have recruitment procedures considered specific approaches to engage underserved populations?

Study conduct

- Are study procedures flexibly organized to accommodate the needs of underrepresented groups?
- Do all participant-facing materials conform to health literacy principles?
- Are participant materials translated? Is back translation necessary? If not, why not?

Payment

- Is payment sufficient to cover costs of participation?

Return of results

- Are study results intended to be returned in a manner that meets the needs of populations studied?

CONTINUING REVIEW

- Has the study fulfilled its recruitment and accrual goals?
- Is demographic distribution on track to approximate the study goals?
- If not, are adequate corrective actions described, sufficient, and likely to be successful?

During review, an IRB should consider the feasibility of study methods that seek to identify, recruit, and retain underrepresented populations. Research team partnerships with patients and their families, advocacy groups, and community representatives have been shown to be effective in informing recruitment and retention strategies (*12*) as well as in providing input on study questions and participant-relevant endpoints, study conduct, and culturally and linguistically appropriate communications. The IRB should require a statement in the study proposal summarizing the nature, process, input, and impact of such patient and community engagement and how this information has shaped the study itself and the recruitment plan; simply asking the question will prompt consideration by investigators.

The IRB can review and provide specific feedback to facilitate successful recruitment of specific populations, including language use, translation, placement of advertisements, and workforce characteristics. The IRB should also ensure that all study materials adhere to health literacy principles and that user-testing is utilized where indicated. The IRB should identify factors, such as excessive time commitment, restricted clinic hours, the costs of travel, and inadequate compensation, that have a foreseeable and negative impact on the enrollment of an appropriately representative sample (*13*).

IRBs should require investigators to detail study inclusion and exclusion criteria and, when not self-evident, to provide a rationale for exclusion. Review of eligibility criteria should ensure that understudied populations are not inadvertently or unnecessarily excluded and that criteria are only as restrictive as necessary for safety and to minimize harm. For example, the exclusion of older populations with a specific age criterion might be revised to exclude individuals with specific health concerns who would be at increased risk, regardless of age. When laboratory measures serve as the basis for eligibility criteria, they should be adapted to reflect known sex-, age-, race-,

or ancestry-specific normal values, when failure to do so would unnecessarily decrease eligibility of some individuals (*14*). IRBs should identify common practices that limit enrollment of immigrant or minority language speakers in multilingual communities, restrict the participation of women of child-bearing potential (when requiring appropriate contraception would suffice), and introduce bias in participant selection by using overly subjective criteria (such as "investigator discretion").

In exercising the regulatory requirement for continuing oversight of ongoing research, the IRB should periodically review the demographic breakdown of the accrued sample by age, race, ethnicity, sex, and social determinants of health where applicable to the research. Along with these data, IRBs should require an explanation of any meaningful departures from the recruitment plan and request, review, and approve proposed corrective action when indicated. Ongoing tracking of accrual by the IRB, as well as dialogue between the IRB and investigator, communicates the importance of diversity, promotes transparency with regard to progress or lack of progress, provides a measure of accountability, and, ultimately, will change behavior.

"Equitable subject selection requires the balancing of inclusion and protection..."

IRB requirements with regard to study demographics should be flexibly tailored to individual study purpose, phase, setting, and size. For example, for some research (e.g., phase 3 studies, comparative effectiveness research), an IRB may adopt the principle, as a rebuttable presumption, that a study sample should reflect the demographic makeup of the condition being studied or for whom the intervention is intended. Other studies, such as small exploratory, proof-of-concept, early phase studies, or research that seeks to learn about specific communities, would not be expected to be representative of those affected by the condition. Similarly, a local site in a multisite study may be selected because it proposes to recruit a specific racial or ethnic group to diversify a larger study population.

Equitable subject selection requires the balancing of inclusion and protection and, like all aspects of research with human participants, grounding in good science. When a study proposes to recruit a sample that is composed predominantly or solely of a racial, ethnic, or other minority, the IRB might reasonably ask why the selection of this sample is scientifically necessary, how the findings are generalizable, and whether an alternative recruitment strategy might yield a more diverse or less burdened, stigmatized, or disadvantaged population.

Flexibly adapting requirements to specific study types will encourage dialogue between investigators and the IRB. When an investigator faces particular challenges in the recruitment and retention of specific populations, the IRB could offer guidance or consultation on protocol revision.

The IRB itself should be diverse in composition, with membership and input reflecting the demographic compositions of the communities and populations studied in the research it reviews through the use of ad hoc consultants and by appointing members with experience working with diverse communities. However, a recent study showed that 87% of IRB members and 91% of IRB chairs were white (*11*). A diverse IRB will be better attuned to the experience and needs of participants and better able to offer input from the perspective of varied populations. At a minimum, training in cultural competence and implicit bias should become part of required ethics education for all IRB members and staff. Finally, IRBs should develop expertise in providing concrete recommendations for investigators in methods and tools to achieve greater diversity (*6*).

Impediments to inclusion of underrepresented and underserved populations in research are numerous and complex. There are no specific regulatory mandates of the kind that typically drive accountability in clinical research. Institutional commitment to diversity is uneven, the research workforce itself is inadequately diverse, and resistance from the research community to any additional oversight is likely. Further, expertise in the engagement and study of hard-to-reach populations is variable and related infrastructure is limited. Finally, in the United States, some question whether Belmont or the Common Rule are appropriately applied to matters of social justice.

Institutions should support, educate, and resource IRBs, investigators and their study teams, and others in research so that they can give necessary attention to diversity as a fundamental value in the ethical conduct of research. The application of diversity to research review is neither simple nor without risk, but we do not believe the requirement fundamentally differs from other components of IRB review. Overly prescriptive approaches by the IRB and REC, specific mandates, or the application of quotas to study samples will not serve the interests of science and would not be justifiable or palatable to the research community. Drawing attention to diversity and inclusion as a goal and setting reasonable expectations as a condition of study approval, however, will give rise to necessary discussion and collaboration between IRBs and among investigators and the evolution of best practices in the field. Of course, the obligation to promote diversity in clinical research does not rest solely on the IRB or REC or the investigators. Sponsors, regulators, research and academic institutions, funders, patients and patient advocates, and others must build capacity and infrastructure in what, in the end, must be a collaborative enterprise.

As entities that hold investigators accountable, IRBs are themselves accountable to their ethical and regulatory mandates and ultimately to those who serve as participants in research. The duty of IRBs to view subject enrollment and retention beyond the lens of "protection," to deliberate on the benefits and risks of greater inclusion, and to exercise their authority to promote diversity should be recognized and actively implemented as a matter of justice. ■

REFERENCES AND NOTES

1. D. B. Chastain *et al*., *N. Engl. J. Med*. **383**, e59 (2020).
2. T. C. Knepper, H. L. McLeod, *Nature* **557**, 157 (2018).
3. U.S. Food and Drug Administration (FDA), "2015-2019 drug trials snapshots summary report: Five-year summary and analysis of clinical trial participation and demographics" (FDA, 2020); www.fda.gov/media/143592/download.
4. S. George, N. Duran, K. Norris, *Am. J. Public Health* **104**, e16 (2014).
5. L. T. Clark *et al*., *Curr. Probl. Cardiol*. **44**, 148 (2019).
6. B. E. Bierer *et al*., "Achieving diversity, inclusion, and equity in clinical research," version 1.0 (Multi-Regional Clinical Trials Center of Brigham and Women's Hospital and Harvard, 2020); https://mrctcenter.org/diversity-in-clinical-trials/.
7. R. C. Warren, M. G. Shedlin, E. Alema-Mensah, C. Obasaju, D. A. Hodge Sr., *Ethics Med. Public Health* **10**, 128 (2019).
8. The National Commission for the Protection of Human Subjects of Biomedical and Behavioral Research, "The Belmont Report: Ethical principles and guidelines for the protection of human subjects of research" (U.S. Department of Health, Education, and Welfare, 1979); www.hhs.gov/ohrp/regulations-and-policy/belmont-report/read-the-belmont-report/index.html.
9. World Health Organization, Council for International Organizations of Medical Sciences (CIOMS), "International ethical guidelines for health-related research involving humans" (CIOMS, ed. 4, 2016); https://cioms.ch/wp-content/uploads/2017/01/WEB-CIOMS-EthicalGuidelines.pdf.
10. World Medical Association, "WMA declaration of Helsinki—Ethical principles for medical research involving human subjects," 9 July 2018; www.wma.net/policies-post/wma-declaration-of-helsinki-ethical-principles-for-medical-research-involving-human-subjects/.
11. S. H. Berry *et al*., "Profile of institutional review board characteristics prior to the 2019 implementation of the revised common rule" (RAND Coproration, 2019); www.rand.org/pubs/research_reports/RR2648.html.
12. T. Greenhalgh *et al*., *Health Expect*. **22**, 785 (2019).
13. L. Gelinas *et al*., *N. Engl. J. Med*. **378**, 766 (2018).
14. D. A. Vyas, L. G. Eisenstein, D. S. Jones, *N. Engl. J. Med*. **383**, 874 (2020).

ACKNOWLEDGMENTS

D.H.S. received consulting fees as a member of the Takeda Pharmaceuticals Bioethics Advisory Council.

10.1126/science.abf2170

Staghorn corals are vulnerable to heat. Researchers hope to create coral that can survive in a hotter world.

BOOKS *et al.*

PLANETARY SCIENCE

Doubling down on our earthly interventions

Can we engineer our way out of the planetary problems we've engineered our way into?

By **Ken Caldeira**

Elizabeth Kolbert's beautifully written new book, *Under a White Sky,* reports from the planetary front lines where modern civilization is colliding with nature and where thoughtful people are working hard to soften the impact. "At this point it might be prudent to scale back our commitments and reduce our impacts," she writes. "But there are so many of us—as of this writing nearly eight billion—and we are stepped in so far, return seems impracticable." If we are unable to retreat and cannot remain where we are, how do we advance? Kolbert is a top journalist, but she is no pundit, and she offers no easy answers.

The book begins with a visit to the canals of Chicago. The Mississippi River basin and the Great Lakes basin were two distinct and biologically separate drainage basins until a little more than a century ago, Kolbert reveals, but early in the 20th century, canals were built, connecting Lake Michigan to a tributary of the Mississippi River.

For most of the past century, the canal was too polluted to allow much biological transfer, but with the passage of the Clean Water Act, it has become passable by fish in recent decades, resulting in a bidirectional invasion of species into previously distinct habitats. To mitigate this problem, engineers have deployed devices in the canal to create an electric field that shocks species attempting to cross between the two waterways. A "bubble barrier" that uses water bubbles and sound as a deterrent, with an estimated cost of $775 million, is also in the works.

From the canals of Chicago, Kolbert takes readers south to New Orleans and the Mississippi River delta. Once a freely meandering river, seasonally flooding and dropping sediment, the Mississippi was gradually tamed and its free flows channeled. Deprived of sediment and undermined by oil and gas drilling, coastal land now sinks into the sea. "Every hour and a half, Louisiana sheds another football field's worth of land," Kolbert writes.

With much of New Orleans below sea level already, society is faced with a stark choice: to retreat or to mount a heroic (but ultimately futile) defense. Short-term interests all but remove the first option from consideration.

Moving westward, we learn that lakes and streams once snaked through U.S. deserts. Over time, as the climate dried up, many of the region's waterways became disconnected, leaving tiny fish isolated and evolving into species not found anywhere else. As ranches drill for irrigating water, and the water tables fall, caves are drying up, likely causing the extinction of some of these evolutionary anomalies. Kolbert describes the extraordinary effort being mounted to head off the extinction of one such creature, the Devils Hole pupfish, which includes a $4.5 million facsimile of the species' isolated cave.

In Hawaii, Kolbert speaks with scientists trying to genetically engineer coral to survive in a hotter world. In Australia, she speaks with scientists studying genetic methods to control poisonous cane toads. Like the book's other examples, both of these efforts are a response to a problem of our own making. Ocean temperatures are rising because of humanity's addiction to fossil fuels. Cane toads are destroying Australian ecosystems because we introduced them to control insects on agricultural lands.

In the last part of the book, Kolbert shifts to the global climate, with reporting on researchers who are working to remove carbon dioxide from the atmosphere and on scientists who hypothesize that shooting reflective particles into the stratosphere may be key to cooling Earth. This latter solution, she notes, "has been described as 'dangerous beyond belief,' 'a broad highway to hell,' 'unimaginably drastic,' and also as 'inevitable.'"

Under a White Sky: The Nature of the Future
Elizabeth Kolbert
Crown, 2021. 256 pp.

Science and technology have brought us this far, but they have also contributed to the current mess in which we find ourselves, so it is only sensible to be skeptical of our ability to engineer ourselves out of this predicament. Most of the researchers with whom Kolbert spoke shared this perspective. Their efforts, rather than being evidence of unmitigated techno-optimism, were "the best [solutions] that anyone could come up with, given the circumstances." Nevertheless, one senses that if we do get out of this mess, it will be because of the efforts of scientists and technologists who are searching for solutions during a time when humanity seems an implacable force and nature an immovable object. ■

The reviewer is at the Department of Global Ecology, Carnegie Institution for Science, Stanford, CA 94305, USA. Email: kcaldeira@carnegiescience.edu

10.1126/science.abg0851

PHOTO: L. NEWMAN & A. FLOWERS/SCIENCE SOURCE

SCIENCE LIVES

Profiling the gene editor

A new biography traces CRISPR's origins and embraces scientist-led oversight of its future

By **George J. Annas**

In *The Code Breaker*, distinguished historian and biographer Walter Isaacson tells the life story of biochemist Jennifer Doudna, who played a major role in discovering the inner workings of the gene editing tool CRISPR-Cas9. Doudna's story is compelling and intersects with others, including French scientist Emmanuelle Charpentier, with whom Doudna shared the 2020 Nobel Prize in Chemistry, and notable figures in contemporary biology, including Eric Lander, George Church, and Feng Zhang.

Writing gracefully and with authority, Isaacson frames Doudna's life story with that of James Watson, who used model-building and photographs to propose the double-helix structure of DNA in 1953. Doudna, who received a copy of Watson's book *The Double Helix* from her father when she was in the sixth grade, recalls reading Watson's account of how he and other male scientists exploited and then minimized the contributions of their colleague Rosalind Franklin, but that was not the part that caught her attention. Doudna explains: "what mainly struck me was that a woman could be a great scientist."

With the help of a family friend who was a biologist, Doudna ignored her high school guidance counselor's discouragement ("Girls don't do science") and studied chemistry and biochemistry at Pomona College in Claremont, California. She completed her graduate work at Harvard, where she became an expert at deciphering RNA. After completing a postdoctoral fellowship at the University of Colorado, she accepted a tenure track position at Yale. In 2002, she and her husband, Jamie Cate, moved to the University of California, Berkeley, where, 4 years later, she would be introduced to CRISPR by microbiologist Jillian Banfield.

Doudna joined the giant biotech company Genentech in January 2009. She regretted the decision almost immediately. "It was a visceral response," she confides. "Every day and night, I felt I had made the wrong decision." She gratefully returned to Berkeley 2 months later, where she formed her own company, Caribou Biosciences—"a cut-and-splice mashup of 'Cas' and 'ribonucleotides'"—with Rachel Haurwitz in 2011. "At that time, the topic of molecular diagnostics was a turn-off to venture capitalists," Doudna tells Isaacson. "I also feel that there is an anti-female undercurrent, and I was worried that if we took venture money, that Rachel might be pushed out as CEO." The pair decided to raise the money they would need themselves.

The reviewer is at the Center for Health Law, Ethics, and Human Rights, Boston University School of Public Health, Boston, MA, USA. Email: annasgj@bu.edu

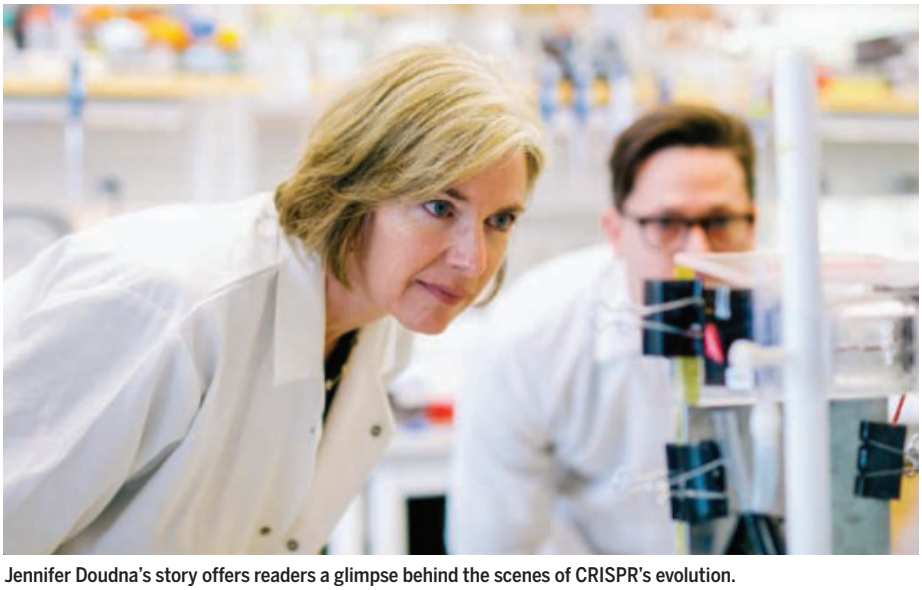

PHOTO: ANASTASIA SAPON/*THE NEW YORK TIMES*/REDUX

Jennifer Doudna's story offers readers a glimpse behind the scenes of CRISPR's evolution.

The Code Breaker: Jennifer Doudna, Gene Editing, and the Future of the Human Race
Walter Isaacson
Simon and Schuster, 2021.
560 pp.

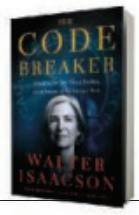

Doudna met Emmanuelle Charpentier for the first time at the 2011 conference of the American Society for Microbiology, where Charpentier suggested they work together to "figure out exactly how [CRISPR-Cas9] works." Fourteen months later, their groundbreaking work describing the essential components and biochemical mechanisms of CRISPR was published in *Science* (*1*). Isaacson describes a celebratory dinner on the day that the final revisions were submitted: "They ordered champagne and toasted what they knew would be a new era in biology."

Although dependable gene editing has almost limitless applications, Isaacson gives over most of the second half of the book to just one: the editing of human embryos. Here, he traces Doudna's evolving position on the matter, from an initial abhorrence to gradual acceptance as she comes to categorize it—wrongly, I think—as simply another in a long series of new reproductive technologies.

Science is necessary but it is not sufficient for decision-making in this realm. Isaacson concedes that society will need "not only scientists, but humanists" to guide us through the gene editing juncture, but this statement, which appears on the final page of the book's epilogue, feels almost like an afterthought.

In his enthusiastic embrace of science—communicated dramatically by the inclusion of two photos of the author in a white lab coat—Isaacson portrays himself as a member of the scientific tribe and no longer as an impartial observer. (Another story told by the book's striking photographs is the movement toward gender equality in science, but—unintentionally, I'm sure—also the persistence of structural racism. Very few people of color appear in these images. But this is a larger issue for another day.)

Although I do not endorse the book's science-centric view of human values, I highly recommend *The Code Breaker* to anyone interested in an insider's view of the politics of high-stakes academic research. We must understand the history of CRISPR before we write, edit, or regulate its future, and books that place the technology in broader context are vital to this pursuit. ■

REFERENCES AND NOTES

1. M. Jinek *et al.*, *Science* **337**, 816 (2012).

10.1126/science.abg5415

China's new protection laws could benefit the Critically Endangered Chinese pangolin (*Manis pentadactyla*).

Edited by **Jennifer Sills**

Seize China's momentum to protect pangolins

Pangolins are the world's most trafficked mammal, with trade epicenters in West and Central Africa, China, and Vietnam (*1*). The annual traditional medicine demand for pangolin scales requires about 200,000 animals (*2*). In January, tons of pangolin scales bound for Vietnam were confiscated in Nigeria (*3*). As a result of the staggering frequency of illegal hunting and trading, along with ecosystem deterioration and human activities that have caused inbreeding and deleterious mutations, all eight pangolin species are designated as at least Vulnerable on the International Union for Conservation of Nature (IUCN) Red List (*4*–*7*), and the Chinese pangolin (*Manis pentadactyla*) is Critically Endangered. In June 2020 and again in February, China made progress by upgrading pangolins to Class I species on its List of Wild Animals Under State Priority Conservation and removing their scales from the list of traditional medicine (*2*, *8*). We must seize the momentum from China's heightened protection to carry conservation of pangolins forward.

The prevention of pangolin poaching and biotope devastation in Africa and Asia (*8*) cannot be implemented through national penalties and fines alone. Because illegal poaching and trade of pangolins cross national borders, only a multilateral and transboundary partnership has the potential to effectively curtail the practice [e.g., (*9*)]. An interdisciplinary collaboration must be formed that includes nongovernmental organizations, the IUCN, and scientists. This coalition should promote local education and support environmentally sustainable behavior in the species' last sanctuaries.

Taking action would help meet UN Sustainable Development Goal 15 (biodiversity for life on land) (*10*). If such holistic measures toward protection are not taken, the misuse of pangolins in Asian traditional medicine will continue, along with the potential for zoonotic pandemics and the possible extinction of pangolin species (*7*, *11*, *12*).

Changlei Xia[1], Su Shiung Lam[2,1], Christian Sonne[3,1]*
[1]Nanjing Forestry University, Nanjing, China. [2]Universiti Malaysia Terengganu, Terengganu, Malaysia. [3]Aarhus University, Roskilde, Denmark.
*Corresponding author: cs@bios.au.dk

REFERENCES AND NOTES

1. United Nations Office on Drugs and Crime, "World Wildlife Crime Report 2020: Trafficking in protected species" (2020), chap. 4; www.unodc.org/documents/data-and-analysis/wildlife/2020/WWLC20_Chapter_4_Pangolin.pdf.
2. M. Standaert, "China raises protection for pangolins by removing scales from medicine list," *The Guardian* (2020); www.theguardian.com/environment/2020/jun/09/china-protect-pangolins-removing-scales-medicine-list-aoe.
3. Phys.org, "Nigeria seizes pangolin scales bound for Vietnam" (2021); https://phys.org/news/2021-01-nigeria-seizes-pangolin-scales-bound.html.
4. J. Y. Hu *et al.*, *Natl. Sci. Rev.* **7**, 798 (2020).
5. M. K. Boakye *et al.*, *PLOS One* **10**, e0117199 (2015).
6. Y. Liu *et al.*, *Science* **345**, 884 (2014).
7. D. Challender *et al.*, "*Manis pentadactyla*" (The IUCN Red List of Threatened Species, 2019): http://iucnredlist.org/species/12764/123585318.
8. K. Obermann, "A new hope for China's endangered animals," *SupChina* (2021); https://supchina.com/2021/02/17/a-new-hope-for-chinas-endangered-animals/.
9. Deutsche Gesellschaft für Internationale Zusammenarbeit, "Partnership against poaching and illegal wildlife trade in Africa and Asia" (2021); www.giz.de/en/worldwide/66553.html.
10. United Nations, Sustainable Development Goals (2015); www.un.org/sustainabledevelopment/biodiversity/.
11. A. Yee, *Science* **363**, 1142 (2019).
12. H. Wang *et al.*, *Science* **367**, 1435 (2020).

10.1126/science.abh3100

Minimize collateral damage in locust control

Since 2018, East Africa, Arabia, and southwestern Asia have been facing a severe upsurge of desert locusts, which began when heavy rains allowed them to breed (*1*, *2*). The locust swarms originated in the Empty Quarter sand desert of the southern Arabian Peninsula (*1*) and expanded rapidly because conflict regions such as Yemen, Somalia, and parts of Ethiopia were not able to implement sufficient locust control. Locust control measures started too late with intensive use of pesticides in large areas of Kenya, Sudan, the Arabian Peninsula, and India (*1*). Locust outbreaks of this dimension substantially threaten human livelihoods and must be controlled, but control efforts should aim to minimize collateral damage to the environment. We should plan now to mitigate the damage caused to both humans and the environment by the next locust swarm event.

Spraying pesticides in large regions will ultimately affect rare and threatened insect species, with particularly dire consequences in biodiversity hotspots such as the Horn of Africa, the Eastern Afromontane region, the Irano-Anatolian region, and the Western Ghats (*3*). The use of *Metarhizium acridum* is environmentally friendlier than other insecticides given that it affects only locusts and grasshoppers (*4*), but hundreds of endemic grasshopper species occur in these hotspots (*5*, *6*). Many of them are already threatened by habitat destruction caused by human land use (*7*). In South Asia, media coverage of locust swarms also prompted measures against harmless grasshopper species that were mistaken for locusts (*8*).

In the future, we must ensure that locust control starts before swarms emerge to prevent their proliferation, their migration, and the extreme control measures that must then be implemented. This will only be made possible by supporting developing countries and particularly regions with

PHOTO: MICHAEL PITTS/NPL/MINDEN PICTURES

human conflicts. We must empower the responsible authorities in such regions to establish proper locust monitoring and to implement environmentally friendly locust control in core areas of new locust outbreaks. Success will require ensuring that equipment remains functional and finding a way to access unsafe areas.

Axel Hochkirch[1]* and Dhaneesh Bhaskar[2,3]
[1]Department of Biogeography and International Union for Conservation of Nature (IUCN) Species Survival Commission Invertebrate Conservation Committee, Trier University, D-54286 Trier, Germany. [2]IUCN Species Survival Commission Grasshopper Specialist Group, Trier University, D-54386 Trier, Germany. [3]Care Earth Trust, Chennai, Tamil Nadu, 600061, India.
*Corresponding author.
Email: hochkirch@uni-trier.de

REFERENCES AND NOTES

1. Food and Agriculture Organization of the United Nations, Locust Watch, Desert Locust, Current upsurge (2019–2021); www.fao.org/ag/locusts/en/info/2094/index.html.
2. A. A. M. Salih, M. Baraibar, K. K. Mwangi, G. Artan, *Nat. Clim. Chan.* **10**, 584 (2020).
3. N. Myers, R. A. Mittermeier, C. G. Mittermeier, G. A. B. da Fonseca, J. Kent, *Nature* **403**, 853 (2000).
4. E. Stokstad, *Science* 10.1126/science.abb2759 (2020).
5. P. Johnsen, G. H. Schmidt, *Monit. Zool. Ital.* **Supp. 16**, 69 (1982).
6. S. H. Hodjat, M. Tork, M. Seiedy, B. Defaut, *Mat. Orth. Entom.* **23**, 35 (2018).
7. S. H. Hodjat, A. Saboori, M. Husemann, *J. Crop Prot.* **8**, 135 (2019).
8. D. Bhaskar, A. C. Rajan, P. S. Easa, "ENVIS Centre on Biodiversity (Fauna) Newsletter" (2020), vol. 27.

10.1126/science.abh3128

Appropriate names for COVID-19 variants

Multiple severe acute respiratory syndrome coronavirus 2 (SARS-CoV-2) variants are now circulating globally. Those with mutations in functional domains such as the receptor binding domain of the spike protein are of particular concern (*1*). In December 2020, three new variants of concern (VOC) with a common mutation at position 501 in the spike protein were reported: VOC-202012/01 (B.1.1.7, 501Y.V1, 20I) (*2*) was first identified in the United Kingdom, 501Y.V2 (B.1.351, 20H) (*1*) was first described by South African researchers, and P.1 (501Y.V3, 20J) was first identified in Japan and described by Brazilian researchers (*3*). Unfortunately, variants are widely being referred to by their country of first description. This naming convention should be avoided.

Using geographical regions to distinguish variants is harmful, as demonstrated by the term "China" virus, which has been used to blame and stigmatize China. The connotation that the variants were created and spread by their respective first locations has already generated political backlash through travel bans [e.g., (*4*)] and negative perceptions of these countries and their people. The risk of being associated with a new variant also disincentivizes country-level genomic surveillance and transparent reporting of their results.

The descriptions are also inaccurate. It is not known whether patient zero of each variant was a resident of or visitor to that country, and all variants have been identified well beyond the first countries in which they were identified (*5*). Variants that are more transmissible quickly become the dominant circulating variant in many countries, just like the D614G variant that rapidly became the dominant global variant early in the COVID-19 pandemic (*6*).

Admittedly, mutation-based or lineage names are difficult to say and write. The World Health Organization is expected to announce a standard nomenclature soon (*7*). Until then, scientific and media reports should not refer to variants by country names.

Salim S. Abdool Karim[1,2]*, Tulio de Oliveira[1,3,4], Glaudina Loots[5]
[1]Centre for the AIDS Program of Research in South Africa, Durban, South Africa. [2]Department of Epidemiology, Columbia University, New York, NY 10032, USA. [3]KwaZulu-Natal Research Innovation and Sequencing Platform, School of Laboratory Medicine & Medical Sciences, University of KwaZulu-Natal, Durban, South Africa. [4]Department of Global Health, University of Washington, Seattle, WA 98195 , USA. [5]Department of Science and Innovation, Pretoria, South Africa.
*Corresponding author.
Email: salim.abdoolkarim@caprisa.org

REFERENCES AND NOTES

1. H. Tegally *et al.*, *Nature* 10.1038/s41586-021-03402-9 (2021).
2. N. Davies *et al.*, "Estimated transmissibility and impact of SARS-CoV-2 lineage B.1.1.7 in England" (CMMID Repository, 2020); https://cmmid.github.io/topics/covid19/uk-novel-variant.html.
3. N. R. Faria *et al.*, "Genomic characterisation of an emergent SARS-CoV-2 lineage in Manaus: Preliminary findings," Virological (2020); https://virological.org/t/genomic-characterisation-of-an-emergent-sars-cov-2-lineage-in-manaus-preliminary-findings/586.
4. *The Guardian*, "Hancock says UK will 'come down hard' on South Africa Covid variant—video" (2021); www.theguardian.com/world/video/2021/feb/02/hancock-says-uk-will-come-down-hard-on-south-africa-covid-variant-video.
5. PANGO lineages, "Global report investigating novel coronavirus haplotypes" (2021); https://cov-lineages.org/global_report.html.
6. B. Korber *et al.*, *Cell* **182**, 812 (2020).
7. World Health Organization, "Statement on the sixth meeting of the International Health Regulations (2005) Emergency Committee regarding the coronavirus disease (COVID-19) pandemic" (2021); www.who.int/news/item/15-01-2021-statement-on-the-sixth-meeting-of-the-international-health-regulations-(2005)-emergency-committee-regarding-the-coronavirus-disease-(covid-19)-pandemic.

10.1126/science.abh0836

Open-Design Upright Microscope

- Optional motorized or fixed XY stage, or motorized translator
- Open-design microscope with motorized focus
- Quickly configurable based on experimental needs
- Optimized *In vivo* and *In vitro* experimentation on one setup
- Uses standard Olympus objectives
- Free Multi-Link™ software coordinates movement with MPC-200 controller
- OCC or DIC transmitted light (LED)
- Epi-fluorescent imaging

BOB™

SUTTER INSTRUMENT®

PHONE: +1.415.883.0128
FAX: +1.415.883.0572
EMAIL: INFO@SUTTER.COM
WWW.SUTTER.COM

RESEARCH

IN *SCIENCE* JOURNALS

Edited by **Michael Funk**

ATMOSPHERIC AEROSOLS

Smoke alarm

Intense, widespread bushfires in Australia injected huge amounts of smoke into the stratosphere in 2020. Hirsch and Koren found that this smoke caused record-breaking levels of aerosols over the Southern Hemisphere, as much as that from a moderate volcanic eruption. The severity was caused by a combination of the vigor of the fires and their location at a latitude with a shallow tropopause and within the midlatitude cyclones belt. This aerosol increase caused considerable cooling over oceanic cloud-free areas. —HJS

Science, this issue p. 1269

Wildfires in Australia in 2020 produced a massive increase in stratospheric aerosols in the Southern Hemisphere.

RIBOZYMES

A processive RNA replicator

The RNA World Hypothesis suggests that, before modern life, there were RNA molecules that were capable of carrying genetic information and driving chemical reactions, a task gradually replaced by DNA and enzymes in modern biology. Central to this theory is an RNA replicase capable of mediating general replication of RNA. Using laboratory evolution, Cojocaru *et al.* isolated a promoter-based RNA polymerase ribozyme that, analogous to modern-day protein polymerases, clamps onto templates to increase its processivity, making it a potential model for replication in early biology. —DJ

Science, this issue p. 1225

2D MATERIALS

Tuning the interactions

Elucidating the nature of the superconducting state in magic-angle twisted bilayer graphene (MATBG) has proven tricky. To study the role of electron-electron correlations in this state, Liu *et al*. placed another graphene bilayer, this one having a conventional arrangement of the graphene sheets, in the immediate vicinity of a sample of MATBG. By varying the carrier density in the conventional bilayer, the researchers controlled the strength of interactions in MATBG. Weakening the interactions strengthened superconductivity, consistent with scenarios in which the electron-phonon coupling competes against Coulomb interactions to stabilize the superconducting phase. —JS

Science, this issue p. 1261

DEVELOPMENT

Genomic sleuthing spots early divergence

After fertilization, the human zygote divides into two cells.

Analysis of adult tissues reveals that the first cell division within a developing embryo is asymmetric.

Fasching *et al*. used genomic analysis from cellular samples taken much later in development to back-calculate the cell division trees that went before. Although the first cell division in human development looks symmetrical from the outside, the fates followed by daughter cells from each of those first two blastomeres are anything but the same. As much as 90% of blood cells are derived from just one of the first two blastomeres. —PJH

Science, this issue p. 1245

ORGANIC CHEMISTRY

Sequentially snipping off fluorines

It is often useful in pharmaceutical or agrochemical research to modify the properties of carbon compounds by appending one or

CREDITS (TOP TO BOTTOM): GEOPIX / ALAMY STOCK PHOTO; JEAN-PAUL CHASSENET/SCIENCE SOURCE

more fluorine atoms. However, the methods used to prepare mono-, di-, or trifluorocarbon centers tend to differ from each other in inconvenient ways. Yu *et al*. developed a radical reaction that can successively remove one or two fluorine atoms from trifluoromethyl groups adjacent to amides or esters. The mechanism relies on a spin-center shift after attack at the carbonyl oxygen by a boryl radical. —JSY

Science, this issue p. 1232

ASTROCHEMISTRY

Identifying PAHs in space

Midinfrared spectroscopy has shown that polycyclic aromatic hydrocarbons (PAHs) are abundant in many astronomical objects, but this technique cannot determine which specific PAH molecules are present. Radio astronomy could provide individual identifications if the molecule is sufficiently abundant and has a large dipole moment, but PAHs are expected to produce large numbers of very weak lines. McGuire *et al*. performed a stacking and matched filter analysis to search for PAHs in radio observations of TMC-1, located within the interstellar Taurus Molecular Cloud. They identified emission from two isomers of the small PAH cyanonapthalene, two fused benzene rings with a CN group attached. —KTS

Science, this issue p. 1265

TOPOLOGICAL OPTICS

Topology in the open

Controlling the topology of a system provides a route to develop devices that are robust against defects. Whereas earlier developments of topological band theory focused on Hermitian (closed) systems, recent efforts have been toward non-Hermitian (open) systems. K. Wang *et al*. report on the measurement and control of topologically nontrivial windings of a non-Hermitian energy band. By implementing non-Hermitian lattice Hamiltonians along a frequency synthetic dimension formed by optical frequency modes in a modulated ring-resonator, they directly visualized the nontrivial topological band winding and showed that the winding can be controlled. Such control provides a route for the experimental synthesis, characterization, and control of topologically nontrivial phases in open physical systems. —ISO

Science, this issue p. 1240

PAIN

Painful intercellular connections

Chronic pain impairs quality of life and is challenging to treat. Wangzhou *et al*. measured ligand and receptor gene expression in sensory neurons and various peripheral cell types from humans and mice. Using these data, the authors constructed a connectome of potential cell type–specific interaction points between sensory nerves and innervated tissues, which suggested that blocking heparin-binding epidermal growth factor (HBEGF) signaling may be an effective way to alleviate chronic pain in multiple diseases. This target was validated in a mouse model of mechanical pain. —LKF

Sci. Signal. **14**, abe1648 (2021).

INNATE IMMUNITY

Deep-sea microbes exhibit immunosilence

The innate immune system of mammals uses pattern recognition receptors (PRRs) to detect conserved ligands displayed by potentially pathogenic microbes. Gauthier *et al.* tested whether bacteria from deep-sea Pacific Ocean water samples could evade such immune surveillance mechanisms. The prototype PRR agonist lipopolysaccharide (LPS) from most strains of the deep-sea genus *Moritella* was deficient at engaging with mouse and human LPS-sensing PRRs despite retaining many common features of LPS in gut bacteria. The broad recognition powers of PRRs are thus not broad enough to detect a subset of microbes recovered from extreme environments. —IRW

Sci. Immunol. **6**, eabe0531 (2021).

IN OTHER JOURNALS

Edited by **Caroline Ash** *and* **Jesse Smith**

POLLINATION ECOLOGY

Insects in the city

The floral landscape for insect pollinators has undergone major changes in human-dominated environments. Tew *et al.* compared the distribution of floral resources in urban areas, nature reserves, and farmland in the United Kingdom. They estimated nectar supply in the three habitats by combining data on nectar sugar production and floral abundance. Nectar sugar production was similar per unit area in all three habitats, but the diversity of nectar sources in cities was substantially higher than that in farmland or nature reserves. Residential gardens were found to be of key importance in providing nectar resources from a wide variety of plant species for pollinating insects. —AMS

J. Ecol. 10.1111/1365-2745.13598 (2021).

The diversity of nectar sources in cities for pollinators such as this meadow brown butterfly now exceeds other major habitats in the UK.

MEDICINE

Bacteriotherapy for the skin

Atopic dermatitis, a form of eczema, can be exacerbated by colonization of the affected skin with *Staphylococcus aureus*. Nakatsuji *et al*. report a phase 1 clinical trial of *Staphylococcus hominis* A9 (*Sh*A9) as a topical treatment for atopic dermatitis. *Sh*A9 is found on the skin of healthy people and selectively

PHOTO: NICK UPTON/ALAMY STOCK PHOTO

SOIL CONSERVATION

Agricultural soil loss

The current era of major loss of agriculturally productive soils has gained relatively little public attention. It seems intuitively unnecessary to spell out what will happen to food production, hydrology, carbon sequestration, and ecological services if we allow soil erosion to proceed at current rates. However, it is difficult to quantify soil loss and to translate that into agricultural loss. Thaler *et al.* focused on the US Corn Belt and used remote sensing to map areas in fields that have no carbon-rich (i.e., A-horizon) soils remaining. Previous attempts to quantify soil loss suggested that little damage had occurred. By contrast, the new estimate indicates that ~35% of an area of ~400,000 square kilometers (a third of the Corn Belt area) has lost its A-horizon soil (~1.4 petagrams), especially on hillslopes. The authors suggest that mechanically working the land (tillage) has been responsible for most soil loss in this region. This degree of erosion translates into a 6% reduction in overall crop yield and ~$3 billion in economic loss. —CA

Proc. Natl. Acad. Sci. U.S.A. **118**, e1922375118 (2021).

Recent estimates show that up to 35% of the US Corn Belt has lost its carbon-rich topsoil, with mechanical tillage promoting erosion.

inhibits strains of *S. aureus* that have been associated with atopic dermatitis. It also improves atopic dermatitis in mice. The authors report that *Sh*A9 treatment did not cause serious adverse events, and *S. aureus* abundance was reduced, even during a short 7-day trial. Additionally, application of *Sh*A9 altered the microbial composition on affected skin, suggesting that the treatment induces a more beneficial skin microbiota. —GKA

Nat. Med. 10.1038/s41591-021-01256-2 (2021).

QUANTUM GASES

A versatile microscope

Quantum microscopes have been used for more than a decade now to image the many-body states of quantum gases in optical lattices. However, their resolution is limited to optical wavelengths, and they can typically image only a single layer of atoms. As a complementary technique for imaging quantum gases, Veit *et al.* developed an ion microscope. Atoms were first ionized by laser light, and the resulting ions were controlled using electrostatic lenses and imaged. Although the technique was demonstrated on rubidium atoms in their ground state, it is expected that it will also work on highly excited Rydberg atoms and will enable three-dimensional and time-dependent imaging. —JS

Phys. Rev. X **11**, 011036 (2021).

POLYMER CHEMISTRY

C–H activation goes macro

Methods to oxidize carbon-hydrogen (C–H) bonds under mild conditions are showing increasing promise in streamlining small-molecule synthesis. Chen *et al.* report an application tailored instead to a macromolecule: polyethylene. The world's most common plastic has proven hard to tweak without damaging its structural integrity, but a ruthenium porphyrin catalyst is just selective enough to introduce hydroxyl and carbonyl substituents without disrupting the backbone. The oxidized polymers remained mechanically robust while showing improved adhesion properties and wettability by simple latex paint. —JSY

Chem **7**, P137 (2021).

MACROCYCLES

Hold that pose

Within proteins, individual peptide bonds have free rotation but typically keep to a narrow conformational space. Macrocycles are already conformationally hindered and provide an interesting venue for pushing peptide bonds into uncharted territory. Diaz *et al*. prepared a series of small macrocycles using so-called dominant rotors, peptide-like units that are kinetically locked in a particular conformation. Structural analysis revealed unusual conformations of the peptide backbone beside the dominant rotor, perhaps indicative of the kinds of fleeting intermediates expected during peptide folding. —MAF

Nat. Chem. **13**, 218 (2021).

REPRODUCTION

Halting the flow of the embryo

After release of ova from the ovary, female germ cells are transported to the uterus through the oviduct or fallopian tubes. Various factors influence transit, including cilia, muscle contractions, and signaling molecules. Many mammalian species display temporary pausing and release, described as "valve-like tubal locking," as ova transit the oviduct, and this arrest may assist in fertilization. However, ova are occasionally inappropriately stalled in the oviduct, and an ectopic pregnancy can result if they are fertilized by sperm. Bianchi *et al.* identified the oviduct-expressed gene adhesion G protein–coupled receptor D1 (Adgrd1) as being important for mouse embryo transport, in particular the restraining mechanism during embryo transit. When the gene is defective, fluid flow in the oviduct is altered and embryos become retained in the oviduct ampulla. —BAP

Nat. Commun. **12**, 1251 (2021).

PHOTO: GRANT HEILMAN PHOTOGRAPHY/ALAMY STOCK PHOTO

REVIEW SUMMARY

SUSTAINABILITY

Using satellite imagery to understand and promote sustainable development

Marshall Burke*, Anne Driscoll, David B. Lobell, Stefano Ermon

BACKGROUND: Accurate and comprehensive measurements of a range of sustainable development outcomes are fundamental inputs into both research and policy. For instance, good measures are needed to monitor progress toward sustainability goals and evaluate interventions designed to improve development outcomes. Traditional approaches to measurement of many key outcomes rely on household surveys that are conducted infrequently in many parts of the world and are often of low accuracy. The paucity of ground data stands in contrast to the rapidly growing abundance and quality of satellite imagery. Multiple public and private sensors launched in recent years provide temporal, spatial, and spectral information on changes happening on Earth's surface.

Here we review a rapidly growing scientific literature that seeks to use this satellite imagery to measure and understand various outcomes related to sustainable development. We pay particular attention to recent approaches that use methods from artificial intelligence to extract information from images, as these methods typically outperform earlier approaches and enable new insights. Our focus is on settings and applications where humans themselves, or what they produce, are the outcome of interest and on where these outcomes are being measured using satellite imagery.

ADVANCES: We describe and synthesize the variety of approaches that have been used to extract information from satellite imagery, with particular attention given to recent machine learning–based approaches and settings in which training data are limited or noisy. We then quantitatively assess predictive performance of these approaches in the domains of smallholder agriculture, economic livelihoods, population, and informal settlements. We show that satellite-based performance in predicting these outcomes is reasonably strong and improving. Performance improvements have come through a combination of more numerous and accurate training data, more abundant and higher-quality imagery, and creative application of advances in computer vision to satellite inputs and sustainability outcomes. Further, our analyses suggest that reported model performance likely understates true performance in many settings, given the noisy data on which predictions are evaluated and the types of noise typically observed in sustainability applications. For multiple outcomes of interest, satellite-based estimates can now equal or exceed the accuracy of traditional approaches to outcome measurement. We describe multiple methods through which the true performance of satellite-based approaches can be better understood.

Integration of satellite-based sustainability measurements into research has been broad, and we describe applications in agriculture, fisheries, health, and economics. Documented uses of these measurements in public-sector decision-making are rarer, which we attribute in part to the novelty of the approaches, their lack of interpretability, and the potential benefits to some policy-makers of not having certain outcomes be measured.

OUTLOOK: The largest constraint to satellite-based model performance is now training data rather than imagery. While imagery has become abundant, the scarcity and frequent unreliability of ground data make both training and validation of satellite-based models difficult. Expanding the quantity and quality of such data will quickly accelerate progress in this field. Other opportunities for advancement include improvements in model interpretability, fusion of satellites with other nontraditional data that provide complementary information, and more-rigorous evaluation of satellite-based approaches (relative to available alternatives) in the context of specific use cases.

Nevertheless, despite the current and future promise of satellite-based approaches, we argue that these approaches will amplify rather than replace existing ground-based data collection efforts in most settings. Many outcomes of interest will likely never be accurately estimated with satellites; for outcomes where satellites do have predictive power, high-quality local training data can nearly always improve model performance. ■

The list of author affiliations is available in the full article online.
*Corresponding author. Email: mburke@stanford.edu
Cite this article as M. Burke *et al.*, *Science* 371, eabe8628 (2021). DOI: 10.1126/science.abe8628

READ THE FULL ARTICLE AT
https://doi.org/10.1126/science.abe8628

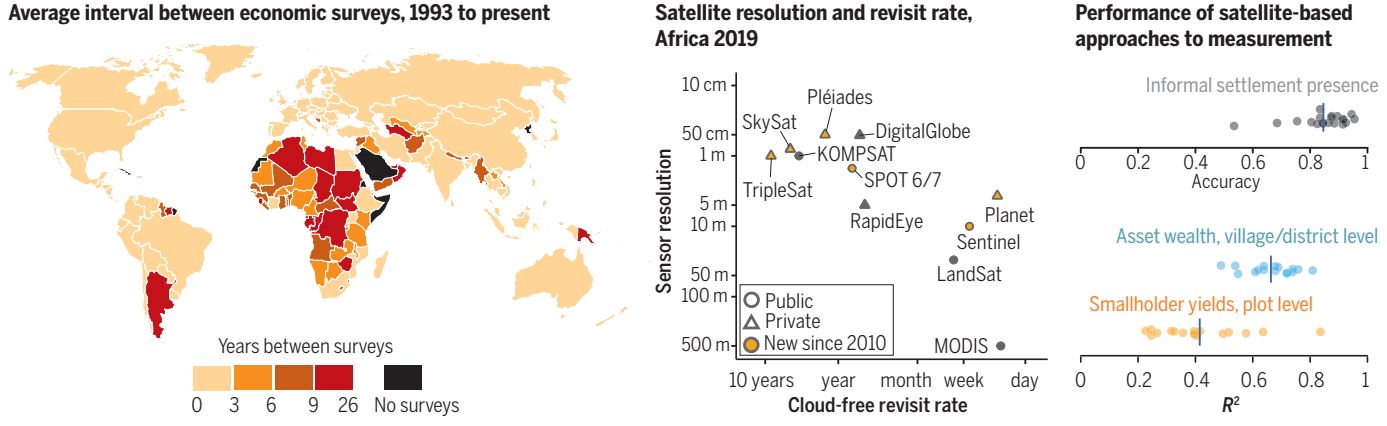

Increasing collection of satellite imagery can help measure livelihood outcomes in areas where ground data are sparse. (Left) Interval between nationally representative economic surveys over the past three decades shows long lags in many developing countries. (Middle) Recently added public and private satellites have broken the traditional trade-off between temporal and spatial resolution. (Right) Performance in measuring the presence of informal settlements, crop yields on smallholder agricultural plots, and village-level asset wealth. R^2, coefficient of determination.

RESEARCH ARTICLE SUMMARY

SPLICEOSOME

Structure of the activated human minor spliceosome

Rui Bai*, Ruixue Wan*†, Lin Wang, Kui Xu, Qiangfeng Zhang, Jianlin Lei, Yigong Shi†

INTRODUCTION: Precursor messenger RNA (pre-mRNA) splicing, which involves the removal of noncoding introns and the ligation of the coding exons, is achieved by the spliceosome. An intron is defined by a 5′ splice site (5′SS), a branch point sequence (BPS), and a 3′ splice site (3′SS). Most introns belong to the U2 type and are removed by the major spliceosome that contains the U2 small nuclear RNA (snRNA). A very small percentage of introns are the U12 type, which is characterized by a distinct 5′SS and BPS. The U12-type genes, present in all major eukaryotic taxa, play an essential role in development. The U12-type intron is removed by the minor spliceosome, which contains five snRNAs: U11, U12, U4atac, U5, and U6atac. Of these snRNAs, only U5 is shared between the major and minor spliceosomes.

Because of its scarcity in cells, the minor spliceosome has represented a challenge for biochemical studies. Before now, there was no structural information or published protocol on the purification of the minor spliceosome. It was unclear how many U12-specific protein components are present in each major functional state of the minor spliceosome and how they may facilitate the splicing reaction. We did not even know whether rules derived from the major spliceosome could apply to the minor spliceosome.

RATIONALE: To address these questions, we need to both develop a protocol for the assembly and purification of the minor spliceosome and determine the structure of the minor spliceosome at resolutions that give sufficiently detailed structural features. Structural comparison between the major and minor spliceosomes may reveal valuable information on protein components specific to either spliceosome, U12-type intron recognition, snRNA conformation, active site configuration, and regulatory mechanisms.

RESULTS: We replaced the U2-type 5′SS, BPS, and 3′SS of the intron in the MINX pre-mRNA with those of the U12-type, generating a MINX-U12 pre-mRNA. In an in vitro splicing assay, MINX-U12 undergoes splicing to produce ligated exons under conditions in which the major spliceosomes are inactivated in the nuclear extract. These results demonstrate the presence of active minor spliceosome in the extract. We then truncated MINX-U12 such that the binding site for the ATPase/helicase PRP2 is absent. This strategy, which was designed to enrich the activated minor spliceosome (B^{act} complex) by preventing its remodeling by PRP2, proved to be successful. We purified the human minor B^{act} complex and determined its cryo–electron microscopy (cryo-EM) structure at an average resolution of 2.9 Å.

Although the overall organization of the RNA elements in the human minor B^{act} complex closely resembles that in the major B^{act} complex, there are notable local differences. Compared with U6 snRNA in the major spliceosome, U6atac snRNA lacks the 5′ stem loop, and the U12/U6atac duplex lacks helix II. Notably, the 3′-end sequences of U6atac snRNA form a characteristic 3′ stem loop that is placed in approximately the same location as that of the U2/U6 helix II in the major B^{act} complex. The distinct 5′SS and BPS of the U12-type intron are recognized through extensive base-pairing interactions by U6atac and U12 snRNA, respectively. Two catalytic metals, M1 and M2, are already loaded in the splicing active site center and poised for catalysis of the branching reaction.

The EM maps allow for the identification of five previously unidentified proteins—SCNM1, RBM48, ARMC7, CRIPT, and PPIL2—that appear to play key roles in the minor spliceosome. SCNM1 mimics the SF3a complex of the major spliceosome. The N-terminal domain of SCNM1 shares sequence homology with SF3a66 of the SF3a complex. Similarly to SF3a66, the N-terminal domain of SCNM1 binds the BPS/U12 duplex and the proteins SF3b155, SF3b145, and CDC5L, whereas the N terminus inserts into the active site to interact with 5′SS, U6atac snRNA, and the splicing factor RNF113A. The C-terminal domain of SCNM1 functionally mimics SF3a60 (another component of the SF3a complex). The RBM48-ARMC7 complex binds the γ-monomethyl phosphate cap of the guanine nucleotide at the 5′ end of U6atac snRNA through extensive interactions. The splicing factor CRIPT binds RNF113A and stabilizes U12 small nuclear ribonucleoprotein (snRNP) through interactions with SF3b14b, SF3b145, and SF3b155. The U-box protein PPIL2 in an extended conformation interacts with a number of proteins and RNA, stabilizing the overall conformation of U5 snRNP. The N terminus of PPIL2 specifically recognizes loop I of U5 snRNA. Additionally, PRP2 and its coactivator SPP2 are bound to the minor B^{act} complex, which suggests similar roles for PRP2 and SPP2 in the minor spliceosome as those observed in the major spliceosome.

CONCLUSION: The cryo-EM structure of the human minor B^{act} complex reveals a number of previously unknown features, including the identification of minor spliceosome–specific proteins. This structure serves as a framework for the mechanistic understanding of the functions of the minor spliceosome. ■

Structure of the minor B^{act} complex at 2.9 Å

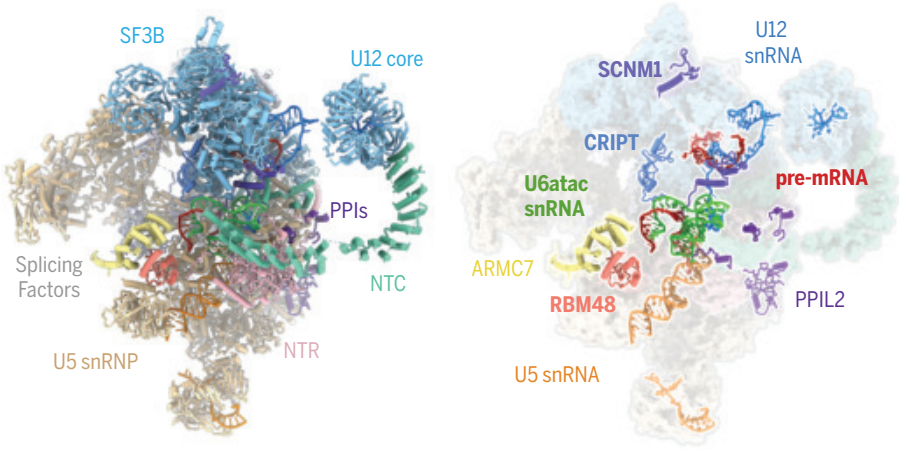

Structure of the activated human minor spliceosome (B^{act} complex). (Left) The minor B^{act} complex comprises U12 snRNP, U5 snRNP, U6atac snRNA, the truncated MINX-U12 pre-mRNA, nineteen complex (NTC), NTC-related (NTR), the retention and splicing (RES) complex, two prolyl peptidyl isomerase (PPIase)–like proteins (PPIs), and nine splicing factors. (Right) Based on EM maps, the minor spliceosome contains five newly identified proteins—SCNM1, RBM48, ARMC7, CRIPT, and PPIL2—which together with snRNAs are highlighted in the foreground. All other components are in the background.

The list of author affiliations is available in the full article online.
*These authors contributed equally to this work.
†Corresponding author. Email: wanruixue@westlake.edu.cn (R.W.); syg@westlake.edu.cn (Y.S.)
Cite this article as R. Bai *et al.*, *Science* 371, eabg0879 (2021). DOI: 10.1126/science.abg0879

READ THE FULL ARTICLE AT
https://doi.org/10.1126/science.abg0879

RESEARCH ARTICLE SUMMARY

INNATE IMMUNITY

Phosphorylation and chromatin tethering prevent cGAS activation during mitosis

Tuo Li*, Tuozhi Huang*, Mingjian Du, Xiang Chen, Fenghe Du, Junyao Ren, Zhijian J. Chen†

INTRODUCTION: Cyclic guanosine monophosphate (GMP)–adenosine monophosphate (AMP) synthase (cGAS) detects microbial DNA in the cytosol to trigger innate immune responses. cGAS also senses self-DNA in the cytoplasm to promote sterile inflammation and cellular senescence. cGAS binds to double-stranded DNA in a sequence-independent manner, and the multivalent interactions between cGAS and DNA lead to their liquid-liquid phase separation and cGAS activation in the resulting liquid droplets. Once activated, cGAS catalyzes the synthesis of cyclic GMP-AMP (cGAMP), a second messenger that activates the adaptor protein stimulator of interferon genes (STING), leading to the induction of type I interferons and other immune mediators. Paradoxically, a large fraction of cGAS is tightly associated with chromatin, especially during mitosis when the nuclear envelope breaks down. How cGAS activity is regulated during mitosis remains poorly understood.

RATIONALE: Accumulating evidence reveals both cytoplasmic and nuclear localization of cGAS in cells. In the nucleus, cGAS is tethered to the chromatin through binding to histones that form the nucleosome core; this interaction has been shown to inhibit cGAS activation by chromatin DNA. However, it is unclear whether additional mechanisms exist to regulate cGAS activity, especially during the cell cycle transition. In particular, the nuclear envelope disassembles when cells enter mitosis, allowing cytoplasmic cGAS to mix with the chromosomes. Direct measurements of cGAS activity and posttranslational modifications at different stages of the cell cycle might unravel the mechanism of cGAS regulation and lead to a better understanding of how cells prevent inadvertent activation of cGAS by chromatin DNA, which might otherwise lead to inflammation and autoimmune responses.

RESULTS: Using a biochemical assay, we found that cGAS activity in human cell lines was selectively suppressed during mitosis. We further showed that when cells enter mitosis, cGAS is hyperphosphorylated by Aurora kinase B and other kinases at its disordered and positively charged N terminus, a region important for DNA binding and liquid phase separation. Mutations that mimic N-terminal hyperphosphorylation abolished cGAS activity, whereas those blocking hyperphosphorylation led to enhanced expression of interferon-stimulated genes. We also developed a split green fluorescent protein (GFP) complementation assay to detect cGAS oligomerization. Chromatin-associated cGAS could not oligomerize, which elucidates how chromatin tethering inhibits cGAS activity in live cells. We found that cGAS mutants defective in chromatin tethering were activated by chromatin DNA in a manner dependent on an unphosphorylated N terminus, underscoring the importance of the cGAS N terminus in sensing chromatin DNA. Unexpectedly, deletion of the N terminus from cGAS exposed a cryptic mitochondrial localization sequence that targeted cGAS to the mitochondrial matrix, where mitochondrial DNA activated cGAS. This result explains why cGAS that lacks the N terminus is constitutively active. Together, our results revealed that hyperphosphorylation and chromatin tethering act in parallel to suppress cGAS activity during mitosis.

CONCLUSION: This work presents direct evidence that cGAS activity is suppressed during mitosis through two mechanisms: hyperphosphorylation at the N terminus and chromatin tethering that inhibits cGAS oligomerization. Both mechanisms prevent cGAS phase separation into liquid droplets where cGAS could efficiently synthesize cGAMP. This fail-safe mechanism of inhibition keeps cGAS silent across the normal cell cycle transition, potentially thereby avoiding autoimmune reactions to nuclear DNA. ■

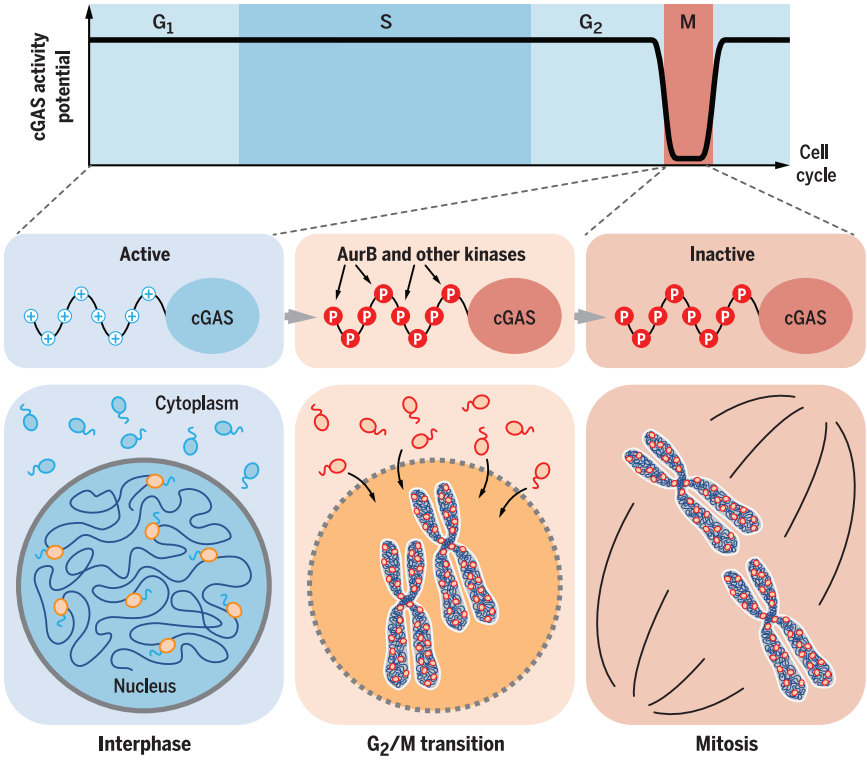

Regulation of cGAS activity during cell cycle transition. When cells enter mitosis, cGAS loses its ability to be activated by DNA (top). During interphase (bottom left), cGAS is poised for activation by DNA in the cytoplasm (blue) but cannot be activated in the nucleus by chromatin (orange). During the G_2-M transition (bottom middle), the N terminus of cGAS is hyperphosphorylated by Aurora kinase B (AurB) and other kinases, thereby blocking cGAS liquid phase separation and activation (red). Upon nuclear envelope breakdown, cytoplasmic cGAS is recruited to condense chromosomes and becomes further inhibited by chromatin tethering, which prevents cGAS oligomerization during mitosis (bottom right). +, positive charge; P, phosphorylation.

The list of author affiliations is available in the full article online.
*These authors contributed equally to this work.
†Corresponding author. Email: zhijian.chen@utsouthwestern.edu
Cite this article as T. Li *et al.*, *Science* **371**, eabc5386 (2021). DOI: 10.1126/science.abc5386

READ THE FULL ARTICLE AT
https://doi.org/10.1126/science.abc5386

RESEARCH ARTICLE SUMMARY

IMMUNOLOGY

Structure-based decoupling of the pro- and anti-inflammatory functions of interleukin-10

Robert A. Saxton, Naotaka Tsutsumi, Leon L. Su, Gita C. Abhiraman, Kritika Mohan, Lukas T. Henneberg, Nanda G. Aduri, Cornelius Gati, K. Christopher Garcia*

INTRODUCTION: Interleukin-10 (IL-10) is an important immunoregulatory cytokine that acts to suppress and terminate inflammatory immune responses, largely through the inhibition of monocyte and macrophage activation. Polymorphisms in genes encoding IL-10 and IL-10 receptor (IL-10R) subunits are associated with autoimmune diseases, most notably inflammatory bowel disease (IBD). IL-10 has consequently garnered substantial clinical interest for use as an anti-inflammatory immune modulating agent. However, IL-10 has shown limited therapeutic efficacy, due in part to its pleiotropic nature and its capacity to also elicit proinflammatory effects, including the stimulation of interferon-γ (IFN-γ) and granzyme B production by $CD8^+$ T cells.

RATIONALE: We hypothesized that obtaining structural information for the complete IL-10 receptor complex would enable the rational design of IL-10 analogs with enhanced functional specificity and improved therapeutic utility. Mechanistically, IL-10 functions as a secreted homodimer that engages two copies of a heterodimeric receptor complex comprising the private receptor subunit, IL-10Rα, and the shared subunit, IL-10Rβ. The IL-10–dependent dimerization of IL-10Rα and IL-10Rβ in turn initiates activation of the transcription factor STAT3, which mediates the diverse biological effects of IL-10. However, structural information for the complete IL-10 receptor signaling complex is lacking, due in part to the extremely low affinity of IL-10 for IL-10Rβ.

RESULTS: To overcome this limitation, we first used yeast display-based directed evolution to engineer a "super-10" variant with greatly enhanced affinity for IL-10Rβ, enabling assembly of the hexameric IL-10–IL-10Rα–IL-10Rβ complex. Using this stabilized complex, we then determined the structure of the complete IL-10 receptor complex at 3.5 Å resolution by cryo–electron microscopy (cryo-EM). The structure revealed how IL-10 engages IL-10Rβ to initiate signal transduction, and also uncovered the molecular basis for a mutation in IL-10Rβ associated with early-onset IBD. In addition, the structure provided an engineering blueprint for the design of IL-10 variants with which we could pharmacologically probe the nature of IL-10's functional pleiotropy.

Characterization of these IL-10 variants revealed that the plasticity of IL-10 signaling varies extensively across immune cell types, inversely correlating with the level of IL-10Rβ expression. In particular, we found that myeloid cells exhibit robust STAT3 activation in response to IL-10 variants across a wide range of IL-10Rβ–binding affinities, whereas IL-10 signaling in lymphocytes was highly tunable. Several engineered IL-10 variants exploited these differences to elicit myeloid-biased signaling in both cell lines and human peripheral blood mononuclear cells (PBMCs). Functionally, these variants effectively inhibited inflammatory monocyte and macrophage activation in vivo and promoted survival in a mouse model of sepsis, thus retaining the major anti-inflammatory effects of IL-10. However, they showed significantly reduced capacity to stimulate proinflammatory gene expression in $CD8^+$ T cells and failed to potentiate IFN-γ or granzyme B production, thereby uncoupling the major opposing functions of IL-10.

CONCLUSION: The cryo-EM structure of the IL-10 receptor complex yields key insights into the mechanisms of IL-10 signaling and functional pleiotropy. Characterization of IL-10–derived partial agonists and super-agonists revealed that modulating receptor affinity can "tune" IL-10 signaling in a cell type–selective manner, exploiting differences in IL-10 response thresholds between immune cell populations. These results suggest a model in which the differential expression of the shared receptor subunit IL-10Rβ results in distinct IL-10 response thresholds across immune cell populations, enhancing the functional specificity of IL-10. By exploiting these natural features of IL-10 signaling, we engineered IL-10 variants exhibiting myeloid cell selectivity, which effectively uncoupled the pro- and anti-inflammatory functions of IL-10. These findings provide a conceptual framework for the development of improved cytokine-based therapeutics. ■

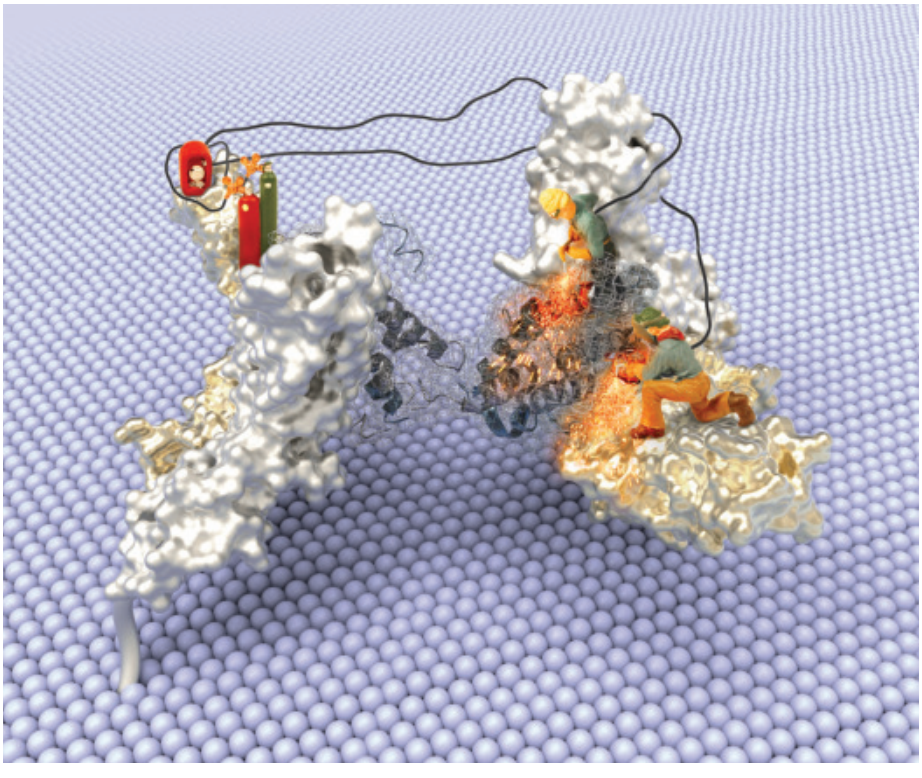

Engineering IL-10. The structure of the IL-10 receptor complex is shown on a cell surface with "engineers" depicted as welders making alterations to IL-10 at the receptor-binding interface that was the focus of Saxton *et al.*

The list of author affiliations is available in the full article online.
*Corresponding author. Email: kcgarcia@stanford.edu
Cite this article as R. A. Saxton *et al.*, *Science* 371, eabc8433 (2021). DOI: 10.1126/science.abc8433

READ THE FULL ARTICLE AT
https://doi.org/10.1126/science.abc8433

ILLUSTRATION: ERIC SMITH AND CHRIS GARCIA

RESEARCH ARTICLE SUMMARY

IMMUNOMETABOLISM

γδ T cells regulate the intestinal response to nutrient sensing

Zuri A. Sullivan, William Khoury-Hanold, Jaechul Lim, Chris Smillie, Moshe Biton, Bernardo S. Reis, Rachel K. Zwick, Scott D. Pope, Kavita Israni-Winger, Roham Parsa, Naomi H. Philip, Saleh Rashed, Noah Palm, Andrew Wang, Daniel Mucida, Aviv Regev, Ruslan Medzhitov*

INTRODUCTION: The gastrointestinal (GI) tract is a multikingdom cellular ecosystem that facilitates the procurement of nutrients from the environment. In constant contact with the external world, the small intestine is at once a gateway for life-threatening pathogens and toxins and the site of absorption for life-sustaining nutrients. Consequently, this tissue is tasked with the challenge of balancing its primary functions of nutrient uptake and host defense in response to a complex and constantly changing environment.

This challenge is particularly daunting for omnivores, whose diets change on daily, seasonal, and developmental time scales. The diverse diets of such generalists stand in contrast to those of specialists—animals that consume restricted diets—such as carnivores and herbivores. Whereas these specialists have evolved fixed morphologic adaptations in the organization of the GI tract that facilitate efficient nutrient uptake from their restricted diets, generalists must constantly adapt to the shifting availability of food sources of diverse nutrient composition encountered throughout life. These ongoing changes in diet exist alongside encounters with ingested toxins, enteric pathogens, and commensal microbes. Omnivorous lifestyles therefore require that the GI tracts of such animals dynamically adapt to the changes in availability of different nutrients. We examined the molecular and cellular mechanisms that regulate intestinal adaptation to diverse foods.

RATIONALE: We investigated how the enzymes and transporters involved in the digestion and absorption of macronutrients are regulated in response to diet. We designed special animal diets that differed only in the ratio of protein to carbohydrates and evaluated gene expression changes in the GI tract, as well as systemic metabolism, after feeding these diets to mice. Recent discoveries pertaining to intestinal defenses against parasitic and microbial pathogens have demonstrated that interactions between intestinal epithelial cells and lymphocytes—the largest population of lymphocytes in the body—coordinate tissue responses to enteric infection. Guided by these findings, we hypothesized that the regulation of nutrient-handling machinery may involve coordination between tissue-resident lymphocytes and intestinal epithelial cells. Furthermore, recent work investigating mechanisms of host defense in this tissue led us to hypothesize that cellular remodeling of the intestinal epithelium, which occurs in response to certain infections, may also underlie its adaptation to different nutrients.

RESULTS: A carbohydrate transcriptional program comprising enzymes and transporters that mediate the digestion and absorption of carbohydrates was induced on demand in small-intestine epithelial cells in response to carbohydrate availability. The induction of this transcriptional program was specifically due to the availability of carbohydrates and reflected functional changes in nutrient handling at the tissue and systemic levels. Mice fed a high-carbohydrate diet exhibited changes in the frequency of specialized enterocyte subsets. This indicated that functional specialization exists within the enterocyte compartment, which constitutes approximately 80% of the intestinal epithelium. This also suggested that the induction of the carbohydrate transcriptional program involved cellular remodeling of the intestinal epithelium. The induction of this program and corresponding epithelial remodeling occurred rapidly, after only 5 days of high-carbohydrate feeding. Unexpectedly, the on-demand induction of this program required γδ T cells, a population of lymphocytes enriched at barrier surfaces whose biology remains poorly understood. Intestinal γδ T cells were altered by diet, with changes observed in their transcriptome, tissue localization, and behavior. The diet-dependent regulation of this program by γδ T cells involved suppression of a negative regulator, interleukin-22 (IL-22). Thus, we defined an epithelial-lymphocyte circuit that regulates the intestinal response to nutrient sensing and facilitates the adaptation to diverse diets.

CONCLUSION: Our work demonstrates a role for intestinal lymphocytes in regulating the tissue response to dietary nutrients. Together with other studies in the realm of host-pathogen interactions, our results indicate that lymphocyte-epithelial circuits and epithelial remodeling represent general features of how the intestine adapts to environmental change. By linking nutrition and barrier function at both the cellular and molecular levels, these adaptations allow this complex tissue to adjust the balance between nutrient uptake and host defense in response to environmental change. ■

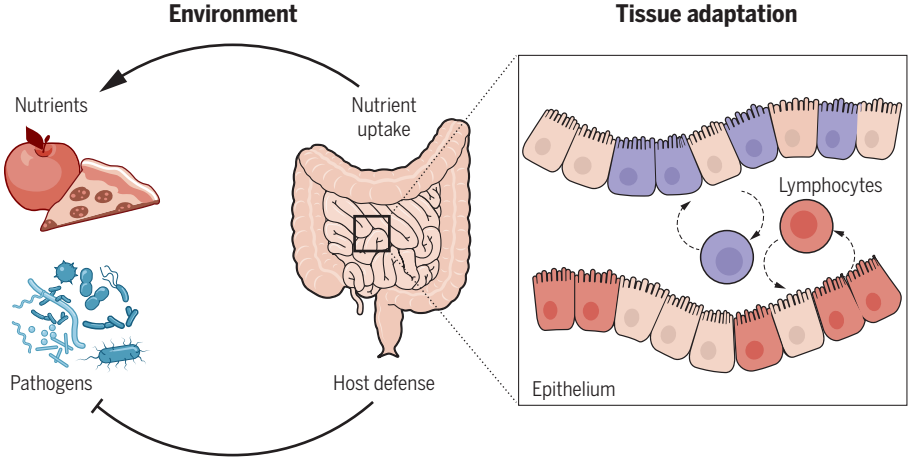

Lymphocyte-epithelial interactions mediate intestinal adaptation to environmental change. The small intestine adjusts the balance between host defense and nutrient uptake in response to environmental signals, including the availability of nutrients and presence of pathogens. The ability of this tissue to adjust the balance between its primary functions in response to environmental cues is mediated through cellular remodeling of the epithelium and lymphocyte-epithelial circuits.

The list of author affiliations is available in the full article online.
*Corresponding author. Email: ruslan.medzhitov@yale.edu
Cite this article as Z. A. Sullivan *et al.*, *Science* **371**, eaba8310 (2021). DOI: 10.1126/science.aba8310

READ THE FULL ARTICLE AT
https://doi.org/10.1126/science.aba8310

RESEARCH ARTICLE SUMMARY

INNATE IMMUNITY

CARD8 is an inflammasome sensor for HIV-1 protease activity

Qiankun Wang, Hongbo Gao, Kolin M. Clark, Christian Shema Mugisha, Keanu Davis, Jack P. Tang, Gray H. Harlan, Carl J. DeSelm, Rachel M. Presti, Sebla B. Kutluay, Liang Shan*

INTRODUCTION: HIV-1 has high mutation rates and exists as mutant swarms within the host. The adaptive immune system recognizes cognate epitopes based on amino acid sequences and associated conformations that are subject to mutation. The within-host diversity of HIV-1 allows rapid selection of antibody and T cell escape variants, leading to viral persistence. In patients who receive antiretroviral therapy (ART), HIV-1 persists in a latent form primarily in quiescent $CD4^+$ T cells. Immune escape variants achieved in the latent viral reservoirs present one of the major obstacles to HIV-1 eradication. Approaches to targeting immutable viral components such as the functions of essential viral proteins are needed to clear HIV-1 infection.

RATIONALE: The host immune system uses germline-encoded pattern recognition receptors (PRRs) to detect microbial products. A set of intracellular PRRs characterized by the presence of a caspase recruitment domain or a pyrin domain co-oligomerize with pro–caspase-1 (pro-CASP1) to form high-molecular-weight inflammasome complexes upon sensing of their cognate ligands. Inflammasome assembly in response to cytoplasmic microbial or danger signals leads to CASP1 activation and pyroptosis, an inflammatory form of programmed cell death. In the present study, we aimed to identify the inflammasome sensor(s) that recognizes intracellular HIV-1 activity. Caspase recruitment domain–containing protein 8 (CARD8) has been implicated in inflammasome activation and pyroptosis of $CD4^+$ T cells and macrophages. A key question is whether CARD8 is an inflammasome sensor and, if so, which pathogens physiologically activate it.

RESULTS: The C terminus of CARD8 contains a "function-to-find" domain (FIIND) followed by a CARD domain. CARD8 undergoes autoproteolytic processing in the FIIND domain at position 296, generating the N-terminal ZU5 and C-terminal UPA-CARD fragments that remain associated noncovalently. Human CARD8 shares structural similarity with the C terminus of human and murine nucleotide-binding domain leucine-rich repeat pyrin domain–containing 1 (NLRP1), which can be cleaved and activated by microbial proteases. We found that CARD8 could be activated by direct proteolysis of its N terminus by HIV-1 protease. N-terminal cleavage of CARD8 by HIV-1 protease creates an unstable neo–N terminus, which is targeted for proteasome degradation. Because of the break in the polypeptide chain by FIIND autoprocessing, the bioactive UPA-CARD subunit is liberated from the proteasome complex and initiates CASP1-dependent inflammasome assembly. In HIV-1–infected cells, CARD8 cannot detect the virus because the viral protease remains inactive as a subunit of unprocessed Gag–Pol polyprotein. Unexpectedly, some HIV-1–specific non-nucleoside reverse transcriptase inhibitors (NNRTIs) can trigger CARD8 sensing because they bind to HIV-1 Pol and enhance intracellular Gag–Pol polyprotein dimerization. This, in turn, causes premature viral protease activation. Treating HIV-1–infected macrophages and $CD4^+$ T cells with NNRTIs leads to CARD8-mediated caspase 1 activation and pyroptotic cell death. The viral protease activity against CARD8 is well conserved across major HIV-1 subtypes. To test whether strategies involving targeted activation of the CARD8 inflammasome could be used for the clearance of latent HIV-1, we obtained blood $CD4^+$ T cells from patients undergoing suppressive ART to measure the size of viral reservoirs. With NNRTI treatment, we showed that the induction of the CARD8 inflammasome activation led to rapid clearance of latent HIV-1 in patient $CD4^+$ T cells after virus reactivation.

CONCLUSION: In this study, we report that the CARD8 inflammasome senses HIV-1 protease activity. NNRTIs clear HIV-1–infected cells by inducing viral protease–mediated CARD8 activation. Our study suggests that enhancement of intracellular viral protease activity may be an effective strategy to clear residual HIV-1 in patients. Application of NNRTIs in HIV-1 cure strategies should facilitate the elimination of residual infected cells after the reversal of viral latency. In addition, the inclusion of NNRTIs in the initial ARV regimen may partially reduce the seeding of latent HIV-1 reservoirs. This work reveals a mechanism of innate sensing of HIV-1 infection that has immediate implications for HIV-1 cure strategies. ■

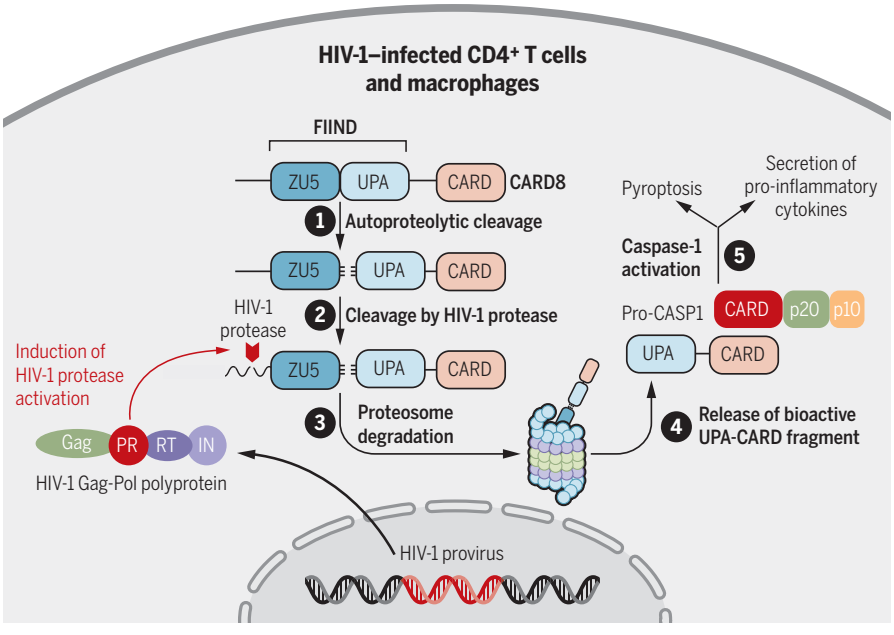

Activation of the CARD8 inflammasome by HIV-1 protease. (1) CARD8 autoproteolytic cleavage. (2) Cleavage of the CARD8 N terminus by HIV-1 protease. (3) Proteosome degradation of the neo–N terminus. (4) Release of the bioactive UPA-CARD fragment. (5) CASP1 activation and pyroptosis of HIV-1–infected cells. (Image was created with BioRender.com.)

The list of author affiliations is available in the full article online.
*Corresponding author. Email: liang.shan@wustl.edu
Cite this article as: Q. Wang *et al.*, *Science* 371, eabe1707 (2021). DOI: 10.1126/science.abe1707

READ THE FULL ARTICLE AT
https://doi.org/10.1126/science.abe1707

RESEARCH ARTICLES

RIBOZYMES

Processive RNA polymerization and promoter recognition in an RNA World

Razvan Cojocaru and Peter J. Unrau*

Early life is thought to have required the self-replication of RNA by RNA replicases. However, how such replicases evolved and subsequently enabled gene expression remains largely unexplored. We engineered and selected a holopolymerase ribozyme that uses a sigma factor–like specificity primer to first recognize an RNA promoter sequence and then, in a second step, rearrange to a processive elongation form. Using its own sequence, the polymerase can also program itself to polymerize from certain RNA promoters and not others. This selective promoter–based polymerization could allow an RNA replicase ribozyme to define "self" from "nonself," an important development for the avoidance of replicative parasites. Moreover, the clamp-like mechanism of this polymerase could eventually enable strand invasion, a critical requirement for replication in the early evolution of life.

The RNA World Hypothesis posits that at the dawn of evolution, RNA played a key role in the establishment of life (*1*). Central to this hypothesis is the existence of an RNA replicase ribozyme capable of copying its own genome using a supply of prebiotically synthesized nucleotide monomers and RNA polymers (*2*, *3*). Ever since the class I ligase ribozyme was isolated from a high-diversity RNA pool (*4*), there has been a sustained effort to produce highly processive polymerase ribozymes (*5*–*12*). Because the affinity of these polymerases for their RNA templates is weak, with Michaelis constant (K_M) values in the millimolar range (*13*), the most successful strategies to date have colocalized polymerase ribozymes with their substrates using concentration-enhancing micelles (*7*) or by anchoring either the RNA template (*8*, *9*) or the RNA primer to be extended (*10*, *11*) to the polymerase ribozyme. These strategies create a high local concentration of primer template with respect to the polymerase but fail to create a truly processive polymerase by virtue of the tethering strategies used to enhance polymerization.

Here, we report a natural linkage between the emergence of processivity and promoter selectivity in an RNA polymerase ribozyme. We hypothesized that an RNA polymerase ribozyme could be partially hybridized to a sigma factor–like specificity primer. This "open" clamp form (Fig. 1, A and D) would be able to search for a single-stranded RNA (ssRNA) promoter. Strand invasion would then allow template sequences containing a promoter to strip the specificity primer away from the primer-binding site (PBS) of the polymerase (Fig. 1B), triggering a structural rearrangement to a processive, "closed" clamp form (Fig. 1, C and E). Such a mechanism is analogous to that used by extant bacterial DNA–dependent RNA polymerases (DdRPs), which have evolved to recognize promoters through a two-step process involving sigma factor–dependent promoter recognition and nucleoside triphosphate (NTP)–dependent structural rearrangement to a final processive elongation form (Fig. 1, A to C, bottom panels) (*14*–*17*). All extant DdRPs, including the bacteriophage polymerases (*18*–*21*), use a variation of this two-step process. Thus, we selected a ribozyme with a similar mechanism to explore the potential connection between promoter recognition and processivity.

Department of Molecular Biology and Biochemistry, Simon Fraser University, Burnaby, British Columbia, Canada V5A 1S6.
*Corresponding author. Email: punrau@sfu.ca

Selection of a promoter-specific RNA polymerase ribozyme

To investigate this hypothesis, we started with the two-domain RNA polymerase ribozyme B6.61 (*6*), which consists of a catalytic ligase core and a secondary accessory domain that confers NTP extension ability through its AJ3/4 element (*11*). We engineered three changes into this parental ribozyme by appending a PBS to its 5′ end, synthesizing a high-diversity pool containing 10^{13} sequence variants by inserting random sequence libraries at three distinct sites, and removing sequence from the B6.61 accessory domain known to be redundant (*11*) (fig. S1 and table S1).

Three selection schemes, a negative selection, a clamping selection, and a processivity selection (fig. S2), were alternated for 30 rounds to select for functional ribozymes (fig. S3 and table S2). The negative selection removed pool molecules that could hybridize to a linear, randomly generated selection template (T1) immobilized onto streptavidin magnetic beads (fig. S2A). The clamping selection (fig. S2B) first formed P1:Pool^{OPEN} molecules by incubating them with the P1 specificity primer (table S3), which is fully complementary to the 22-nucleotide (nt) promoter found within the T1 template. To retain pool molecules that could make the transition to the Pool^{CLOSED} state, P1:Pool^{OPEN} molecules were added to circularized T1 (cT1) immobilized on streptavidin beads. Correctly clamped closed pool molecules retained on cT1 were then recovered by adding fresh specificity primer to again reform the open state and release correctly clamped pool molecules from the circular template. This process of transitioning from open to closed and back to open was performed either once or twice during clamping rounds of selection for increased selective pressure.

The processivity selection scheme incorporated polymerization activity into the clamping selection (fig. S2C). Here, activated P1:Pool^{OPEN} complexes were added to free circular template and incubated with adenosine triphosphate (ATP), guanosine triphosphate (GTP), and uridine triphosphate (UTP) (4 mM each), together with 1 mM biotin-11-cytidine-5′-triphosphate (CTP^B). Templates encoding for CTP incorporation at the first, third, or 10th extension position were then used to select for polymerization through the incorporation of CTP^B (tables S2 and S3). After this incubation, the pool-primer-template mixture was bound to streptavidin beads and washed. As before, captured pool ribozymes were recovered by adding specificity primer, reforming the open state, and allowing the recovery of clamping polymerase (CP) ribozymes with significant polymerization activity. After every round of selection, recovered pool RNA was reverse transcribed, polymerase chain reaction (PCR) amplified, and transcribed for the next round of in vitro selection (see the supplemental materials).

After 16 rounds of selection, the pool exhibited the anticipated clamping activity but only minor polymerization ability relative to the B6.61 progenitor. The selection pool was therefore mixed with three new subpools in which the existing clamping domain pool diversity was preserved but the ligase and accessary core of the polymerase were modified to contain the following: (i) nine high-frequency mutations found throughout the cloned pool, (ii) 11 point mutations and a deletion found previously by other groups (*8*, *10*), and (iii) the union of subpools 1 and 2 mutations. To further increase diversity, the combined pools were subjected to mutagenic PCR. After 23 rounds of selection, the pool was found to add CTP^B to the 3′ terminus of pool molecules. This was suppressed by extending the 3′ terminus of the pool by a single A residue (fig. S4 and table S1C).

After 25 rounds of selection, a substantial decrease in pool diversity occurred, with the final five rounds of selection being dominated by five major ribozyme polymerase families

(Fig. 2A). This loss in diversity was directly correlated with the emergence of significant polymerization on the cT1 template (Fig. 2B). One ribozyme from family 1, CP, was characterized further. The CP ribozyme contained seven point mutations and deletions in the ligase core and 17 point mutations or insertions in the accessory domain relative to the progenitor B6.61 ribozyme. Of the 24 mutations found, 14 were activity-enhancing mutations that have been found previously (*8*, *10*); of these 14 mutations, 11 were deliberately designed into the selection pool at round 16 and three evolved independently (Fig. 1D and table S3).

Clamping domain characterization

Removal of the newly selected 3′ clamping domain abolished polymerization activity (fig. S5

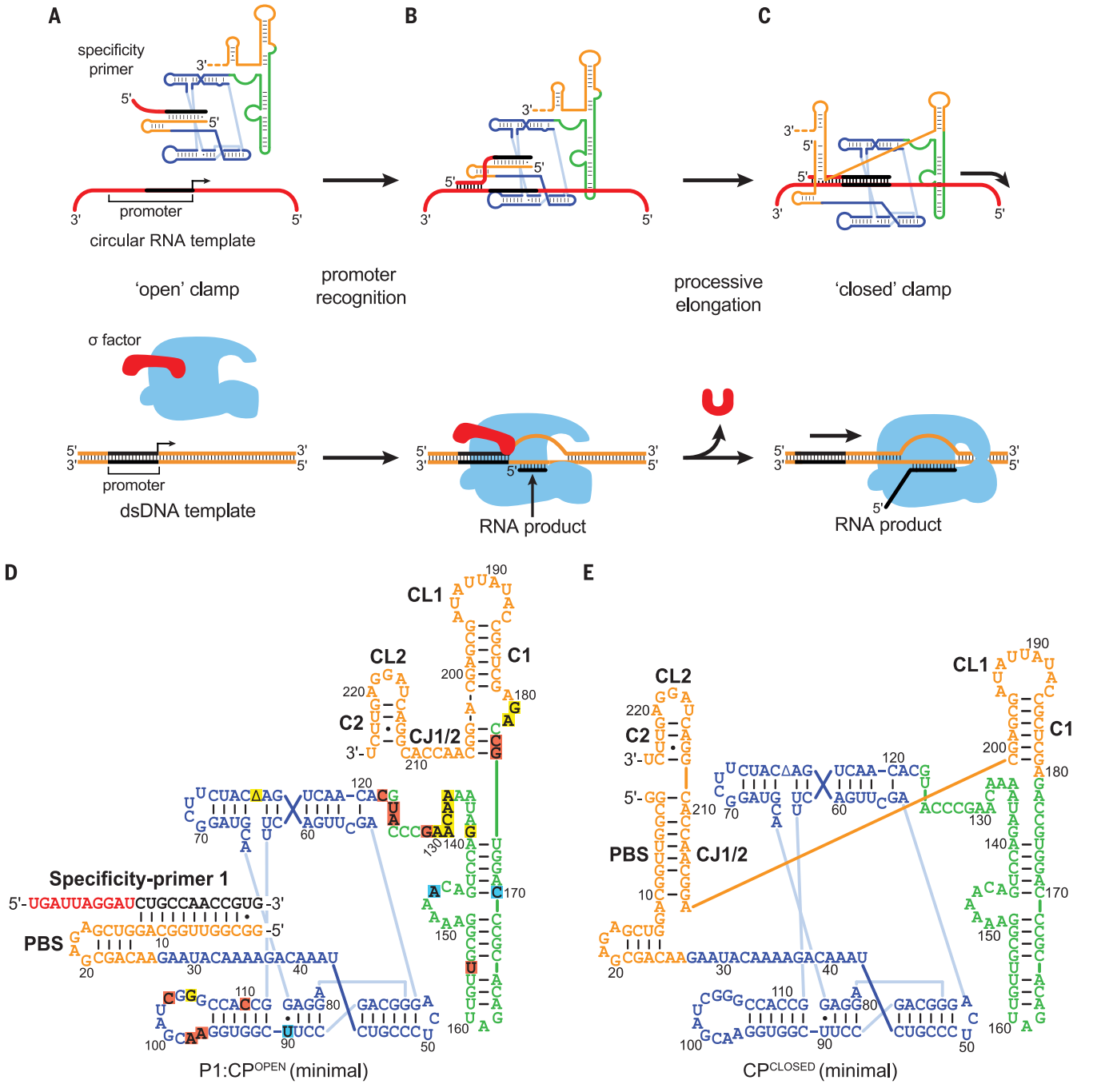

Fig. 1. Clamping RNA–dependent RNA polymerase (CP RdRP) ribozyme and DNA-dependent RNA polymerase (DdRP) transcriptional initiation processes. (**A**) RNA specificity primer–activated "open" form P1:CP^{OPEN} (top) and DdRP holo-enzyme (bottom). (**B**) The specificity primer localizes CP to an ssRNA promoter (top), whereas a sigma factor localizes the DdRP to a DNA promoter (bottom). (**C**) In both cases, a clamped "closed" state forms, enhancing polymerization. (**D** and **E**) Secondary structure of the minimal P1:CP^{OPEN} form (D) and the CP^{CLOSED} form (E). Colored lines indicate the ligase core (blue), accessory domain (green), and minimal clamping domain (orange). Up mutations designed into the selection are shown in red boxes, rediscovered up mutations in teal boxes, and newly discovered mutations in yellow boxes.

and table S4, construct 5), whereas transplanting the clamping domain from the family 1 CP onto a lower-activity family 4 ribozyme (12% activity of CP) enhanced its activity to CP's level (fig. S6), implicating this new domain in processive polymerization. Truncation analysis (table S4, constructs 1 to 18) and secondary structure prediction of the 3′ clamping domain revealed a minimal 45-nt domain composed of two stem-loop structures, C1-CL1 and C2-CL2, separated by a junction sequence, CJ1/2, shown in the predicted P1:CP^{OPEN} form (Fig. 1D). In the CP^{CLOSED} form, the C1 helix shortens by up to three base pairs (bp), allowing the CJ1/2 junction to form a 7-bp noncontinuous helix with the 5′ PBS sequence as the specificity primer transfers to the template sequence (Fig. 1E). The closed form of the minimal clamping domain is highly structured, naturally precluding base-pair interactions with template sequence.

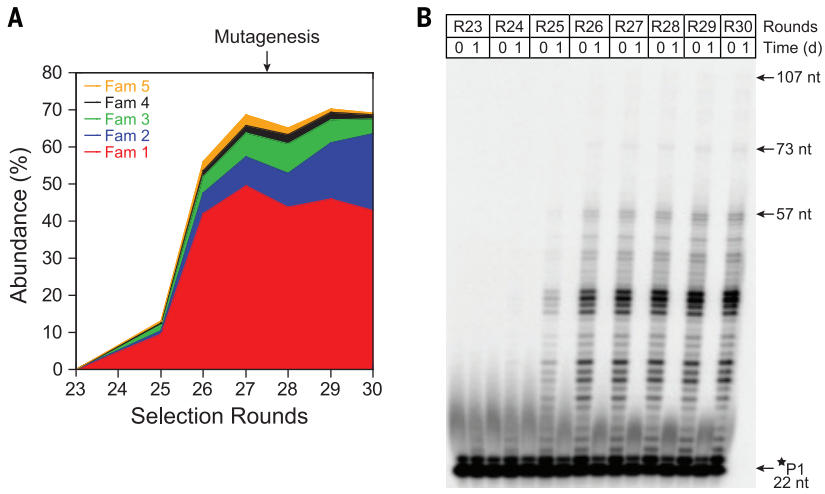

Fig. 2. Pool diversity and the emergence of polymerization. (**A**) Pool diversity from rounds 23 to 30. Families contain sequences with a pairwise distance $d \leq 2$. Arrow indicates 2% mutagenesis of the R28 DNA pool. (**B**) Extension activity of P1:Pool^{OPEN} on cT1 by selection rounds. Reaction conditions: P1 specificity primer (0.1 μM) was mixed with ribozyme pools (0.12 μM) in 100 mM $MgCl_2$, 100 mM KCl, and 100 mM Tris-HCl at pH 8.5 for 20 min at room temperature. Reactions were started by the addition of 4 mM concentrations of each NTP and 0.14 μM cT1 template. Reactions were stopped by heating at 95°C for 5 min after adding equivolume 80% formamide, 200 mM EDTA, 0.025% xylene cyanol, 0.025% bromophenol blue, and 10-fold excess of an RNA oligonucleotide complementary to cT1 before loading on 10% PAGE.

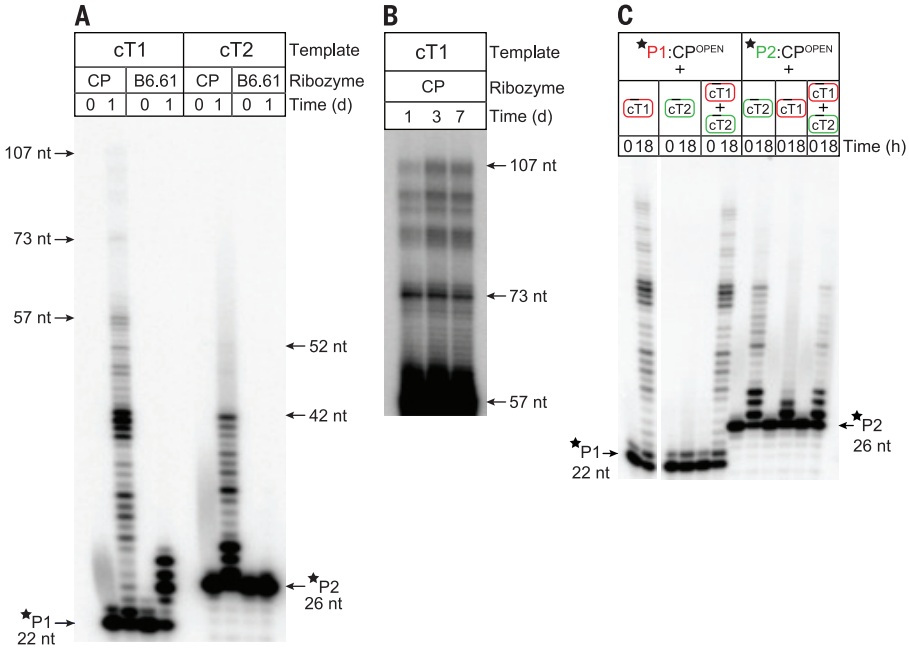

Fig. 3. Promoter-specific polymerization by CP on random sequence templates. (**A**) P1:CP^{OPEN} and P2:CP^{OPEN} extension relative to its progenitor, B6.61, on cT1 and cT2 promoter templates. (**B**) Contrast-enhanced long-range extension for a 7-day time course (full gel of both templates in fig. S6). (**C**) Promoter-mediated template selectivity by CP. Shown are P1:CP^{OPEN} or P2:CP^{OPEN} extensions with cT1, cT2, or both templates simultaneously.

Removing the C1-CL1 stem-loop structure destroyed polymerization activity, whereas replacing either the stem sequence or the loop sequence with a GCAA tetraloop had a minimal effect on activity (table S4, constructs 19 to 25). Hybridization of a DNA oligonucleotide to this region also suppressed activity (table S4, DNA 1). Thus, the C1-CL1 stem-loop structure plays an important mechanistic role in forming the active form of the clamped polymerase. The C2-CL2 stem-loop structure was less critical because removing or mutating it had only an intermediate effect on activity.

The CJ1/2 region, which hybridizes to the PBS in the closed state (Fig. 1, D and E), showed the highest effect on activity when blocked or mutated (table S4, constructs 26 to 51 and DNAs 2 to 7). Introducing a G5:C208U wobble mutation in the PBS:CJ1/2 helix resulted in a 19% increase in extension compared with wild-type on cT1 (construct 36). Weakening this stem further affected activity, with G8:C205U and U6:A207G lowering extension to 43 and 50%, respectively, whereas combining the two mutations lowered activity to 11% (constructs 34 to 35 and 38). Changing the CJ1/2 sequence by seven nucleotides from …A GGC AAC CAC G… to …A CGG CCA AAA G… (underlined residues are predicted to hybridize to PBS; fig. S7A) was predicted to preserve the net hybridization between the PBS and the CJ1/2 in the clamped helix, and indeed had 53% activity, indicating that base-pair formation rather than sequence in this region is essential for forming a correctly closed clamp (construct 26). Conversely, strengthening hybridization in the PBS:CJ/2 stem through A11:A202U or C3:A210G mutations lowered extension to 34 or 47%, respectively (constructs 29 and 30), while strengthening by 3 bp with A11:A202U, G9:G204C, and C3:A210G mutations dropped extension to only 2% (construct 31). Construct 31 prevented P1 hybridization and formation of the P1:CP^{OPEN} complex (fig. S7B, C). Because both stabilization and destabilization of the clamping helix can lower polymerization activity, a thermodynamic balance between the open, primer-bound form and the closed form of the polymerase is required for correct promoter-dependent polymerase function.

The clamping domain confers long-range extension and promoter selectivity

In addition to the cT1 template, we created a second template called cT2. This template,

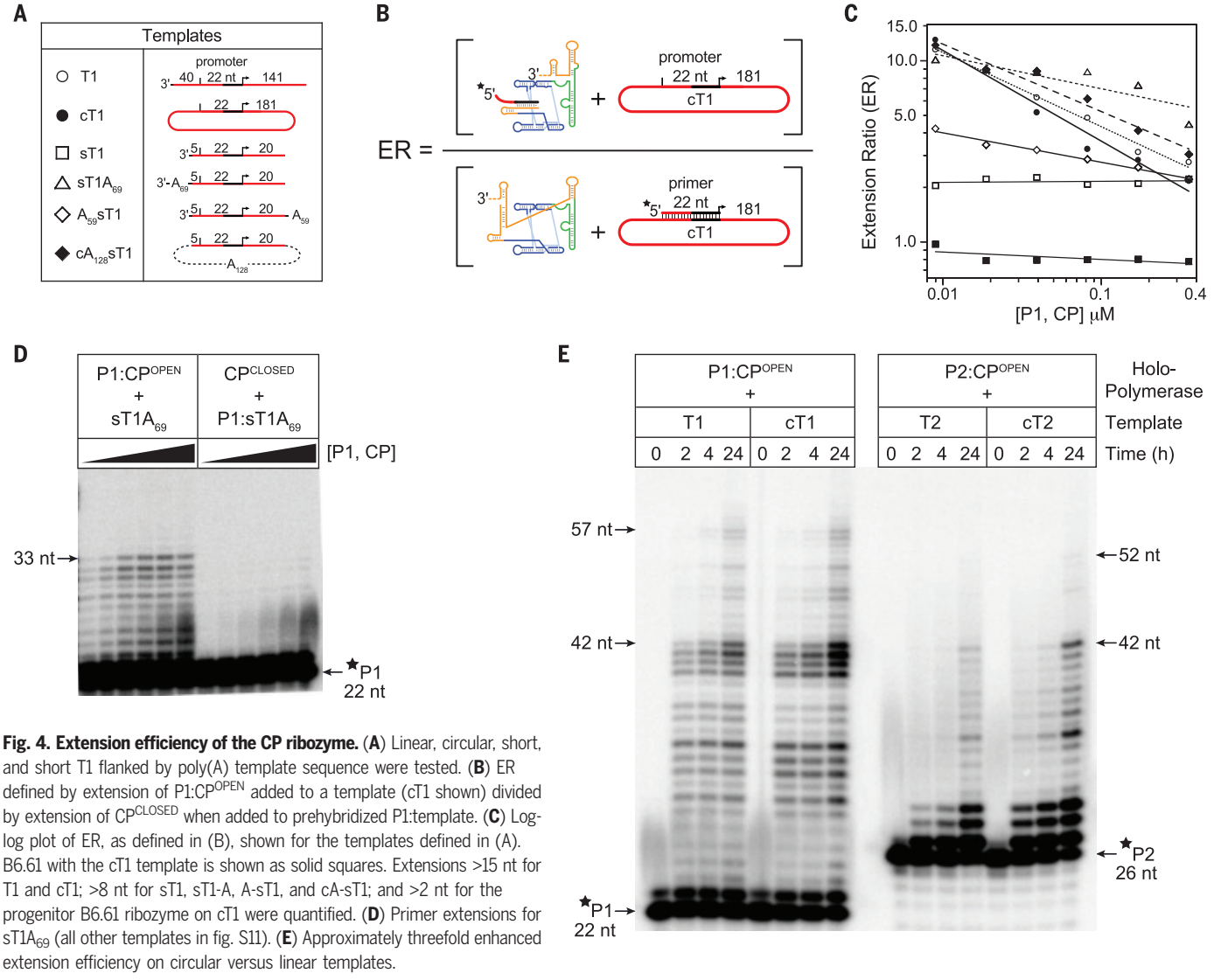

Fig. 4. Extension efficiency of the CP ribozyme. (**A**) Linear, circular, short, and short T1 flanked by poly(A) template sequence were tested. (**B**) ER defined by extension of P1:CP^{OPEN} added to a template (cT1 shown) divided by extension of CP^{CLOSED} when added to prehybridized P1:template. (**C**) Log-log plot of ER, as defined in (B), shown for the templates defined in (A). B6.61 with the cT1 template is shown as solid squares. Extensions >15 nt for T1 and cT1; >8 nt for sT1, sT1-A, A-sT1, and cA-sT1; and >2 nt for the progenitor B6.61 ribozyme on cT1 were quantified. (**D**) Primer extensions for sT1A$_{69}$ (all other templates in fig. S11). (**E**) Approximately threefold enhanced extension efficiency on circular versus linear templates.

also generated from random sequence, is distinct from cT1 and contains a new promoter region complementary to a 26-nt P2 specificity primer (table S3). P2 shares 10 nt in common with P1 at its 3′ end, enabling its hybridization to the PBS just as P1 does (Fig. 1D). When incubated with cT1 for 24 hours, P1:CP^{OPEN} extends P1 by 85 nt, whereas P2:CP^{OPEN} extends P2 on cT2 by 26 nt. By contrast, the progenitor B6.61 ribozyme extended only 5 nt on cT1 and had no observable extension on cT2 (Fig. 3A). The long-range extension on cT1 saturated at ~85 nt after 3 days of incubation, whereas cT2 extended by up to ~40 nt (Fig. 3B and fig. S8). The holocomplexes formed from either P1 or P2 were template specific, with P1:CP^{OPEN} being specific for the cT1 promoter and P2:CP^{OPEN} being specific for the cT2 promoter, even when mixtures of cT1 and cT2 were presented simultaneously to either holopolymerase (Fig. 3C).

Relative to the B6.61 progenitor, the CP ribozyme also requires less Mg^{2+} to become fully functional, with the emergence of polymerization occurring at 50 mM Mg^{2+} and saturating at 75 to 100 mM. By contrast, B6.61 polymerization showed no such saturation, with polymerization extension doubling from 75 to 100 mM and then tripling from 100 to 200 mM Mg^{2+} (fig. S9).

The clamping domain confers polymerization efficiency

A correctly clamped CP ribozyme should ideally stay localized to the primer-template complex that triggered the formation of its closed elongation form, whereas a less-processive ribozyme might dissociate. However, just as in extant biology, the CP ribozyme should only initiate elongation when its open holopolymerase form is presented to an ssRNA promoter template and should not polymerize efficiently when its closed form is presented to a primer-promoter-template complex. We found this to be the case, with P1:CP^{OPEN} extension on cT1 being significantly better than CP^{CLOSED} extension on P1:cT1 (fig. S10).

To quantify clamp-driven extension efficiency, we defined and measured an extension ratio (ER) for a range of promoter templates (Fig. 4A). The numerator was defined as the percentage extension past a particular RNA product size when the open holopolymerase ribozyme was added to a promoter template (P1:CP^{OPEN} + template). The denominator was defined as the extension when the promoter template was first hybridized to the P1 specificity primer, and then added to the closed polymerase ribozyme (CP^{CLOSED} + P1:template; Fig. 4B).

We measured ER by maintaining a one-to-one stoichiometric ratio of the P1 primer and CP ribozyme, which was then titrated over two orders of magnitude of concentration on fixed 1-μM templates (Fig. 4C and fig. S11). As expected, the B6.61 progenitor ribozyme had a concentration-independent ER value of ~1,

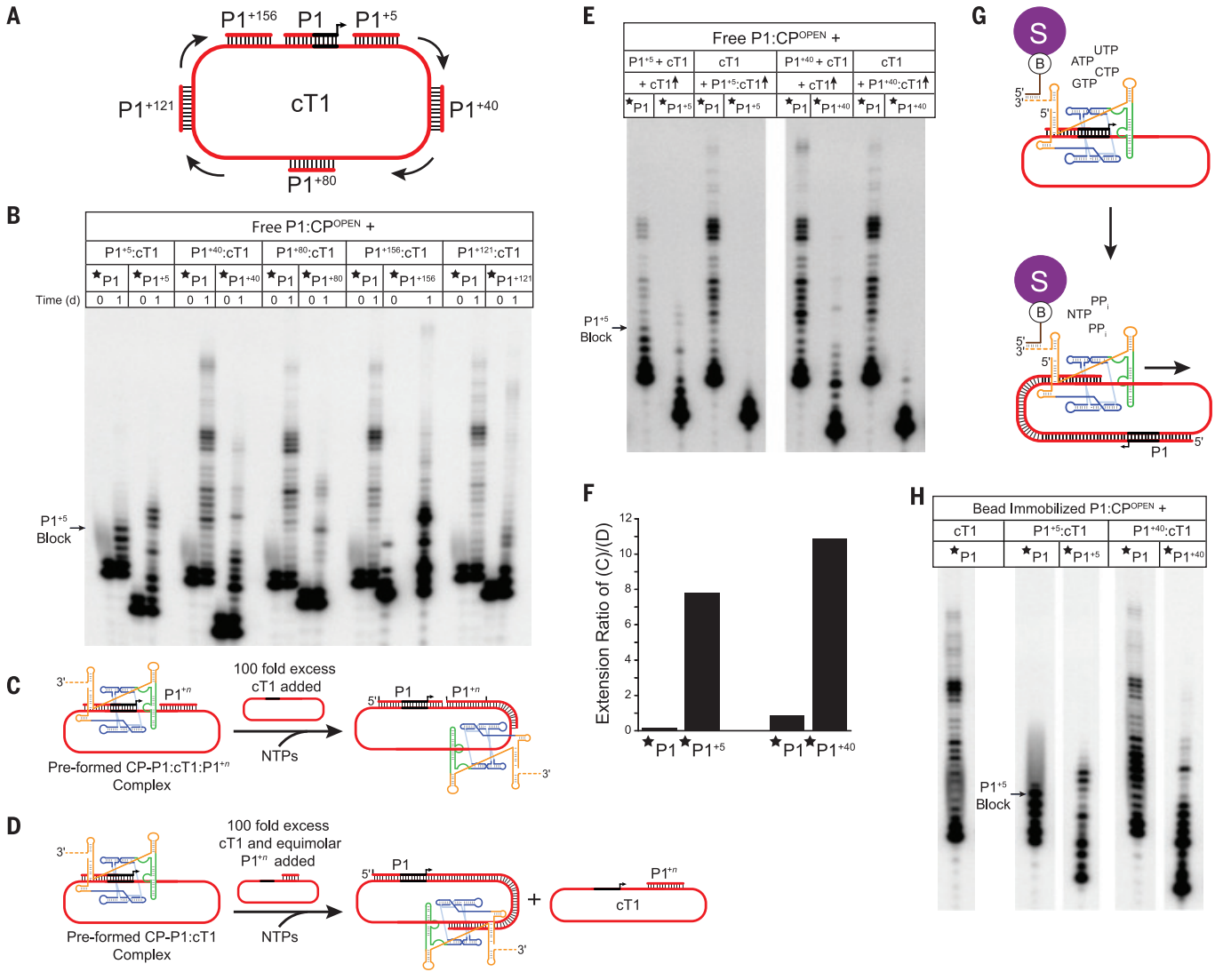

Fig. 5. CP processively extends multiple primers on the same promoter template. (**A**) Distal primer locations relative to the P1:cT1 initiation site. Arrows indicate direction of polymerization. (**B**) Extension assay of P1:CP^{OPEN} and P1^{+n} (n = 5, 40, 80, 121, and 156) primers added to cT1. Either P1 or the P1^{+n} primers were radiolabeled as indicated (star). (**C**) To prepare primers in a correlated fashion, a CP^{CLOSED}-P1:cT1:P1^{+n} complex (n = 5 or 40) was preformed by mixing P1:CP^{OPEN} (0.1 μM), P1^{+n} (0.2 μM), and cT1 (0.1 μM), and then rapidly diluted 10-fold into cT1 (final concentration: 1 μM, CT↑). (**D**) To prepare uncorrelated mixtures, preformed CP^{CLOSED}-P1:cT1 complex was diluted into high cT1 (1 μM) containing prehybridized P1^{+n} (0.02 μM). (**E**) Correlated (C) and uncorrelated (D) 4-hour extensions with P1^{+5} (left) and P1^{+40} (right). (**F**) Ratio of quantified correlated and uncorrelated extensions (>5 nt for P1 and >2 nt for P1^{+n}). (**G**) CP^{CLOSED}-P1:cT1 immobilized on streptavidin beads were washed for 1 hour and extended with NTPs. (**H**) Four-hour extensions of cT1 or cT1 prehybridized with P1^{+n} (n = 5 or 40, respectively) by bead immobilized P1:CP^{OPEN}.

consistent with this polymerase lacking a clamping domain (Fig. 4C, solid squares). However, CP showed an ~12-fold higher ER at low primer-polymerase concentrations with both linear and circular T1 (Fig. 4C, solid and empty circles). Truncating the linear T1 to the much shorter sT1 construct resulted in a low ER value that was completely independent of polymerase concentration (Fig. 4C, open squares). This lack of polymerization efficiency could be rescued by adding oligo(A) template sequence either to the 5′ terminus (A_{59}sT1, open diamonds) or the 3′ terminus (sT1A_{69}, open triangles) of sT1, with the 3′ rescue being more pronounced (Fig. 4, C and D). Similarly, circularizing the sT1 construct with oligo (A) fully rescued polymerization efficiency (cA_{128}sT1; Fig. 4C, solid diamonds).

Template extension efficiency was about threefold superior on circular cT1 and cT2 templates relative to their linear counterparts, where efficiency was defined as: E = Extension (P1:CP^{OPEN} + cTemplate)/Extension(P1:CP^{OPEN} + Template) (Fig. 4E). Further highlighting the importance of correct clamping for efficient polymerization, we eliminated the 5′ primer-binding region within the PBS, preventing both the P1:CP^{OPEN} and the CP^{CLOSED} states from forming. The removal of this region reduced the extension ratio to ~1, as expected (fig. S12). These data are consistent with the promoter triggering correct clamping of the polymerase, forming a processive elongation complex able to extend a range of templates provided they have sufficiently long sequence flanking the specificity-primer:promoter duplex.

The clamped complex is stable and allows extension at multiple primed sites

Extant DNA polymerases use multimeric clamp proteins to facilitate high polymerization rates and processivity (*22*). Without the clamping

domain of the CP ribozyme, a close relative of the B6.61 polymerase ribozyme has been reported to have negligible processivity, where on average only ~50% of nucleotide extensions results in a second nucleotide being added by the same polymerase on the same template (*13*). To explore the mechanism of processivity further, we immobilized the P1:CP^{OPEN} complex to streptavidin magnetic beads by hybridizing the ribozyme's 3′ terminus to a biotinylated DNA oligonucleotide (fig. S13). The P1:CP^{OPEN} complex was then incubated with a range of templates, and the off-rate of either the radiolabeled P1 or template was measured by scintillation counting. The reverse complement of P1 and the sT1 template nearly quantitatively stripped P1 off the immobilized P1:CP^{OPEN} complex (fig. S13, C to E). All other templates were retained together with P1 on the immobilized CP ribozyme (fig. S13, C to E). Addition of cT1 in twofold excess retained 64% of P1, whereas the addition of sT1 retained only 8% after 1 hour of stringent washing (fig. S13D). Likewise, after 4 hours of washing, 41 to 53% of the cA$_{128}$sT1, sT1A$_{69}$, and A$_{59}$sT1 templates were retained, whereas only 1% of sT1 remained bound (fig. S13E). Because these templates differ from sT1 only by the addition of oligo(A) residues, the CP clamp must intrinsically operate in a sequence-independent fashion to retain the immobilized complex.

Mechanistically, the formation of the clamped state allows the polymerase to reach and extend primers found a substantial distance away from the promoter-binding site. A set of primers (P1^{+n}: n = 5, 40, 80, 121, and 156, where n indicates the distance of the 5′ termini of each primer hybridized downstream from the P1 specificity primer promoter start site on cT1) could all be significantly extended by the polymerase (Fig. 5, A and B, and fig. S14). As expected, the P1 specificity primer could only be extended by 5 and 40 nt before being blocked by the P1^{+5} and P1^{+40} primers, respectively (Fig. 5 and fig. S14).

When P1:CP^{OPEN} was mixed with cT1 prehybridized to the P1^{+5} or P1^{+40} primers and the resultant complex diluted into 100-fold excess cT1 (Fig. 5E), simultaneous extension of P1 and the P1^{+5} or P1^{+40} occurred to a much greater extent than if the P1 and P1^{+n} primers were found on distinct templates (Fig. 5, D and E, and fig. S15). The extension ratios for P1^{+5} and P1^{+40} were eightfold and 11-fold higher when correctly clamped (Fig. 5F), similar to the ratios observed for P1 extension (Fig. 4C). Further, immobilizing P1:CP^{OPEN} onto streptavidin beads (Fig. 5G) resulted in similar extension of templates with P1^{+n} primers, with 75 to 90% of the correctly clamped complexes remaining on the beads after 4 hours of polymerization (Fig. 5H and fig. S16). The three-component complex (CP^{CLOSED}-P1:cT1) is therefore a stable and processive polymerase-primer:template complex.

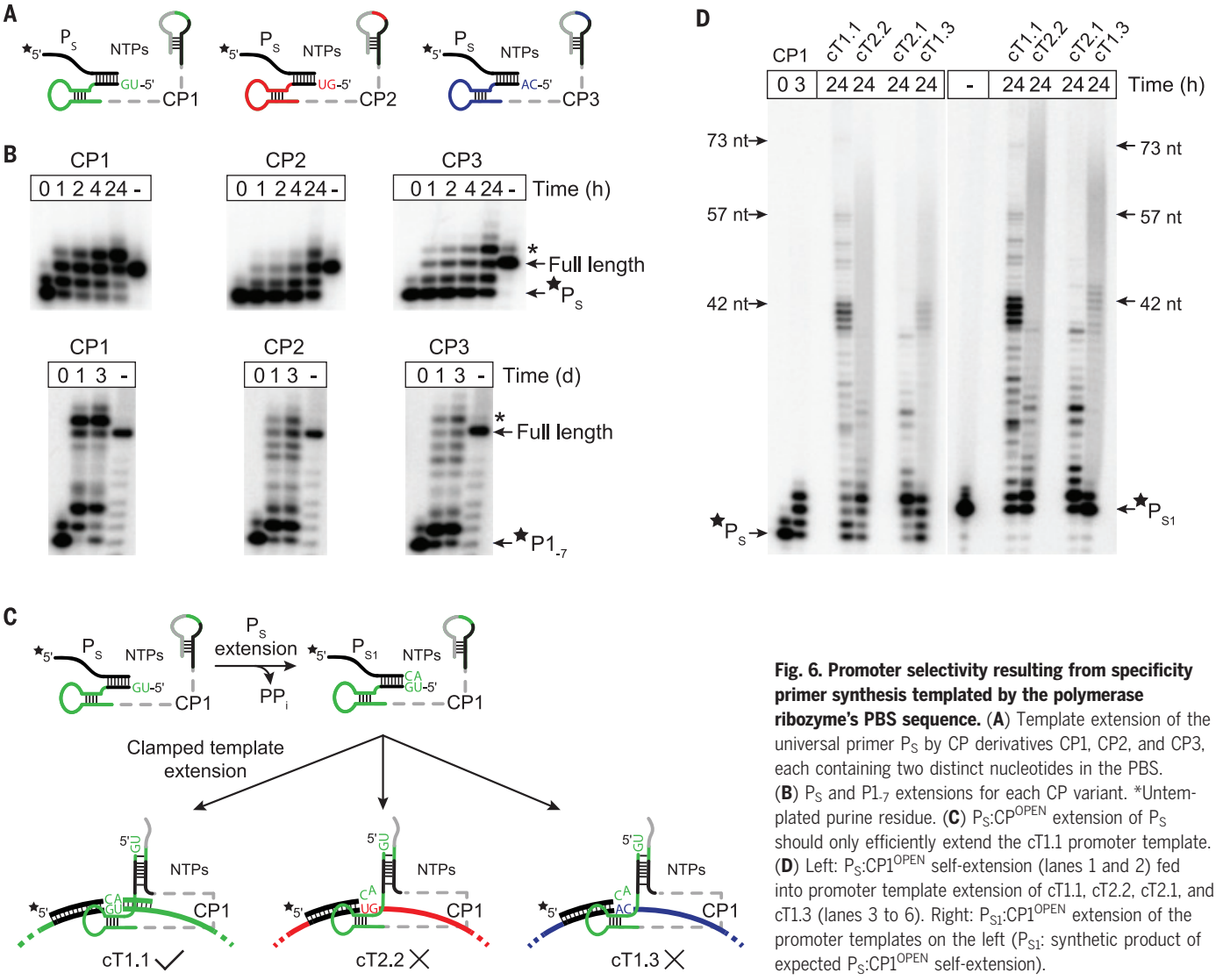

Fig. 6. Promoter selectivity resulting from specificity primer synthesis templated by the polymerase ribozyme's PBS sequence. (**A**) Template extension of the universal primer P$_S$ by CP derivatives CP1, CP2, and CP3, each containing two distinct nucleotides in the PBS. (**B**) P$_S$ and P1$_{-7}$ extensions for each CP variant. *Untemplated purine residue. (**C**) P$_S$:CP^{OPEN} extension of P$_S$ should only efficiently extend the cT1.1 promoter template. (**D**) Left: P$_S$:CP1^{OPEN} self-extension (lanes 1 and 2) fed into promoter template extension of cT1.1, cT2.2, cT2.1, and cT1.3 (lanes 3 to 6). Right: P$_{S1}$:CP1^{OPEN} extension of the promoter templates on the left (P$_{S1}$: synthetic product of expected P$_S$:CP1^{OPEN} self-extension).

In aggregate, these data indicate that the CP ribozyme uses a sequence-independent topological clamp of the form shown in Fig. 1; however, we cannot rule out the possibility of a "gripping" type clamp model known to form by fusing DNA-binding domains to *Taq* polymerase (*23*). In either case, an organized transition exists from the open holopolymerase to the closed-clamp form, which allows the active site of the polymerase to extend a broad set of RNA templates often by multiple helical turns. Simultaneously, but only when correctly triggered by a specificity primer, the clamp confers the ability to find and extend primers found at widely spaced locations within a single RNA template.

Programmable promoter recognition by the holopolymerase

The CP ribozyme can use its PBS sequence as a template to extend shortened specificity primers. To find the minimal primer that the CP^{OPEN} complex can extend, we partially hydrolyzed 5′ end-labeled P1. We found that a 7-nt 3′ truncation of P1 ($P1_{-7}$) was the shortest primer that could be efficiently extended by the CP ribozyme (fig. S17), consistent with the proposed hybridization mechanism of P1 to the CP ribozyme's PBS domain (Fig. 1D). Three new CP variants were created, each having a specific 5′-terminal dinucleotide sequence appended to the CP ribozyme after first removing its 5′ G. The variants were activated with a shortened universal primer, P_S (fig. S17B), designed to allow two nucleotides of self-templated extension (Fig. 6A and table S3). P_S was extended nearly quantitatively by the CP1 variant (5′ UG template), whereas the CP2 (5′ GU template) and the CP3 (5′ CA template) variants showed lower extension after 24 hours of incubation (Fig. 6B). This extension behavior was quite robust, with all three polymerase constructs also extending the $P1_{-7}$-truncated primer (Fig. 6B). All polymerase variants added at least one untemplated purine residue (Fig. 6B and fig. S18), similar to many protein repair polymerases such as *Taq*, which add primarily an untemplated A to blunt-ended duplex DNA (*24*).

Such holopolymerase-dependent extension of the universal primer sequence allows some promoter template RNAs but not others to be copied based on the sequence of the polymerase itself (Fig. 6C). We replaced the P1 and P2 promoters in the cT1 and cT2 constructs with three new promoter sequences corresponding to primer sequences synthesized by the CP1, CP2, and CP3 ribozymes. Forming the P_S:$CP1^{OPEN}$ holopolymerase, the P_S primer was extended by incubation for 3 hours (Fig. 6D). The holopolymerase ribozymes containing the extended P_S primer ($P_{S\text{-}ext}$:$CP1^{OPEN}$) were then incubated with the newly constructed promoter templates and the primer extension was measured. Polymerization by CP1 was ~12-fold better on the cT1 template with the CP1 promoter (cT1.1) compared with the same template having a CP3 promoter (cT1.3; Fig. 6D). Likewise, extension on the cT2 template having a CP1 promoter (cT2.1) was about fourfold superior to extension on the same template with a CP2 promoter (cT2.2; Fig. 6D). Other combinations of CP derivatives and their promoters were less significantly regulated, but these permutations demonstrate that self-templated primer synthesis by the polymerase itself can have a marked effect on selective polymerization ability.

Discussion

The ability of a polymerase to recognize a promoter presents a fundamental evolutionary tension: Molecular recognition of a promoter is a static process, whereas processive polymerization is a dynamic one. Through in vitro evolution, we have found an RNA polymerase that can search for a promoter by first forming a functional open holopolymerase complex and then in a second step rearrange into a processive elongation form. The correct assembly of this CP^{CLOSED} complex results in a more than one order of magnitude increase in extension, with extension on randomly generated templates being directly comparable to the best RNA polymerase ribozymes isolated to date, which on highly repetitive tethered templates are able to synthesize 75 to 203 nt of sequence (*8*–*10*).

RNA replication results in long stretches of duplex RNA. Thus, just as in modern biology, the ability of an RNA polymerase ribozyme to invade duplex RNA would be of fundamental importance in early evolution. Although the CP polymerase is incapable of strand invasion (Fig. 5), its processivity and correlated primer extension ability indicates that it entrains templates through a "sticky" topological clamp when correctly clamped (Fig. 1). The CP can synthesize duplexes from ~50 to 107 bp in size, a linear extent ranging from 175 to 360 Å, which is threefold to sixfold larger than its class I ligase catalytic core (*25*). The polymerase must therefore move while not disengaging from the template because polymerization can occur while washing the immobilized processive complex. Precedent for such a sticky clamp exists in modern RNA biology. The ribosome creates a topological clamp by assembling the large and small subunits around an mRNA. This clamp is stable (*26*) but allows robust movement of mRNA 3 nt at a time during translation. Similarly, coupling the force generated from NTP incorporation with the embryonic CP clamp could lead to the development of a polymerase ribozyme with ratchet-like and strand invasion capabilities (*27*).

The CP ribozyme can also synthesize part of its own specificity primer, providing evidence that a replicase in an RNA World could have avoided replicative parasites by a strategy akin to the genomic tag hypothesis of Weiner and Maizels (*28*). Compartmentalization has long been recognized as a key element in the solution to this problem (*29*), but early evolution may have undergone a period during which replicating systems existed without cellularization. In such a situation, a replicase able to synthesis all or part of its own specificity primer could, through mutations to its own sequence, have rapidly evolved a sense of self to avoid replicative parasites early in evolution.

Although many outstanding challenges remain to producing a self-evolving system in the laboratory, including increased polymerization rate, fidelity, and, most importantly, strand displacement, the development of a promoter-dependent RNA polymerase ribozyme with processive clamping ability offers many insights into the dilemmas faced by life in the earliest periods of evolution on this planet.

REFERENCES AND NOTES

1. W. Gilbert, *Nature* **319**, 618–618 (1986).
2. J. W. Szostak, D. P. Bartel, P. L. Luisi, *Nature* **409**, 387–390 (2001).
3. G. F. Joyce, *Nature* **418**, 214–221 (2002).
4. D. P. Bartel, J. W. Szostak, *Science* **261**, 1411–1418 (1993).
5. W. K. Johnston, P. J. Unrau, M. S. Lawrence, M. E. Glasner, D. P. Bartel, *Science* **292**, 1319–1325 (2001).
6. H. S. Zaher, P. J. Unrau, *RNA* **13**, 1017–1026 (2007).
7. U. F. Müller, D. P. Bartel, *RNA* **14**, 552–562 (2008).
8. A. Wochner, J. Attwater, A. Coulson, P. Holliger, *Science* **332**, 209–212 (2011).
9. J. Attwater, A. Wochner, P. Holliger, *Nat. Chem.* **5**, 1011–1018 (2013).
10. D. P. Horning, G. F. Joyce, *Proc. Natl. Acad. Sci. U.S.A.* **113**, 9786–9791 (2016).
11. Q. S. Wang, L. K. L. Cheng, P. J. Unrau, *RNA* **17**, 469–477 (2011).
12. J. T. Sczepanski, G. F. Joyce, *Nature* **515**, 440–442 (2014).
13. M. S. Lawrence, D. P. Bartel, *Biochemistry* **42**, 8748–8755 (2003).
14. T. M. Gruber, C. A. Gross, *Annu. Rev. Microbiol.* **57**, 441–466 (2003).
15. H. Maeda, N. Fujita, A. Ishihama, *Nucleic Acids Res.* **28**, 3497–3503 (2000).
16. B. A. Young, T. M. Gruber, C. A. Gross, *Cell* **109**, 417–420 (2002).
17. K. S. Murakami, S. A. Darst, *Curr. Opin. Struct. Biol.* **13**, 31–39 (2003).
18. G. M. T. Cheetham, T. A. Steitz, *Science* **286**, 2305–2309 (1999).
19. Y. W. Yin, T. A. Steitz, *Science* **298**, 1387–1395 (2002).
20. T. H. Tahirov *et al.*, *Nature* **420**, 43–50 (2002).
21. K. J. Durniak, S. Bailey, T. A. Stetiz, *Science* **322**, 553–557 (2008).
22. S. J. Benkovic, A. M. Valentine, F. Salinas, *Annu. Rev. Biochem.* **70**, 181–208 (2001).
23. Y. Wang *et al.*, *Nucleic Acids Res.* **32**, 1197–1207 (2004).
24. G. Hu, *DNA Cell Biol.* **12**, 763–770 (1993).
25. D. M. Shechner *et al.*, *Science* **326**, 1271–1275 (2009).
26. J. A. Steitz, *Nature* **224**, 957–964 (1969).
27. L. K. L. Cheng, P. J. Unrau, *Cold Spring Harb. Perspect. Biol.* **2**, a002204 (2010).
28. A. M. Weiner, N. Maizels, *Proc. Natl. Acad. Sci. U.S.A.* **84**, 7383–7387 (1987).
29. G. F. Joyce, J. W. Szostak, *Cold Spring Harb. Perspect. Biol.* **10**, a034801 (2018).

ACKNOWLEDGMENTS

We thank I. Yaseen and members of the Unrau laboratory; M. Leroux (SFU), D. Sen (SFU), and U. Muller (UC San Diego) for critical reading of the manuscript; and E. Yingqi Han (software

engineer) for help with processing high-throughput sequencing data. **Funding:** This work was supported by a NSERC Discovery Grant to P.J.U. **Author contributions:** R.C. and P.J.U. designed the experiments, analyzed the data, and wrote the manuscript. R.C. performed the experiments. **Competing interests:** The authors declare no competing interests. **Data and materials availability:** All data are available in the main text or the supplementary materials.

SUPPLEMENTARY MATERIALS

science.sciencemag.org/content/371/6535/1225/suppl/DC1
Materials and Methods
Supplementary Text
Figs. S1 to S19
Tables S1 to S4
References (*30*, *31*)
Sequenced DNA Libraries
MDAR Reproducibility Checklist

3 August 2020; accepted 4 February 2021
10.1126/science.abd9191

ORGANIC CHEMISTRY

Sequential C–F bond functionalizations of trifluoroacetamides and acetates via spin-center shifts

You-Jie Yu[1]*, Feng-Lian Zhang[1]*, Tian-Yu Peng[1], Chang-Ling Wang[1], Jie Cheng[1], Chen Chen[1], Kendall N. Houk[2]†, Yi-Feng Wang[1,3,4]†

Defluorinative functionalization of readily accessible trifluoromethyl groups constitutes an economical route to partially fluorinated molecules. However, the controllable replacement of one or two fluorine atoms while maintaining high chemoselectivity remains a formidable challenge. Here we describe a general strategy for sequential carbon-fluorine (C–F) bond functionalizations of trifluoroacetamides and trifluoroacetates. The reaction begins with the activation of a carbonyl oxygen atom by a 4-dimethylaminopyridine-boryl radical, followed by a spin-center shift to trigger the C–F bond scission. A chemoselectivity-controllable two-stage process enables sequential generation of difluoro- and monofluoroalkyl radicals, which are selectively functionalized with different radical traps to afford diverse fluorinated products. The reaction mechanism and the origin of chemoselectivity were established by experimental and computational approaches.

Mono- and difluoroalkyl-substituted organic molecules have valuable applications as pharmaceuticals (*1*, *2*), agrochemicals (*3*), and materials (*4*) owing to the distinctive physical and biological properties of fluorine atoms (*5*, *6*). The synthesis of these target molecules has thus been of long-standing interest. Over the past decades, many mono- and difluoroalkylating precursors, as well as fluorination reagents and strategies, have shown robust applications (*7*–*16*). The C–F bond functionalization of readily accessible trifluoromethyl groups has also proven an effective pathway, in particular for the synthesis of challenging or otherwise unattainable products (*17*–*29*). However, successively replacing two fluorine atoms with various functionalities while maintaining high chemoselectivity is exceedingly difficult (*30*, *31*) because the C–F bond strength continuously decreases as defluorination proceeds (*5*), which often results in exhaustive defluorination (*17*, *19*, *32*, *33*). Developing strategies to address this issue would provide a particularly economical and valuable route to di- and monofluorinated products from inexpensive CF_3 sources.

The functionalization of CF_3 groups generally proceeds through heterolytic cleavage of a C–F bond, affording difluoro-substituted carbocation or carbanion intermediates (Fig. 1A, top left) (*17*–*22*). By contrast, transformations by means of fluoroalkyl radical intermediates, which can provide different reaction pathways for chemical bond formation, are insufficiently studied because of the high bond dissociation energy (BDE) of the C–F bond constraining homolytic cleavage (*5*). Recently, the groups of König (*34*), Jui (*35*, *36*), Bandar (*37*), and Gouverneur (*38*) disclosed a strategy to generate aryldifluoromethyl radicals from CF_3-substituted arenes, in which arene radical anions generated through single-electron reduction serve as intermediates and a fluoride anion is eliminated (Fig. 1A, top right). However, a general method applicable to readily accessible trifluoroacetic acid derivatives and capable of selectively forming di- and monofluoroalkyl radicals (Fig. 1A, bottom) has not been developed.

In seeking a solution to achieve the aforementioned transformations, we were drawn to a spin-center shift (SCS)–based radical process, which involves 1,2-radical delocalization and leaving group elimination (*39*). This process has been observed and studied in various biological applications (*40*, *41*). For example, during DNA biosynthesis, the SCS pathway catalyzed by ribonucleotide reductase class (**I** to **III**) is known to be a key step in the formation of deoxyribonucleoside diphosphates (Fig. 1B, top) (*42*). The mechanism involves a β-C–O bond scission of radical **Int-I**, forming a carbon-centered radical with the elimination of water as a coproduct. There have also been reports on SCS in organic synthesis, with chloride, bromide, and hydroxyl groups or their activators as the β leaving group (Fig. 1B, bottom) (*43*–*48*). Recently, MacMillan reported robust alkylation approaches mimicking this SCS process with the use of alcohols as alkylating agents (*49*, *50*). More recently, Melchiorre (*51*), Wang (*52*), and Rovis (*53*) also described elegant SCS-involved alkylation reactions. Despite these advances, the SCS-promoted C–F bond cleavage remains an unanswered challenge in organic synthesis (*54*). Such a transformation could offer a mechanistically distinct strategy for defluorinative functionalization of CF_3 groups. Were a stepwise SCS to proceed in a controllable manner, an approach to enable sequential C–F bond replacement would be achievable.

With this in mind, we posited a discrete two-stage process with each stage involving an SCS for the C–F bond cleavage of trifluoroacetic acid derivatives (Fig. 1C). In stage A, the first SCS of the transient **Int-II** generated through the attack of the carbonyl oxygen atom by a radical promotor occurs, resulting in the cleavage of a single β-C–F bond. The resulting α,α-difluorocarbonyl radical, **Int-III**, can be subsequently captured by a radical trap to provide an α,α-difluoroacetyl product and complete the monodefluorinative transformation. In stage B, if the radical promotor is continuously present, the stage A product participates in a second SCS to generate the radical **Int-V**, which is then trapped by a second component to furnish monofluorinated products. The use of different traps in stages A and B should enable rapid and efficient synthesis of densely functionalized monofluoro products. The challenge is how to make the two-stage sequence controllable while circumventing exhaustive defluorination.

Controllable mono- and dihydrodefluorination reactions

To verify the feasibility of the proposed two-stage process, we began by investigating the

[1]Hefei National Laboratory for Physical Sciences at the Microscale, Department of Chemistry, University of Science and Technology of China, Hefei, Anhui 230026, China. [2]Department of Chemistry and Biochemistry, University of California, Los Angeles, CA 90095, USA. [3]Center for Excellence in Molecular Synthesis of CAS, Hefei, Anhui 230026, China. [4]State Key Laboratory of Elemento-Organic Chemistry, Nankai University, Tianjin 300071, China.
*These authors contributed equally to this work.
†Corresponding author. Email: houk@chem.ucla.edu (K.N.H.); yfwangzj@ustc.edu.cn (Y.-F.W.)

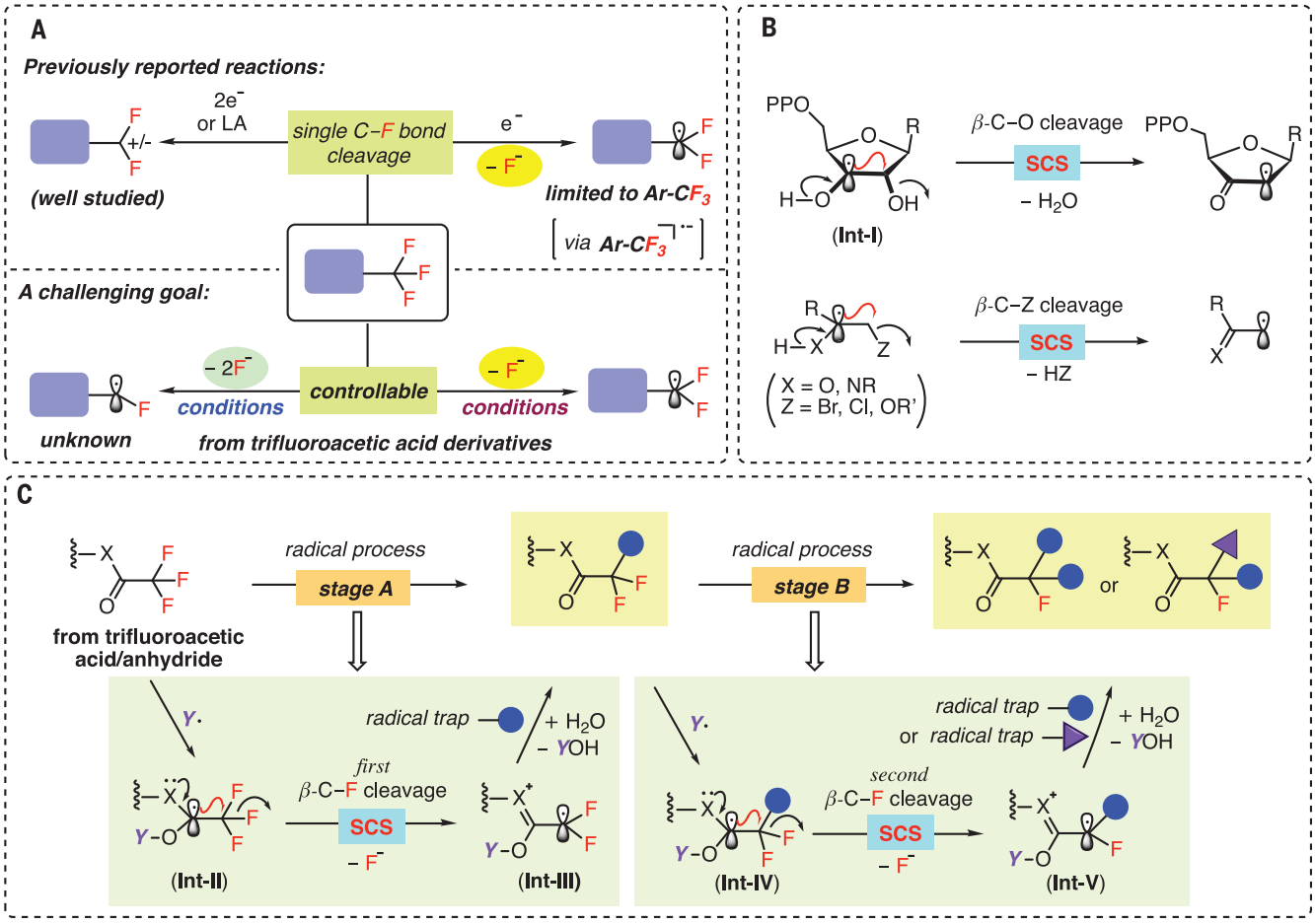

Fig. 1. Strategies for C–F bond functionalizations of CF_3 groups. (**A**) Defluorination of CF_3 groups to difluoro-substituted intermediates (top) and the challenging goal of controllably generating di- and monofluoroalkyl radicals (bottom). LA, Lewis acid. (**B**) SCS in biochemical conversions and organic synthesis. R = H, aryl, or alkyl; R′ = H, $COCH_3$, $PO(OEt)_2$, or SO_2Me; PP, diphosphate. (**C**) This work: two-stage process for sequential C–F bond cleavage by means of SCS.

controllable mono- and dihydrodefluorination reactions of trifluoroacetamides and trifluoroacetates, in which one or two C–F bonds are selectively reduced. On the basis of recent findings, certain Lewis base–boryl radicals (*55*–*58*) are nucleophilic (*59*, *60*) and can attack carbonyl oxygen sites (*61*); our initial studies focused on the application of these radicals as promotor. We found that 4-dimethylaminopyridine (DMAP)-BH_2•, which is generated by hydrogen atom abstraction from DMAP-BH_3 using di-*tert*-butyl hyponitrite (TBHN) as a radical initiator (*62*), could promote the defluorination. *N*-heterocyclic carbene-boryl radical (*57*), pyridine-boryl radical (*62*), tributylstannyl radical, and tris(trimethylsilyl)silyl radical were ineffective (table S1, entries 12 to 15). Thiophenol (PhSH) was used as a polarity reversal catalyst (*63*, *64*). As shown in Fig. 2, the reaction of trifluoroacetamide **1a** with 1.5 equiv of DMAP-BH_3 in the presence of NaH_2PO_4•$2H_2O$ (1.2 equiv) as a base in CH_3CN (method 1) gave the monohydrodefluorination product **2a** in 82% yield, along with dihydrodefluorination product **3a** in 7% yield. Compound **3a** was formed as the sole product (85% yield) when increased amounts of DMAP-BH_3 (3 equiv) and Na_2HPO_4•$12H_2O$ (2.4 equiv) in 1,4-dioxane were used (method 2). In both protocols, no trihydrodefluorination product was detected. Gram-scale syntheses of **2a** and **3a** were also achieved with good yields.

Both methods show broad substrate scope and good chemoselectivity (Fig. 2). In some cases, minor over-reduction occurred with method 1 to give CFH_2 products, but usually in less than 15% yields. *N*-Aryl trifluoroacetamides bearing a wide range of functional groups (**1b** to **1l**) were converted into CF_2H- and CFH_2-containing products with high yields and chemoselectivity, whereas the presence of an alkene tether (**1m**) resulted in an inferior yield. Tertiary amide **1n** reacted well under both sets of reaction conditions. For the reactions of pentafluoropropanamides (**1o** to **1s**), only the C–F bonds α to the carbonyl group were selectively reduced, and the CF_3 group was inert. This result suggests that C–F bond cleavage is likely assisted by the adjacent carbonyl moiety. *N*-Heteroaryls, such as indole (**1p**) and benzofuran (**1r**) motifs, were compatible. Monohydrodefluorination of *N*-alkyl pentafluoropanamide **1s** gave **2s** in 44% yield, but the dihydrodefluorination using method 2 was unsuccessful, yielding **2s** as the sole product. Both protocols were applied for the insertion of di- and monofluoroacetyl units onto a β-estradiol system (**2t** and **3t**). Incorporation of a trifluoroacetate tether onto the cholesterol framework followed by method 1 delivered the desired difluoro product **2u**, although method 2 mainly led to hydrolysis and only a trace amount of monofluorinated product was detected.

Controlled defluorinative coupling reactions with alkenes

Alkenes were then used as the radical trap to capture the resulting α,α-difluorocarbonyl radical **Int-III**. As demonstrated in Fig. 3, the coupling reaction proceeded smoothly, affording a broad range of α,α-difluorocarbonyl products.

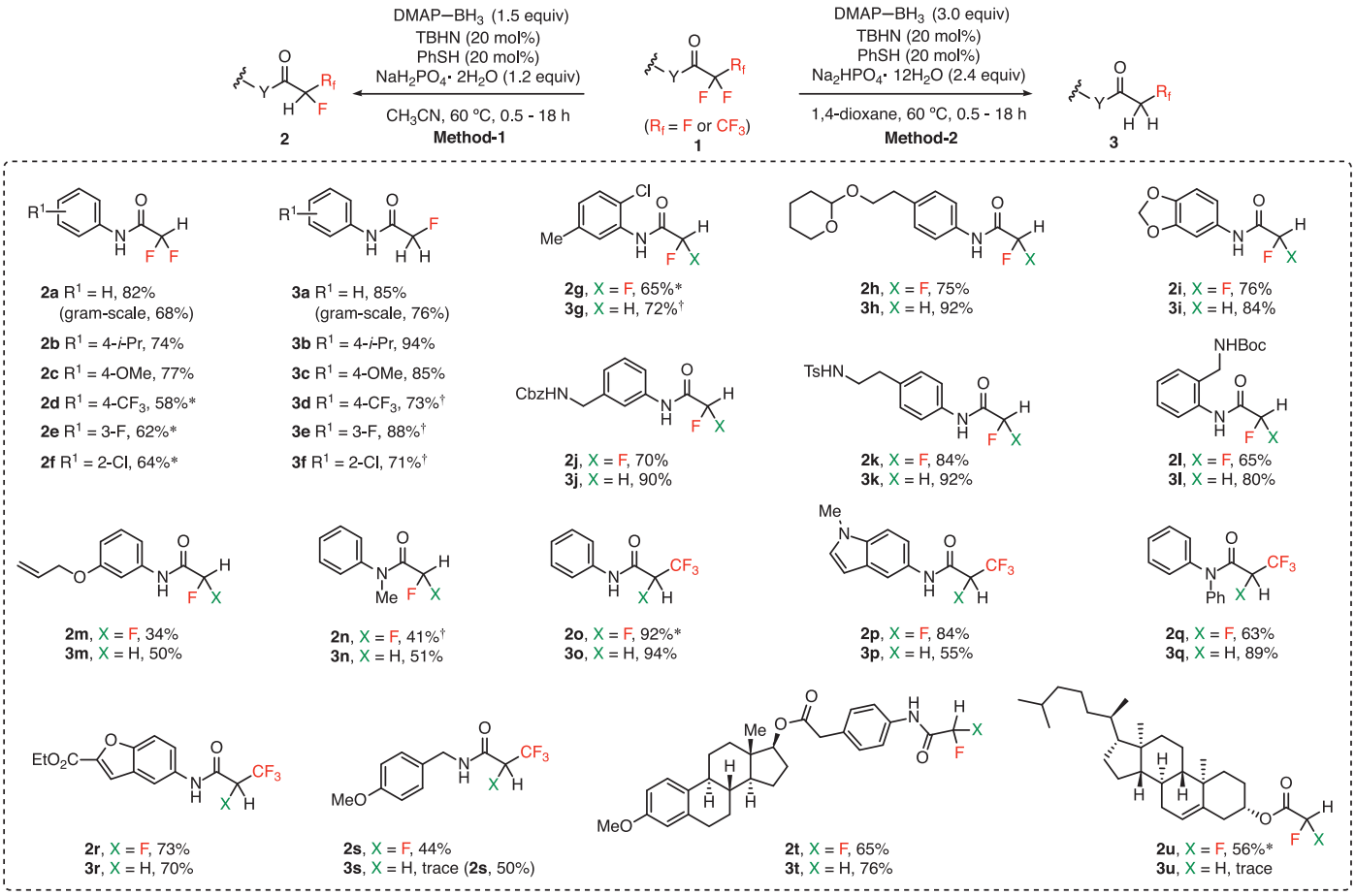

Fig. 2. Scope of mono- and dihydrodefluorination reactions. Method 1: **1** (0.3 to 0.5 mmol), DMAP-BH_3 (1.5 equiv), TBHN (20 mol %), PhSH (20 mol %), $NaH_2PO_4{\cdot}2H_2O$ (1.2 equiv) in CH_3CN (0.1 M), 60°C, 0.5 to 18 hours, under nitrogen. Method 2: **1** (0.3 to 0.5 mmol), DMAP-BH_3 (3.0 equiv), TBHN (20 mol %), PhSH (20 mol %), $Na_2HPO_4{\cdot}12H_2O$ (2.4 equiv) in dioxane (0.1 M), 60°C, 0.5 to 18 hours, under nitrogen. Isolated yields after chromatography are given. *1.2 equiv of DMAP-BH_3 were used. †2.0 equiv of DMAP-BH_3 were used. Cbz, carboxybenzyl; Et, ethyl; Me, methyl; Boc, *tert*-butyloxycarbonyl; Ts, tosyl; *i*-Pr, iso-propyl.

It should be noted that an excess amount of radical initiator was required to maintain high efficiency, and di-*tert*-butyl peroxide (DTBP) was found to be optimal (table S3, entry 6). To enable the efficient initiation of DTBP, a higher reaction temperature (120°C) was necessary. Competing hydrodefluorination products **2** were observed in some cases. This competing reaction could be suppressed by adding a slight excess of the alkenes. Although several examples of coupling reactions between α-bromo- and α-iododifluoroacetamides with alkenes have recently been reported (*10*, *65*), the present protocol using more easily accessible trifluoroacetamides as precursors is more atom and step economical. The coupling reaction proceeded well for styrenes bearing various functional groups (**4a** to **4i**). Gram-scale synthesis of **5a** was accomplished in 59% yield. A series of vinyl ethers (**4j** to **4m**) and nonactivated alkenes (**4n** to **4p**) also underwent coupling, demonstrating broad synthetic applicability. A range of *N*-aryl trifluoroacetamides **1** could react with styrene to afford **5q** to **5x** in good yields. α,α-difluoro *N*-pyridyl amide **5y** and tertiary amide **5z** were obtained in 65 and 43% yields, respectively. However, the coupling reaction of pentafluoropropanamide **1o** was unsuccessful, and the competing reduction product **2o** was formed in 47% yield instead. Coupling was also found to proceed efficiently for α,α,α-trifluoroacetates, furnishing various α,α-difluoroesters **5ab** to **5ag** in synthetically useful yields. This protocol was applied to the modification of drug molecules and naturally occurring bioactive molecules. For example, the modification of vorinostat, which is a histone deacetylase inhibitor (*66*), with the replacement of the oxidation-labile α-carbonyl hydrogen atoms with fluorine atoms (difluoro-vorinostat, **6**) was synthesized by means of the coupling of **1a** with commercially available 5-hexenoic acid, followed by amidation with hydroxylamine (Fig. 3D, yellow box). For natural product derivatives that contain an alkene moiety, coupling with a trifluoroacetamide could introduce an α,α-difluoroamide moiety (**5ai** and **5aj**). Conversely, amine- and alcohol-containing molecules could insert a trifluoroacetyl group through an initial simple acylation reaction, and the subsequent coupling reaction incorporated a variety of α,α-difluoroacetyl functionalities (**5ak** to **5ao**). In these transformations, trifluoroacetates participate in the reaction, and the simple ester moiety remains intact. Such a recognition is likely due to the different electron property of the carbonyl groups that influences the reactivity with DMAP-BH_2•. The connection of two bioactive molecules through an α,α-difluoroamide linker (**5ap**) was also achieved. An attempt to trap the α,α-difluorocarbonyl radical with an intramolecular alkene moiety was performed, and the cyclized product was obtained in a low yield along with the detection of deallylation products (fig. S1).

As shown above, a diverse range of α,α-difluorocarbonyl products (**2** and **5**) were obtained with good yields and selectivity in stage A. We next sought to induce the second β-C–F bond cleavage and capture the resulting α-monofluorocarbonyl radical intermediates with different radical traps to afford densely functionalized α-monofluorocarbonyl derivatives. As depicted in Fig. 4A, compounds **2**

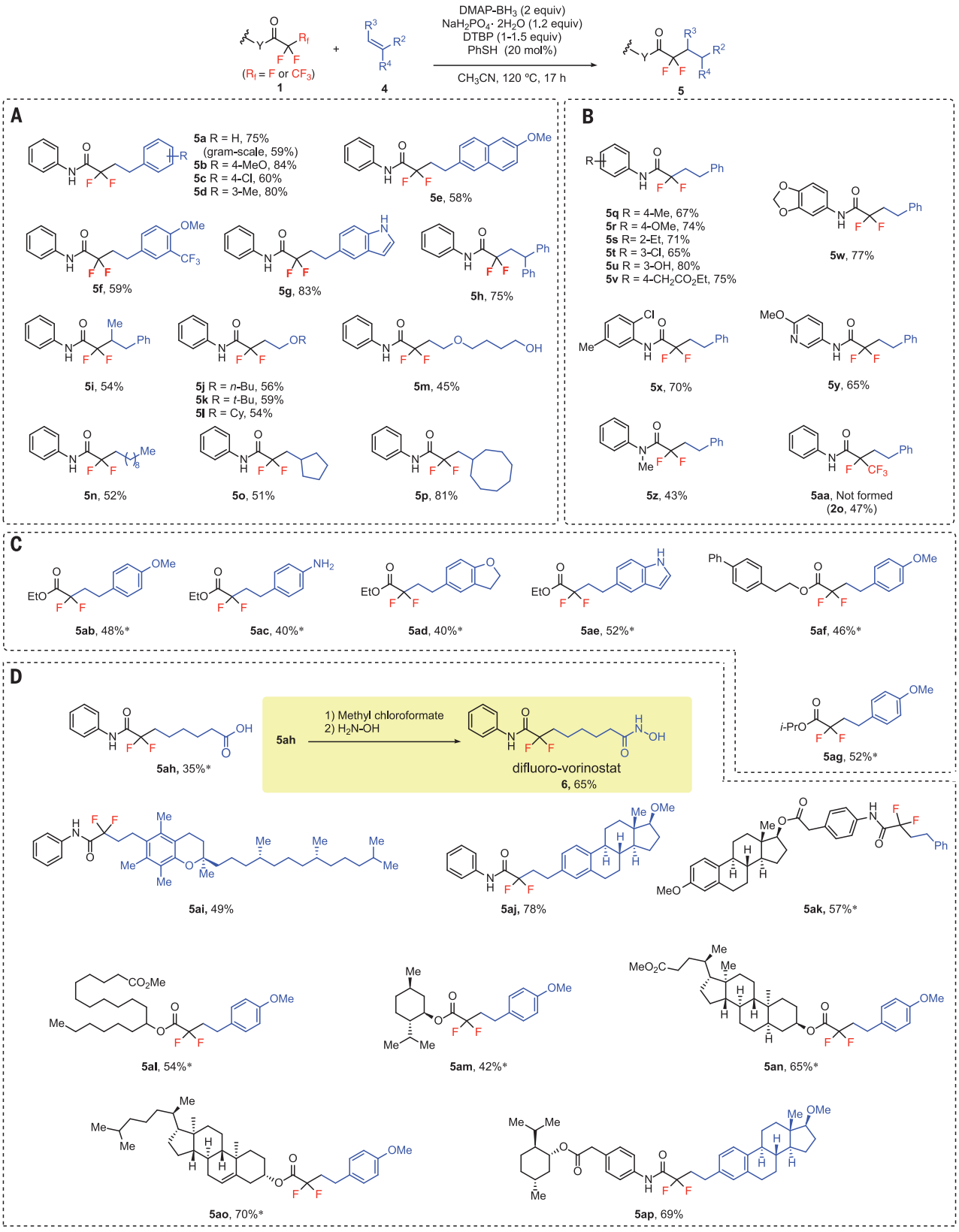

Fig. 3. Scope of defluorinative coupling reactions. Reaction conditions: substrate **1** (0.2 to 0.3 mmol), alkene **4** (2 to 4 equiv), DMAP-BH_3 (2 to 3 equiv), DTBP (1 to 1.5 equiv), PhSH (20 mol %), $NaH_2PO_4{\cdot}2H_2O$ (1.2 equiv) in CH_3CN (0.1 M), 120°C, 17 hours, under nitrogen. Isolated yields after chromatography are given. (**A**) Scope of alkenes. Bu, butyl; Ph, phenyl; Cy, cyclohexyl. (**B**) Scope of trifluoroacetamides. (**C**) Scope of coupling reactions between trifluoroacetates and alkenes. (**D**) Application to the synthesis of difluoroalkyl-substituted bioactive molecules. *The reactions were carried out using alkene **4** (0.5 mmol), **1** (2 equiv), DTBP (1.5 equiv), PhSH (20 mol %), $NaH_2PO_4{\cdot}2H_2O$ (2 equiv) in CH_3CN (0.1 M), 120°C, 12 hours.

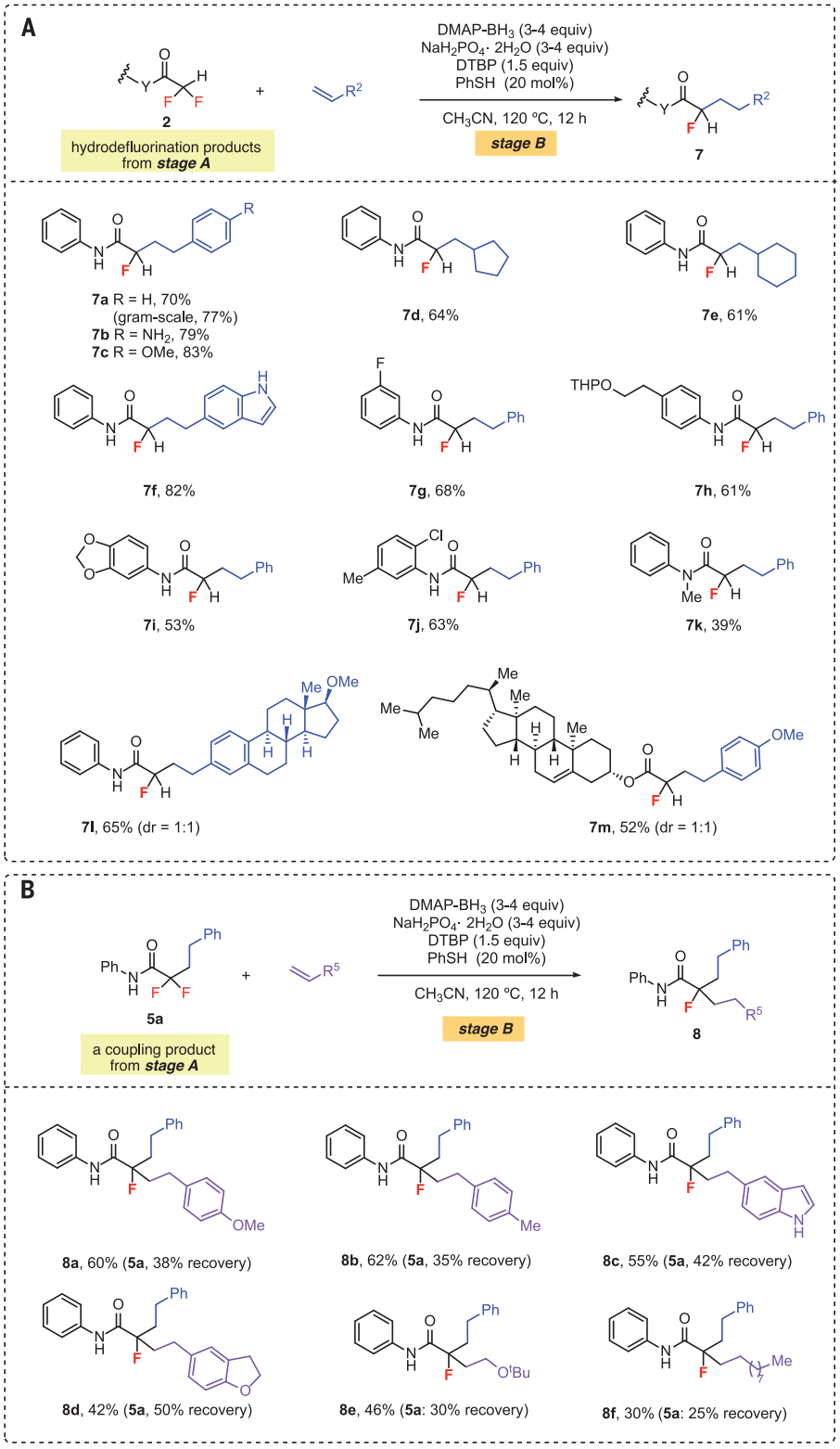

Fig. 4. Scope of various radical traps in two stages. Reaction conditions: compounds **2** or **5** (0.2 to 0.3 mmol), alkene **4** (3 to 4 equiv), DMAP-BH_3 (3 to 4 equiv), DTBP (1.5 equiv), PhSH (20 mol %), $NaH_2PO_4{\cdot}2H_2O$ (3 to 4 equiv) in CH_3CN (0.1 M), 120°C, 12 hours, under nitrogen. Isolated yields after chromatography are given. (**A**) Scope of monohydrodefluorination and coupling sequence. dr, diastereomeric ratio; THP, tetrahydropyran. (**B**) Scope of two successive defluorinative coupling reactions using different alkene partners.

were successfully transformed to products **7** through the defluorinative coupling reaction with alkenes (**7a** to **7k**). The synthetic utility was demonstrated by a gram-scale synthesis of **7a**. This protocol was applicable to the synthesis of monofluorinated bioactive molecules (for **7l** and **7m**). We next probed the feasibility of a second coupling reaction of difluoro product **5a** by using a different alkene as the coupling partner. The reaction was again found to be effective, forming products **8**, which contained a monofluorinated-tertiary stereogenic center (Fig. 4B) (*67*), although moderate yields were achieved, along with the recovery of the unreacted **5a**.

Synthetic applications

By taking advantage of the rich chemistry of the carbonyl moiety, the resulting di- and monofluorocarbonyl products are transferable to a broad range of versatile fluorinated building blocks that are of great value in synthetic and medicinal chemistry. For example, the reduction of difluoro amides **2** and **5** and monofluoro amides **3** and **7** with the BH_3-tetrahydrofuran (THF) complex provided β-mono- and β,β-difluoroamines **9** and **10** in good yields (Fig. 5A). In addition, as depicted in Fig. 5B, **5ab** could be readily transformed into various useful difluoro products, such as β,β-difluoroalcohol **11** and **12**, β,β-difluoroamine **13**, and α,α-difluoroketone **14**. The fluoroalkyl moiety in these products is derived from low-cost trifluoroacetic acid or anhydride.

Mechanistic studies

To explore the nature of the radical defluorination process, mechanistic experiments and computational studies were conducted. A control experiment showed that no reaction occurred when the radical initiator was omitted (table S1, entry 6), confirming the radical nature of this reaction. When alkenes **15** and **17** bearing a radical clock (*68*) were subjected to the coupling reaction conditions, cyclopropane and cyclobutane ring-opening products **16** and **18** were obtained, respectively (Fig. 6A), indicating the intermediacy of difluoroalkyl radical **Int-1** in the reaction.

On the basis of these results, we posit that the defluorination mechanism for **1a** is as follows (Fig. 6, B and C). DMAP-BH_2• is generated from DMAP-BH_3 by using TBHN as a radical initiator (*62*). The addition of DMAP-BH_2• to the carbonyl oxygen of amide **1a** gives **Int-2**. Then, an SCS process occurs to provide **Int-3** with the cleavage of a C–F bond. Although obtaining direct experimental evidence for this process is difficult, an analogous reaction of an α-fluorothioamide containing a cyclopropyl radical clock provided additional support of SCS (fig. S4). 1,2-F radical rearrangement has been posited during the isomerization of perfluorinated radicals (*69*). However, in our case,

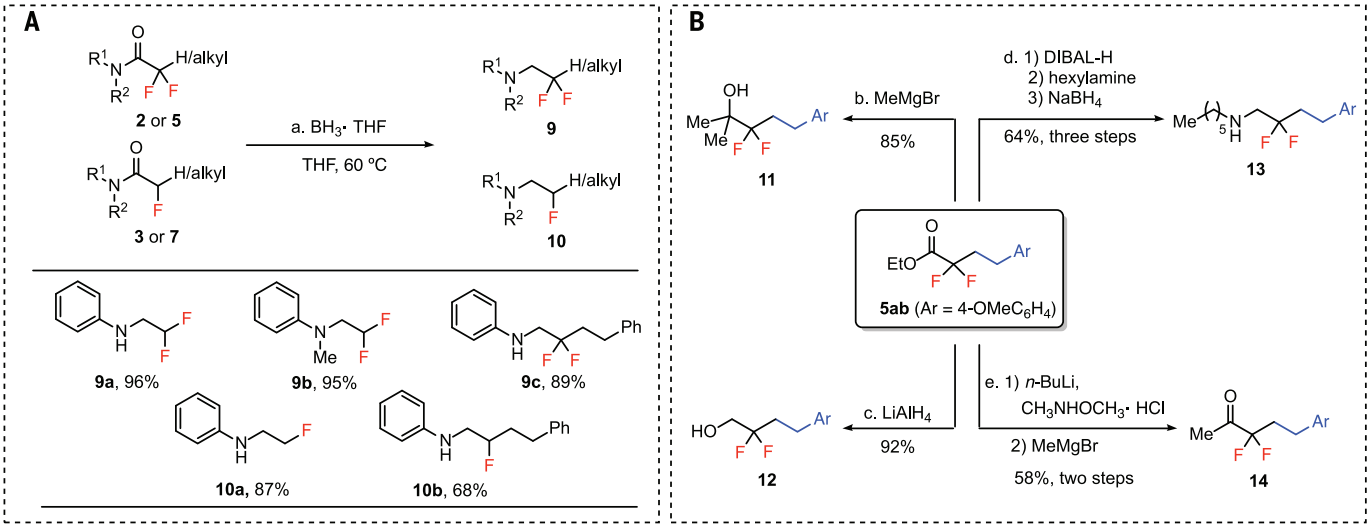

Fig. 5. Synthetic applications. (**A**) Reduction of di- and monofluoro amides for the synthesis of β-mono- and β-difluoroamines. (**B**) Transformations of difluoro acetate **5ab** to various difluoro products. Reaction conditions: (a) BH_3-THF (2 to 3 equiv), THF, 60°C, 6 to 13 hours; (b) MeMgBr (3.0 equiv), THF, 0°C to room temperature (rt), 22 hours; (c) $LiAlH_4$ (3.0 equiv), THF, 0°C to rt, 11 hours; (d) 1) DIBAL-H (1.0 equiv), Et_2O, −78°C, 5 hours; 2) hexylamine (1.0 equiv), toluene, reflux, 4 hours; 3) $NaBH_4$ (5.0 equiv), MeOH, 0°C to rt, 2 hours; (e) 1) *n*-BuLi (4.0 equiv), *N*,*O*-dimethylhydroxylamine hydrochloride (4.0 equiv), THF, −78°C to rt, 13 hours; 2) MeMgBr (4.0 equiv), THF, 0°C to rt, 4 hours. DIBAL-H, di-isobutyl aluminum hydride.

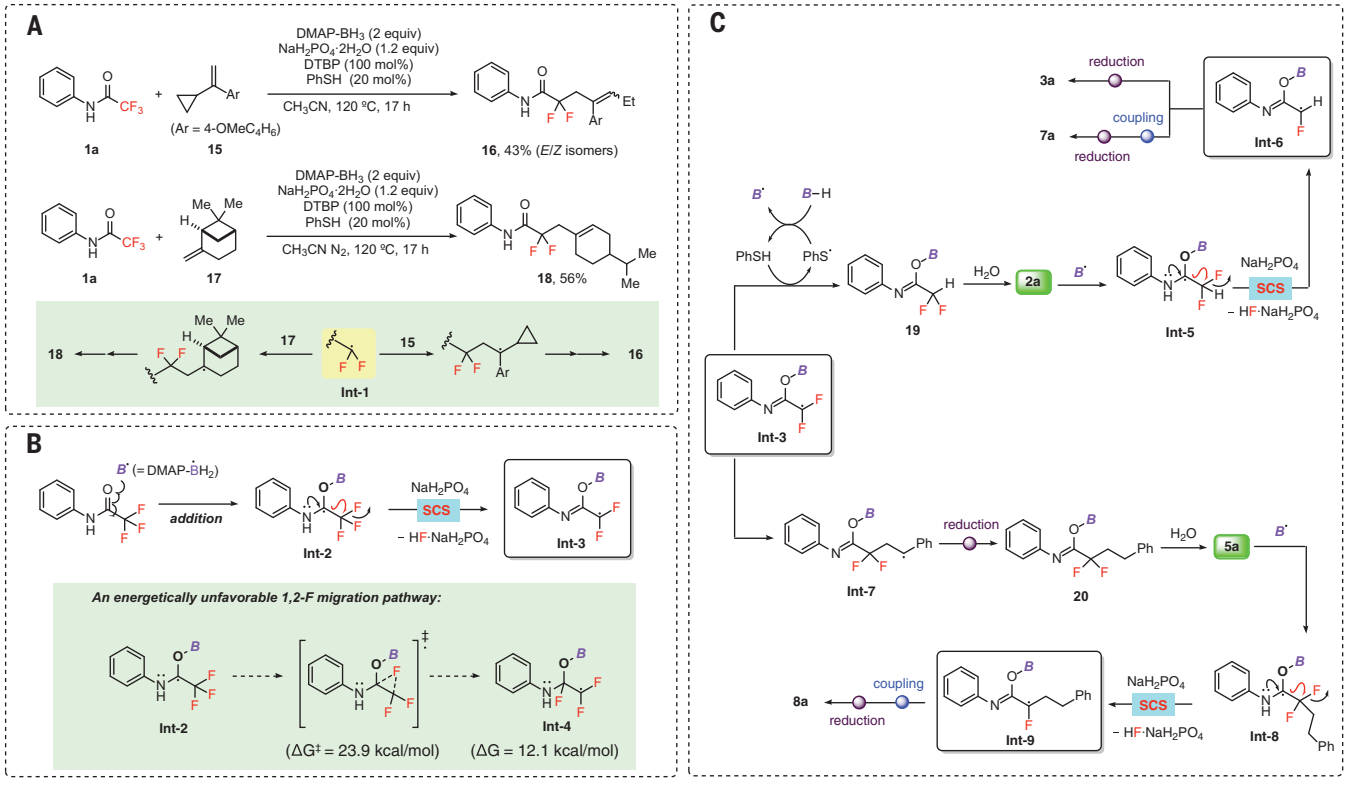

Fig. 6. Mechanistic studies and plausible mechanisms. (**A**) Radical clock experiments to verify the generation of the α,α-difluorocarbonyl radical intermediate. (**B**) Possible pathways for C–F bond cleavage. (**C**) Proposed reaction pathways for the hydrodefluorination and defluorinative coupling reactions.

density functional theory (DFT) calculations revealed that such a 1,2-F migration of **Int-2** requires a high activation free energy ($\Delta G^{\ddagger}$ = 23.9 kcal/mol) and is endergonic by 12.1 kcal/mol (fig. S8). Thus, this route is considered less feasible. From **Int-3**, hydrogen atom transfer from PhSH occurs, and the subsequent hydrolysis affords difluoro product **2a** (Fig. 6B). The resulting thiyl radical then abstracts a hydrogen atom from DMAP-BH_3 to regenerate DMAP-BH_2• and PhSH, thereby propagating the radical chain process (*70*). When styrene is present, the coupling reaction proceeds preferentially over reduction to give **Int-7**, which then participates in an analogous polarity reversal catalysis, affording coupling product **5a**. When further amounts of DMAP-BH_3 are added to **2a** and **5a**, the

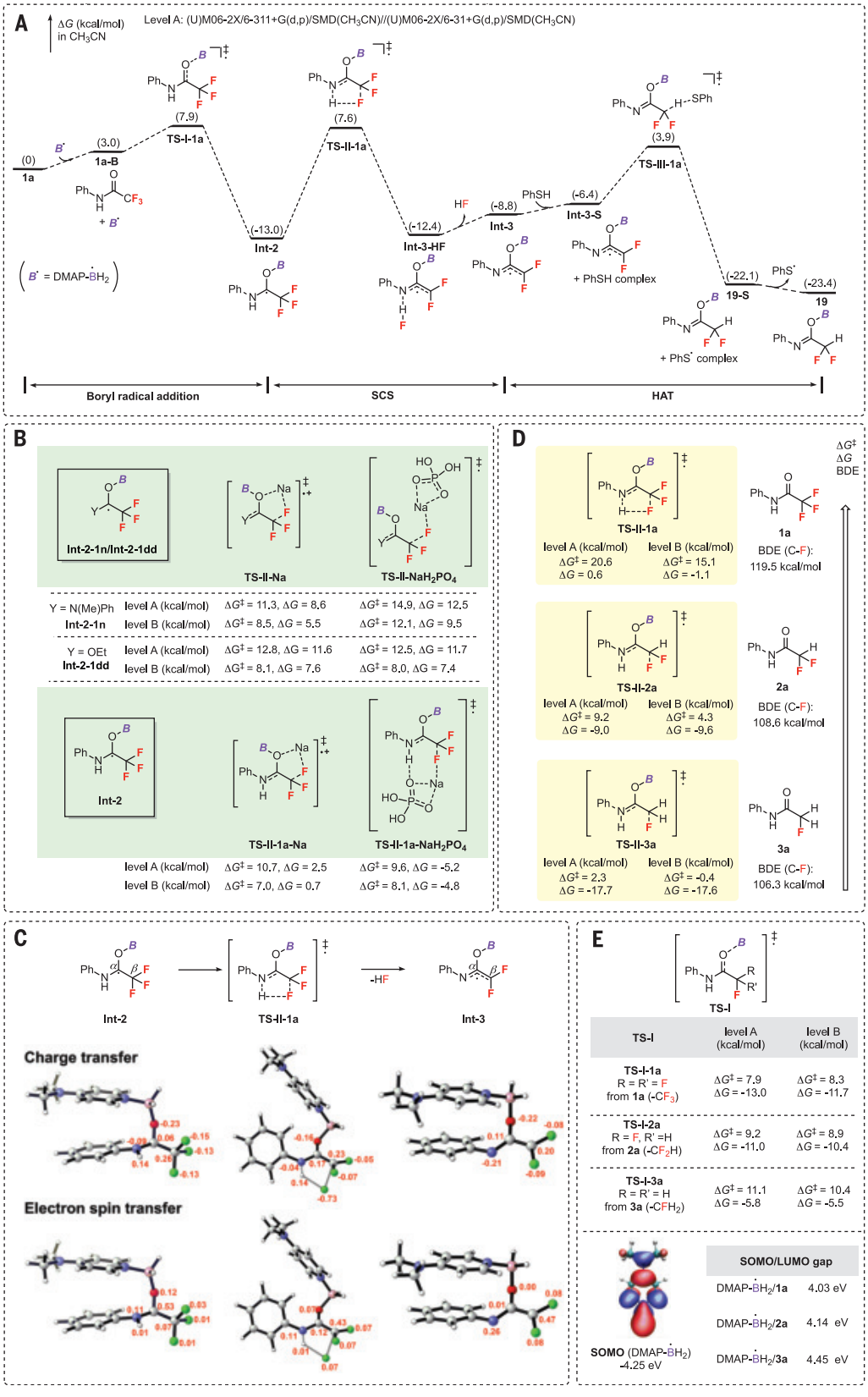

Fig. 7. Computational studies. Level A: (U)M06-2X/6-311+G(d,p)/SMD(CH_3CN)//(U)M06-2X/6-31+G(d,p)/SMD(CH_3CN); level B: (U)ωB97XD/6-311+G(d,p)/SMD(CH_3CN)//(U)M06-2X/6-31+G(d,p)/SMD(CH_3CN). (**A**) Gibbs energy profile for the monohydrodefluorination of **1a**; free energies at level A are displayed. HAT, hydrogen atom transfer. (**B**) SCS of intermediates (**Int-2-1n**, **Int-2-1dd**, and **Int-2**) assisted by Na^+ or NaH_2PO_4. (**C**) Charge and electron spin transfer in the SCS of **1a**; Hirshfeld charges and spin distributions were computed with Multiwfn 3.7, and three-dimensional structures were generated by CYLview (*72*). (**D**) Trend in the SCS processes of **1a**, **2a**, and **3a**; BDEs were calculated at the CBS-4M (complete basis set 4M) level. (**E**) Trend in the addition of DMAP-BH_2• to the substrates; SOMO and LUMO energies were computed at the (U)M06-2X/6-31+G(d,p)/SMD(CH_3CN) level, isovalue = 0.02.

second SCS occurs, and monofluoro-substituted radicals **Int-6** and **Int-9** are generated. The subsequent reduction or coupling reactions provide monofluoro products **3a**, **7a**, and **8a**.

To gain deeper insights into the reaction mechanism, DFT calculations were performed at both the (U)M06-2X/6-311+G(d,p)/SMD(CH_3CN)//(U)M06-2X/6-31+G(d,p)/SMD(CH_3CN) (level A) and (U)ωB97XD/6-311+G(d,p)/SMD(CH_3CN)//(U)M06-2X/6-31+G(d,p)/SMD(CH_3CN) (level B) levels of theory (details are provided in the supplementary materials). Because the reaction

of **1a** could proceed as well in the absence of any additive (table S1, entry 1), DFT calculations were carried out using this reaction as an exemplary model. Figure 7A shows the energy profile of the monohydrodefluorination of **1a** at level A. The addition of the 4-aminopyridine-boryl radical to **1a** is exergonic to give a stabilized radical **Int-2**. Then, SCS of **Int-2** occurs through **TS-II-1a** with an energy barrier of 20.6 kcal/mol, which is found to be the rate-determining step. An alternative SCS process of the deprotonated species derived from **Int-2** is also possible with a surmountable energy barrier (see figs. S6 and S7). However, when the reactions of tertiary amide **1n** and acetate **1dd** both lacking acidic protons were also examined without any additive, no defluorination was observed (tables S2, entry 2, and S5, entry 2). DFT calculations imply that direct fluoride eliminations from **Int-2-1n** and **Int-2-1dd** are highly endergonic (ΔG = 24.5 kcal/mol at level A for **Int-2-1n**, ΔG = 29.0 kcal/mol at level A for **Int-2-1dd**; see figs. S18 and S22). A scan of C–F bond length in these two intermediates indicates that there is no maximum (see figs. S19 and S23). Further investigations revealed that the presence of alkali metal salts is indispensable to promote the defluorination, and NaH_2PO_4 was found to be optimal (tables S2, entries 5 to 12, and S5, entries 4 to 13). DFT calculations at level A and level B both suggest that the addition of either the naked Na^+ or the Na^+ in NaH_2PO_4 favors the loss of fluoride anion, rendering the SCS energetically possible (Fig. 7B and figs. S20, S21, S24, and S25). Moreover, for the reaction of N-H amide **1a**, the activation free energies for the SCS of **Int-2** also decrease when the naked Na^+ (level A: $\Delta G^{\ddagger}$ = 10.7 kcal/mol) (fig. S10) or the Na^+ in NaH_2PO_4 (level A: $\Delta G^{\ddagger}$ = 9.6 kcal/mol) (fig. S11) is present as compared with the one without any additive (level A: $\Delta G^{\ddagger}$ = 20.6 kcal/mol). Experimental results showed that the addition of NaH_2PO_4 is beneficial to accelerate the reaction and improve the product yield (table S1, entries 1 to 4), which is consistent with the computational studies. These results hint that the Na^+ most likely plays an important role to assist the cleavage of C–F bond in these reactions (*30*). The reaction of **Int-3** with styrene has been also calculated (fig. S12). The results show that the addition step is irreversible and that a lower activation energy (level A, $\Delta G^{\ddagger}$ = 10.8 kcal/mol) than that of the competing hydrogen atom transfer from PhSH (level A, $\Delta G^{\ddagger}$ = 12.7 kcal/mol) is required, thus rendering the coupling reaction predominant.

Next, we analyzed the charge and electron spin transfer in the SCS of **Int-2** with Multiwfn (Fig. 7C) (*71*). In **TS-II-1a**, the departing fluoride has a negative charge (−0.73) and a relatively low spin density (0.07), which implies that the cleavage of the C–F bond is heterolytic. The fluoride is highly basic in this medium and deprotonates the cation. In **Int-2**, most of the spin density is located on the α carbon atom (0.53). During the SCS, the spin density shifts gradually to the adjacent β carbon and N atoms, and the spin population is mainly divided between the β carbon atom (0.47) and N atom (0.26) in the resulting **Int-3**.

DFT calculations at level A and level B both suggest that the SCS of **2a** bearing two fluorine atoms is kinetically and thermodynamically more favorable than that of **1a**, and the SCS of **3a** is nearly a barrierless process (Fig. 7D). This trend is in accordance with the gradually decreasing BDE of the C–F bonds from **1a** to **3a** (*5*). However, in our protocols, the defluorination proceeds with an inverse reactivity. Namely, the reaction of trifluoromethyl **1a** is more favorable than that of difluoromethyl **2a** and much more favorable than that of monofluoromethyl **3a**. This selectivity is probably due to the declining reactivity of DMAP-BH_2• toward the addition to the defluorinated products (Fig. 7E). DFT calculations reveal that the reaction between DMAP-BH_2• and **1a** is exergonic, with an activation free energy of 7.9 kcal/mol (level A) and 8.3 kcal/mol (level B), whereas the reactions with **2a** (9.2 kcal/mol at level A, 8.9 kcal/mol at level B) and **3a** (11.1 kcal/mol at level A, 10.4 kcal/mol at level B) have higher energy barriers. This reactivity trend is attributed to the increasing singly occupied molecular orbital (SOMO) and lowest unoccupied molecular orbital (LUMO) gaps between DMAP-BH_2• and the substrates. From **1a** to **3a**, as the number of fluorine atoms decreased, the LUMO energies increased (−0.22 eV for **1a**, −0.10 eV for **2a**, and 0.20 eV for **3a**) (fig. S26), thus increasing the SOMO and LUMO gaps. These reactivity characteristics are crucial to ensure exquisite chemoselectivity during defluorination.

We anticipate that the SCS strategy reported here will be applicable to other carbon-heteroatom bond (i.e., C–O, C–N, and C–Cl, among others) scissions and could enable highly economical syntheses.

REFERENCES AND NOTES

1. E. P. Gillis, K. J. Eastman, M. D. Hill, D. J. Donnelly, N. A. Meanwell, *J. Med. Chem.* **58**, 8315–8359 (2015).
2. Y. Zhou *et al*., *Chem. Rev.* **116**, 422–518 (2016).
3. T. Fujiwara, D. O'Hagan, *J. Fluor. Chem.* **167**, 16–29 (2014).
4. R. Berger, G. Resnati, P. Metrangolo, E. Weber, J. Hulliger, *Chem. Soc. Rev.* **40**, 3496–3508 (2011).
5. D. O'Hagan, *Chem. Soc. Rev.* **37**, 308–319 (2008).
6. W. K. Hagmann, *J. Med. Chem.* **51**, 4359–4369 (2008).
7. T. Furuya, A. S. Kamlet, T. Ritter, *Nature* **473**, 470–477 (2011).
8. X. Yang, T. Wu, R. J. Phipps, F. D. Toste, *Chem. Rev.* **115**, 826–870 (2015).
9. C. Ni, M. Hu, J. Hu, *Chem. Rev.* **115**, 765–825 (2015).
10. Z. Feng, Y.-L. Xiao, X. Zhang, *Acc. Chem. Res.* **51**, 2264–2278 (2018).
11. V. Rauniyar, A. D. Lackner, G. L. Hamilton, F. D. Toste, *Science* **334**, 1681–1684 (2011).
12. Y. Fujiwara *et al*., *Nature* **492**, 95–99 (2012).
13. J. Saadi, H. Wennemers, *Nat. Chem.* **8**, 276–280 (2016).
14. Z. Feng, Q.-Q. Min, X.-P. Fu, L. An, X. Zhang, *Nat. Chem.* **9**, 918–923 (2017).
15. P. Adler *et al*., *Nat. Chem.* **11**, 329–334 (2019).
16. R. R. Merchant *et al*., *Science* **360**, 75–80 (2018).
17. H. Amii, K. Uneyama, *Chem. Rev.* **109**, 2119–2183 (2009).
18. T. Ahrens, J. Kohlmann, M. Ahrens, T. Braun, *Chem. Rev.* **115**, 931–972 (2015).
19. Q. Shen *et al*., *J. Fluor. Chem.* **179**, 14–22 (2015).
20. F. Jaroschik, *Chem. Eur. J.* **24**, 14572–14582 (2018).
21. X. Ma, Q. Song, *Chem. Soc. Rev.* **49**, 9197–9219 (2020).
22. K. Uneyama, H. Amii, *J. Fluor. Chem.* **114**, 127–131 (2002).
23. K. Uneyama, G. Mizutani, K. Maeda, T. Kato, *J. Org. Chem.* **64**, 6717–6723 (1999).
24. G. Blond, T. Billard, B. R. Langlois, *Chem. Eur. J.* **8**, 2917–2922 (2002).
25. S. Yoshida, K. Shimomori, Y. Kim, T. Hosoya, *Angew. Chem. Int. Ed.* **55**, 10406–10409 (2016).
26. T. Fujita, K. Fuchibe, J. Ichikawa, *Angew. Chem. Int. Ed.* **58**, 390–402 (2019).
27. D. Mandal, R. Gupta, A. K. Jaiswal, R. D. Young, *J. Am. Chem. Soc.* **142**, 2572–2578 (2020).
28. M. M. Wade Wolfe, J. P. Shanahan, J. W. Kampf, N. K. Szymczak, *J. Am. Chem. Soc.* **142**, 18698–18705 (2020).
29. M. D. Levin *et al*., *Science* **356**, 1272–1276 (2017).
30. T. W. Butcher *et al*., *Nature* **583**, 548–553 (2020).
31. G. K. Surya Prakash, J. Hu, G. A. Olah, *J. Fluor. Chem.* **112**, 355–360 (2001).
32. J. Wettergren, T. Ankner, G. Hilmersson, *Chem. Commun.* **46**, 7596–7597 (2010).
33. H. Iwamoto, H. Imiya, M. Ohashi, S. Ogoshi, *J. Am. Chem. Soc.* **142**, 19360–19367 (2020).
34. K. Chen, N. Berg, R. Gschwind, B. König, *J. Am. Chem. Soc.* **139**, 18444–18447 (2017).
35. D. B. Vogt, C. P. Seath, H. Wang, N. T. Jui, *J. Am. Chem. Soc.* **141**, 13203–13211 (2019).
36. H. Wang, N. T. Jui, *J. Am. Chem. Soc.* **140**, 163–166 (2018).
37. C. Luo, J. S. Bandar, *J. Am. Chem. Soc.* **141**, 14120–14125 (2019).
38. J. B. I. Sap *et al*., *J. Am. Chem. Soc.* **142**, 9181–9187 (2020).
39. P. Wessig, O. Muehling, *Eur. J. Org. Chem.* **2007**, 2219–2232 (2007).
40. B. Halliwell, J. M. C. Gutteridge, *Free Radicals in Biology and Medicine* (Oxford Univ. Press, 5th ed., 2015).
41. J. Li *et al*., *Nat. Chem. Biol.* **14**, 853–860 (2018).
42. H. Eklund, U. Uhlin, M. Färnegårdh, D. T. Logan, P. Nordlund, *Prog. Biophys. Mol. Biol.* **77**, 177–268 (2001).
43. A. L. J. Beckwith, D. Crich, P. J. Duggan, Q. Yao, *Chem. Rev.* **97**, 3273–3312 (1997).
44. M. Newcomb *et al*., *J. Am. Chem. Soc.* **121**, 10685–10694 (1999).
45. H. Zipse, *Acc. Chem. Res.* **32**, 571–578 (1999).
46. P. Wessig, O. Mühling, *Angew. Chem. Int. Ed.* **40**, 1064–1065 (2001).
47. J. H. Horner, L. Bagnol, M. Newcomb, *J. Am. Chem. Soc.* **126**, 14979–14987 (2004).
48. H. Fuse *et al*., *Chem. Sci.* **11**, 12206–12211 (2020).
49. J. Jin, D. W. C. MacMillan, *Nature* **525**, 87–90 (2015).
50. E. D. Nacsa, D. W. C. MacMillan, *J. Am. Chem. Soc.* **140**, 3322–3330 (2018).
51. B. Bieszczad, L. A. Perego, P. Melchiorre, *Angew. Chem. Int. Ed.* **58**, 16878–16883 (2019).
52. J. Dong *et al*., *Sci. Adv.* **5**, eaax9955 (2019).
53. M. A. Ashley, T. Rovis, *J. Am. Chem. Soc.* **142**, 18310–18316 (2020).
54. Y. Laot, L. Petit, S. Z. Zard, *Org. Lett.* **12**, 3426–3429 (2010).
55. F.-L. Zhang, Y.-F. Wang, in *Science of Synthesis: Advances in Organoboron Chemistry towards Organic Synthesis*, E. Fernández, Ed. (Thieme, 2019), pp. 355–392.
56. T. Taniguchi, *Eur. J. Org. Chem.* **2019**, 6308–6319 (2019).
57. S.-H. Ueng *et al*., *J. Am. Chem. Soc.* **130**, 10082–10083 (2008).
58. S.-C. Ren *et al*., *J. Am. Chem. Soc.* **139**, 6050–6053 (2017).
59. C. Wu, X. Hou, Y. Zheng, P. Li, D. Lu, *J. Org. Chem.* **82**, 2898–2905 (2017).
60. S.-H. Ueng *et al*., *J. Am. Chem. Soc.* **131**, 11256–11262 (2009).
61. W. Dai, T. R. McFadden, D. P. Curran, H. A. Früchtl, J. C. Walton, *J. Am. Chem. Soc.* **140**, 15868–15875 (2018).
62. J. Lalevée, N. Blanchard, M.-A. Tehfe, A.-C. Chany, J.-P. Fouassier, *Chem. Eur. J.* **16**, 12920–12927 (2010).
63. F. Dénès, M. Pichowicz, G. Povie, P. Renaud, *Chem. Rev.* **114**, 2587–2693 (2014).
64. B. P. Roberts, *Chem. Soc. Rev.* **28**, 25–35 (1999).
65. W. Huang *et al*., *ACS Catal.* **6**, 7471–7474 (2016).
66. B. S. Mann, J. R. Johnson, M. H. Cohen, R. Justice, R. Pazdur, *Oncologist* **12**, 1247–1252 (2007).
67. Y. Zhu *et al*., *Chem. Rev.* **118**, 3887–3964 (2018).
68. D. Griller, K. U. Ingold, *Acc. Chem. Res.* **13**, 317–323 (1980).
69. D. J. Van Hoomissen, S. Vyas, *J. Phys. Chem. A* **121**, 8675–8687 (2017).

70. X. Pan, E. Lacôte, J. Lalevée, D. P. Curran, *J. Am. Chem. Soc.* **134**, 5669–5674 (2012).
71. T. Lu, F. Chen, *J. Comput. Chem.* **33**, 580–592 (2012).
72. C. Y. Legault, CYLview, 1.0b (Université de Sherbrooke, 2009); www.cylview.org.
73. Y.-J. Yu *et al.*, Sequential C–F bond functionalizations of trifluoroacetamides and trifluoroacetates via spin-center shifts, Zenodo (2021); https://doi.org/10.5281/zenodo.4510886.

ACKNOWLEDGMENTS

We thank S. Chiba (Nanyang Technological University, Singapore) and S. Z. Zard (Ecole Polytechnique, France) for valuable discussions on the reaction mechanism. **Funding:** We thank the National Natural Science Foundation of China (21672195, 21702201, and 21971226) and the Fundamental Research Funds for the Central Universities (WK2060000017) for financial support. K.N.H. was supported by the U.S. National Science Foundation (CHE-1764328). The numerical calculations in this study have been done on the supercomputing system in the Super-computing Center of the University of Science and Technology of China. **Author contributions:** Y.-F.W. conceived the project and directed the research. Y.-J.Y. conducted most of the experiments. T.-Y.P., C.-L.W., J.C., and C.C. performed parts of the optimization studies and substrate screening experiments. F.-L.Z. conducted the DFT calculations and provided mechanism analysis. K.N.H. directed the DFT calculations and mechanism analysis. F.-L.Z., K.N.H., and Y.-F.W. co-wrote the manuscript. **Competing interests:** The authors declare no competing interests. **Data and materials availability:** Additional optimization, experimental procedures, characterization of new compounds, and all other data supporting the findings are available in the supplementary materials. Raw data underlying the nuclear magnetic resonance spectra are available in Zenodo (*73*).

SUPPLEMENTARY MATERIALS

science.sciencemag.org/content/371/6535/1232/suppl/DC1
Materials and Methods
Supplementary Text
Figs. S1 to S26
Tables S1 to S7
Spectral Data
Calculation Data
References (*74*–*99*)

9 December 2020; accepted 9 February 2021
Published online 4 March 2021
10.1126/science.abg0781

REPORTS

TOPOLOGICAL OPTICS

Generating arbitrary topological windings of a non-Hermitian band

Kai Wang*, Avik Dutt*, Ki Youl Yang, Casey C. Wojcik, Jelena Vučković, Shanhui Fan†

The nontrivial topological features in the energy band of non-Hermitian systems provide promising pathways to achieve robust physical behaviors in classical or quantum open systems. A key topological feature of non-Hermitian systems is the nontrivial winding of the energy band in the complex energy plane. We provide experimental demonstrations of such nontrivial winding by implementing non-Hermitian lattice Hamiltonians along a frequency synthetic dimension formed in a ring resonator undergoing simultaneous phase and amplitude modulations, and by directly characterizing the complex band structures. Moreover, we show that the topological winding can be controlled by changing the modulation waveform. Our results allow for the synthesis and characterization of topologically nontrivial phases in nonconservative systems.

The discoveries of a wide variety of topological materials, such as topological insulators (*1*, *2*) and Weyl semimetals (*3*, *4*), highlight the importance of topological band theory, which seeks to develop fundamental understandings of topological properties of energy band structures. Early efforts on topological band theory have focused on Hermitian Hamiltonians (*5*). Motivated in part by the developments in topological photonics (*6*), where gain and/or loss are common features (*7*–*9*), there have been emerging interests in developing topological band theory for non-Hermitian Hamiltonians (*10*–*12*).

The energy bands of non-Hermitian Hamiltonians exhibit nontrivial topological features that are absent in Hermitian systems. In particular, because the energy bands of non-Hermitian Hamiltonians are in general complex, generically even a single energy band in one dimension can form a nontrivial loop in the complex plane, as characterized by integer nonzero winding numbers (*11*, *12*). This is in contrast with Hermitian systems, where nontrivial topology requires at least two bands, and moreover requires symmetry protection in one dimension. Such nontrivial winding, which is specific to non-Hermitian systems, provides the topological underpinnings of notable phenomena such as the non-Hermitian skin effect (*13*, *14*) and necessitates the generalization of bulk-edge correspondence (*15*, *16*).

In spite of the central importance of energy band winding in the topological band theory of non-Hermitian systems, direct experimental observation and control of such winding have been lacking. Recent experiments have demonstrated the non-Hermitian skin effect (*13*, *15*, *17*) as well as the collapse of eigenspectrum as induced by the presence of an edge (*18*). These experiments, however, only provide indirect evidence of energy-band winding in non-Hermitian systems. Moreover, energy bands are defined only for infinite systems. For non-Hermitian systems, the eigenstates of a finite lattice can be qualitatively different from those in an infinite lattice. Thus, it is not obvious how one can measure the band structure in experimentally feasible non-Hermitian lattices, which are typically finite.

We experimentally implement a class of non-Hermitian Hamiltonians and measure its momentum-resolved complex band energy. Our implementation uses the concept of a synthetic dimension (*19*–*22*), a synthetic frequency dimension (*23*–*25*) as formed by multiple frequency modes in a ring resonator under amplitude and phase modulations.

We implement in the frequency synthetic dimension the one-dimensional (1D) lattice Hamiltonian

$$\hat{H} = \sum\nolimits_{m,n}\left(\kappa_{+m}\hat{a}_{n+m}^{\dagger}\hat{a}_n + \kappa_{-m}\hat{a}_n^{\dagger}\hat{a}_{n+m}\right) \quad (1)$$

where $\hat{a}_n^{\dagger}$ ($\hat{a}_n$) is the creation (annihilation) operator of the n-th lattice site with $m = 1, 2, \ldots, M$ running over the coupling orders. This Hamiltonian becomes non-Hermitian if $\kappa_{+m} \neq \kappa_{-m}^{*}$ for some m in Eq. 1. A general non-Hermitian form of the coupling constant $\kappa_{\pm m}$ can be given by $\kappa_{\pm m} = C_m\exp(\pm i\alpha_m) \pm \Delta_m\exp(\pm i\beta_m)$ with the coupling strengths $C_m, \Delta_m \geq 0$ and phases $\alpha_m, \beta_m \in (-\pi, \pi]$, where $C_m\exp(\pm i\alpha_m)$ is the Hermitian part and $\pm\Delta_m\exp(\pm i\beta_m)$ is the skew-Hermitian part. The Hamiltonian of Eq. 1 has been extensively explored theoretically (*11*, *26*); however, it has been challenging to implement such a Hamiltonian experimentally. The usual implementation of non-Hermitian Hamiltonians through the use of space-dependent gain and loss (*7*, *8*, *27*) does not straightforwardly create the non-Hermitian coupling in Eq. 1. Non-Hermitian couplings were only realized very recently on platforms that include pulse trains (*13*) and electronic circuits (*18*); these demonstrations, however, implemented only a limited subset of non-Hermitian coupling, i.e., nearest-neighbor coupling (exclusively $m = 1$) with restricted in-phase Hermitian and skew-Hermitian parts ($\alpha_1 = \beta_1$). It remains an open question if one can realize general non-Hermitian couplings, which include a control over coupling strengths (C_m, Δ_m), phases (α_m, β_m), and long coupling ranges ($m > 1$)

Ginzton Laboratory and Department of Electrical Engineering, Stanford University, Stanford, CA 94305, USA.
*These authors contributed equally to this work.
†Corresponding author. Email: shanhui@stanford.edu

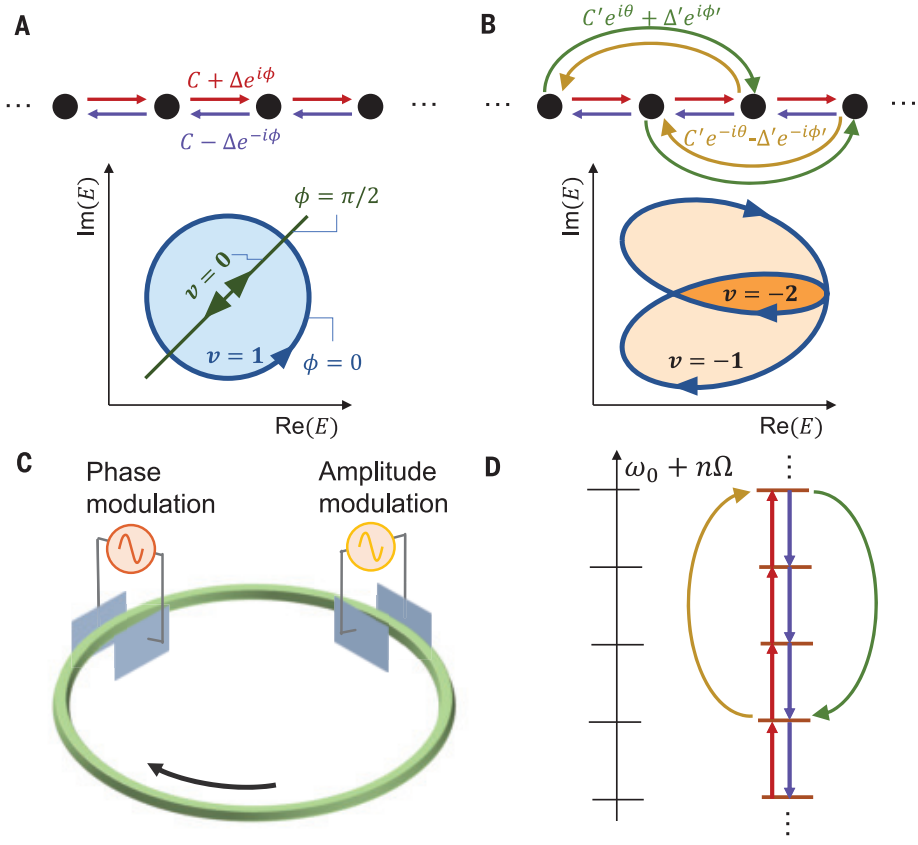

Fig. 1. Topological winding in a non-Hermitian 1D lattice and its realization in a synthetic frequency dimension. (**A**) A non-Hermitian 1D lattice with nearest-neighbor non-Hermitian coupling is shown at the top. The corresponding band energy winding in the complex plane, as k goes from 0 to 2π, is shown at the bottom. (**B**) Same as in (A) but with long-range coupling. A representative example of $v = -2$ is realized when a reference energy ϵ is in the inner dark orange–shaded region of the complex plane. (**C**) Realization of non-Hermitian 1D lattices using a ring resonator undergoing simultaneous amplitude and phase modulation at integer multiples of the free-spectral range Ω. (**D**) Frequency modes separated by Ω in the unmodulated resonator are presented on the left. Non-Hermitian coupling among the frequency modes created by both phase and amplitude modulation, shown for first- and third-order couplings as an illustrative example, are presented on the right.

(*23*, *24*, *28*). Our results illustrate the potential of the platform of synthetic dimensions to explore non-Hermitian topological physics and to implement Hamiltonians that are difficult to achieve by other means.

The Hamiltonian of Eq. 1 exhibits a rich set of nontrivial topological behaviors that depend on the strength, phase, and range of the coupling. We first consider the case with only nearest-neighbor coupling, where the only nonzero coupling constants are $\kappa_{-1} = C - \Delta\exp(-i\phi)$ and $\kappa_{+1} = C + \Delta\exp(i\phi)$ with C, $\Delta \geq 0$. The special case with $\phi = 0$ gives rise to the Hatano-Nelson model (*26*), where the band winds along an ellipse in the complex plane (Fig. 1A, bottom). For a reference energy $\epsilon \in \mathbb{C}$, a winding number (v) of such a 1D band can be defined by (*11*, *14*)

$$v := \int_0^{2\pi} \frac{\mathrm{d}k}{2\pi i} \frac{\mathrm{d}}{\mathrm{d}k} \ln\left[E(k) - \epsilon\right] \qquad (2)$$

For the Hatano-Nelson model (Fig. 1A), if the reference energy ϵ is in the interior of the winding loop, e.g., in the shaded area of Fig. 1A, bottom, one obtains $v = 1$. We note that such a nontrivial winding is a topological feature that is specific to non-Hermitian Hamiltonians. For a Hermitian Hamiltonian, $E(k)$ is restricted to the real axis, and $v = 0$. We also note that the phase difference ϕ between the Hermitian and skew-Hermitian parts of the coupling strongly influences the shape of the loop. In the special example of $\phi = \pi/2$, $E(k)$ is restricted to a line and hence $v = 0$ (green line in Fig. 1A, bottom). More complex winding of the band structure can be achieved by introducing long-range coupling. As an example, we consider the case with $C = 0$, $\Delta/C' = \Delta'/C' = 1$, $\phi = \pi$, $\theta = 0$, and $\phi' = \pi$, where $v = -2$ for a suitable choice of the reference energy (Fig. 1B). In general, the sign of v is determined by the handedness of the winding, and $|v|$ depends on how many times the reference point ϵ is enclosed by the loop in each orientation.

To experimentally realize the Hamiltonian of Eq. 1, we use the synthetic space as formed by the multiple frequency modes of a ring resonator. In the absence of modulation, the ring supports a set of resonant modes propagating along a specific direction (e.g., clockwise, as shown in Fig. 1C). These modes have frequencies $\omega_n = \omega_0 + n\Omega$, where n is an integer that indexes the mode. Ω is the free spectral range (FSR) (Fig. 1D, left). Hermitian coupling between nearest-neighbor frequency modes can be formed with the use of a phase modulation having an associated amplitude transmission factor $T_{\mathrm{Ph}} = \exp(-i\delta\Phi)$ with $\delta\Phi(t) = A_1\cos\Omega t$, where $\delta\Phi$ is the modulated phase, A_1 is the phase-modulation strength, and t is time. The strength of Hermitian coupling is $C \propto A_1$. Similarly, skew-Hermitian coupling can be formed with the use of an amplitude modulation having a transmission factor $T_{\mathrm{Am}} = 1 + B_1\sin(\Omega t + \phi)$, where B_1 is the modulation strength, because the amplitude modulation is not energy conserving. This gives rise to a skew-Hermitian coupling $\kappa_{\pm 1} = \pm\Delta\exp(\pm i\phi)$ with the strength $\Delta \propto B_1$. With simultaneous phase and amplitude modulations, the model of Fig. 1A is realized. Longer-range coupling can be achieved with modulators having modulation frequencies $m\Omega$ with $m > 1$. Specifically, simultaneous implementation of the phase modulation $T_{\mathrm{Ph}} = \exp[-i\sum_m A_m\cos(m\Omega t + \alpha_m)]$ and the amplitude modulation $T_{\mathrm{Am}} = 1 + \sum_m B_m\sin(m\Omega t + \beta_m)$ will give rise to the Hamiltonian in Eq. 1, where $\kappa_{\pm m} = C_m\exp(\pm i\alpha_m) \pm \Delta_m\exp(\pm i\beta_m)$ [for more details, see supplementary section S1A (*29*)]. Consequently, this method allows for the realization of an arbitrary complex band structure for such one-band 1D non-Hermitian lattices, as illustrated in Fig. 1D, right, for a specific example. Note that the ability to simultaneously incorporate phase and amplitude modulations is essential for demonstrating topological winding. Hamiltonians with phase or amplitude modulation (*30*) alone do not exhibit nontrivial winding in their energy bands.

To directly measure the k-resolved non-Hermitian band structure in synthetic frequency space, we use a fiber ring resonator

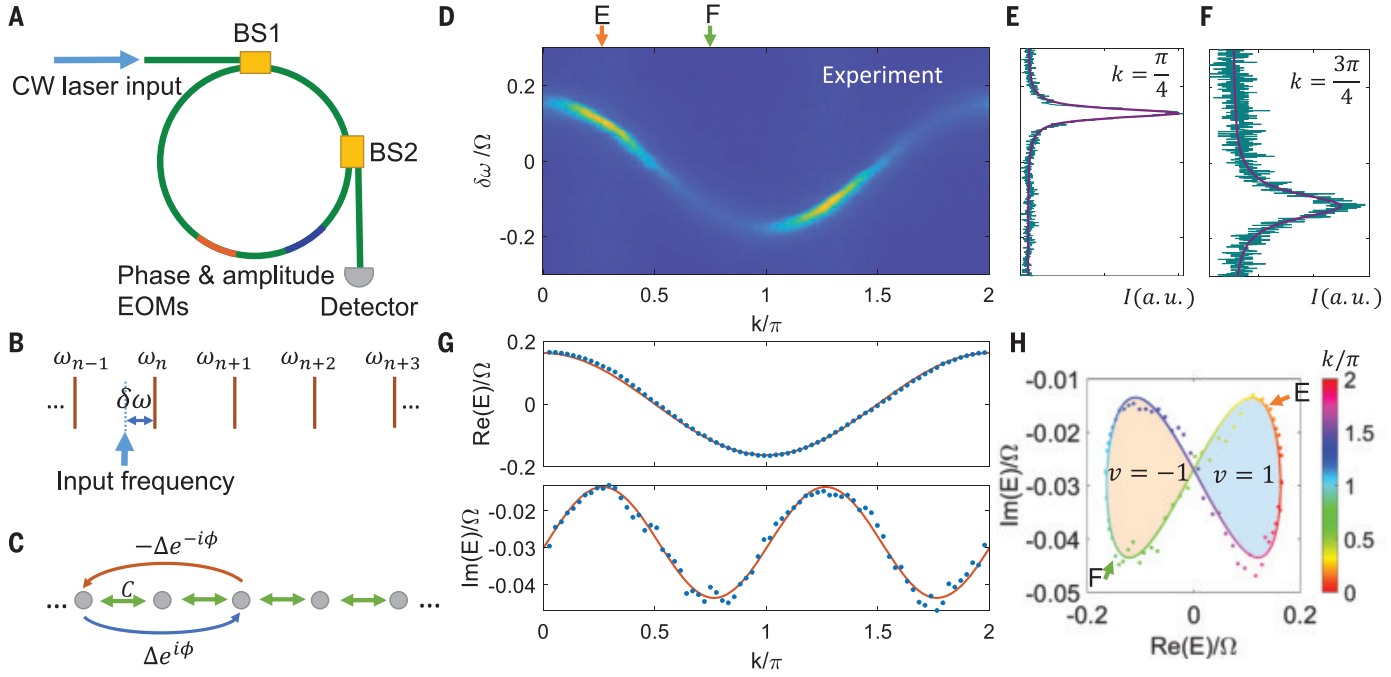

Fig. 2. Measurement of the *k*-resolved complex band energy in synthetic frequency space. (**A**) Input and output schematic of an optical fiber resonator simultaneously modulated by phase and amplitude EOMs. (**B**) A diagram of several resonant modes of the unmodulated resonator separated by Ω, where the input laser frequency (arrow) is detuned by δω from one of the resonance frequencies. (**C**) An example of the formed non-Hermitian lattice. (**D**) Color plot of experimentally measured output intensity $I(k, \delta\omega)$. (**E** and **F**) Measurement signal from two example vertical slices (teal curve) and Lorentzian fitting (purple curve) with (E) $k = \pi/4$ and (F) $k = 3\pi/4$. (**G**) Extracted *k*-dependent Re(*E*) and Im(*E*) (dots) from (D) compared with the theoretical prediction (curve). (**H**) The winding of the measured energy in the complex plane. Arrows indicate the corresponding points of the *k*-slices shown in (E) and (F).

undergoing both phase and amplitude modulations by electro-optic modulators (EOMs) (Fig. 2A). We excite the system with a tunable continuous-wave (CW) laser via a beam splitter (BS1). We choose the input laser frequency ω to be near a certain resonance ω_n, and sweep the detuning $\delta\omega = \omega_n - \omega$ (Fig. 2B). For each detuning, we allow the system to reach steady state and then measure the output from a second beam splitter (BS2) that samples a small portion of the intracavity light for time-resolved detection [for more details on the experimental setup, see supplementary section S2 (*29*)]. Because the lattice space is formed by frequency modes, its reciprocal space is inherently time *t* (*24*), with a round-trip time equivalent to one Brillouin zone; hence, we can define $k = t\Omega$ as the quasimomentum. The steady state resulting from our excitation contains all *k* components at that detuning δω. As we measure the output light at time $t = k/\Omega$, the detection selects a single *k*. Thus, the detected signal $I(k, \delta\omega)$ can be understood as the steady state projected to the discrete Bloch state $|k\rangle$. $I(k, \delta\omega)$ is related to the Green's function, $G(k, \delta\omega) = i[\delta\omega - E(k)]^{-1}$, as

$$I(k,\delta\omega) \propto |G(k,\delta\omega)|^2 = \frac{1}{[\mathrm{Re}(E)-\delta\omega]^2 + [\mathrm{Im}(E)]^2} \quad (3)$$

Here, the band energy is

$$E(k) = \langle k|\hat{H} - i\gamma|k\rangle \quad (4)$$

where γ denotes all sources of loss in the absence of modulation. For a given *k*, *I* is a Lorentzian function of δω. Then, at each *k*, it is possible to deduce the values of Re(*E*) and |Im(*E*)| by fitting $I(\delta\omega)$ to the form of Eq. 3. In our setup, we use a cavity with a sufficiently large loss, i.e., a sufficiently large positive $\gamma \approx 2\Delta + 0.02\Omega$, such that Im(*E*) < 0 is ensured for all *k*. For a γ that is independent of *k*, *E*(*k*) differs from the dispersion of $\hat{H}$ by a translation in the complex energy plane. The topological properties are not affected by such a translation.

To illustrate the specific process of the band-structure measurement, we show a representative experiment forming a lattice in synthetic frequency space (Fig. 2C). There is a first-order Hermitian coupling $\kappa_{\pm 1} = C$ and a second-order skew-Hermitian coupling $\kappa_{\pm 2} = \pm\Delta\exp(\pm i\phi)$. By scanning *k* over one Brillouin zone and δω over one FSR Ω, we obtain the $I(k, \delta\omega)$ readouts (Fig. 2D). Here, we show two representative slices of $I(\delta\omega)$ at $k = \pi/4$ and $k = 3\pi/4$ (Fig. 2, E and F, respectively). According to Eq. 3, Re(*E*) and Im(*E*) can be obtained by a Lorentzian fit for each *k*-slice of *I* (purple curves in Fig. 2, E and F). We plot Re(*E*) and Im(*E*) that are thus obtained as the dots in Fig. 2G. The red curves in Fig. 2G indicate the theoretically predicted form of the dispersion, which agrees well with the experimentally measured dots. Finally, we plot *E* in the complex plane and visualize the winding (Fig. 2H). For the specific dispersion in this example, the complex band winds into a bow-tie shape. For *k* going from 0 to 2π, the left-side loop (light orange shading) is traversed clockwise once with the winding number $v = -1$, and the right-side counterclockwise loop (light blue shading) has $v = 1$.

Band structures are only defined for infinite systems that fulfill Bloch's theorem, whereas all practical structures in experiments are finite. Thus, in seeking to experimentally measure a band structure, one is always attempting to infer the property of an infinite system through the measurement on a corresponding finite system. For the Hermitian system, this does not present an issue. Within the energy range of the band in an infinite system, the eigenstates of the corresponding finite system are also extended and provide an increasingly better approximation of the eigenstates of the infinite system as the size of the finite system increases. For the non-Hermitian system, on the other hand, the eigenstates of the finite system can be drastically different from those of the infinite system. As an extreme example, a finite non-Hermitian lattice truncated with an open boundary condition (OBC) can exhibit the

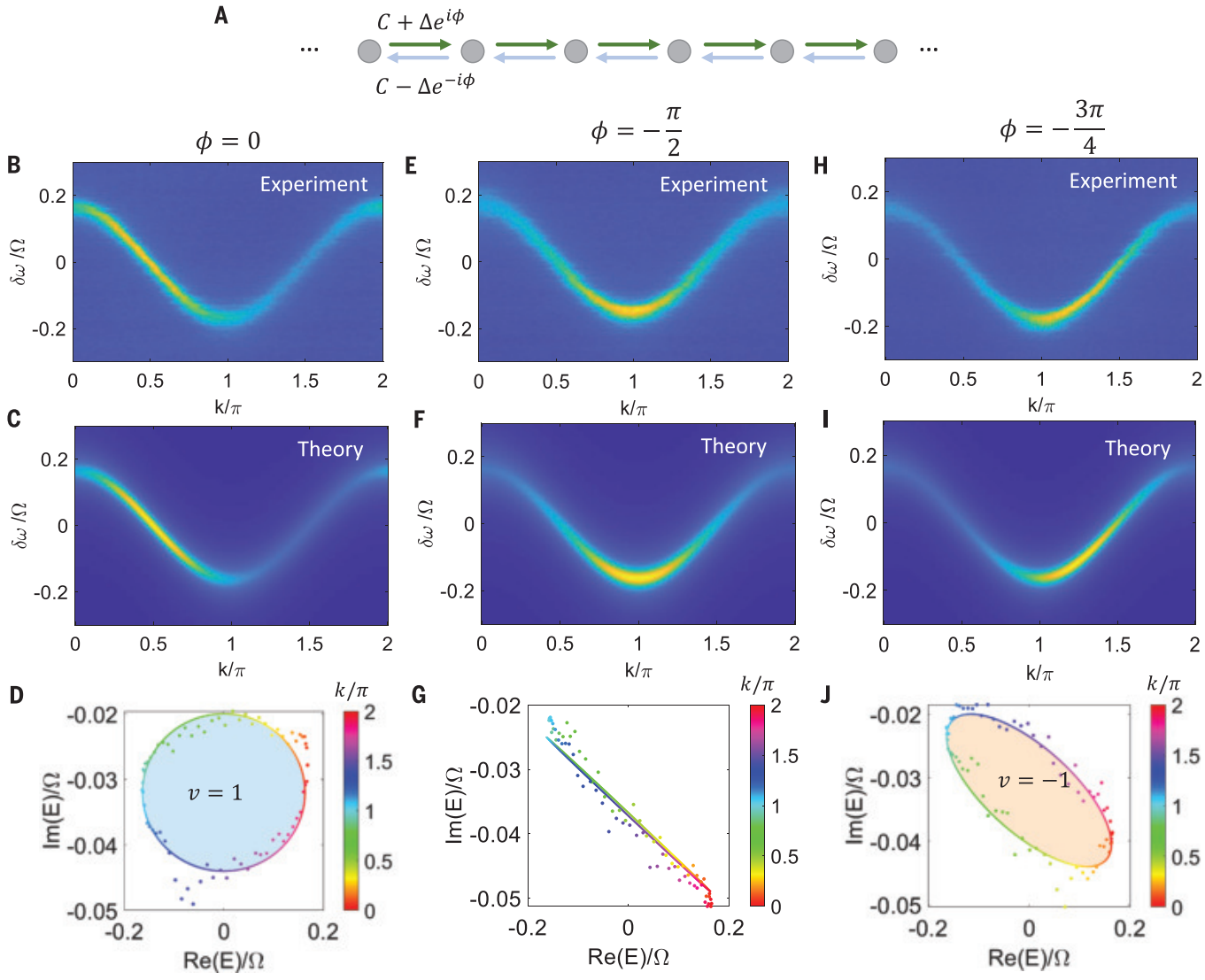

Fig. 3. Experimental realization of a generalized Hatano-Nelson model and the measured topological windings. (**A**) Lattice model with nearest-neighbor non-Hermitian couplings. (**B**, **E**, and **H**) Experimentally measured $I(k, \delta\omega)$ for $\phi = 0$, $-\pi/2$, and $-3\pi/4$, respectively. (**C**, **F**, and **I**) Theoretical predictions for the measurements shown in (B), (E), and (H), respectively. (**D**, **G**, and **J**) The dots represent the band energy extracted from (B), (E), and (H), respectively. The lines denote theoretical predictions.

non-Hermitian skin effect with all eigenstates localized on the edge, and the eigenspectra are thus completely different from those of the corresponding infinite system (*14*, *18*). Thus, it was noted that the winding number defined in Eq. 2 cannot be simply identified from the eigenspectrum of a finite non-Hermitian system (*11*). And hence it may appear surprising that through Eq. 3 we are able to measure the band structure of an infinite system by experiments on a finite system. We emphasize that our experiments probe $E(k)$ as defined by Eq. 4. $E(k)$ is not an eigenenergy of the finite system but rather the expectation value of the Hamiltonian of the finite system at state $|k\rangle$. The state $|k\rangle$ is always extended and moreover naturally approaches the Bloch state of an infinite system as the system size increases. Consequently, our experiments can provide a measurement of the band structure of an infinite system satisfying Bloch's theorem. As an illustration, in supplementary section S1B and fig. S1 (*29*) we consider a numerical experiment where we apply our technique for the extreme case as mentioned above where a finite non-Hermitian lattice is truncated by the OBC. Even though such a finite lattice exhibits a non-Hermitian skin effect, our technique still provides a faithful measurement of the band structure of the infinite system.

We now present an example where the winding of the band can be straightforwardly controlled. In Fig. 3A, we sketch a lattice with nearest-neighbor non-Hermitian couplings in the form $\kappa_{\pm 1} = C \pm \Delta \exp(\pm i\phi)$. Importantly, the topological winding is largely determined by the value of the phase ϕ, which can readily be tuned in our experiments by varying the relative phase between the amplitude and phase modulations. Figure 3, B and C, shows the band structure measurement for $\phi = 0$ accompanied by a theoretical prediction. This case serves as a faithful realization of the Hatano-Nelson model (*26*). The complex band encircles an elliptical area in the counterclockwise direction (Fig. 3D) corresponding to a winding number $v = 1$ (light blue shading). By contrast, if we have $\phi = -\pi/2$ (Fig. 3, E and F), the topology is trivial—the band forms a line in the complex plane (Fig. 3G). As we further choose $\phi = -3\pi/4$ (Fig. 3, H and I), the band becomes a

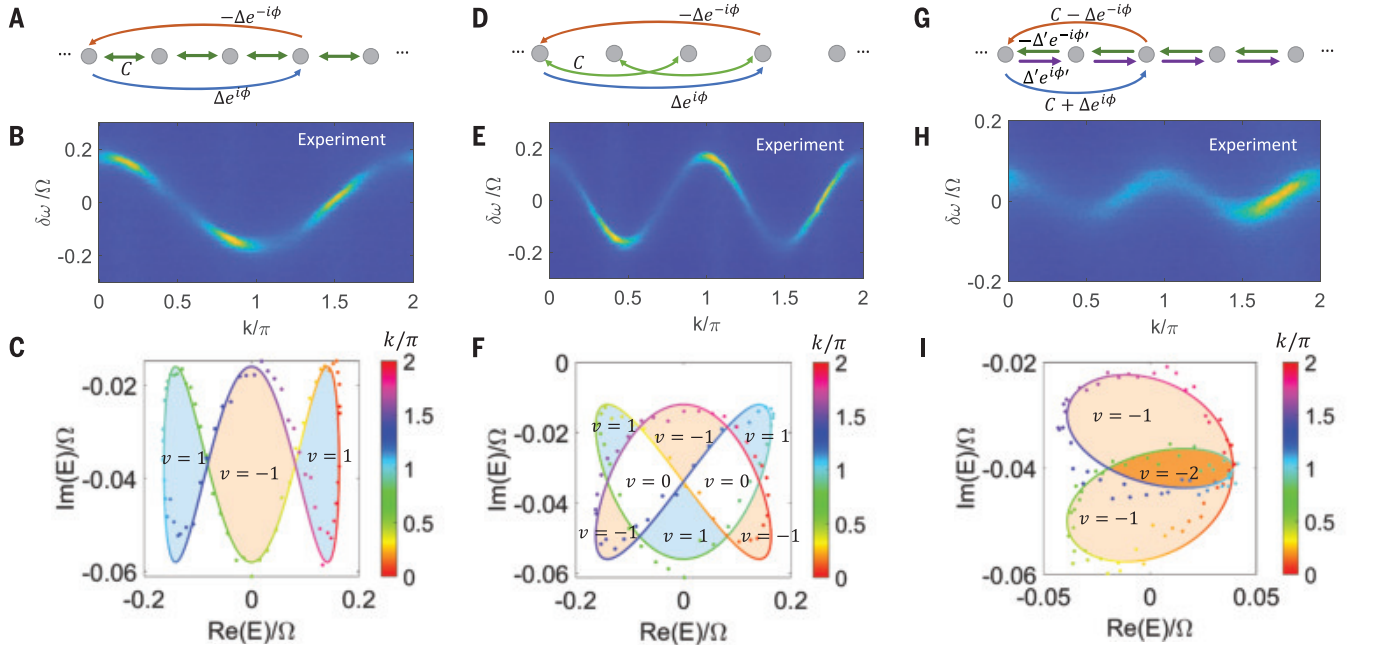

Fig. 4. Realization and band-winding measurements of non-Hermitian lattices incorporating long-range interactions. (**A**) A lattice with first-order Hermitian coupling and third-order skew-Hermitian coupling. (**D**) A lattice with second-order Hermitian coupling and third-order skew-Hermitian coupling. (**G**) A lattice with first-order skew-Hermitian coupling and second-order non-Hermitian coupling. (**B**, **E**, and **H**) Measured $I(k, \delta\omega)$ for the lattices in (A), (D), and (G), respectively. (**C**, **F**, and **I**) Deduced complex E in complex plane for the lattices in (A), (D), and (G), respectively. The dots are from experiments, and the lines are from theory.

tilted ellipse with a clockwise handedness (Fig. 3J). The winding number with respect to a reference energy inside the loop becomes $v = -1$.

A strength of the synthetic-dimension approach lies in the ability to readily incorporate long-range couplings, which can also be non-Hermitian. We harness this ability to produce more complex windings. In Fig. 4A, we sketch a lattice model with a Hermitian first-order coupling $\kappa_{\pm1} = C$ and a skew-Hermitian third-order coupling $\kappa_{\pm3} = \pm\Delta\exp(\pm i\phi)$. This lattice has a dispersion $E(k) = 2C\cos(k) + 2i\Delta\sin(3k + \phi) - i\gamma$. Figure 4, B and C, shows the measurement results for $\phi = 0$. The extracted complex band winding is shown in Fig. 4C, which encloses three areas with the winding number $v = 1$, -1, and 1 from left to right, respectively. As another example, in Fig. 4D, the Hermitian coupling is varied to second order compared with the lattice in Fig. 4A, and hence the dispersion becomes $E(k) = 2C\cos(2k) + 2i\Delta\sin(3k + \phi) - i\gamma$. We show a measurement and the extracted complex band winding with $\phi = -3\pi/4$ (Fig. 4, E and F, respectively). The winding loop encloses three areas with $v = 1$ (light blue shading), three areas with $v = -1$ (light orange shading), and two areas with $v = 0$ (no shading). These examples act as longer-range generalizations of the instances shown in Fig. 3. Additionally, because the winding number v theoretically can take any integer value, to showcase the capability of implementing and measuring windings with $|v| > 1$, we also present an instance as shown in Fig. 4, G to I. The lattice model illustrated in Fig. 4G incorporates non-Hermitian couplings of both first and second orders, where we have $\kappa_{\pm1} = \pm\Delta'\exp(\pm i\phi')$, $\kappa_{\pm2} = C \pm \Delta\exp(\pm i\phi)$. The Bloch band is given by $E(k) = 2C\cos(2k) + 2i\Delta'\sin(k + \phi') + 2i\Delta\sin(2k + \phi) - i\gamma$. In Fig. 4H, we show the measurement for the case $\phi = \phi' = \pi$, and the winding loop encloses not only areas with $v = -1$ (light orange shading) but also an area that winds twice clockwise, which corresponds to $v = -2$ (dark orange shading). In this example, we use a different phase modulation strength that alters the range of Re(E) (Fig. 4I; see also fig. S7). More examples of experimental results can be found in supplementary section S3 (*29*).

Our experimental observation of topological windings of the complex band energy shows that non-Hermitian lattice Hamiltonians in the frequency synthetic space can be implemented through simultaneous amplitude and phase modulations of a ring resonator supporting multiple resonant modes. The realization of non-Hermitian lattice Hamiltonians in synthetic space brings unprecedented flexibility to arbitrarily tailor the complex band structure, fully combining non-Hermitian, long-range, and complex-valued couplings. Such an experimental platform holds great promise in the exploration of highly complex behaviors in synthetic frequency space, such as the interplay of gain, loss, topology, dimensionality, nonlinearity, and lasing.

REFERENCES AND NOTES

1. C. L. Kane, E. J. Mele, *Phys. Rev. Lett.* **95**, 146802 (2005).
2. M. König *et al.*, *Science* **318**, 766–770 (2007).
3. L. Lu *et al.*, *Science* **349**, 622–624 (2015).
4. S.-Y. Xu *et al.*, *Science* **349**, 613–617 (2015).
5. X.-L. Qi, S.-C. Zhang, *Rev. Mod. Phys.* **83**, 1057–1110 (2011).
6. T. Ozawa *et al.*, *Rev. Mod. Phys.* **91**, 015006 (2019).
7. M. A. Bandres *et al.*, *Science* **359**, eaar4005 (2018).
8. H. Zhao *et al.*, *Science* **365**, 1163–1166 (2019).
9. B. Bahari *et al.*, *Science* **358**, 636–640 (2017).
10. H. Shen, B. Zhen, L. Fu, *Phys. Rev. Lett.* **120**, 146402 (2018).
11. Z. Gong *et al.*, *Phys. Rev. X* **8**, 031079 (2018).
12. C. C. Wojcik, X.-Q. Sun, T. Bzdušek, S. Fan, *Phys. Rev. B* **101**, 205417 (2020).
13. S. Weidemann *et al.*, *Science* **368**, 311–314 (2020).
14. N. Okuma, K. Kawabata, K. Shiozaki, M. Sato, *Phys. Rev. Lett.* **124**, 086801 (2020).
15. L. Xiao *et al.*, *Nat. Phys.* **16**, 761–766 (2020).
16. S. Yao, Z. Wang, *Phys. Rev. Lett.* **121**, 086803 (2018).
17. A. Ghatak, M. Brandenbourger, J. van Wezel, C. Coulais, *Proc. Natl. Acad. Sci. U.S.A.* **117**, 29561–29568 (2020).
18. T. Helbig *et al.*, *Nat. Phys.* **16**, 747–750 (2020).
19. O. Boada, A. Celi, J. I. Latorre, M. Lewenstein, *Phys. Rev. Lett.* **108**, 133001 (2012).
20. L. Yuan, Q. Lin, M. Xiao, S. Fan, *Optica* **5**, 1396 (2018).
21. T. Ozawa, H. M. Price, *Nat. Rev. Phys.* **1**, 349–357 (2019).
22. E. Lustig *et al.*, *Nature* **567**, 356–360 (2019).
23. B. A. Bell *et al.*, *Optica* **4**, 1433 (2017).
24. A. Dutt *et al.*, *Nat. Commun.* **10**, 3122 (2019).
25. A. Dutt *et al.*, *Science* **367**, 59–64 (2020).
26. N. Hatano, D. R. Nelson, *Phys. Rev. Lett.* **77**, 570–573 (1996).
27. M. Wimmer, M.-A. Miri, D. Christodoulides, U. Peschel, *Sci. Rep.* **5**, 17760 (2015).

28. A. González-Tudela, C.-L. Hung, D. E. Chang, J. I. Cirac, H. J. Kimble, *Nat. Photonics* **9**, 320–325 (2015).
29. See supplementary materials.
30. L. Yuan, Q. Lin, M. Xiao, A. Dutt, S. Fan, *APL Photonics* **3**, 086103 (2018).

ACKNOWLEDGMENTS

We acknowledge D. A. B. Miller for providing lab space and equipment and M. Orenstein for useful discussions. **Funding:** This work is supported by a MURI project from the U.S. Air Force Office of Scientific Research (grant no. FA9550-18-1-0379) and by a Vannevar Bush Faculty Fellowship from the U.S. Department of Defense (grant no. N00014-17-1-3030). **Author contributions:** K.W., A.D., and S.F. initiated the idea; K.W. and A.D. developed the theory, with input from C.C.W.; K.W. and A.D. performed the experiments, with input from K.Y.Y. and J.V.; and K.W. and A.D. processed the data. All authors discussed the results and contributed to writing the manuscript. S.F. supervised the work. **Competing interests:** The authors declare no competing interests. **Data and materials availability:** All data needed to evaluate the conclusions in this study are presented in the paper and in the supplementary materials.

SUPPLEMENTARY MATERIALS

science.sciencemag.org/content/371/6535/1240/suppl/DC1
Materials and Methods
Figs. S1 to S7
References (*31*–*45*)

10 November 2020; accepted 9 February 2021
10.1126/science.abf6568

DEVELOPMENT

Early developmental asymmetries in cell lineage trees in living individuals

Liana Fasching[1]*, Yeongjun Jang[2]*, Simone Tomasi[1], Jeremy Schreiner[1], Livia Tomasini[1], Melanie V. Brady[1], Taejeong Bae[2], Vivekananda Sarangi[2], Nikolaos Vasmatzis[2], Yifan Wang[2], Anna Szekely[3], Thomas V. Fernandez[1,4], James F. Leckman[1,4], Alexej Abyzov[2]†, Flora M. Vaccarino[1,5,6]†

Mosaic mutations can be used to track cell lineages in humans. We used cell cloning to analyze embryonic cell lineages in two living individuals and a postmortem human specimen. Of 10 reconstructed postzygotic divisions, none resulted in balanced contributions of daughter lineages to tissues. In both living individuals, one of two lineages from the first cleavage was dominant across tissues, with 90% frequency in blood. We propose that the efficiency of DNA repair contributes to lineage imbalance. Allocation of lineages in postmortem brain correlated with anterior-posterior axis, associating lineage history with cell fate choices in embryos. We establish a minimally invasive framework for defining cell lineages in any living individual, which paves the way for studying their relevance in health and disease.

Somatic mutations, generated after formation of the zygote, can be used as permanent cellular markers to trace cell lineages and their spread throughout the human body (*1*, *2*). It was observed that lineages contribute unequally to the blood beginning from cleavages of the zygote (*1*). Similarly, normal development may result in unequal characteristics of symmetrical organs, such as different volumes of left and right frontal and occipital cerebral cortex (*3*); and several pathological conditions exhibit asymmetrical manifestations, such as motor symptoms in Parkinson's disease. However, the timing and rules of cell lineage separation, left-right asymmetry, spread, and local expansion in organs are largely unknown.

To study this question, we reconstructed and analyzed early cell lineages in three unrelated individuals: a phenotypically normal living 66-year-old female (NC0), a living 29-year-old male (LB), and a postmortem female fetus in which we previously studied somatic mutations during neurogenesis, sample 316 (*2*). For the living individuals, we collected skin biopsies from two locations on left and right arms and one location on left and right thighs (Fig. 1A) and cultured fibroblasts from each biopsy. Multiple induced pluripotent stem cell (iPSC) lines were derived (a total of 74 for LB and 15 for NC0), and a selection of iPSC lines was sequenced from each fibroblast sample (table S1). For the postmortem fetal specimen, we reanalyzed sequencing data for 11 clones previously derived from telencephalic neuronal progenitors (*2*) and also sequenced two iPSC lines derived from dural fibroblasts. Most iPSC lines are clonal, and indeed, out of all iPSC lines, only one line showed evidence of being founded by two cells (fig. S1). Comparing the genomes of iPSC lines and clones from the same person allowed us to discover the somatic mutations present in the founder cells of each clone (i.e., skin fibroblasts for LB and NC0 and brain progenitor cells for 316) (fig. S2 and materials and methods). Sites with somatic variants were also analyzed in high-coverage sequencing data for bulk blood, saliva, and urine from the living individuals, and multiple brain regions and spleen from the fetal specimen, to determine presence and allele frequency in those tissues.

To reconstruct the early developmental cell lineages starting from the first zygotic cleavage of each individual, we selected somatic variants shared by clones and lines or by multiple bulk tissues (Fig. 1, fig. S3, table S2, and materials and methods). To make branches in the lineage, we relied on variant sharing by lines and clones and on the rule that in a clone or a line, variants from consecutive cell divisions must be present in tissues at progressively decreasing frequencies. Unrepaired DNA damage that propagates through several cell cycles and may result in multiple mutations at the same genomic position (*4*) is unlikely to interfere with lineage tree reconstruction (materials and methods). As expected from our selection criteria, all variants in the trees were shared by at least two tissues from different germ layers, i.e., mesoderm (fibroblasts, blood, and spleen), ectoderm (brain and, in part, saliva), and endoderm (urine), and therefore arise in common progenitors of the three germ layers before gastrulation.

Occasionally, owing to absence of variants, lineages could not be assigned to a particular division, and multiple solutions in tree branching were possible (polytomy). In such cases, we chose the solution for which sister branches had the most balanced frequencies in tissues, but alternative solutions were also recorded (figs. S3 and S4). To ensure completeness of reconstructed cell divisions, we compared frequencies of the reconstructed sister branches at each division in tissues. Normalized to the frequency of the mother cell, such frequencies should sum up to 100% in all tissues, i.e., should be located on a $f_1 + f_2 = 100\%$ line in a squared plot (fig. S5). Within measurement errors, the frequencies of 10 reconstructed divisions (two in NC0, five in LB, and three in 316) fit the line, suggesting that these divisions are fully reconstructed (Fig. 1 and fig. S3).

For any given cell division, an equal 50%:50% representation of corresponding daughter lineages in the progeny would correspond to stars in the squared plots (fig. S5). For all reconstructed divisions (starting from the first one), we observed imbalanced contributions of sister lineages in tissues, such that dots in the

[1]Child Study Center, Yale University, New Haven, CT 06520, USA. [2]Department of Quantitative Health Sciences, Center for Individualized Medicine, Mayo Clinic, Rochester, MN 55905, USA. [3]Department of Neurology, Yale University, New Haven, CT 06520, USA. [4]Department of Psychiatry, Yale University, New Haven, CT 06520, USA. [5]Department of Neuroscience, Yale University, New Haven, CT 06520, USA. [6]Yale Kavli Institute for Neuroscience, New Haven, CT 06520, USA.
*These authors contributed equally to this work.
†Corresponding author. Email: abyzov.alexej@mayo.edu (A.A.); flora.vaccarino@yale.edu (F.M.V.)

squared plots are on the diagonal but away from the stars (Fig. 1 and fig. S3). In the two living individuals, the largest imbalance was observed for the first two blastomeres, revealing the presence of a dominant and a recessive cell lineage (Figs. 1 and 2A). In both individuals, one of the blastomeres generated 70 to 90% of cells in tissues, with the second blastomere generating the remaining 30 to 10%. The largest imbalance was present in blood, with a contribution ratio of 90:10 from dominant:recessive blastomeres in both NC0 and LB, whereas the smallest difference was in cells from the urinary tract, with roughly a 70:30/80:20 contribution ratio in the two individuals; urinary tract cells showed the least deviation also in subsequent cell divisions (fig. S6). In the postmortem individual, no marked imbalance of the first two blastomeres existed, though one of the two alternative trees is consistent with a 90:10 imbalance in the first division (fig. S3). The ambiguity also existed for LB, but the alternative trees only increase the imbalance (fig. S4).

Higher prevalence of one sister lineage over the other one was typically consistent across tissues for all divisions (Fig. 2B and fig. S6), suggesting consistency of early lineage allocations across germ layers and the body. We noticed that in LB (Fig. 1), there is a higher fraction of insertions and deletions (indels) among variants of the recessive lineage as opposed to the dominant lineage (5 versus 1, $p = 0.03$ by Fisher's exact test) (materials and methods). Instead, in NC0, the cell at the origin of the recessive lineage had 10 single-nucleotide variants (SNVs) and two indels (compared with only one SNV in the dominant lineage) (Fig. 1). Consistent with NC0, one of the alternative lineage trees for 316 with the largest imbalance in sister lineages also had a disproportionately large count of SNVs (11 versus 0) in the recessive as compared with the dominant lineage (fig. S3C). On the basis of these observations, we hypothesize that the efficiency of DNA repair in the early divisions of the human embryo contributes to lineage imbalance.

The available data allowed us to gain insight into lineages from the first to fourth cell division (first week of development), which corresponds to the human embryo preimplantation stage. It is not known whether there exists a systematic bias in lineage allocation with respect to body axes at this early (pregastrulation) stage. To test this, we genotyped mosaic SNVs from high-depth resequencing and inferred frequencies of early lineages across multiple brain regions of specimen 316 (see materials and methods). Six lineages showed significant correlations ($p < 0.05$ by Spearman rank-order) and three more marginally significant correlations ($p < 0.1$) between their frequencies in dorsal brain regions and the arrangement of these regions along the anterior-posterior (A-P) axis, as exemplified by the order FR-GZ → FR-CX → PA-CX → OC-CX → CB (Fig. 2, C and D). The two remaining lineages had the lowest frequencies, consistent with significance not being detected because of larger errors in measuring their tissue frequencies. This analysis revealed a systematic relationship between early lineage distribution and A-P axis in the brain.

We also sampled and sequenced the blood of LB's father and mother (table S1). Two early mosaic SNVs used for reconstruction of the LB lineage tree (β and ε, see table S2) matched to germline single-nucleotide polymorphisms (SNPs) in LB's mother (Fig. 3 and

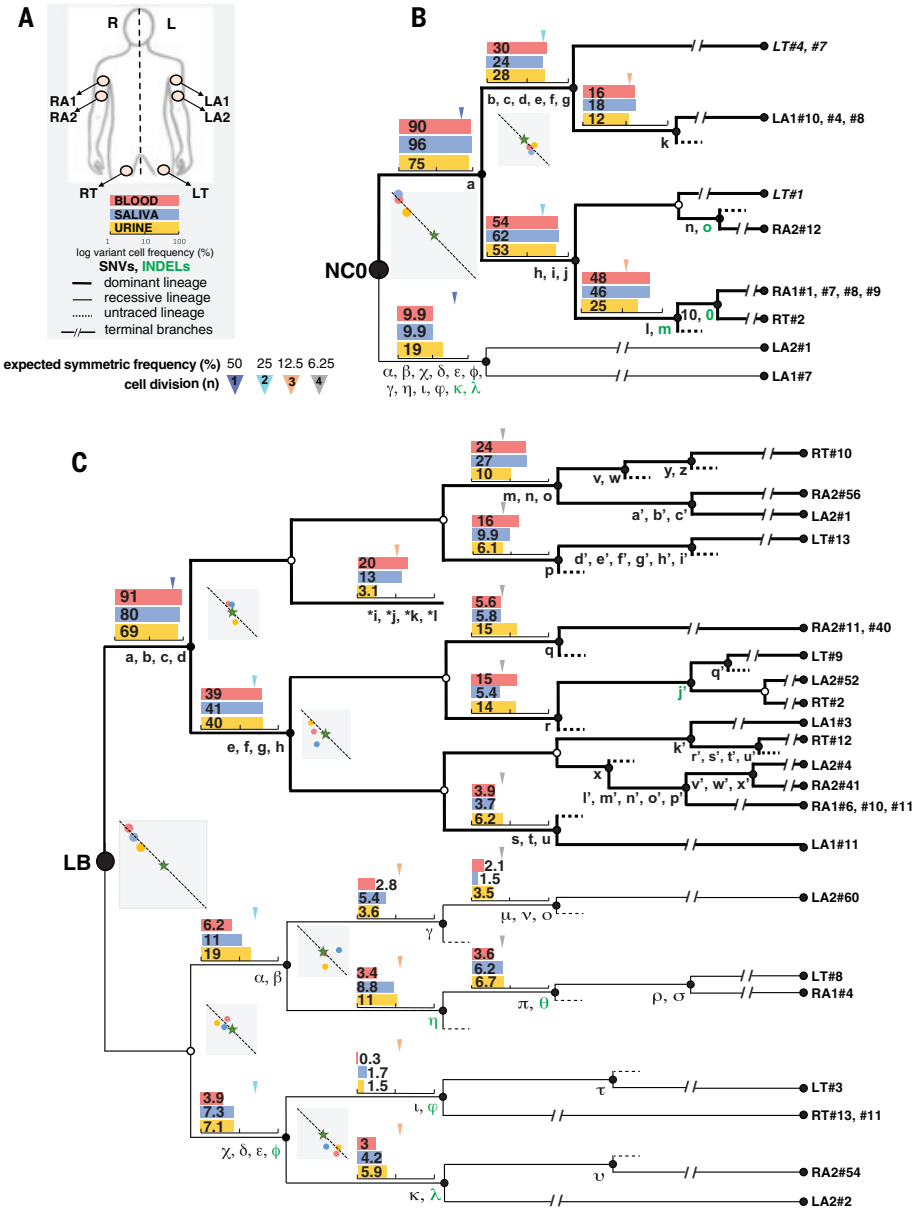

Fig. 1. Reconstruction of early cell lineages in two individuals reveals lineage imbalance across tissues. (**A**) Outline showing location of the biopsies used to derive iPSC lines from skin fibroblasts. Sequenced iPSC lines are listed in (B) and (C) at the terminus of each branch (LT#4, LT#7, LT#1 with shallow coverage are italicized). Counts of mutations per line are shown in fig. S2. (**B** and **C**) Early lineage trees, with circles representing cells and lines likely parental relationships. Open circles mark cells with no mosaic variant, leading to ambiguous branching. Mosaic SNVs (black) and indels (green) are denoted by Latin and Greek letters. SNVs found only in bulk tissues are marked with asterisks. Lineage frequencies in bulk samples are shown in logarithmic scale by bar graphs, with arrows indicating the expected frequencies for a balanced lineage contribution. Squared plots show correlations between the frequencies in bulk samples for upper (*y*-axis) and lower (*x*-axis) branches, with stars indicating expected frequencies for balanced contributions. Division at branch marked by e, f, g, and h may not be fully captured, as frequencies in saliva are inconsistent with the diagonal line.

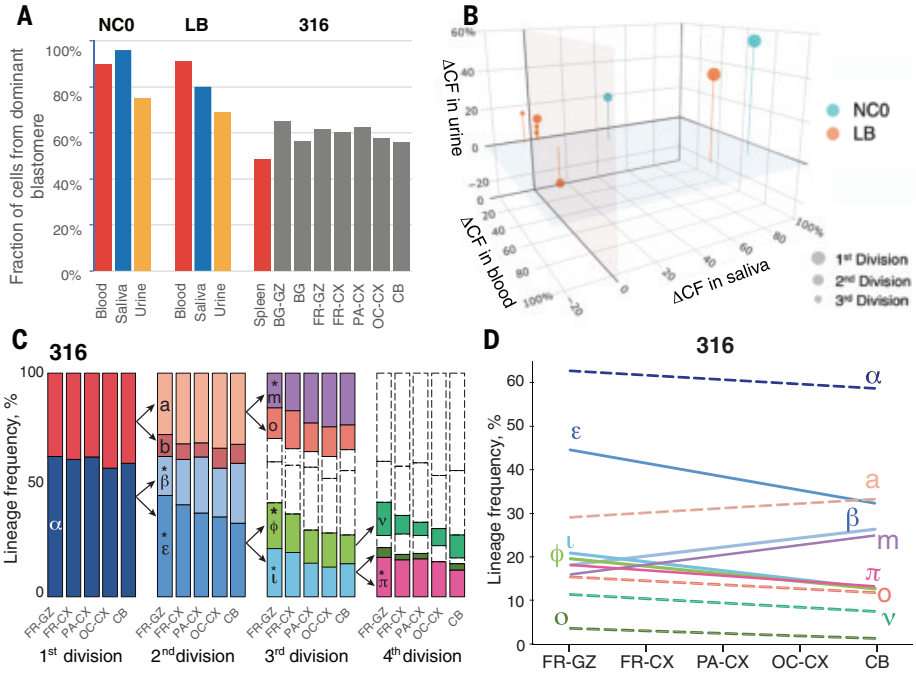

Fig. 2. (**A**) Fraction of cells contributed from the dominant blastomeres in the first cell division to various tissues. (**B**) Difference of sister lineage's contribution to blood, saliva, and urine for fully reconstructed cell divisions. (**C**) Lineage contribution to different brain regions at each cell division; lineages marked by one of the corresponding mutations. FR-GZ, frontal germinal zone; FR-CX, PA-CX, and OC-CX, frontal, parietal, and occipital cortex, respectively; CB, cerebellum. Arrows indicate the correspondence between mother and daughter lineages. (**D**) Regression of lineage frequency across brain regions. Significant correlations ($p < 0.05$) are shown by solid lines and are marked by stars in (C), and nonsignificant correlations are shown by dashed lines. Lineages with marginal significance ($p < 0.1$) are marked by variants α, a, and o. Regressions are shown for 11 lineages with independent frequencies (see materials and methods).

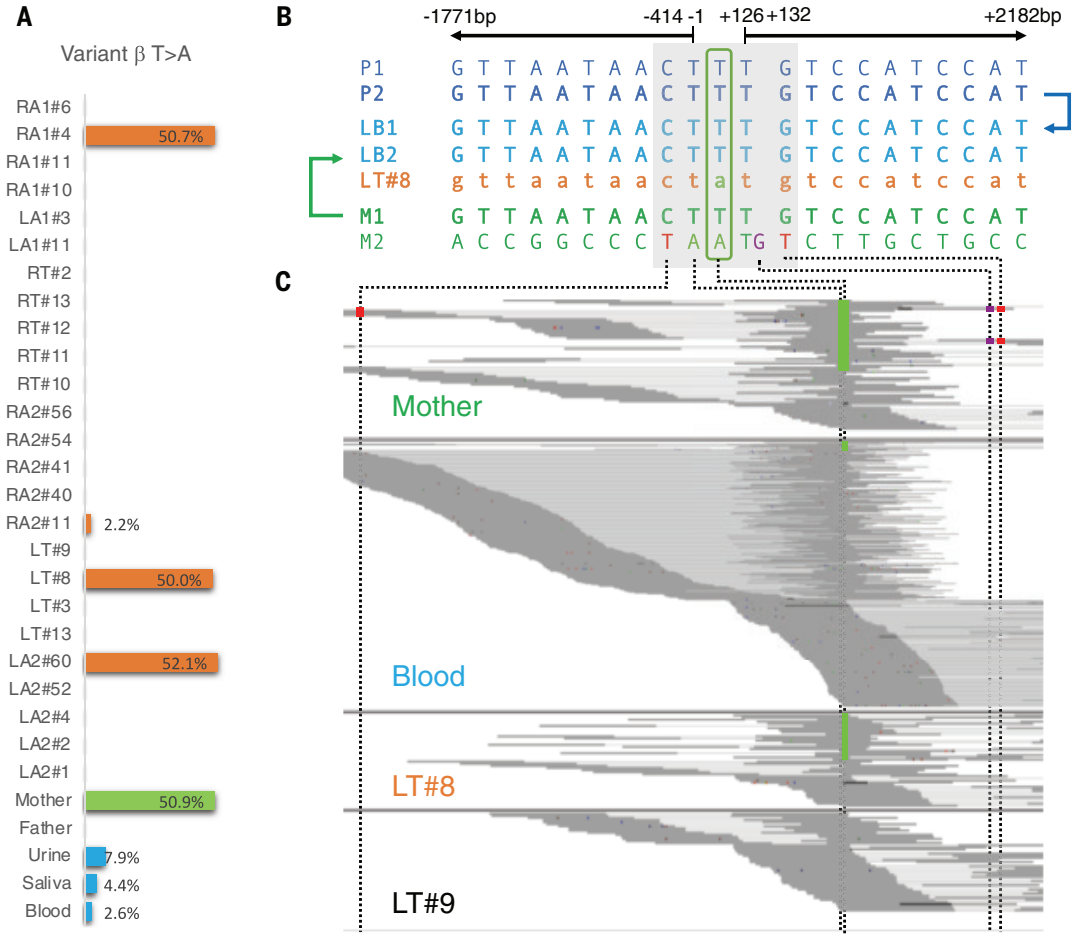

Fig. 3. Recurrence of a germline SNP in LB's mother as a mosaic SNV in LB. (**A**) Variant allele frequency of the T>A somatic SNV variant across LB's iPSC lines (orange), LB's bulk samples (blue), and blood of his parents (green). (**B**) Schematics of germline haplotype inheritance based on population-based SNP phasing for LB (LB1, LB2), father (P1, P2), and mother (M1, M2). Ten noncontiguous variable positions in parents downstream and upstream from the somatic SNV are shown. (**C**) Read-level evidence for the maternal haplotype with the variant not being inherited by LB. Every row has a single connected (light gray lines) pair of reads (dark gray lines). The SNP in the mother is in phase with four nearby variants, none of which is present in LB.

fig. S7). Both SNPs were also present in the catalog of germline variants by gnomAD (one with frequencies in human population of more than 0.001). Examination of the SNV sites revealed nearly 50% variant allele frequency in all iPSC lines in which the SNVs were called, 0% (or near 0% in one line) allele frequency in all iPSC lines in which the SNVs were not called, and intermediate frequency in blood, saliva, and urine (table S2). We found no deletion or loss of heterozygosity in the lines missing the variants, which could have accounted for the variants being inherited but absent in some lines. Furthermore, population-based phasing of germline variants in LB and his parents was consistent with the scenario that haplotypes with the matching SNPs in LB's mother were not inherited by LB. Ultimately, physical read–backed phasing confirmed the nonhereditary nature of the mosaic SNV β in LB (Fig. 3). We, therefore, concluded that these SNVs are bona fide mosaic variants recurrent of known population variants. Sequence context–aware simulation (materials and methods) of a random match of mosaic and germline variants suggested that a count of two recurrent SNVs is unlikely to happen by chance ($p = 0.006$). In addition, we also found that three, one, and three early mosaic SNVs in LB, NC0, and 316, respectively, match known frequent (>0.001 allele frequency) population variants in gnomAD (table S2), which is unlikely to happen by chance, according to the same simulation ($p = 0.03$). In sum, we detect a high recurrence of population variants as postzygotic variants during embryonic development. SNV β discussed above occurs at the boundary of two homopolymers $(T)_{12}(A)_6$. Homopolymers are known to be prone to expansion and contraction (*5*). It is therefore possible that the SNV is the result of T-homopolymer contraction and A-homopolymer expansion, i.e., due to overlap of two indels: TT>T and A>AA. This possibility is also consistent with the above hypothesis that the recessive lineage has a higher fraction of indels, as the discussed SNV is found in branches within the recessive lineage (Fig. 1).

Here we developed and applied a minimally invasive framework for studying early lineages and their imbalance in living human individuals, an approach that consists of two components: (i) derivation and analysis of genomes of clonal iPSC lines to discover somatic mutations and conduct lineage reconstruction; and (ii) analysis of variant distribution in bulk tissues such as saliva, blood, and urine to establish their hierarchy in development. The iPSC derivation could be expanded to other cell types, such as epithelial cells from urine (*6*), erythroblast from blood (*7*), and keratinocytes from skin (*8*), increasing the diversity of sampling of early lineages. Variant distribution analysis in DNA from bulk blood, saliva, and urine can be complemented by the analysis of DNA from buccal swabs, multiple skin regions, hair follicles, feces, vaginal cells, and sperm. Therefore, our study paves the way for comprehensive and large-scale analyses of early lineages and understanding their role in human health and disease.

Our study supports previous observations of an imbalanced lineage contribution to tissues in the human body after the first cleavage (*1*, *9*); however, our results point to a generally higher imbalance of 90:10 versus 2:1 proposed previously, thereby suggesting, at least in some individuals and perhaps more generally, the existence of dominant and recessive lineages starting from the first division of the human zygote. Only minor deviations from the general trend in lineage allocation at each division were observed within each germ layer, implying that the imbalance was established by an intrinsic mechanism in the original lineage precursor cells rather than by selective processes within each tissue compartment. The ordered pattern of lineage distribution along the A-P axis across several brain regions suggests that lineage founder cells may bias their daughter's allocation according to an A-P axial rule at very early stages of human embryonic development.

For LB, we observed an excess of indels in the recessive versus the dominant lineage, and we hypothesize that one factor contributing to this imbalance is the efficiency of DNA repair. Indels can be created from polymerase slippage and from faulty mismatch repair (*10*), whereas in development, most SNVs arise from spontaneous deamination of 5-methylcytosine (*11*). Additional time spent by a cell on DNA repair may decrease proliferation rate, leading to lower contribution to tissues (fig. S8A). For NC0 and possibly for the fetal specimen, no excess of indels but rather an increase in SNV burden in the founder cell of the recessive lineage was observed. We hypothesize that this increased burden could also be caused by deficient DNA repair generating genomic instability in the recessive lineage, a phenomenon hypothesized to exist in vivo based on analysis of in vitro–fertilized embryos (*12*). The instability may result in multiple consecutive cleavages giving only one viable daughter cell, thus leading to accumulation of point mutations from such cleavages in the viable cell; these mutations would retrospectively seem to occur from a single division (fig. S8B). An alternative explanation could be that at the first cleavage, one of the created blastomeres commits mostly to the extraembryonic lineages, whereas the other blastomere mostly commits to inner cell mass and becomes the dominant lineage. Although debated (*13*), such a possibility was previously proposed for mammalian embryos (*14*, *15*). In such case, cell segregation into trophoblast would play the same role as nonviable cells resulting from genome instability, i.e., they will not be present in the adult body (fig. S8B). Thus, lineage studies can shed light on mechanisms that regulate cell fate decisions during development as well as representation of different lineages in tissues of any living individual and across the human population.

REFERENCES AND NOTES

1. Y. S. Ju *et al.*, *Nature* **543**, 714–718 (2017).
2. T. Bae *et al.*, *Science* **359**, 550–555 (2018).
3. D. R. Weinberger, D. J. Luchins, J. Morihisa, R. J. Wyatt, *Ann. Neurol.* **11**, 97–100 (1982).
4. S. J. Aitken *et al.*, *Nature* **583**, 265–270 (2020).
5. H. Ellegren, *Trends Genet.* **16**, 551–558 (2000).
6. T. Zhou *et al.*, *Nat. Protoc.* **7**, 2080–2089 (2012).
7. E. Varga, M. Hansen, T. Wüst, M. von Lindern, E. van den Akker, *Stem Cell Res. (Amst.)* **25**, 30–33 (2017).
8. T. Aasen *et al.*, *Nat. Biotechnol.* **26**, 1276–1284 (2008).
9. H. Lee-Six *et al.*, *Nature* **561**, 473–478 (2018).
10. M. Garcia-Diaz, T. A. Kunkel, *Trends Biochem. Sci.* **31**, 206–214 (2006).
11. M. Ehrlich, X. Y. Zhang, N. M. Inamdar, *Mutat. Res.* **238**, 277–286 (1990).
12. E. Vanneste *et al.*, *Nat. Med.* **15**, 577–583 (2009).
13. K. Takaoka, H. Hamada, *Development* **139**, 3–14 (2012).
14. K. Piotrowska, M. Zernicka-Goetz, *Nature* **409**, 517–521 (2001).
15. K. Piotrowska, F. Wianny, R. A. Pedersen, M. Zernicka-Goetz, *Development* **128**, 3739–3748 (2001).
16. F. Vaccarino *et al.*, Early developmental asymmetries in cell lineage trees in living individuals, National Institute of Mental Health Data Archive (2020); https://doi.org/10.15154/1520633.

ACKNOWLEDGMENTS

We are most grateful to LB and his parents, as well as NC0, for their willingness to participate in this study. We acknowledge the Yale Center for Clinical Investigation for clinical support in obtaining the biopsy specimens. We thank C. Qiu and J. Thomson of the Yale Stem Cell Center Core Services for the generation of iPSC lines. We thank BGI Americas Corporation for library preparation and deep sequencing. We thank the Keck DNA Sequencing Facility at Yale for their assistance with DNA sequencing service. We thank J. Mariani and S. Scuderi for the generation and amplification of brain neurosphere clones. We acknowledge members of the Brain Somatic Mosaicism Network (BSMN) for helpful comments and discussions. **Funding:** This work was funded by the National Institute of Mental Health (grants R01 MH100914, U01 MH106876) and by the Simons Foundation (grant 399558). **Author contributions:** F.M.V., A.A., and J.F.L. conceived the study. F.M.V. and A.A. supervised the study. L.F., S.T., and T.V.F. designed and performed experiments and collected data. Y.J., T.B., V.S., N.V., and Y.W. performed computational data analyses. A.S. evaluated human donors and obtained tissue biopsies. J.S., L.T., and M.B. grew iPSC lines. L.F., Y.J., A.A., and F.M.V. prepared display items. A.A. and F.M.V. wrote the initial draft of the manuscript. All authors participated in discussions of results and manuscript editing. **Competing interests:** The authors declare no competing interests. **Data and materials availability:** All data presented in our work are included in the text and supplementary materials. All primary data are accessible at NDAR (study no. 1057) (*16*) and freely available for download.

SUPPLEMENTARY MATERIALS

science.sciencemag.org/content/371/6535/1245/suppl/DC1
Materials and Methods
Figs. S1 to S11
Tables S1 to S3
References (*17*–*19*)
MDAR Reproducibility Checklist

10 August 2020; accepted 9 February 2021
10.1126/science.abe0981

DEVELOPMENT

Landmarks of human embryonic development inscribed in somatic mutations

Sara Bizzotto[1,2,3]*, Yanmei Dou[4]*, Javier Ganz[1,2,3]*, Ryan N. Doan[1], Minseok Kwon[4], Craig L. Bohrson[4], Sonia N. Kim[1,2,3,5], Taejeong Bae[6], Alexej Abyzov[6], NIMH Brain Somatic Mosaicism Network†, Peter J. Park[4,7]‡, Christopher A. Walsh[1,2,3]‡

Although cell lineage information is fundamental to understanding organismal development, very little direct information is available for humans. We performed high-depth (250×) whole-genome sequencing of multiple tissues from three individuals to identify hundreds of somatic single-nucleotide variants (sSNVs). Using these variants as "endogenous barcodes" in single cells, we reconstructed early embryonic cell divisions. Targeted sequencing of clonal sSNVs in different organs (about 25,000×) and in more than 1000 cortical single cells, as well as single-nucleus RNA sequencing and single-nucleus assay for transposase-accessible chromatin sequencing of ~100,000 cortical single cells, demonstrated asymmetric contributions of early progenitors to extraembryonic tissues, distinct germ layers, and organs. Our data suggest onset of gastrulation at an effective progenitor pool of about 170 cells and about 50 to 100 founders for the forebrain. Thus, mosaic mutations provide a permanent record of human embryonic development at very high resolution.

Although recent strategies involving DNA editing have used molecular barcodes as clonal markers to map the developmental processes of proliferation, migration, and tissue formation (*1*), such methods are not applicable to understanding human development. Single-cell RNA-sequencing (RNA-seq) methods have been used to analyze transcriptional changes and cell differentiation during human development (*2*), but they are inadequate for lineage tracing, leaving global lineage patterns in humans still largely unexplored. Here, to examine developmental ancestries and clonal composition across the body, we characterized somatic single-nucleotide variants (sSNVs), which are suitable as lineage markers because they accumulate with each cell division (*3*) and most mutations are predicted to be functionally silent (*4*, *5*).

High-depth whole-genome sequencing (WGS; >250× per sample) was performed for five bulk DNA samples from a 17-year-old male (ID: UMB1465) who died with no medical diagnosis [prefrontal cortex (PFC) section 2 gray matter (GM) and white matter (WM), heart, spleen, and liver (>1250× total); Fig. 1A and table S1]. Similarly, >250× WGS was also performed for PFC and two visual cortex samples [Brodmann area (BA)17 and BA18] from two additional individuals who also died with no medical diagnosis, a 15-year-old female (ID: UMB4638) and a 42-year-old female (ID: UMB4643). Applying MosaicForecast, a machine-learning algorithm (*4*), to bulk data and integrating with previously published single-cell WGS (*6*, *7*), we identified 516 total sSNVs (*8*) (table S2). Among the 297 sSNVs detected in UMB1465, 65 (22%) were found across all tissues and 181 (61%) in at least two (Fig. 1B and table S2). All 65 widely shared sSNVs showed alternate allele frequency (AAF) >1%, with 38 (58%) showing >3% (Fig. 1B and table S2). Sensitivity estimates suggest that our approach achieved nearly 100% sensitivity for detecting sSNVs of 3 to 30% AAF (*8*) (Fig. 1C and fig. S1, A to C). Most sSNVs were predicted to be functionally neutral (only two of 297 sSNVs in UMB1465 were exonic; table S3) and thus represent unbiased lineage markers.

Clonal sSNVs in all organs showed similar base substitution patterns, with 55% being C>T substitutions (Fig. 1D and fig. S1, D and E). The trinucleotide context resembled that of sSNVs seen in proliferating tissues and cancer, e.g., clock-like Signature 1 in the COSMIC catalog (*9*), which likely reflects faulty repair of cytosine deamination in cycling cells (*5*, *7*). Liver-specific variants were more common than heart- or brain-specific variants (n = 57, 33, and 19, respectively), consistent with known patterns of clonal amplification and replacement of hepatic units from resident stem cells (*10*), whereas spleen-specific variants were the least common (Fig. 1B and table S2). Amplicon-based targeted sequencing (~25,000× on average) of 94 samples from 17 organs (Fig. 1A and

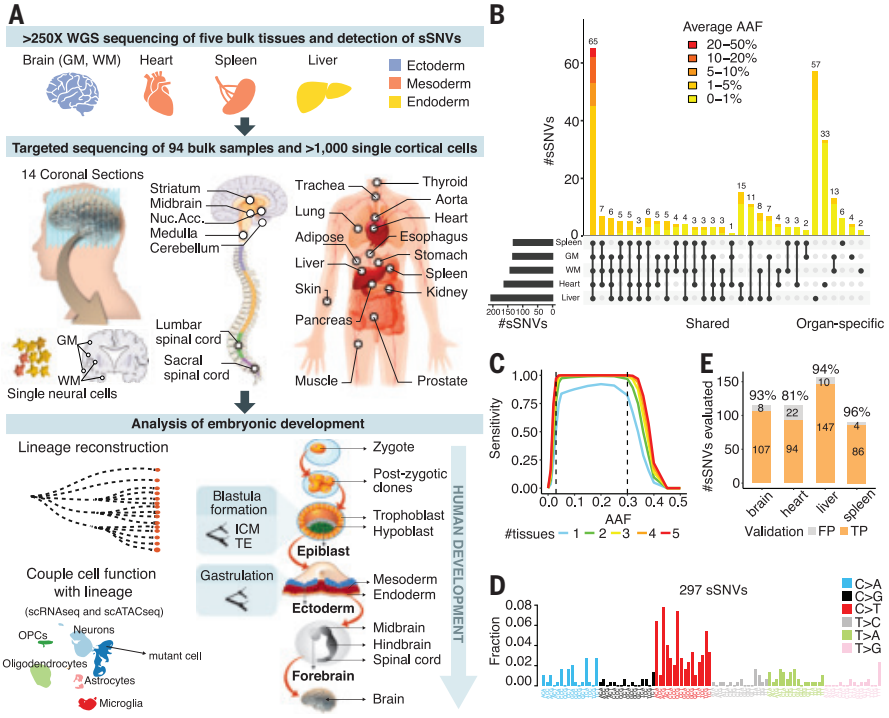

Fig. 1. Mosaic events of human development. (**A**) Schematic of the workflow for individual UMB1465. (**B**) Number and AAF of sSNVs detected across samples from individual UMB1465. (**C**) Sensitivity of MosaicForecast in detecting sSNVs from five 250× WGS data. (**D**) Trinucleotide context profile of the identified sSNVs. (**E**) Numbers of true-positive (TP) and false-positive (FP) sSNVs present in the WGS data validated by deep-amplicon sequencing.

[1]Division of Genetics and Genomics, Manton Center for Orphan Disease Research, Department of Pediatrics, and Howard Hughes Medical Institute, Boston Children's Hospital, Boston, MA 02115, USA. [2]Departments of Pediatrics and Neurology, Harvard Medical School, Boston, MA 02115, USA. [3]Broad Institute of MIT and Harvard, Cambridge, MA 02142, USA. [4]Department of Biomedical Informatics, Harvard Medical School, Boston, MA 02115, USA. [5]PhD Program in Biological and Biomedical Sciences, Harvard University, Boston, MA 02115, USA. [6]Department of Health Sciences Research, Center for Individualized Medicine, Mayo Clinic, Rochester, MN 55905, USA. [7]Division of Genetics, Brigham and Women's Hospital, Boston, MA 02115, USA.
*These authors contributed equally to this work. †NIMH Brain Somatic Mosaicism Network members and affiliations are listed in the supplementary materials.
‡Corresponding author. Email: christopher.walsh@childrens.harvard.edu (C.A.W.); peter_park@hms.harvard.edu (P.J.P.)

table S1) reidentified most sSNVs (>93%) when the same biopsy used for WGS was profiled (table S1); it identified slightly fewer when distinct tissue biopsies were profiled (81%), and, overall, 196 of 229 (86%) of targeted variants were validated (Fig. 1E, fig. S1F, and table S4).

Single-cell WGS data of 20 single neurons (*6*, *7*) from UMB1465 resolved 82 of 297 sSNVs into branching clades or clones, producing a lineage tree that spans early postzygotic cell generations and traces the origin of each mutation back to the embryo (Fig. 2A, fig. S2A, and tables S2 and S5). As expected, earlier sSNVs showed higher mosaic fractions (MFs), which are the fractions of cells carrying the variant, defined as 2×bulk AAF for autosomal SNV, with the MFs from daughter clades summing to that of the mother clone. Similar patterns of early lineage were also identified in the two additional individuals based on bulk WGS and single-cell (*7*, *11*) analysis (Fig. 2, B and C; fig. S2, B and C; and table S5). In UMB1465, we identified the first eight postzygotic progenitors corresponding to the third-cell generation (c1 to c8, with c5 to c6 not fully resolved and annotated as a second-generation clone), with the MFs of c1 to c8 summing to ≈100%, suggesting that all major early lineages were captured; we then traced their relative contributions to each organ (Fig. 2D and fig. S2D) (*8*). Contributions of c1 to c8 were highly unequal across organs, with c4 undetected in heart and spleen, and c3 and c8 together contributed >50% of the cellular content (Fig. 2D).

Changes in MFs across cell generations suggest highly asymmetrical segregation of the earliest progenitors between embryonic and extraembryonic tissues and in the several germ layers within the embryo. Instead of the expected twofold reduction of MFs with cell division, observed MFs for one branch (c8) barely decreased (30, 26, and 24%; $P < 10^{-6}$, $P < 10^{-22}$, and $P < 10^{-56}$, respectively; two-tailed binomial test); deviations from twofold reduction were also observed in other branches (Fig. 2, A and E, and fig. S2A) and in the two additional individuals (Fig. 2, B and C, and fig. S2, B and C). This pattern suggests unequal clonal partitioning during blastula formation, when extraembryonic tissues separate from embryonic tissue lineages (Fig. 1A). The observed MF asymmetries indicate that lineage segregation in human embryo might happen as early as the two-cell stage, as suggested in the mouse (*12*–*14*). To further test this hypothesis, we analyzed published (*11*) bulk WGS data (250×)

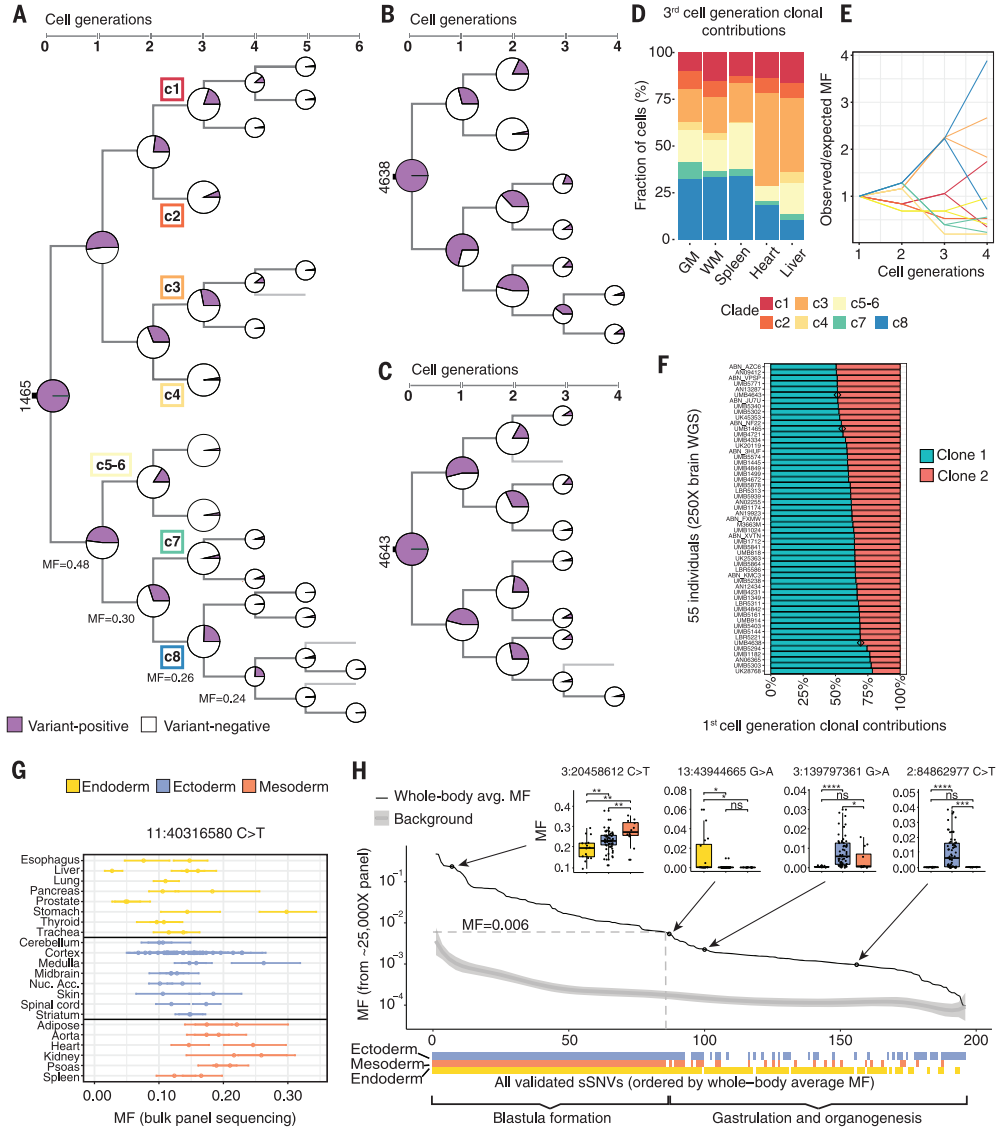

Fig. 2. Asymmetric contribution of early embryonic clones to the human body. (**A** to **C**) Phylogenetic trees of individuals UMB1465 (A), UMB4638 (B), and UMB4643 (C). The cell-generation numbers for later sSNVs (fifth and sixth) are likely to be underestimates because of the limited number of cells used for lineage reconstruction and the reduced power of detecting very-low-MF sSNVs. (**D**) Third-cell-generation clones (c1 to c8) of UMB1465 showing unequal contributions to specific organs ($P < 10^{-15}$, chi-square test), with the fraction of cells in each tissue contributed by clones c1 to c8 normalized by summing to 100% (see fig. S2D for non-normalized values). (**E**) Observed whole-body MFs for sSNVs from clades c1 to c8 across the two- to four-cell generations strongly deviate from expected values based on a symmetrical model of development. The 95% confidence intervals (95% CIs) calculated with binomial sampling are reported in table S2. (**F**) First-cell-generation clonal contributions are asymmetric and variable across 55 individuals ($P < 10^{-13}$, Kolmogorov-Smirnov test for the null hypothesis of symmetry). Individuals UMB1465, UMB4638, and UMB4643 are marked with diamond symbols. (**G**) High intra-organ fluctuation of MFs for early-embryonic mosaic variants illustrated for chr11:40316580 C>T. (**H**) sSNVs restricted to one or two germ layers mark the beginning of gastrulation. A total of 196 validated sSNVs are ordered "chronologically" by their whole-body MFs (*8*). MFs in different germ layers are compared in four examples (two-tailed Wilcoxon rank sum test; ns, nonsignificant; *$P \le 0.05$; **$P \le 0.01$; ***$P \le 0.001$; ****$P \le 0.0001$).

from 74 individuals. Our maximum likelihood estimates (*8*) indicate overall asymmetric contributions of the first-cell-generation clones to the human body with strong interindividual variability, from a 50:50 symmetry in some individuals to a 20:80 asymmetry and potentially higher (Fig. 2F and table S6).

MFs of 196 sSNVs across 94 biopsies from 17 different organs (table S1) from UMB1465 also revealed asymmetric contributions of early lineages to embryonic germ layers during gastrulation (Fig. 1A; fig. S3, A to C; and table S4) (*8*). The relative contributions of several clades to organs of endoderm, ectoderm, and mesoderm varied up to several fold (fig. S3, B and C). Furthermore, multiple biopsies from the same organ showed noticeable intra-organ MF differences (Fig. 2G and fig. S3D). For example, MFs for sSNV chr11:40316580 (C>T) ranged from 5 to 26% across cerebral cortex samples, suggesting highly variable local clonal amplification in all tissues (Fig. 2G).

The tissue distribution of sSNVs identified the effective progenitor pool size at the onset of gastrulation. sSNVs with higher MFs were found in all organs and germ layers (*8*) (Fig. 2H, fig. S3E, and tables S4 and S7), but as MFs decreased past ~0.6%, many sSNVs became undetectable in one or two germ layers (Fig. 2H, fig. S3E, and table S7), reflecting lineage divergence during gastrulation. The effective cell number at the time of mutation occurrence can be inferred as ~1/MF; therefore, 0.6% MF corresponds to ~170 epiblast cells. Despite the asymmetries of clonal contributions to various tissues, multiple germ layer–restricted variants gave similar estimates (Fig. 2H), and our in vivo estimates are consistent with counts from cultured human embryos (*15*).

The earliest brain-specific sSNVs provide similar estimates for the number of brain founder cells. Fourteen sSNVs were present in at least one of 64 central nervous system (CNS) samples but not in 30 non-CNS samples (Fig. 3A and tables S1 and S8), with 10 sSNVs showing significantly higher MFs in the forebrain than in other CNS regions [Fig. 3A and table S8, e.g. $P \leq 0.0001$ for variant chr17:53347250 (A>G)]. The earliest-occurring sSNVs were confirmed from analysis of 1228 single cortical cells [88% were from PFC section 2, so forebrain MFs estimated from single cells may be biased (*8*); table S9], of which 791 were successfully placed in a lineage tree (Fig. 3B, figs. S4 and S5, and table S9), with the neuronal and non-neuronal cells differentially distributed across the clades. The two earliest sSNVs showed wider presence in single cells (Fig. 3C and fig. S5) and a higher overall bulk MF (~2.2%) than other CNS-specific mutations from the same c8 branch (Fig. 3A). We also examined CNS-specific sSNVs with the highest bulk MF (~1%) in clade c1 (Fig. 3, A and D, and fig. S5). These early variants showed wide distribution across the forebrain (fig. S6, A and B) at relatively high MFs (table S8), but were undetectable in most other samples. These variants therefore serve as markers of the first forebrain progenitors and, based on their average bulk MFs, the number of forebrain founder cells is estimated to be ~50 to 100 of an estimated 600 to 1300 epiblasts (Fig. 3E and fig. S6C).

Analysis of sSNVs in 47 DNA samples spanning the rostrocaudal extent of the cerebral cortex (Fig. 1A and table S1) confirmed previous descriptions of widespread clonal distribution at low MFs (*6*, *16*), and suggested broadly definable topographic variation between the frontal (sections 1 to 7) and posterior cortex (sections 8 to 14) (*8*) (Fig. 4A and table S8). Early (first- to fourth-cell-generation) sSNVs were found in all rostrocaudal sections

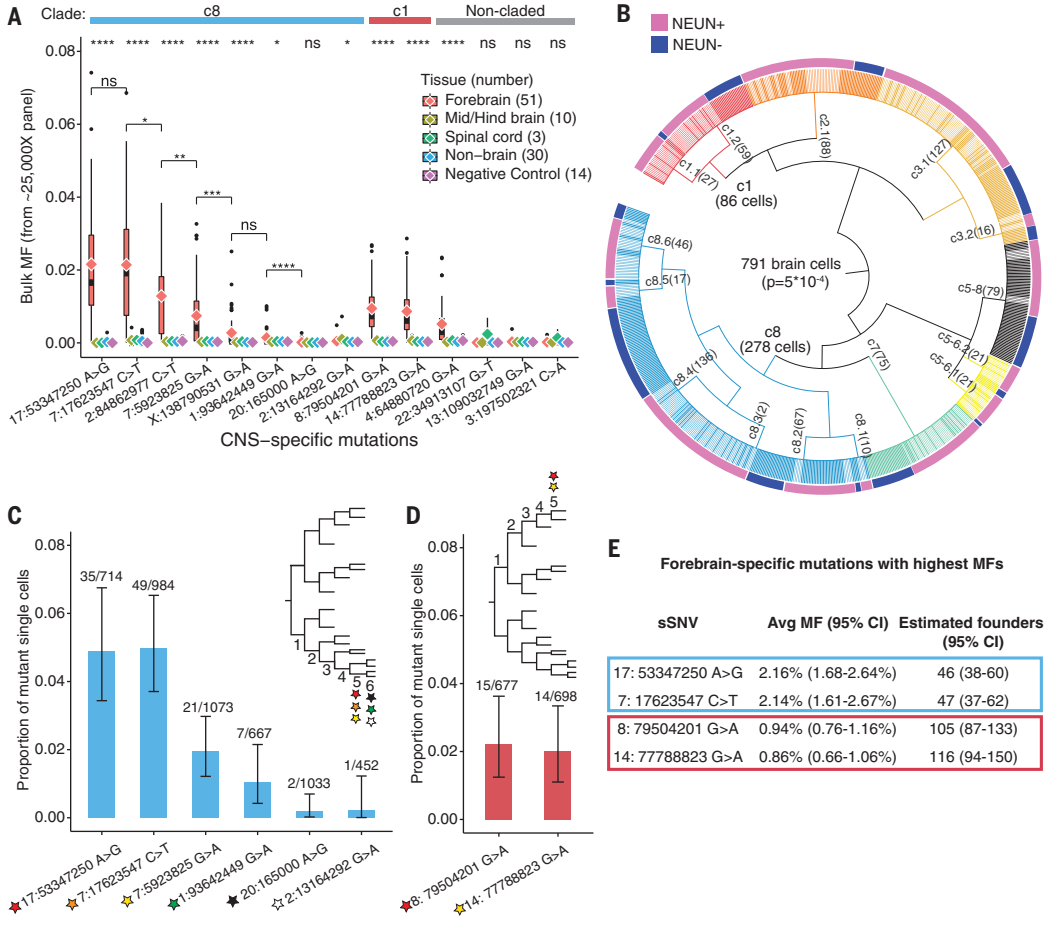

E Forebrain-specific mutations with highest MFs

sSNV	Avg MF (95% CI)	Estimated founders (95% CI)
17: 53347250 A>G	2.16% (1.68-2.64%)	46 (38-60)
7: 17623547 C>T	2.14% (1.61-2.67%)	47 (37-62)
8: 79504201 G>A	0.94% (0.76-1.16%)	105 (87-133)
14: 77788823 G>A	0.86% (0.66-1.06%)	116 (94-150)

Fig. 3. Brain-specific sSNVs estimate the number of forebrain founder cells. (**A**) MFs of 14 CNS-restricted sSNVs showing significant enrichment of some variants in forebrain-derived samples (two-tailed Wilcoxon rank sum test; significance levels are shown at the top). c8 and c1 (Fig. 2A) and noncladed variants are indicated. chr17:53347250 A>G and chr7:17623547 C>T are the earliest brain-specific sSNVs in c8, based on average forebrain MFs (diamond symbols). The forebrain MFs between sSNVs were compared with the estimate of the likelihood that they arose at the same generation (two-tailed Wilcoxon rank sum test). (**B**) A total of 791 single cells (of 1228) were successfully assigned to lineage clades upon targeted sequencing of 37 sSNVs (*8*). $NEUN^+$ and $NEUN^-$ cells are differentially distributed across clades (two-tailed Fisher's exact test). (**C**) chr17:53347250 A>G and chr7:17623547 C>T were confirmed as the earliest lineage markers within c8 by single-cell genotyping (shown are the number of mutant cells over the number of cells with >10× coverage at the position). (**D**) Same as (C) but for c1. (**E**) Estimates of forebrain founder cells based on average MFs (25,000× sequencing).

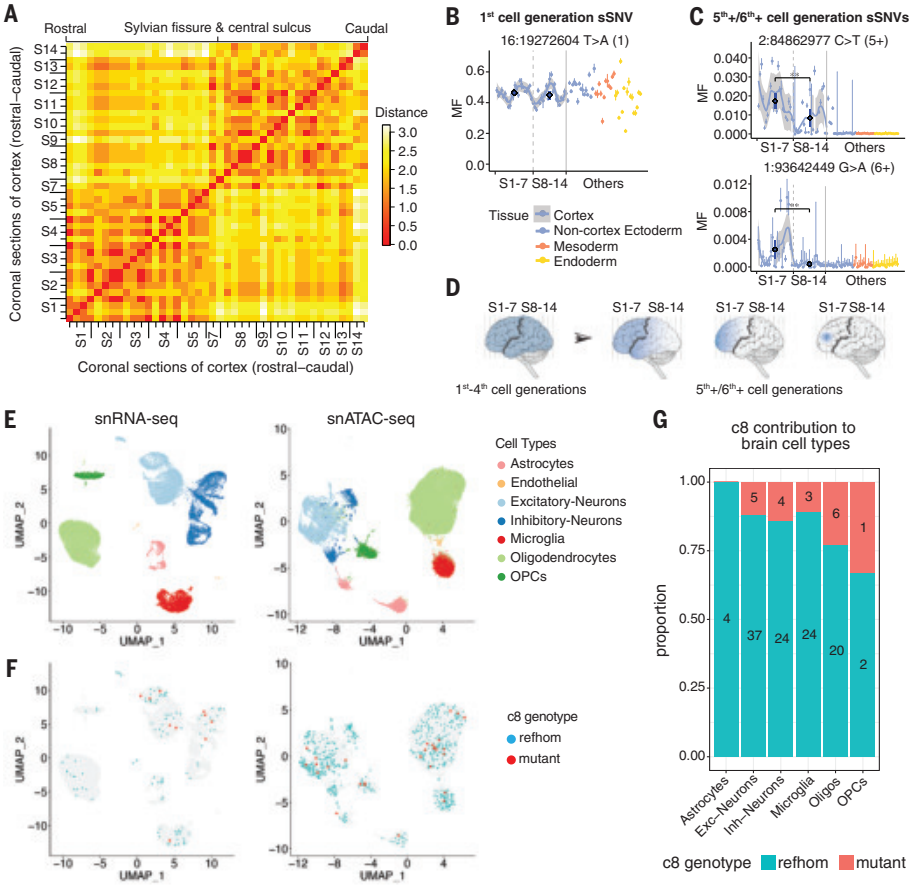

Fig. 4. Topographic patterns and function of embryonic clones in the rostrocaudal cerebral cortex. (**A**) Frontal regions (sections 1 to 7) and posterior regions (sections 8 to 14) form two broadly definable lineage clusters. Euclidian distances were computed based on the presence (score = 1) or absence (score = 0) of sSNVs. (*8*). (**B**) Earlier clones from the first- to the fourth-cell generations contribute to all rostrocaudal sections, as illustrated by an sSNV from the first-cell generation (fig. S6A). The AAFs across sequential sections of cortex are shown with a confidence band. The average MFs (dark blue) in the two regions are compared using a Wilcoxon rank sum test. (**C**) Fifth- and sixth-(or later)cell-generation clones from the lineage tree showing restriction in the frontal cortex regions (fig. S6B). (**D**) Successive subclones from the first- to the sixth-(or later)cell generations showing progressive restriction to frontal cortical areas separated by Sylvian fissure and central sulcus (black line). (**E**) Clusters of major brain cell types identified by PFC snRNA-seq and snATAC-seq. (**F**) Distribution of reference homozygous ("refhom") and mutant cells for clade c8 markers with >0 coverage across cell types. (**G**) Proportions of refhom cells and mutant cells for fourth-cell-generation clade c8 markers across brain cell types. P = 0.58, Fisher's exact test (see also table S10).

(*8*) (Fig. 4B and fig. S6, A and B), although their widely varying mosaic fractions highlighted unexpectedly large local nonuniformities in clonal amplification (Fig. 4B and fig. S6, A and B). Later (fifth- and sixth-(or later)cell-generation) sSNVs showed progressive restriction to the frontal cortex (Fig. 4C and fig. S6, A and B) and finally the PFC, where they were discovered. Thus, whereas founder clones of the cortex show little topographic restriction for MFs of ~1% or higher, lower MF clones show evidence of broad differences in distribution from frontal to posterior regions, separated approximately by the Sylvian fissure and the central sulcus (Fig. 4D).

Single-nucleus RNA-seq (snRNA-seq) and single-nucleus assay for transposase-accessible chromatin sequencing (snATAC-seq) data reveal cell-type classification, but the clusters can also be linked to genotypes. Although limited by the per-cell coverage sparsity, snATAC-seq reads were more uniformly distributed across the genome compared with snRNA-seq reads (fig. S7A), suggesting that snATAC-seq may be better suited to detecting sSNVs genome wide (fig. S7). At the 297 sSNV positions, 5.6% of snRNA-seq cells (1933 of 34,325) and 12.8% of snATAC-seq cells (8356 of 65,199) obtained coverage over at least one of the 297 sSNV loci (table S10). To link cell lineage information with cell types, we classified all ~100,000 cells into seven groups (Fig. 4E and figs. S8 and S9) (*8*, *17*) and checked cells with at least one lineage marker from fig. S2A (Fig. 4F; fig. S7, B to F; and table S10). The sparse coverage of late-occurring variants generally prevents observations of lineage divergence with this approach, although a few trends of c8 contributions to distinct cell types were seen (Fig. 4, E to G, and fig. S10). Our data point to the potential of newer methods for combining analysis of DNA and RNA (*18*, *19*) at high throughput to systematically analyze the formation of distinct cell types at scale in humans.

Our analysis shows that hundreds of sSNVs occurring over several postzygotic cell divisions mark the landmarks of embryonic human development and inform the patterns of clonal distribution within and between organs and tissues. Although analysis of peripheral blood DNA had suggested asymmetries in the contribution of early postzygotic clones to embryonic tissues (*5*), we show here sequential asymmetries and variabilities in clonal proliferation at later steps during gastrulation and organogenesis. The high intra-organ fluctuation of MFs (Fig. 2G and fig. S3D) highlights a stochastic clonal pattern within and across all tissues examined.

We found that clones generated by brain-specific progenitors have average MFs <2.2% across the cortex, underscoring the need for single-cell sequencing for their identification. Regional restrictions of sSNVs to the frontal lobe are seen at even lower MFs (≤0.6%). The observed dispersion of founder clones is consistent with previous estimates (*19*) that a given zone of the human cerebral cortex is formed from ~10 progenitors specified to form excitatory neurons that intermingle widely over a broad region of the cortex (*6*, *16*, *19*). Given the growing list of conditions associated with somatic mutations (*20*, *21*), a deeper understanding of the patterns of cell lineage described here coupled with functional information will help to elucidate the origin and consequence of mosaicism in these diseases.

REFERENCES AND NOTES

1. R. Kalhor *et al.*, *Science* **361**, eaat9804 (2018).
2. X. Han *et al.*, *Nature* **581**, 303–309 (2020).
3. R. E. Rodin *et al.*, *Nat. Neurosci.* **24**, 176–185 (2021).
4. Y. Dou *et al.*, *Nat. Biotechnol.* **38**, 314–319 (2020).
5. Y. S. Ju *et al.*, *Nature* **543**, 714–718 (2017).
6. M. A. Lodato *et al.*, *Science* **350**, 94–98 (2015).
7. M. A. Lodato *et al.*, *Science* **359**, 555–559 (2018).
8. Materials and methods are available as supplementary materials.
9. J. G. Tate *et al.*, *Nucleic Acids Res.* **47** (D1), D941–D947 (2019).
10. R. R. Zhang *et al.*, *Stem Cell Res. Ther.* **9**, 29 (2018).
11. R. E. Rodin *et al.*, The landscape of mutational mosaicism in autistic and normal human cerebral cortex. *bioRxiv*, 2020.2002.2011.944413 (2020).
12. A. Hupalowska *et al.*, *Cell* **175**, 1902–1916.e13 (2018).
13. M. D. White *et al.*, *Cell* **165**, 75–87 (2016).
14. K. Piotrowska, M. Zernicka-Goetz, *Nature* **409**, 517–521 (2001).
15. L. Xiang *et al.*, *Nature* **577**, 537–542 (2020).
16. G. D. Evrony *et al.*, *Neuron* **85**, 49–59 (2015).
17. T. Stuart *et al.*, *Cell* **177**, 1888–1902.e21 (2019).
18. A. S. Nam *et al.*, *Nature* **571**, 355–360 (2019).
19. A. Y. Huang *et al.*, *Proc. Natl. Acad. Sci. U.S.A.* **117**, 13886–13895 (2020).

20. H. Y. Koh, J. H. Lee, *Mol. Cells* **41**, 881–888 (2018).
21. S. Baldassari *et al.*, *Acta Neuropathol.* **138**, 885–900 (2019).
22. S. Bizzotto *et al.*, Landmarks of human embryonic development inscribed in somatic mutations, NIMH Data Archive (2021); https://doi.org/10.15154/1503337.

ACKNOWLEDGMENTS

We thank R. S. Hill, J. E. Neil, D. Gonzalez, S. Yip, and M. Chin for assistance; S. R. Ehmsen for help with graphics; H. Gold, E. Maury, and T. Shin for help with data analysis; A. Y. Huang and P. Li for sharing their snRNA-seq data; Walsh and Park laboratory members, especially R. E. Andersen, C. M. Dias, M. B. Miller, and V. V. Viswanadham, for discussions; the Boston Children's Hospital Flow Cytometry Core and IDDRC Molecular Genetics Core; the Biopolymers Facility and Research Computing at HMS; and the donors and their families for human tissues obtained from the NIH NeuroBioBank at the University of Maryland. **Funding:** This work was supported by National Institute of Mental Health (NIMH Brain Somatic Mosaicism Network grant U01MH106883 to C.A.W. and P.J.P.); NINDS (grant R01NS032457 to C.A.W. and P.J.P.); and the Allen Discovery Center program, a Paul G. Allen Frontiers Group advised program of the Paul G. Allen Family Foundation. Boston Children's Hospital Intellectual and Developmental Disabilities Research Center is funded by NIH grant U54HD090255. S.B. was supported by the Manton Center for Orphan Disease Research at Boston Children's Hospital. J.G. was supported by a Basic Research Fellowship from the American Brain Tumor Association (BRF1900016) and by Brain SPORE grant P50CA165952. S.N.K. is a Stuart H.Q. & Victoria Quan fellow at Harvard Medical School. C.A.W. is an investigator of the Howard Hughes Medical Institute. **Author contributions:** S.B., Y.D., and J.G. conceived the study. S.B. and J.G. performed the experiments. Y.D. led bioinformatics analysis and performed WGS and amplicon-sequencing data analysis. S.B. and Y.D. performed snRNA-seq and snATAC-seq data analyses. R.N.D. designed the targeted-sequencing protocol and contributed to analysis. M.K., C.L.B., T.B., and A.A. contributed to variant analysis. S.N.K. contributed additional brain WGS data. S.B. and Y.D. wrote the manuscript, greatly helped by J.G. C.A.W. and P.J.P. directed the research. **Competing interests:** The authors declare no competing interests. **Data and materials availability:** All genomic data are available from dbGaP under accession number phs001485.v2.p1 and from the NIMH Data Archive (*22*). Other materials are available from the authors upon reasonable request.

SUPPLEMENTARY MATERIALS

science.sciencemag.org/content/371/6535/1249/suppl/DC1
Materials and Methods
Supplementary Text
Figs. S1 to S10
References (*23*–*42*)
Tables S1 to S10
MDAR Reproducibility Checklist

10 August 2020; accepted 9 February 2021
10.1126/science.abe1544

PALEONTOLOGY

Manta-like planktivorous sharks in Late Cretaceous oceans

Romain Vullo[1]*, Eberhard Frey[2], Christina Ifrim[3], Margarito A. González González[4], Eva S. Stinnesbeck[5], Wolfgang Stinnesbeck[6]

The ecomorphological diversity of extinct elasmobranchs is incompletely known. Here, we describe *Aquilolamna milarcae*, a bizarre probable planktivorous shark from early Late Cretaceous open marine deposits in Mexico. *Aquilolamna*, tentatively assigned to Lamniformes, is characterized by hypertrophied, slender pectoral fins. This previously unknown body plan represents an unexpected evolutionary experimentation with underwater flight among sharks, more than 30 million years before the rise of manta and devil rays (Mobulidae), and shows that winglike pectoral fins have evolved independently in two distantly related clades of filter-feeding elasmobranchs. This newly described group of highly specialized long-winged sharks (Aquilolamnidae) displays an aquilopelagic-like ecomorphotype and may have occupied, in late Mesozoic seas, the ecological niche filled by mobulids and other batoids after the Cretaceous–Paleogene boundary.

Elasmobranchs—the group of cartilaginous fishes including sharks, skates, and rays—are a successful group of ecomorphologically diverse cartilaginous fishes that first appeared around 380 million years ago, during the Late Devonian period (*1*). Modern plankton-feeding elasmobranchs are represented by two main ecomorphotypes corresponding, on one hand, to the whale shark (Rhincodontidae), the basking shark (Cetorhinidae) and the megamouth shark (Megachasmidae) (i.e., a macroceanic-tachypelagic morphotype characterized by a large fusiform body) and, on the other hand, to manta and devil rays (Mobulidae) (i.e., an aquilopelagic morphotype characterized by a dorsoventrally flattened body and winglike pectoral fins with a narrowly angular shape) (*1*–*3*). Whereas the former ecomorphotype convergently evolved during the Mesozoic in giant pachycormid bony fishes (*4*), the latter ecomorphotype has not been identified so far in the pre-Cenozoic fossil record (*3*, *5*, *6*). We report here a new, bizarre fossil shark showing a previously unknown bauplan and morphological features indicative of filter-feeding habits. This complete specimen from the early Late Cretaceous (Turonian) of Mexico offers important insights into the Mesozoic evolution of medium- to large-sized planktivorous fishes and the rise of "winged" pelagic elasmobranchs, long before the Paleogene origin and opportunistic radiation of mobulid rays (*4*–*6*).

Aquilolamna milarcae gen. et sp. nov. (formal taxonomic description is provided in the supplementary materials; Figs. 1 and 2 and figs. S3 to S6) stands out among both living and fossil elasmobranchs, with a body plan characterized by the acquisition of unusually hypertrophied pectoral fins combined with the persistence of a powerful tail showing a well-developed caudal fin (mosaic evolution). Among selachimorphs (modern sharks), narrow, distally expanded bladelike pectoral fins are known in various macroceanic sharks (*1*, *7*), but these predatory (e.g., *Isurus paucus* and *Carcharhinus longimanus*) or planktivorous (e.g., *Megachasma pelagios*) forms are less specialized than *Aquilolamna*. Another notable feature of *Aquilolamna* is its apparent lack of dorsal and pelvic fins, although a taphonomic cause cannot be ruled out. Among neoselachians (modern elasmobranchs), dorsal fins are absent in the enigmatic Early Jurassic eel-shaped shark *Ostenoselache* (*8*) as well as in various rajiform and myliobatiform rays (*9*, *10*). The assumed dorsal fin secondary loss (or reduction) in *Aquilolamna* could be interpreted as a direct consequence of the acquisition of hypertrophied pectoral fins. In contrast, pelvic fins were lost only in a few extinct chondrichthyan taxa, including eugeneodontiforms (*10*) and possibly *Squatinactis*, a small-sized Paleozoic cladodont shark with enlarged pectoral fins (*11*).

Aquilolamna is tentatively assigned to Lamniformes (mackerel sharks) on the basis of features such as the radial asterospondylic-type vertebrae (*12*) and the caudal fin skeleton showing a high hypochordal ray angle (i.e., ventrally directed hypochordal rays) (*13*). The discovery of *Aquilolamna* provides further insight into the Late Cretaceous diversification of neoselachians (*14*, *15*) and likely represents another example of the ecomorphological plasticity and disparity of lamniform sharks, a group that appeared during the Early Cretaceous and today comprises mainly highly autapomorphic taxa that share relatively few synapomorphies (*16*–*18*). Living lamniforms show an impressive variety of morphologies, habitats, behaviors, and diets, with forms ranging from filter-feeders (Cetorhinidae and

[1]Univ Rennes, CNRS, Géosciences Rennes, UMR 6118, Rennes, France. [2]Staatliches Museum für Naturkunde Karlsruhe, Karlsruhe, Germany. [3]SNSB–Jura-Museum, Willibaldsburg, Eichstätt, Germany. [4]Indepedent Researcher, Sabinas Hidalgo, Nuevo León, Mexico. [5]Steinmann-Institut für Geologie, Mineralogie und Paläontologie, Rheinische Friedrich-Wilhelms-Universität, Bonn, Germany. [6]Institute für Geowissenschaften, Ruprecht-Karls-Universität, Heidelberg, Germany.
***Corresponding author. Email: romain.vullo@univ-rennes1.fr**

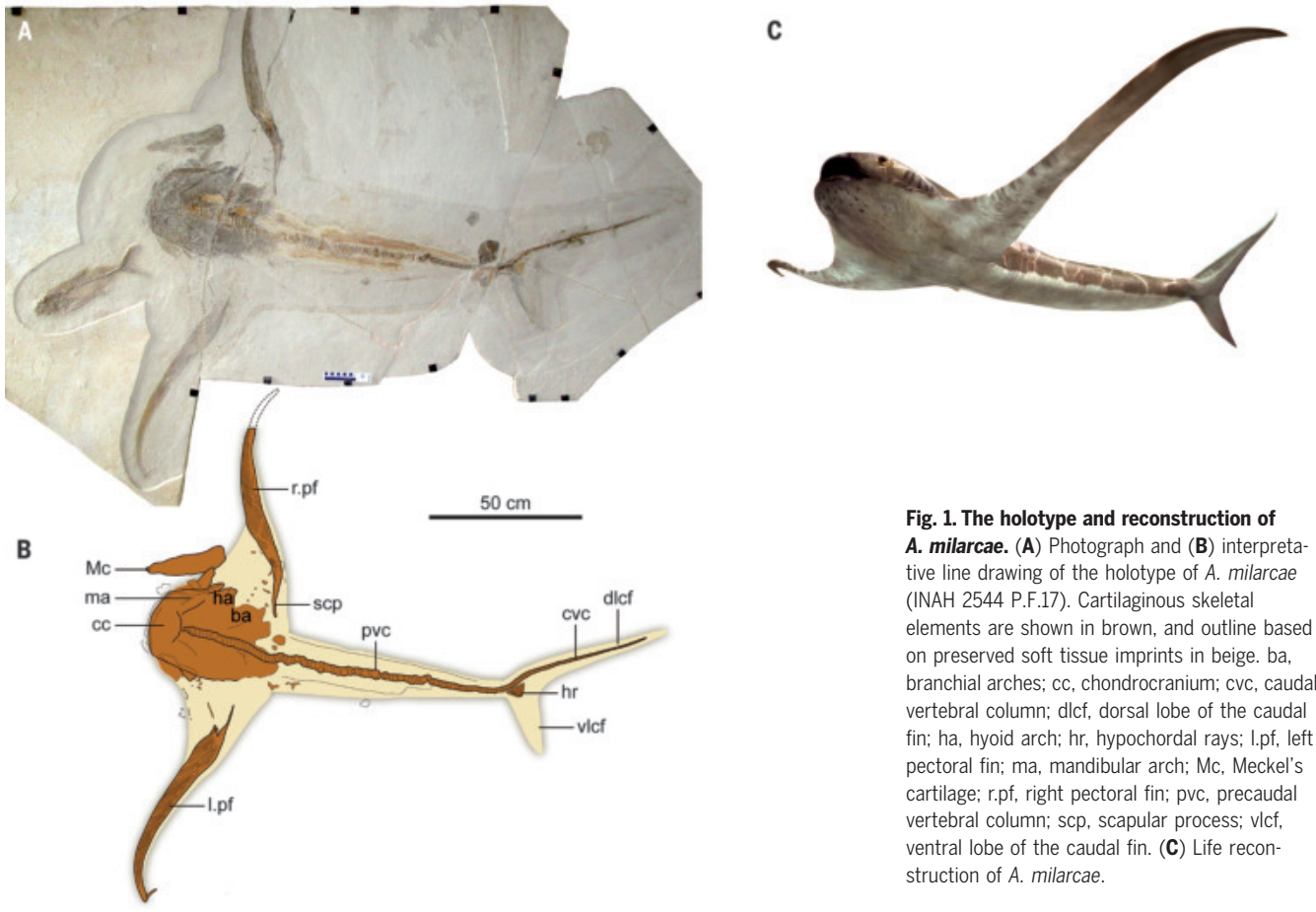

Fig. 1. The holotype and reconstruction of *A. milarcae*. (**A**) Photograph and (**B**) interpretative line drawing of the holotype of *A. milarcae* (INAH 2544 P.F.17). Cartilaginous skeletal elements are shown in brown, and outline based on preserved soft tissue imprints in beige. ba, branchial arches; cc, chondrocranium; cvc, caudal vertebral column; dlcf, dorsal lobe of the caudal fin; ha, hyoid arch; hr, hypochordal rays; l.pf, left pectoral fin; ma, mandibular arch; Mc, Meckel's cartilage; r.pf, right pectoral fin; pvc, precaudal vertebral column; scp, scapular process; vlcf, ventral lobe of the caudal fin. (**C**) Life reconstruction of *A. milarcae*.

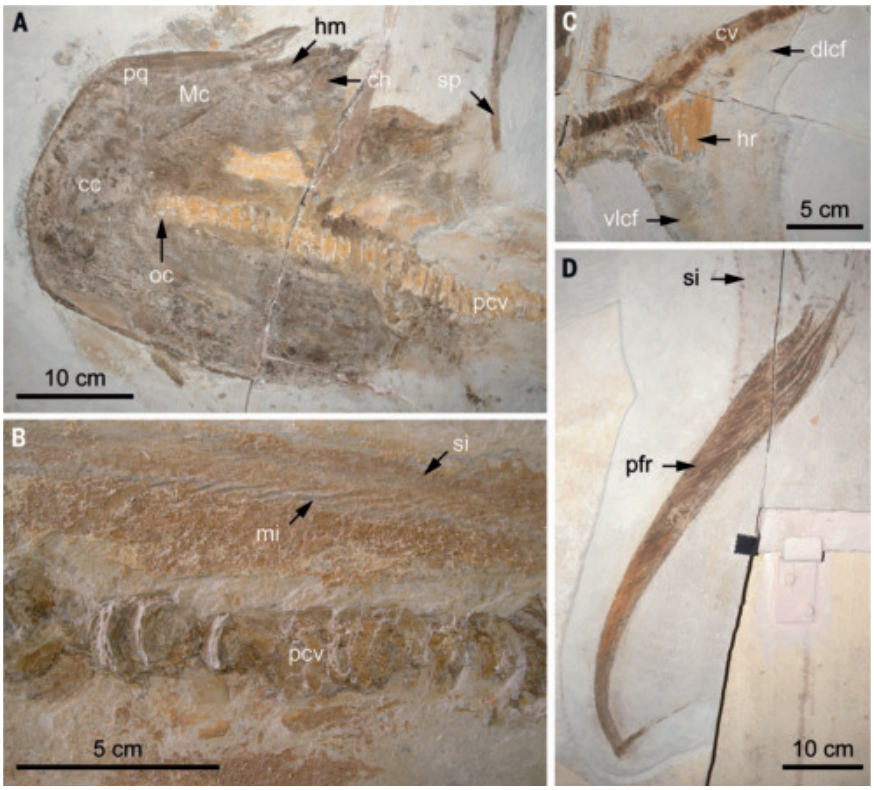

Fig. 2. Anatomical details of *A. milarcae*. (**A**) Cephalic region. (**B**) Trunk region. (**C**) Caudal region. (**D**) Left pectoral fin. ch, ceratohyal; cv, caudal vertebrae; hm, hyomandibula; mi, muscle imprint; oc, occipital centrum; pcv, precaudal vertebrae; pfr, pectoral fin radials; pq, palatoquadrate; si, skin imprint; sp, scapular process.

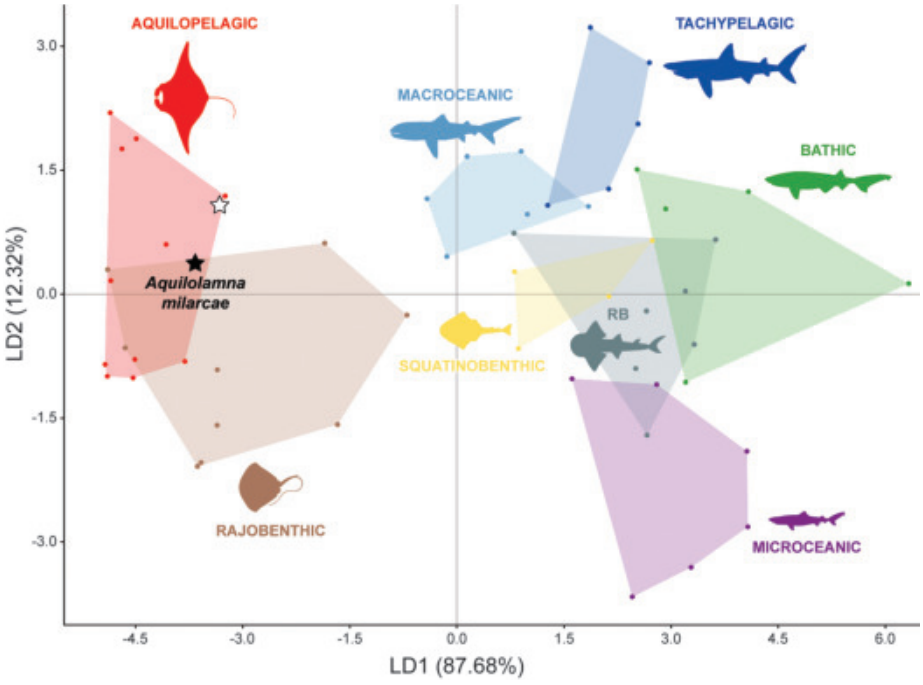

Fig. 3. Ecomorphotype of *A. milarcae*. Linear discriminant (LD) analysis based on log-transformed precaudal length (or disc length) and pectoral fin span (or disc width) measurements for 53 living elasmobranch species belonging to eight specialized ecomorphotypes, with *Aquilolamna milarcae* added. Note the position of *A. milarcae* (black star), clearly separated from other selachimorph taxa and suggesting an aquilopelagic-like ecomorphotype for this distinctive shark; this is confirmed when a 250-cm hypothetical maximum total length is used for *A. milarcae* (white star) (see supplementary materials). RB, rhinobenthic; light-blue silhouette, *Megachasma pelagios*; dark-blue silhouette, *Cetorhinus maximus*; green silhouette, *Hexanchus griseus*; purple silhouette, *Pseudocarcharias kamoharai*; yellow silhouette, *Squatina japonica*; gray silhouette, *Rhina ancylostoma*; red silhouette, *Mobula birostris*; brown silhouette, *Pteroplatytrygon violacea*.

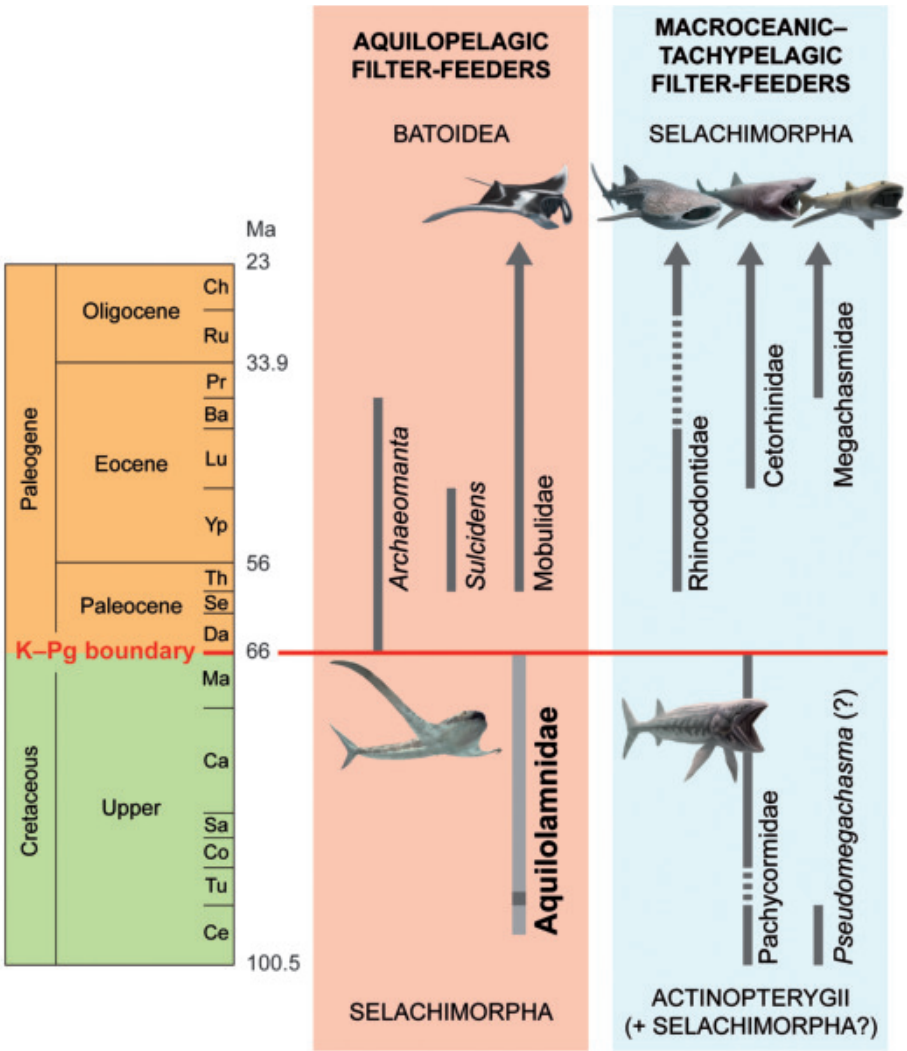

Fig. 4. Aquilopelagic and macroceanic–tachypelagic planktivorous fishes (Neoselachii and Actinopterygii) before and after the Cretaceous–Paleogene boundary. The stratigraphic distribution (Cenomanian–Maastrichtian) of Aquilolamnidae is based on *Aquilolamna* (dark gray) and known occurrences of the enigmatic genera *Cretomanta* and *Platylithophycus* (light gray), two other possible members of the family; arrowed lineages represent still-living groups. Ba, Bartonian; Ca, Campanian; Ce, Cenomanian; Ch, Chattian; Co, Coniacian; Da, Danian; Lu, Lutetian; Ma, Maastrichtian; Pr, Priabonian; Ru, Rupelian; Sa, Santonian; Se, Selandian; Th, Thanetian; Tu, Turonian; Yp, Ypresian.

Megachasmidae) to top predators (Lamnidae) (*1*, *16*, *17*). Aquilolamnids would reinforce the view that lamniforms achieved high levels of ecomorphological disparity precociously in their evolutionary history, as early as the mid-Cretaceous (*15*, *18*, *19*).

The overall morphology and peculiar features of *Aquilolamna* (i.e., broad head with wide and near-terminal mouth, dentition most likely consisting of minute teeth, wing-shaped pectoral fins; see supplementary materials) strongly suggest that this shark was a suspension feeder, more closely related to the aquilopelagic than to the macroceanic–tachypelagic ecomorphotype category (Fig. 3 and figs. S10 and S11). *Aquilolamna* was probably a relatively slow swimmer, comparable to other suspension-feeding elasmobranchs (*20*). The long and slender pectoral fins of *Aquilolamna* most likely acted as stabilizers, but they may also have been used for propulsion by slow flapping movements. In addition, *Aquilolamna* had a typical, well-developed heterocercal caudal fin, similar to that of most macroceanic sharks (e.g., *Megachasma*) (*1*). Therefore, *Aquilolamna* probably used a combination of axial-based undulation and pectoral-fin-based oscillation for its locomotion, with main thrust generated by the caudal fin and pectoral fins activated for increasing speed and for maneuvering. This contrasts with the strict pectoral fin-based locomotion of modern suspension-feeding aquilopelagic forms (i.e., mobulids), which are characterized by powerful enlarged pectoral fins (broad-based "wings" used for propulsion by oscillation) and a whip-like tail (*21*, *22*). Among neoselachians, the combination of axial and pectoral locomotion is known only in guitarfishes (Rhinopristiformes) and some electric rays (Torpediniformes) (*21*, *22*); however, these batoids are undulatory appendage propulsors (*21*, *22*), unlike *Aquilolamna*.

The skeleton-based genus *Aquilolamna* may correspond to the enigmatic tooth-based genus *Cretomanta* (fig. S9), known from the Late Cretaceous (Cenomanian–Maastrichtian) of North America and North Africa (*6*). *Cretomanta* is especially common in the Eagle Ford Group of Texas (*23*), a lateral equivalent of the Agua Nueva Formation that yielded the holotype of *A. milarcae* (figs. S1 and S9). *Cretomanta* is characterized by simple, minute hooked teeth (less than 2 mm high) that are indicative of planktivory, like teeth of manta rays and whale and basking sharks. *Cretomanta* was originally described as an early member of Mobulidae (*24*) and subsequently regarded as a possible planktivorous lamniform shark (*19*, *25*). The microstructure of *Cretomanta* teeth, characterized by the presence of parallel-bundled and tangled-bundled enameloid layers typical of selachimorphs, strongly favors the latter hypothesis (*26*). The interpretation of *Cretomanta* as a suspension-feeding lamniform is consistent with the taxonomic and trophic positions proposed here for *Aquilolamna*. Therefore, we tentatively assign the genus *Cretomanta* to Aquilolamnidae. *Platylithophycus* from the Niobrara Chalk (*27*) is another mysterious Late Cretaceous (Coniacian–Campanian) genus that might also belong to Aquilolamnidae. On the basis of a single incomplete specimen consisting of gill arches and associated cartilage fragments, *Platylithophycus* was recently recognized as a large, possible filter-feeding elasmobranch of uncertain affinities, characterized by the presence of gill rakers of unusual morphology (*27*). A third putative Late Cretaceous plankton-feeding shark is the tooth-based genus *Pseudomegachasma*, a lamniform restricted to the Cenomanian and interpreted as a specialized sand tiger shark (Odontaspididae) (*28*). Given its tooth morphology and systematic placement, it can be reasonably assumed that *Pseudomegachasma* had an *Odontaspis*-like or *Megachasma*-like general appearance, clearly distinct from that of *Aquilolamna*.

Late Cretaceous aquilolamnid sharks (*Aquilolamna* and possibly *Cretomanta* and *Platylithophycus*) and giant suspension-feeding pachycormid bony fishes (*Bonnerichthys* and *Rhinconichthys*) (*4*) may have been directly affected by the severe end-Cretaceous extinction of calcifying planktonic organisms resulting from an extreme acidification of surface oceans (*29*–*31*). Aquilolamnids and giant pachycormids all became extinct at the Cretaceous–Paleogene (K–Pg) event and were ecologically replaced during the early Paleogene (Paleocene) by pelagic planktivorous batoids (*Archaeomanta*, *Sulcidens*, and the stem mobulid *Burnhamia*) (*4*–*6*) and rhincodontid sharks (*Palaeorhincodon*) (*4*), respectively (Fig. 4). The discovery of aquilolamnids suggests that the guild of large filter-feeding fishes changed in composition but not in structure after the end-Cretaceous mass extinction event, with both aquilopelagic and macroceanic–tachypelagic convergent forms being represented in pre- and post-K–Pg open marine ecosystems.

REFERENCES AND NOTES

1. L. J. V. Compagno, *Environ. Biol. Fishes* **28**, 33–75 (1990).
2. L. J. V. Compagno, in *Sharks of the Open Ocean: Biology, Fisheries and Conservation*, M. D. Camhi, E. K. Pikitch, E. A. Babcock, Eds. (Blackwell, 2008), pp. 14–23.
3. C. Pimiento, J. L. Cantalapiedra, K. Shimada, D. J. Field, J. B. Smaers, *Evolution* **73**, 588–599 (2019).
4. M. Friedman *et al*., *Science* **327**, 990–993 (2010).
5. C. J. Underwood, M. A. Kolmann, D. J. Ward, *J. Vertebr. Paleontol.* **37**, e1293068 (2017).
6. S. Adnet, H. Cappetta, G. Guinot, G. Notarbartolo di Sciara, *Zool. J. Linn. Soc.* **166**, 132–159 (2012).
7. T. Tomita, S. Tanaka, K. Sato, K. Nakaya, *PLOS ONE* **9**, e86205 (2014).
8. C. J. Duffin, *Paleontologia Lombarda* **9**, 3–27 (1998).
9. L. J. V. Compagno, *Am. Zool.* **17**, 303–322 (1977).
10. O. Larouche, M. L. Zelditch, R. Cloutier, *BMC Biol.* **15**, 32 (2017).
11. R. Lund, R. Zangerl, *Ann. Carnegie Mus.* **45**, 43–55 (1974).
12. E. G. White, *Bull. Am. Mus. Nat. Hist.* **74**, 25–138 (1937).
13. S. H. Kim, K. Shimada, C. K. Rigsby, *Anat. Rec.* **296**, 433–442 (2013).
14. C. J. Underwood, *Paleobiology* **32**, 215–235 (2006).
15. G. Guinot, L. Cavin, *Biol. Rev. Camb. Philos. Soc.* **91**, 950–981 (2016).
16. L. J. V. Compagno, *NOAA Tech. Rep. NMFS* **90**, 357–379 (1990).
17. L. J. V. Compagno, *FAO Species Cat. Fish. Purp.* **1**, 1–269 (2001).
18. R. Vullo, G. Guinot, G. Barbe, *J. Syst. Palaeontol.* **14**, 1003–1024 (2016).
19. F. L. Condamine, J. Romieu, G. Guinot, *Proc. Natl. Acad. Sci. U.S.A.* **116**, 20584–20590 (2019).
20. D. W. Sims, *J. Exp. Mar. Biol. Ecol.* **249**, 65–76 (2000).
21. L. J. Rosenberger, *J. Exp. Biol.* **204**, 379–394 (2001).
22. C. A. D. Wilga, G. V. Lauder, in *Biology of Sharks and Their Relatives*, J. C. Carrier, J. A. Musick, M. R. Heithaus, Eds. (CRC Press, 2004), pp. 139–164.
23. B. J. Welton, R. F. Farish, *The Collector's Guide to Fossil Sharks and Rays from the Cretaceous of Texas* (Before Time, 1993).
24. G. R. Case, T. T. Tokaryk, D. Baird, *Can. J. Earth Sci.* **27**, 1084–1094 (1990).
25. A. Noubhani, H. Cappetta, *Palaeo Ichthyologica* **8**, 1–327 (1997).
26. S. Enault, H. Cappetta, S. Adnet, *Zool. J. Linn. Soc.* **169**, 144–155 (2013).
27. A. W. Bronson, J. G. Maisey, *J. Paleontol.* **92**, 743–750 (2018).
28. K. Shimada, E. V. Popov, M. Siversson, B. J. Welton, D. J. Long, *J. Vertebr. Paleontol.* **35**, e981335 (2015).
29. L. Alegret, E. Thomas, K. C. Lohmann, *Proc. Natl. Acad. Sci. U.S.A.* **109**, 728–732 (2012).
30. A. Tajika, A. Nützel, C. Klug, *PeerJ* **6**, e4219 (2018).
31. M. J. Henehan *et al*., *Proc. Natl. Acad. Sci. U.S.A.* **116**, 22500–22504 (2019).

ACKNOWLEDGMENTS

We are grateful to M. Fernández Garza, who made the specimen accessible for scientific research and supports our paleontological work at Vallecillo. We thank A. H. González González and J. M. Padilla Gutiérrez for logistic support and access to the Museo del Desierto collection in Saltillo; O. Sanisidro for the lifelike reconstruction of *A. milarcae*; T. Tomita for information on *Megachasma*; B. J. Welton for providing *Cretomanta* teeth; L. Joanny for SEM imaging; and three anonymous reviewers for their insightful comments on the manuscript. **Funding:** Financial support was provided by a scholarship of the DAAD (57381316 to E.S.S.) and by Géosciences Rennes, UMR CNRS 6118 (to R.V.). **Author contributions:** W.S. designed the Vallecillo research project. R.V. and W.S. designed the study. M.A.G.G. secured, collected, and prepared the specimen. R.V., E.F., E.S.S., and W.S. collected the data and participated in the observation and interpretation of the specimen. C.I. and W.S. provided information on the stratigraphic context, associated invertebrates, and age of the specimen. R.V., E.F., E.S.S., and W.S. photographed the specimen. R.V. prepared the figures and wrote the manuscript, with input from all authors. **Competing interests:** The authors declare no competing interests. **Data and materials availability:** All data are available in the main text and the supplementary materials; the holotype of *Aquilolamna milarcae* is housed and displayed in the Museo La Milarca in San Pedro Garza García (MMSP), Nuevo León State, Mexico, under Instituto Nacional de Antropología e Historia (INAH) registration number 2544 P.F.17. The teeth of *Cretomanta* are stored in the paleontological collection of the Geological Institute of the University of Rennes 1 (IGR), Rennes, France.

SUPPLEMENTARY MATERIALS

science.sciencemag.org/content/371/6535/1253/suppl/DC1
Materials and Methods
Supplementary Text
Figs. S1 to S11
Tables S1 to S6
References (*32*–*58*)
MDAR Reproducibility Checklist

8 April 2020; accepted 9 February 2021
10.1126/science.abc1490

CATALYSIS

Tandem In_2O_3-Pt/Al_2O_3 catalyst for coupling of propane dehydrogenation to selective H_2 combustion

Huan Yan[1], Kun He[2], Izabela A. Samek[3], Dian Jing[3], Macy G. Nanda[3], Peter C. Stair[1]*, Justin M. Notestein[3]*

Tandem catalysis couples multiple reactions and promises to improve chemical processing, but precise spatiotemporal control over reactive intermediates remains elusive. We used atomic layer deposition to grow In_2O_3 over Pt/Al_2O_3, and this nanostructure kinetically couples the domains through surface hydrogen atom transfer, resulting in propane dehydrogenation (PDH) to propylene by platinum, then selective hydrogen combustion by In_2O_3, without excessive hydrocarbon combustion. Other nanostructures, including platinum on In_2O_3 or platinum mixed with In_2O_3, favor propane combustion because they cannot organize the reactions sequentially. The net effect is rapid and stable oxidative dehydrogenation of propane at high per-pass yields exceeding the PDH equilibrium. Tandem catalysis using this nanoscale overcoating geometry is validated as an opportunity for highly selective catalytic performance in a grand challenge reaction.

Tandem and cooperative catalysis could revolutionize chemical production (*1*, *2*) by minimizing separations, coupling reactions to drive transformations forward, or controlling selectivity in reaction networks (*3*). Examples include single-site cascade or domino reactions (*4*–*6*), multisite systems with exchange of fluid-phase intermediates (*7*, *8*), and interfacial catalysis (*9*, *10*). Some complex biomolecular assemblies can pass reactive intermediates sequentially among catalyst sites (*11*), but heterogeneous catalysts generally do not have the precise positioning of different functions required to do this. In this work, a tandem catalyst was developed for selective catalytic dehydrogenation of propane to propylene. Propylene is an essential industrial intermediate with a gap between supply and anticipated demand (*12*). Nonoxidative propane dehydrogenation (PDH) is endothermic and equilibrium-limited, necessitating high temperatures to achieve commercially viable per-pass yields (*13*). Oxidative dehydrogenation of propane (ODHP) has been proposed to overcome equilibrium limitations and avoid thermal cracking but suffers from decreasing selectivity with increasing conversion, giving yields below the PDH equilibrium, in spite of decades of research (*12*, *14*). Similar issues face other grand-challenge, selective oxidations (*15*, *16*), especially in cases in which challenging olefin-parafin separation necessitates high per-pass yields. Process engineering concepts such as reactor cascades, membrane reactors, and chemical looping address some limitations through physical or temporal separation of dehydrogenation and combustion (*17*–*19*), but they can be challenging to implement.

We translated these macroscale engineering strategies into a single nanoscale tandem catalyst particle for ODHP-like propane to propylene. A known PDH catalyst, Pt/Al_2O_3, was interfaced with a known catalyst for selective H_2 combustion (SHC), In_2O_3 (*20*), by means of atomic layer deposition (ALD) of In_2O_3, denoted ***@In₂O₃***. We investigated three designs that changed the relative location of In_2O_3: (i) a physical mixture of Pt/Al_2O_3 + Al_2O_3***@In₂O₃***, (ii) Pt supported on Al_2O_3***@In₂O₃*** [Pt/(Al_2O_3***@In₂O₃***)]; and (iii) Pt/Al_2O_3 overcoated by a porous In_2O_3 film [(Pt/Al_2O_3) ***@XcIn₂O₃***; "Xc" indicates the number of ALD cycles] with extensive metal-oxide interface (Fig. 1). In this last catalyst design, the In_2O_3 overcoat is intended to be neither an inert shell (*21*, *22*) nor strong metal-support interaction (SMSI)–like, totally encapsulating the Pt (*23*, *24*). The propane conversion and propylene selectivity for the three designs are summarized in Fig. 2; full product distributions are found in figs. S1 and S2. Coking is minimal in all In_2O_3-containing catalysts, with >98.5% carbon balance. F_{tandem} is also reported, which we define as (1-H_2/C_3H_6) ×100%. Ideal PDH gives F_{tandem} = 0 (H_2/C_3H_6 = 1) (fig. S3), whereas

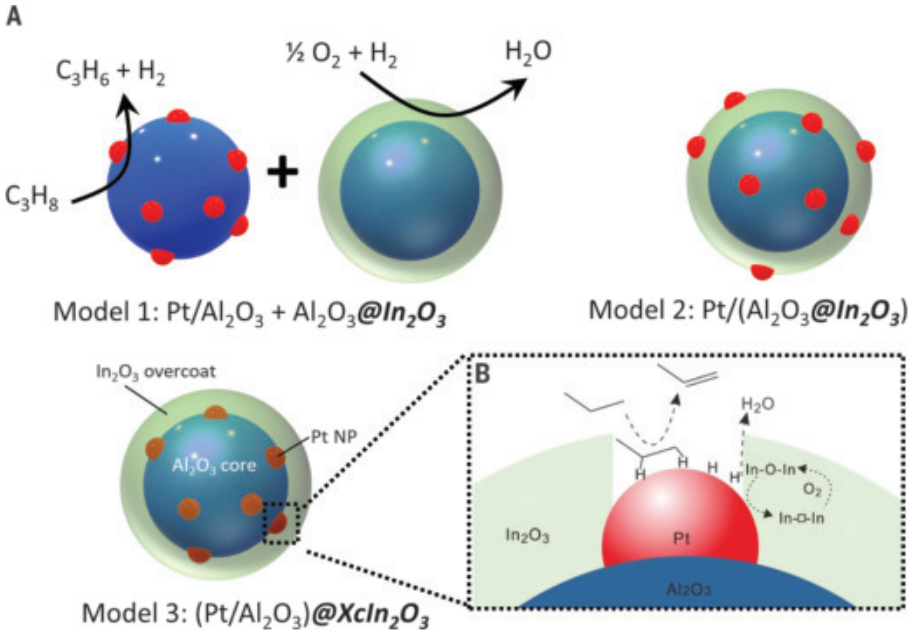

Fig. 1. Tandem catalyst models. (**A**) Three tandem catalyst models comprising a microporous In_2O_3 selective H_2 combustion catalyst (green) and a Pt/Al_2O_3 propane dehydrogenation catalyst (red Pt nanoparticles, blue Al_2O_3 particle). Tandem catalyst model 3, (Pt/Al_2O_3)***@35cIn₂O₃*** (35 cycles of In_2O_3 deposition), possesses a ~2-nm In_2O_3 overcoat and 2.0- to 2.3-nm Pt nanoparticles and is the best performing. (**B**) Tandem PDH-SHC reaction scheme for (Pt/Al_2O_3)***@35cIn₂O₃***. PDH occurs on Pt, and SHC consumes H over the In_2O_3 coating to pull the reaction forward to a high propylene yield. O_2 rapidly reacts with the resulting In_2O_{3-x}, minimizing undesired combustion on Pt. The overcoat also stabilizes Pt nanoparticles against aggregation during reaction.

[1]Department of Chemistry, Northwestern University, Evanston, IL 60208, USA. [2]Northwestern University Atomic and Nanoscale Characterization Experimental Center (NUANCE), Northwestern University, Evanston, IL 60208, USA. [3]Department of Chemical and Biological Engineering, Northwestern University, Evanston, IL 60208, USA.
*Corresponding author. Email: pstair@northwestern.edu (P.C.S.); j-notestein@northwestern.edu (J.M.N.)

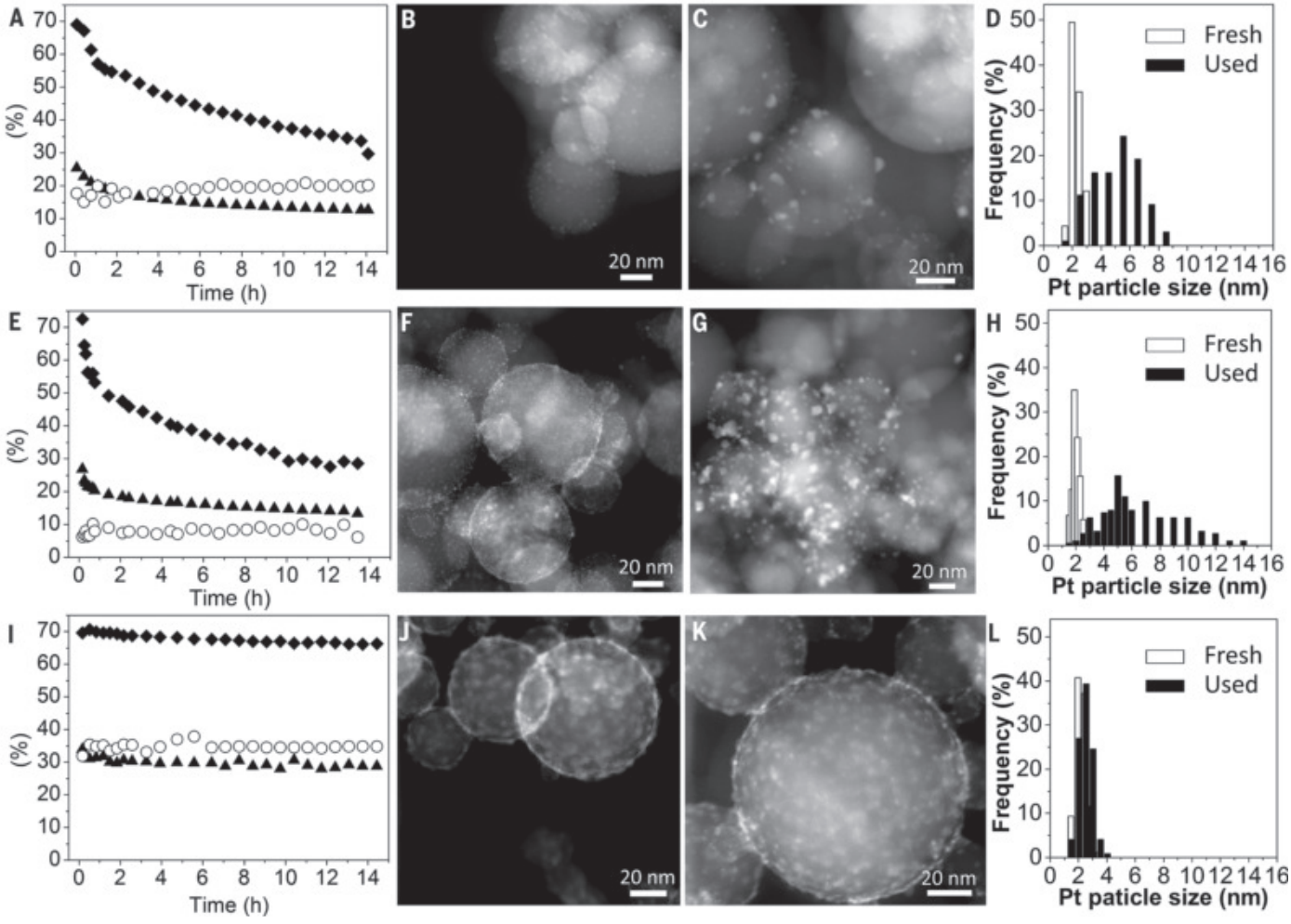

Fig. 2. Summary of catalyst activity and structure. (**A**, **E**, and **I**) Propane conversion(solid triangles), propylene selectivity (solid diamonds), and F_{tandem} (open circles) for the tandem PDH-SHC reaction over the model catalysts (top row) Pt/Al_2O_3 + Al_2O_3***@In$_2$O$_3$***, (middle row) $Pt/(Al_2O_3$***@35cIn$_2$O$_3$***), and (bottom row) (Pt/Al_2O_3)***@35cIn$_2$O$_3$***. Temperature (T) = 450°C, P_{C3H8}:P_{O2}:P_{N2} = 10:5:85 kPa. Inverse weight hourly space velocity ($WHSV^{-1}$) = 1.55 g_{C3H8}^{-1} $g_{catalyst}$ hours for (Pt/Al_2O_3)***@35cIn$_2$O$_3$*** and $Pt/(Al_2O_3$@35cIn$_2O_3$) and 3.1 g_{C3H8}^{-1} $g_{catalyst}$ hours for Pt/Al_2O_3 + Al_2O_3@In_2O_3. (**B**, **F**, and **J**) STEM images of fresh catalysts. (**C**, **G**, and **K**) STEM images of used catalysts after 14 hours time on stream. (**D**, **H**, and **L**) Pt particle size distributions of fresh and used catalysts.

obligate ODH catalysts (for example, supported VOx) give $F_{tandem} \approx 100\%$ ($H_2/C_3H_6 \approx 0$). Combined with conventional selectivity and conversion metrics, F_{tandem} is illustrative insomuch that values nearer 0 indicate that propane combustion consumes available O_2 separate from PDH, whereas values nearer to 100% indicate kinetic coupling between PDH and SHC functions.

The physical mixture Pt/Al_2O_3 + Al_2O_3***@In$_2$O$_3$*** performed well initially, but performance decayed rapidly with time on stream (TOS) (Fig. 2A). F_{tandem} was 19 ± 1% (Fig. 2A) at all TOS, indicating a small amount of H_2 consumed by SHC on the Al_2O_3***@In$_2$O$_3$*** particles. A simplified reactor model (fig. S4) explains the data as loss of Pt-catalyzed PDH with TOS, whereas undesired hydrocarbon combustion remained constant. The Pt nanoparticles also aggregated from 2.3 ± 0.7 nm to 5.0 ± 3.3 nm after 14 hours TOS (Fig. 2, B to D). Stabilizing the Pt nanoparticles with an Al_2O_3 overcoat (*25*) did not prevent deactivation (fig. S5), showing that Pt nanoparticle stabilization is insufficient for good catalyst performance. Next, the supported catalyst $Pt/(Al_2O_3$***@35cIn$_2$O$_3$***) also aggregated and behaved similarly to the physical mixture (Fig. 2, E to H), with lower F_{tandem} (~10% at all TOS), indicating relatively little kinetic coupling even though the Pt and In_2O_3 phases were in contact. The third design, overcoated (Pt/Al_2O_3)***@35cIn$_2$O$_3$***, gave the highest conversion (32%), selectivity (70%), and propylene yield (22%) and maintained this high performance for 14 hours TOS with only minor deactivation (Fig. 2I), which was readily reversed through in situ oxidation at reaction temperature (fig. S6). F_{tandem} was ~40%, demonstrating greater kinetic coupling between PDH and SHC, and the In_2O_3 overcoat prevented Pt nanoparticle aggregation (constant 2.0 ± 0.8 nm) (Fig. 2, J to L). These designs demonstrate that the benefits of high propylene selectivity, tight coupling between PDH and SHC, and high stability required the extensive and intimate connectivity afforded by the particular geometry of the overcoated nanostructure.

Performance of the overcoated catalyst was strongly dependent on catalyst composition. Increasing amounts of In_2O_3 improved conversion, selectivity, and stability up to 35 cycles of deposition (figs. S7 to S9), whereas a

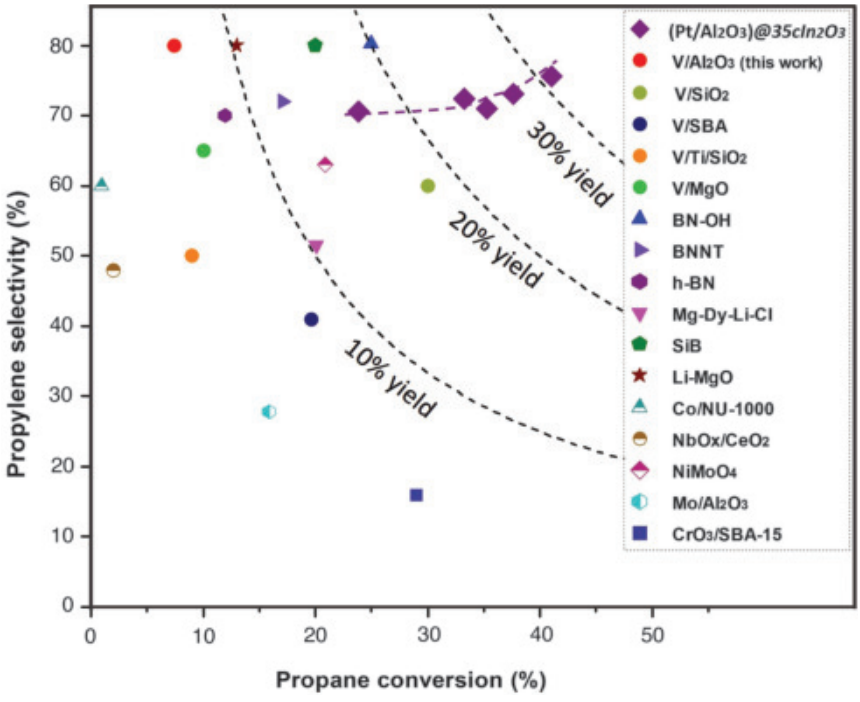

Fig. 3. Comparison of (Pt/Al_2O_3)@*35cIn$_2O_3$* with the catalytic performance of established ODHP catalysts at their maximum reported per-pass yields. Propane conversion was varied by changing $WHSV^{-1}$ from 0.77 to 5.72 g_{C3H8}^{-1} $g_{catalyst}$ hours at 450°C with C_3H_8:O_2 = 2:1. All reaction conditions and citations are listed in table S2.

55-cycle material performed similarly to Pt-free Al_2O_3***@In$_2O_3$***. F_{tandem} also increased with In_2O_3, demonstrating beneficial kinetic coupling between PDH and SHC. In addition, only the 35- and 55-cycle materials suppressed the total yield of CO_2 from hydrocarbon combustion. The best performance over (Pt/Al_2O_3)***@35cIn$_2O_3$*** was 75% selectivity at 40% conversion at 450°C, which occurred at longer contact times (fig. S10) and near a 2:1 ratio of propane:O_2 (fig. S11). O_2 removal was fully reversible (fig. S12) and showed the substantial yield gains under oxidizing conditions. These effects were captured in a reactor model with O_2-enhanced dehydrogenation and effective rate constants for dehydrogenation and H_2 combustion that were higher on (Pt/Al_2O_3)***@35cIn$_2O_3$*** than on the physical mixture (fig. S10). In additional experiments, we observed a stable 37% yield at 500°C, with higher, but less-stable, yields at 550°C (figs. S13 and S14). As summarized in Fig. 3, the overcoated, tandem catalyst outperformed state-of-the-art ODHP catalysts (table S1 and fig S15), and yields also exceeded the thermodynamic equilibrium conversion of ~24% for nonoxidative PDH. Last, a simple packed bed of the overcoated tandem catalyst performs comparable with or better than more complex and lower-throughput designs such as membrane, staged, or chemical looping reactors (table S2).

To characterize the overcoated catalyst, scanning transmission electron microscopy (STEM) and energy-dispersive x-ray spectroscopy (EDS) elemental analysis confirmed a ~2.0-nm conformal indium oxide coating after 35 cycles of ALD (Fig. 4, A and B, and fig. S16) and an unchanged Pt nanoparticle size distribution. N_2 physisorption (fig. S17), CO pulse chemisorption, and CO diffuse reflectance infrared Fourier transform spectroscopy (DRIFTS) showed that the ALD process initially blocked 99% of the Pt surface, but heating to 450°C uncovered approximately half the surface Pt atoms (Fig. 4C and table S3). Reexposing surfaces initially covered through ALD has been previously observed after similar treatments (*25*). Samples with different numbers of In_2O_3 or Al_2O_3 ALD layers showed no systematic differences in the shape of their CO DRIFTS spectra (fig. S18), which argued against site-selective coverage or electronic modification of the surface Pt atoms by the overcoat. Pt x-ray photoelectron spectroscopy (XPS) and x-ray absorption spectroscopy (XAS) showed identical spectra for Pt/Al_2O_3 and (Pt/Al_2O_3) ***@35cIn$_2O_3$*** after reaction (figs. S19 and S20), and the In $3d_{5/2}$ XPS feature was indicative of In_2O_3 (fig. S21), arguing against Pt-In alloy formation. The onset of H_2–temperature-programmed reduction (TPR) and H_2O evolution was lowered by ~100°C when Pt and In_2O_3 were in intimate contact [for example, (Pt/Al_2O_3)***@35cIn$_2O_3$***] (figs. S22 and S23), and in situ DRIFTS under H_2 (Fig. 4D) produced a broad feature from 1200 to 3000 cm^{-1} in (Pt/Al_2O_3)***@35cIn$_2O_3$*** owing to formation of In_2O_{3-x} (*26*, *27*), which did not form for any other material. This same feature was seen for (Pt/Al_2O_3)***@35cIn$_2O_3$*** in the presence of pure propane above 150°C (fig. S24). TPR and in situ DRIFTS are consistent with an overall catalytic cycle involving direct H transfer across catalytic domains (Fig. 1B). This characterization provides initial verification of our structural hypothesis and provided evidence that intimate and extensive contact between Pt and In_2O_3 kinetically coupled PDH and SHC through the direct diffusion of chemisorbed H atoms.

Additional in situ and operando experiments, as well as microkinetic modeling, will be needed to fully understand this complex material. Overall, this tandem catalyst design shows that overcoats can stabilize metal nanoparticles and tightly couple reactions on the nanoscale to balance activity (on Pt) and selectivity (on In_2O_3) for biomimetic, direct transfer of reactive intermediates between two different catalyst functions. Beyond the results shown here, we expect that further improvements and examples are possible from optimization of process conditions and independent tuning of the identity and amount of dehydrogenation and SHC sites.

In this work, supported Pt nanoparticles were synthesized by means of ALD on Al_2O_3 (NanoDur) or In_2O_3-coated Al_2O_3 by using a single cycle of trimethyl(methylcyclopentadienyl) Pt and O_3 to give a final loading of 1.3 wt % Pt (fig. S25, A and B). Other routes could likely be used. In_2O_3 films of variable thickness were synthesized by means of 2 to 55 cycles of In_2O_3 ALD, alternating cyclopentadienyl indium (InCp) and O_3, corresponding to 0.22 to 15.4 wt % In (table S4). Most catalytic experiments were performed by using materials with 35 cycles of In_2O_3 ALD, designated

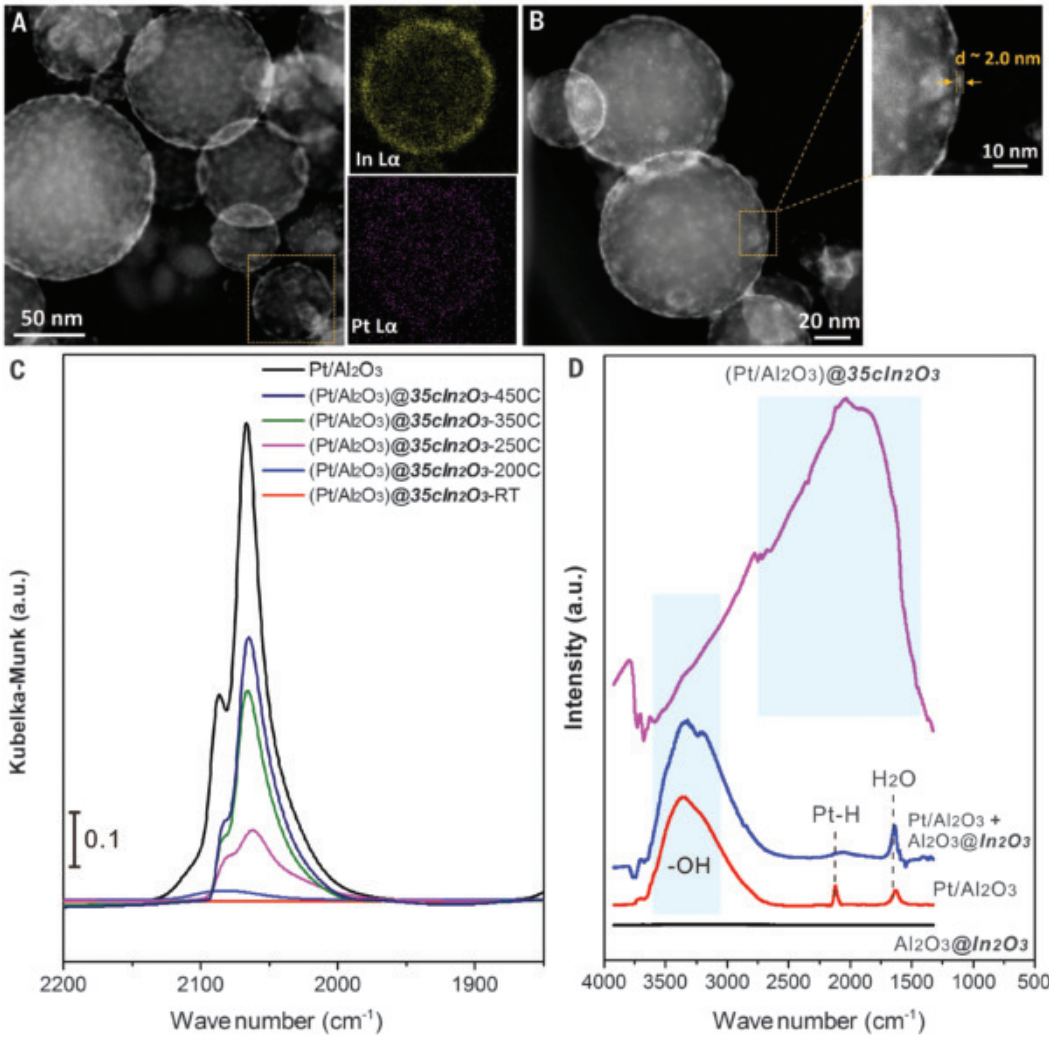

Fig. 4. Characterization of the tandem catalyst. (**A** and **B**) STEM of (Pt/Al_2O_3) ***@35cIn$_2$O$_3$*** and selected-area EDS elemental analysis mapping. (**C**) Infrared spectra of adsorbed linear CO on Pt/Al_2O_3 and (Pt/Al_2O_3)***@35cIn$_2$O$_3$*** with feature intensity increasing with increasing pretreatment temperatures. (**D**) In situ H_2 DRIFTS at room temperature of several catalysts. The broad band across the spectral window is associated with In_2O_{3-x}. a.u., arbitrary units.

@35cIn$_2$O$_3$, containing 7 wt % In (fig. S25, C and D). Al_2O_3 films (fig. S26) were synthesized by using 35 cycles alternating trimethylaluminum and water.

REFERENCES AND NOTES

1. D. E. Fogg, E. N. dos Santos, *Coord. Chem. Rev.* **248**, 2365–2379 (2004).
2. T. L. Lohr, Z. Li, T. J. Marks, *Acc. Chem. Res.* **49**, 824–834 (2016).
3. Z. Ma, M. D. Porosoff, *ACS Catal.* **9**, 2639–2656 (2019).
4. R. A. Periana, O. Mironov, D. Taube, G. Bhalla, C. J. Jones, *Science* **301**, 814–818 (2003).
5. J. Shan, M. Li, L. F. Allard, S. Lee, M. Flytzani-Stephanopoulos, *Nature* **551**, 605–608 (2017).
6. F. Zhang *et al.*, *Science* **370**, 437–441 (2020).
7. A. S. Goldman *et al.*, *Science* **312**, 257–261 (2006).
8. Z. Li *et al.*, *Joule* **3**, 570–583 (2019).
9. Y. Yamada *et al.*, *Nat. Chem.* **3**, 372–376 (2011).
10. J. Su *et al.*, *J. Am. Chem. Soc.* **138**, 11568–11574 (2016).
11. A. Nivina, K. P. Yuet, J. Hsu, C. Khosla, *Chem. Rev.* **119**, 12524–12547 (2019).
12. C. Carrero, R. Schlögl, I. Wachs, R. Schomaecker, *ACS Catal.* **4**, 3357–3380 (2014).
13. L. Liu *et al.*, *Nat. Mater.* **18**, 866–873 (2019).
14. J. T. Grant *et al.*, *Science* **354**, 1570–1573 (2016).
15. K. Narsimhan, K. Iyoki, K. Dinh, Y. Román-Leshkov, *ACS Cent. Sci.* **2**, 424–429 (2016).
16. Y. Gambo, A. Jalil, S. Triwahyono, A. Abdulrasheed, *J. Ind. Eng. Chem.* **59**, 218–229 (2018).
17. J. J. Sattler, J. Ruiz-Martinez, E. Santillan-Jimenez, B. M. Weckhuysen, *Chem. Rev.* **114**, 10613–10653 (2014).
18. K. J. Caspary, H. Gehrke, M. Heinritz-Adrian, M. Schwefer, Dehydrogenation of alkanes, in *Handbook of Heterogeneous Catalysis: Online* (2008), pp. 3206–3229.
19. S. Chen *et al.*, *J. Am. Chem. Soc.* **141**, 18653–18657 (2019).
20. J. G. Tsikoyiannis, D. L. Stern, R. K. Grasselli, *J. Catal.* **184**, 77–86 (1999).
21. Q. Zhang, I. Lee, J. B. Joo, F. Zaera, Y. Yin, *Acc. Chem. Res.* **46**, 1816–1824 (2013).
22. H. O. Otor, J. B. Steiner, C. García-Sancho, A. C. Alba-Rubio, *ACS Catal.* **10**, 7630–7656 (2020).
23. S. Kattel, P. Liu, J. G. Chen, *J. Am. Chem. Soc.* **139**, 9739–9754 (2017).
24. J. C. Matsubu *et al.*, *Nat. Chem.* **9**, 120–127 (2017).
25. J. Lu, J. W. Elam, P. C. Stair, *Acc. Chem. Res.* **46**, 1806–1815 (2013).
26. N. Siedl, P. Gügel, O. Diwald, *J. Phys. Chem. C* **117**, 20722–20729 (2013).
27. L. Wang *et al.*, *Nat. Commun.* **11**, 2432 (2020).

ACKNOWLEDGMENTS

We acknowledge N. Schweitzer (CCSS) for XAS acquisition and X. Hu (NUANCE) for discussion of electron microscopy.
Funding: This paper is based on work supported primarily by the National Science Foundation under Cooperative Agreement EEC-1647722. Any opinions, findings, and conclusions or recommendations expressed in this material are those of the authors and do not necessarily reflect the views of the National Science Foundation. I.A.S. acknowledges support by the U.S. Department of Energy (DOE) under award DE-FG02-03-ER154757. This work made use of REACT, EPIC, and Keck- II facilities of Northwestern University. This research used MRCAT and the resources of the Advanced Photon Source, a DOE Office of Science User Facility operated for the DOE Office of Science by Argonne National Laboratory under contract DE-AC02-06CH11357. **Author contributions:** H.Y. performed most experiments and wrote the initial draft. K.H. carried out the microscopy. I.A.S. and M.G.N. developed the ALD method. D.J. developed the reactor model. P.C.S. and J.M.N. were responsible for supervision, funding acquisition, project administration, review, and editing. **Competing interests:** The authors declare no competing interests. A provisional U.S. patent application has been filed on this work. **Data and materials availability:** All data and images are available in the manuscript or the supplementary materials.

SUPPLEMENTARY MATERIALS

science.sciencemag.org/content/371/6535/1257/suppl/DC1
Materials and Methods
Figs. S1 to S26
Tables S1 to S4
References (*28*–*79*)

22 June 2020; accepted 3 February 2021
10.1126/science.abd4441

2D MATERIALS

Tuning electron correlation in magic-angle twisted bilayer graphene using Coulomb screening

Xiaoxue Liu[1], Zhi Wang[1], K. Watanabe[2], T. Taniguchi[2], Oskar Vafek[3,4], J. I. A. Li[1]*

Controlling the strength of interactions is essential for studying quantum phenomena emerging in systems of correlated fermions. We introduce a device geometry whereby magic-angle twisted bilayer graphene is placed in close proximity to a Bernal bilayer graphene, separated by a 3-nanometer-thick barrier. By using charge screening from the Bernal bilayer, the strength of electron-electron Coulomb interaction within the twisted bilayer can be continuously tuned. Transport measurements show that tuning Coulomb screening has opposite effects on the insulating and superconducting states: As Coulomb interaction is weakened by screening, the insulating states become less robust, whereas the stability of superconductivity at the optimal doping is enhanced. The results provide important constraints on theoretical models for understanding the mechanism of superconductivity in magic-angle twisted bilayer graphene.

The discovery of superconductivity in magic-angle twisted bilayer graphene (tBLG) has raised intriguing questions about the nature of the superconducting order parameter (*1*–*3*). The phase diagram of magic-angle tBLG, featuring both the correlated insulator (CI) and superconducting phases, resembles that of cuprate materials, suggesting that the superconducting phase arises from an unconventional origin (*1*, *4*–*6*, *7*–*12*). By contrast, the more recent observations of superconductivity in the absence of CI appear to indicate that superconductivity arises through electron-phonon coupling (*13*–*15*), an interpretation that is backed by a range of theoretical models (*16*–*18*).

It has long been recognized that elucidating the role of Coulomb interaction is essential to determining the nature of superconductivity. For a conventional superconductor, electron-phonon coupling competes against Coulomb repulsion in stabilizing superconductivity at low temperature (*19*, *20*). As such, a weaker Coulomb repulsion will lead to more robust superconducting order parameters. By contrast, an unconventional superconducting phase arises from an all-electron mechanism, whereby the order parameter strengthens with increasing Coulomb interaction (*4*, *5*). For conventional solid-state materials, it remains an experimental challenge to directly control Coulomb interaction within a superconductor without introducing additional changes to the material. The flexibility of the van der Waals materials offers a valuable opportunity to control Coulomb interaction in magic-angle tBLG structure using proximity screening (*13*, *14*, *21*).

A major roadblock for addressing the mechanism underlying the superconducting phase is the vastly different behavior across different

[1]Department of Physics, Brown University, Providence, RI 02912, USA. [2]National Institute for Materials Science, 1-1 Namiki, Tsukuba 305-0044, Japan. [3]Department of Physics, Florida State University, Tallahassee, FL 32306, USA. [4]National High Magnetic Field Laboratory, Tallahassee, FL 32310, USA.
*Corresponding author. Email: jia_li@brown.edu

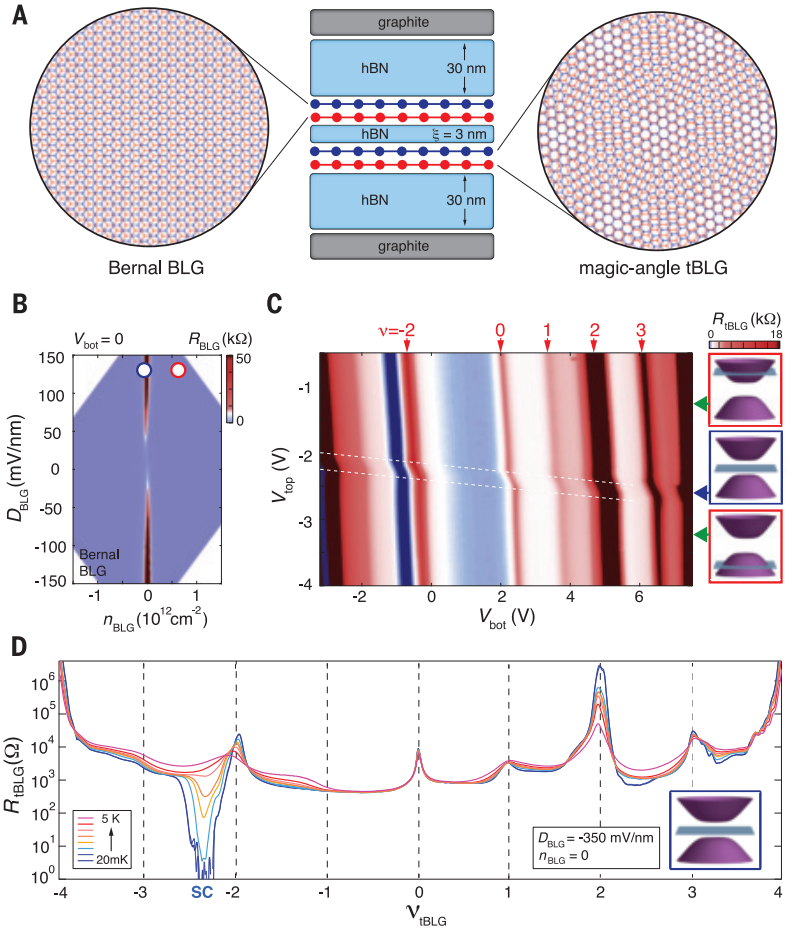

Fig. 1. Hybrid double-layer structure with Bernal BLG and tBLG. (**A**) Schematic of the hybrid double-layer structure consisting of a Bernal BLG and a magic-angle tBLG, separated by a thin insulating barrier with thickness of $\xi = 3$ nm. The structure is encapsulated with dual hexagonal boron nitride (hBN) dielectric and graphite gate electrodes. (**B**) Longitudinal resistance of Bernal BLG R_{BLG} as a function of D_{BLG} and n_{BLG} at $T = 20$ mK. (**C**) Longitudinal resistance of tBLG R_{tBLG} as a function of V_{top} and V_{bot} measured at $T = 20$ mK and $V_{int} = -200$ mV. Screening from BLG is minimal between the white dashed lines, where BLG is fully insulating and tBLG is tuned with both top and bottom graphite gates, giving rise to the distortion in transport features. Inset: Schematic energy structure of BLG at large D_{BLG} for three values of n_{BLG}. (**D**) R_{tBLG} as a function of filling fraction in tBLG ν_{tBLG}, measured at $D_{BLG} = -350$ mV/nm and $n_{BLG} = 0$ with varying temperature.

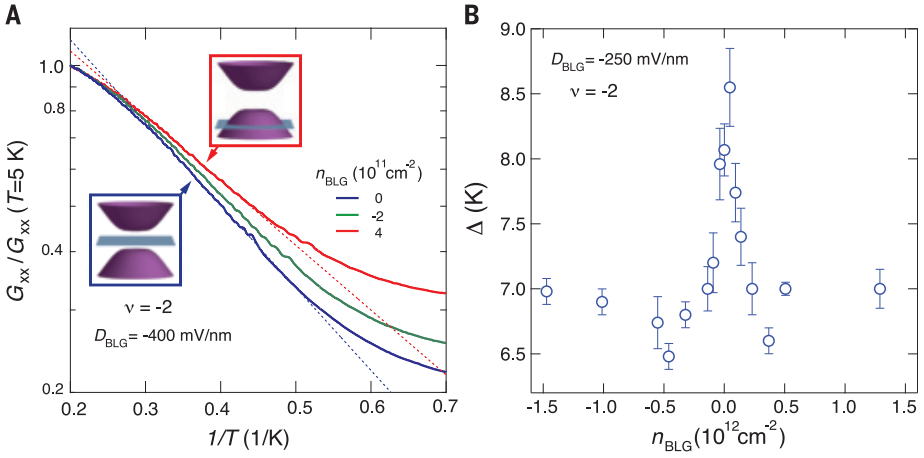

Fig. 2. The effect of Coulomb screening on the CI. (**A**) Arrhenius plot for the correlated insulating state at $\nu_{tBLG} = -2$, measured at $D_{BLG} = -400$ mV/nm with varying carrier density n_{BLG}. Four-terminal conductances G_{xx} measured at different n_{BLG} are normalized by their value at $T = 5$ K. (**B**) Activation energy gap of the $\nu_{tBLG} = -2$ CI state as a function of n_{BLG}.

tBLG samples near the magic angle, which may result from the spatial inhomogeneity of the moiré pattern (*22*–*24*). The variation between different samples makes it difficult to provide reliable experimental constraints on a theoretical model. Here, we address this obstacle by tuning the strength of the Coulomb interaction in a single device using screening, while studying the response in both the CIs and the superconducting phase using transport measurement. We use a hybrid double-layer structure, in which a Bernal bilayer graphene (BLG) and a magic-angle twisted bilayer graphene (tBLG) are separated by a thin insulating barrier with a $\xi = 3$ nm thickness (Fig. 1A). The close proximity allows charge carriers from BLG to screen the Coulomb interaction in the tBLG, offering direct control of electron correlations in the moiré flat band.

Charge carrier density in BLG and tBLG, n_{BLG} and n_{tBLG}, can be independently controlled by varying the applied voltage to the top and bottom graphite gates, V_{top} and V_{bot} (*25*). Additionally, a voltage bias across two layers V_{int} induces a perpendicular electric field, D, providing experimental control for the energy gap at the charge neutrality point in BLG (*26*–*28*). Longitudinal resistance measured from the Bernal BLG displays a well-defined peak at the neutrality point, which grows more insulating with increasing D-field (Fig. 1B). At large D-field, Bernal BLG can be tuned from fully insulating at $n_{BLG} = 0$ (blue circle in Fig. 1B) to highly conductive at large n_{BLG} (red circle in Fig. 1B), offering a large contrast in the strength of Coulomb screening. Figure 1C plots the transport response of tBLG with a twist angle of $\theta = 1.04^o$ (*25*), as n_{BLG} and n_{tBLG} are both tuned by varying V_{top} and V_{bot}. A normalized density scale, marked by red arrows, is defined to describe partial filling ν of the moiré band on the basis of the fourfold degeneracy of spin and valley degrees of freedom for both electron- and hole-type carriers.

The static e^2/r Coulomb interaction among the electrons with charge e, separated by distance r in the tBLG, is modified by the presence of BLG, leading to an effective interaction energy

$$V^{\text{eff}}(r) = \int \frac{d^2q}{(2\pi)^2}\frac{2\pi e^2}{|q|}\left[1 - e^{-2|q|\xi}\left(1 - \frac{1}{\epsilon_{AB}(q)}\right)\right]e^{iq\cdot r}$$

The wave vector q-dependent dielectric constant of the BLG can be related to its static polarization function Π_q^0 as $\epsilon_{AB}(q) = 1 + \frac{2\pi e^2}{|q|}\Pi_q^0$. When the BLG is gated to a finite carrier density and thus acts as a metal, $\Pi_{q\to 0}^0 \to$ const. and the $\epsilon_{AB}(q \to 0)$ diverges. At long distances, $V^{\text{eff}}(r)$ then corresponds to the real space potential produced by the test charge and its mirror image a distance 2ξ above the twisted bilayer. When the BLG is insulating, $\Pi_{q\to 0}^0 \sim q^2$ and the $V^{\text{eff}}(r)$ is unchanged at long distances by the presence of the BLG [see (*25*) for details of Coulomb screening in a hybrid double-layer structure at any r]. Because the strength of Coulomb screening is correlated with the conductivity of BLG, its effect can be studied by comparing transport properties of tBLG in and outside the density range marked by the white dashed lines in Fig. 1C.

First, we examine the transport response of tBLG in the absence of Coulomb screening, by measuring inside the white dashed lines in Fig. 1C, where BLG is fully insulating. Figure 1D plots the longitudinal resistance of tBLG, R_{tBLG}, over the full filling range of the moiré flat band. Apart from the charge neutral point (CNP), a series of resistive features emerge at $\nu = \pm 2, +1$, and $+3$, which are consistent with the CI states from previous observation (*1*–*3*). In addition, a robust superconducting phase emerges at low temperature, evidenced by R_{tBLG} dropping to zero. The robust CI and superconducting states establish an excellent starting point, allowing us to quantitatively examine the effect of Coulomb screening by studying the variation in transport behavior while varying n_{BLG}.

Figure 2A plots the temperature dependence of four-terminal conductance of the CIs at $\nu = -2$, which exhibits thermally activated behavior with strong n_{BLG} dependence. An energy gap Δ can be extracted from the slope of the Arrhenius plot (dashed lines in Fig. 2A), providing a measure for the strength of the CI state. The effect of Coulomb screening is investigated by measuring the energy gap Δ while varying density in BLG n_{BLG} (Fig. 2B). $\Delta_{\nu=-2}$ is largest when BLG is fully insulating at $n_{BLG} = 0$. Similar behavior in the energy gap is observed at $\nu = 2$ and 3 as a function of n_{BLG} [see figs. S11 and S12 (*25*)]. Because CIs at integer fillings arise from Coulomb correlation within the moiré flat band (*6*, *29*, *30*, *31*), the trend in Δ provides strong evidence that electron correlations in tBLG are directly tunable using Coulomb screening: Screening from the BLG decreases as BLG becomes insulating, leading to stronger Coulomb interactions and a larger Δ for the CI states. In addition, a minimum in $\Delta_{\nu=-2}$ is observed near the band edge of BLG at $n_{BLG} \sim 5 \times 10^{11}$ cm^{-2}, suggesting that Coulomb screening is strongest when the Fermi level of BLG is near the van Hove singularities, where the density of states is largest (*32*, *33*). We note that BLG at $n_{BLG} = 0$ remains insulating over the temperature range of the thermal activation measurement, ensuring that the strength of Coulomb screening remains constant with varying temperature and is controlled only by n_{BLG} [see figs. S13 and S14 (*25*)]. The robustness of the CI at $\nu = -2$ in the presence of strong Coulomb screening suggests that CIs cannot be fully suppressed by Coulomb screening alone (*13*). The effect of Coulomb screening on CIs shows excellent agreement with theoretical models (*25*), which provides an important reference for studying the nature of superconductivity in tBLG using Coulomb screening from BLG.

Having established the effect of Coulomb screening on CIs, we turn our attention to the superconducting phase on the hole-doping side of $\nu = -2$. Figure 3A plots R_{tBLG} at $T = 20$ mK as a function of carrier density in tBLG, n_{tBLG}. The superconducting phase is stable over a wider density range in the regime where BLG is metallic (red trace in Fig. 3A), as compared to when BLG is fully insulating (blue trace in Fig. 3A). The boundary of the superconducting region is defined by the density where R_{tBLG}

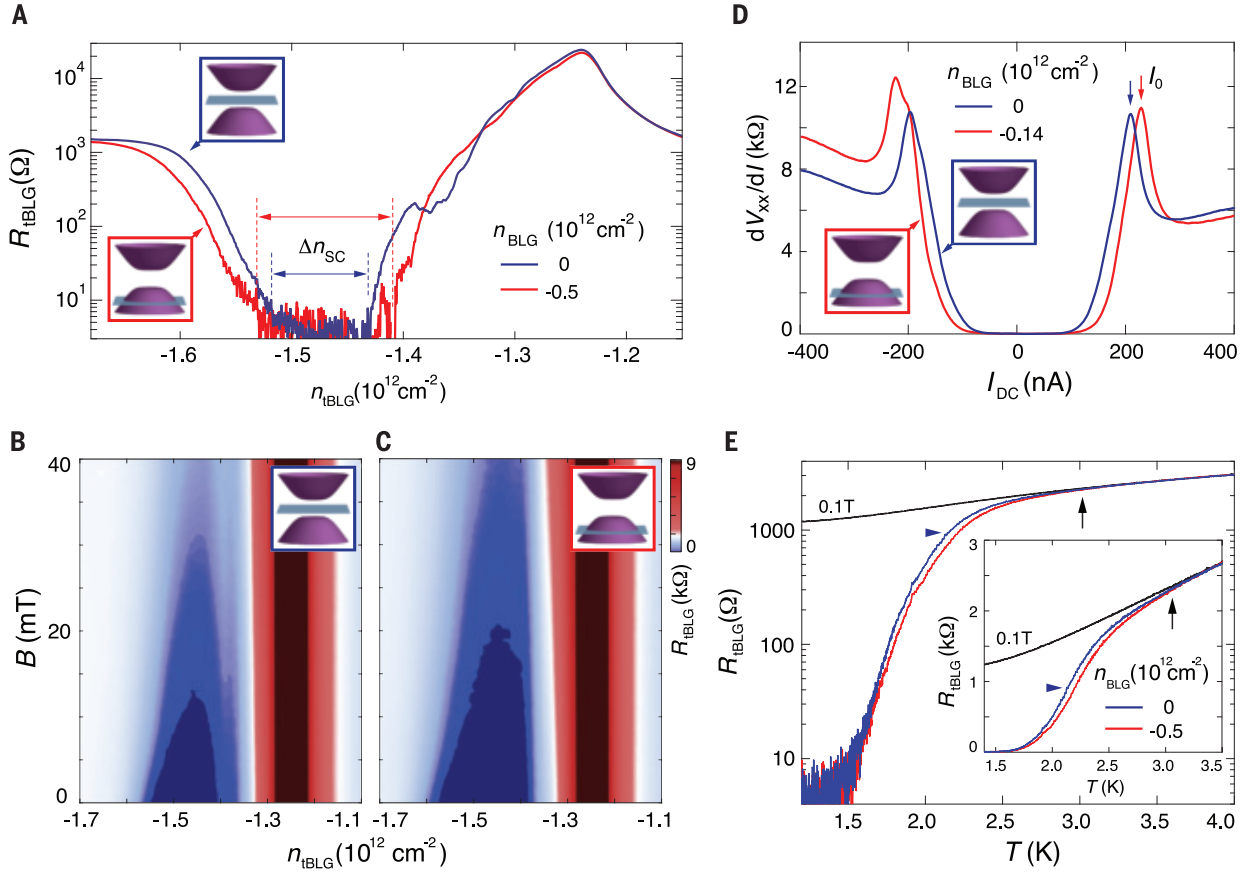

Fig. 3. The effect of tuning n_{BLG} in the presence of a large *D*-field–induced energy gap in BLG. (**A**) R_{tBLG} as a function of carrier density in tBLG, n_{tBLG}, measured at $D_{BLG} = -350$ mV/nm with different n_{tBLG} at $T = 20$ mK. (**B** and **C**) R_{tBLG} as a function of carrier density n_{tBLG} and perpendicular magnetic field B at $T = 20$ mK. BLG is tuned to $D_{BLG} = -350$ mV/nm with (B) $n_{BLG} = 0$ and (C) $n_{BLG} = -0.5 \times 10^{12}$ cm^{-2}. (**D**) Differential resistance dV_{xx}/dI versus d.c. bias current I_{DC} measured at optimal doping $n_{tBLG} = -1.48 \times 10^{12}$ cm^{-2} and base temperature of $T = 20$ mK, with D_{BLG} = 350 mV/nm and BLG tuned to different density. A critical current I_o is defined by the peak in dV_{xx}/dI, where superconductivity is destroyed and the differential resistance goes over to the normal state value (*40*). (**E**) R_{tBLG} as a function of temperature measured at optimal doping $n_{tBLG} = -1.48 \times 10^{12}$ cm^{-2} and $D_{BLG} = -350$ mV/nm for different n_{BLG}. The blue and red traces are measured at $B = 0$, whereas the black trace is measured at the perpendicular magnetic field $B = 0.1$ T where superconductivity is fully suppressed. Inset: Temperature dependence of R_{tBLG} on a linear scale. T_c is operationally defined by 50% of normal state resistance and marked by the blue horizontal arrowhead. The separation of $B = 0$ and $B = 0.1$ T curves marks the onset of pairing (black vertical arrow).

increases above the noise level, which determines the density range of the superconducting dome, Δn_{SC}, as shown in Fig. 3A. The effect of n_{BLG} tuning is also observed in the density-magnetic field phase diagram, where zero resistance is shown as dark blue in the chosen color scale. A larger superconducting region is observed at large n_{BLG} (Fig. 3C) compared with $n_{BLG} = 0$ (Fig. 3B). Figure 3, D and E, respectively, show the measurements of the critical current I_o and critical temperature T_c of the superconducting phase at the optimal doping, which confirm the same trend: The superconducting phase is more robust when BLG is metallic as compared to fully insulating. We note that R_{tBLG} measured at $B = 0.1$ T, where superconductivity is fully suppressed, reflects the transport behavior of tBLG in the normal state. The transition temperature T_c, operationally defined as 50% of extrapolated normal state resistance, is shown to be ~2.2 K in Fig. 3E, which is in line with previous observations in tBLG with a similar twist angle (*14*). The temperature dependence of R_{tBLG} leads to a few important observations: (i) The normal state ($T \gtrsim 3$ K) resistance in tBLG is insensitive to changes in BLG, demonstrating that modifications in impurity scattering resulting from a nearby metallic layer do not play a dominating role (*34*); (ii) the onset of Cooper pairing is observed at $T \sim 3$ K (vertical black arrow in Fig. 3E), evidenced by the bifurcation between R_{tBLG} measured at $B = 0$ and 0.1 T. We note that the n_{BLG}-tuning and Cooper pairing onset at a similar temperature, as shown by the red and blue traces in Fig. 3E. The stability of the superconducting phase can be further explored by plotting I_o, T_c, and Δn_{SC} as a function of n_{BLG}. The values of all three properties closely follow the conductance of BLG, as shown in Fig. 4, A to D, with the superconducting phase at the optimal doping being more robust when BLG is metallic. Taken together, our measurements suggest that n_{BLG} tuning has a direct impact on the stability of the superconducting phase in tBLG.

The enhancement of superconductivity by a nearby metallic BLG layer could, in principle, result from suppressed phase fluctuations in tBLG, without an appreciable effect on Cooper pair formation, giving rise to a higher Berezinskii-Kosterlitz-Thouless transition temperature T_{BKT} (*35*). We can rule out this scenario because the n_{BLG} tuning onsets at roughly the same temperature as Cooper

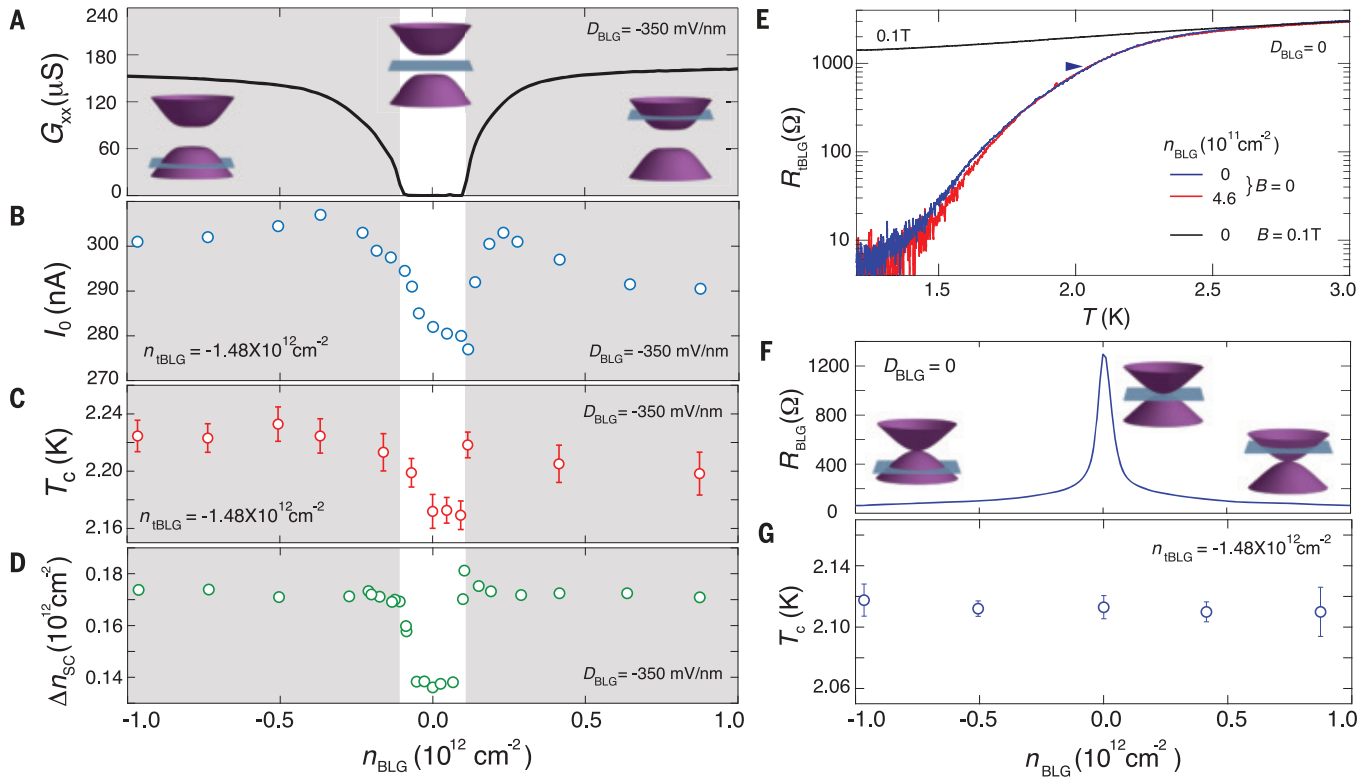

Fig. 4. The effect of tuning n_{BLG} on the superconductivity at the optimal doping in magic-angle tBLG. (**A**)The longitudinal conductance G_{xx} in BLG as a function of carrier density n_{BLG} measured at $D_{BLG} = -350$ mV/nm and $T = 20$ mK. Insets show the position of Fermi level relative to the energy band structure in BLG at different carrier densities. (**B**) I_o, (**C**) T_c, and (**D**) Δn_{SC} as a function of carrier density in BLG, n_{BLG}, measured at $D_{BLG} = -350$ mV/nm. I_o and T_c are measured at optimal doping $n_{tBLG} = -1.48 \times 10^{12}$ cm^{-2}, I_o and Δn_{SC} are measured at $T = 20$ mK. A large energy gap is induced in BLG by D-field. (**E**) R_{tBLG} as a function of temperature measured at optimal doping $n_{tBLG} = -1.48 \times 10^{12}$ cm^{-2} and $D_{BLG} = 0$ for different n_{BLG}. The blue and red traces are measured at $B = 0$, whereas the black trace is measured at $B = 0.1$ T, where superconductivity is fully suppressed. Tuning n_{BLG} gives rise to small differences in R_{tBLG} at temperatures much lower than T_c; no effect is observed in the temperature range near T_c. (**F**) R_{xx} in BLG as a function of carrier density n_{BLG} measured at $D_{BLG} = 0$ and $T = 20$ mK. (**G**) T_c as a function of carrier density in BLG, n_{BLG}, measured at $D_{BLG} = 0$ and optimal doping $n_{tBLG} = -1.48 \times 10^{12}$ cm^{-2}.

pairing (Fig. 3E). Additional support for this conclusion is provided by our data at $D_{BLG} = 0$; in this regime, the gap at the neutrality point of BLG is zero and BLG is always conducting, although the resistivity of BLG varies by about a factor of 20 between the CNP and away from it (Fig. 4F). As a result, tuning n_{BLG} away from the CNP suppresses phase fluctuation in tBLG, which is evidenced by small changes in R_{tBLG} at a temperature much lower than T_c. However, the temperature dependence of R_{tBLG} remained the same on the Cooper pairing scale at $T \sim 2$ K (Fig. 4E), giving rise to a constant value in T_c over a wide range of n_{BLG} (Fig. 4G), indicating that tuning n_{BLG} at $D_{BLG} = 0$ does not change the strength of Coulomb screening.

In addition, we note that in the absence of filtering, the superconducting phase is greatly suppressed when BLG is metallic (*25*). This is possibly due to the influence of radio frequency noise from outside the measurement apparatus (*36*), which is amplified by the capacitive coupling across the insulating barrier in a double-layer structure (*37*). The influence of such external radiation can be eliminated by installing a low-pass filter [see fig. S3 (*25*)]. The enhancement of superconductivity by a nearby metallic layer indicates that the influence of an external high-frequency radiation is sufficiently eliminated by filtering.

It is also worth pointing out that changes in Coulomb screening do not influence the linear-in-T behavior in tBLG at high temperature (fig. S10). It has been suggested that the slope of R_{tBLG} in the T-linear regime is associated with the strength of quasielastic electron scattering off acoustic phonon modes (*38*, *39*). Transport measurement in this regime demonstrates a constant slope of R_{tBLG} independent of carrier density in BLG, n_{BLG} (fig. S10), which would imply that the strength of acoustic electron-phonon coupling is not influenced by Coulomb screening. Our result suggests that the dominant effect of n_{BLG} tuning is changing the strength of Coulomb interactions in the magic-angle tBLG. That Cooper pair formation and superconductivity at the optimal doping become more robust with increasing screening appears consistent with electron-phonon coupling competing against Coulomb interaction to stabilize the superconducting phase (*19*). Alternatively, Coulomb screening could affect superconductivity by modifying properties of the moiré flatband, such as the size of fermi surface. The ability to control Coulomb interaction promises to provide important constraints on theoretical models aiming to accurately describe superconductivity in magic-angle tBLG.

REFERENCES AND NOTES

1. Y. Cao *et al.*, *Nature* **556**, 43–50 (2018).
2. M. Yankowitz *et al.*, *Science* **363**, 1059–1064 (2019).
3. X. Lu *et al.*, *Nature* **574**, 653–657 (2019).
4. B. Keimer, S. A. Kivelson, M. R. Norman, S. Uchida, J. Zaanen, *Nature* **518**, 179–186 (2015).
5. P. A. Lee, N. Nagaosa, X.-G. Wen, *Rev. Mod. Phys.* **78**, 17–85 (2006).
6. Y. Cao *et al.*, *Nature* **556**, 80–84 (2018).
7. Y. Cao *et al.*, *Phys. Rev. Lett.* **124**, 076801 (2020).
8. C. Xu, L. Balents, *Phys. Rev. Lett.* **121**, 087001 (2018).
9. H. Isobe, N. F. Q. Yuan, L. Fu, *Phys. Rev. X* **8**, 041041 (2018).

10. H. Guo, X. Zhu, S. Feng, R. T. Scalettar, *Phys. Rev. B* **97**, 235453 (2018).
11. S. Ray, J. Jung, T. Das, *Phys. Rev. B* **99**, 134515 (2019).
12. D. V. Chichinadze, L. Classen, A. V. Chubukov, *Phys. Rev. B* **101**, 224513 (2020).
13. P. Stepanov *et al.*, *Nature* **583**, 375–378 (2020).
14. Y. Saito, J. Ge, K. Watanabe, T. Taniguchi, A. F. Young, *Nat. Phys.* **16**, 926–930 (2020).
15. H. S. Arora *et al.*, *Nature* **583**, 379–384 (2020).
16. M. Ochi, M. Koshino, K. Kuroki, *Phys. Rev. B* **98**, 081102 (2018).
17. B. Lian, Z. Wang, B. A. Bernevig, *Phys. Rev. Lett.* **122**, 257002 (2019).
18. F. Wu, A. H. MacDonald, I. Martin, *Phys. Rev. Lett.* **121**, 257001 (2018).
19. W. L. McMillan, *Phys. Rev.* **167**, 331–344 (1968).
20. P. B. Allen, R. C. Dynes, *Phys. Rev. B* **12**, 905–922 (1975).
21. J. M. Pizarro, M. Rösner, R. Thomale, R. Valentí, T. O. Wehling, *Phys. Rev. B* **100**, 161102 (2019).
22. H. Yoo *et al.*, *Nat. Mater.* **18**, 448–453 (2019).
23. L. J. McGilly *et al.*, arXiv:1912.06629 [cond-mat.mes-hall] (2019).
24. A. Uri *et al.*, *Nature* **581**, 47–52 (2020).
25. See the supplementary materials.
26. Y. Zhang *et al.*, *Nature* **116**, 136802 (2009).
27. J. I. A. Li *et al.*, *Science* **358**, 648–652 (2017).
28. A. A. Zibrov *et al.*, *Nature* **549**, 360–364 (2017).
29. R. Bistritzer, A. H. MacDonald, *Proc. Natl. Acad. Sci. U.S.A.* **108**, 12233–12237 (2011).
30. C. Wu, D. Bergman, L. Balents, S. Das Sarma, *Phys. Rev. Lett.* **99**, 070401 (2007).
31. J. Kang, O. Vafek, *Phys. Rev. Lett.* **122**, 246401 (2019).
32. A. F. Young, L. S. Levitov, *Phys. Rev. B Condens. Matter Mater. Phys.* **84**, 085441 (2011).
33. B. M. Hunt *et al.*, *Nat. Commun.* **8**, 948 (2017).
34. L. Ponomarenko *et al.*, *Nat. Phys.* **7**, 958–961 (2011).
35. L. Merchant, J. Ostrick, R. P. Barber, R. C. Dynes, *Phys. Rev. B Condens. Matter Mater. Phys.* **63**, 134508 (2001).
36. I. Tamir *et al.*, *Sci. Adv.* **5**, eaau3826 (2019).
37. M. J. Kellogg, Evidence for excitonic superfluidity in a bilayer two-dimensional electron system, Ph.D. thesis, California Institute of Technology (2005).
38. F. Wu, E. Hwang, S. Das Sarma, *Phys. Rev. B* **99**, 165112 (2019).
39. H. Polshyn *et al.*, *Nat. Phys.* **15**, 1011–1016 (2019).
40. A. Benyamini *et al.*, *Nat. Phys.* **15**, 947–953 (2019).
41. X. Liu *et al.*, Data repository for: Tuning electron correlation in magic-angle twisted bilayer graphene using Coulomb screening, Version 1.0, Open Science Framework (2020). https://osf.io/uewx4/?view only=d112e55af9bc46f294a7fea4c087248d

ACKNOWLEDGMENTS

We thank M. Yankowitz, A. F. Young, C. R. Dean, Q. Shi, S. Todadri, and S. A. Kivelson for discussions and Y. Zeng for helpful input on fabrication. **Funding:** This work was primarily supported by Brown University. Device fabrication was performed in the Institute for Molecular and Nanoscale Innovation at Brown University. The authors acknowledge the use of equipment funded by the MRI award DMR-1827453. O.V. was supported by NSF DMR-1916958, and by the National High Magnetic Field Laboratory through NSF grant no. DMR-1157490 and the State of Florida. K.W. and T.T. acknowledge support from the EMEXT Element Strategy Initiative to Form Core Research Center through grant no. JPMXP0112101001 and the CREST(JPMJCR15F3), JST. **Author contributions:** X.L. and Z.W. fabricated the device and performed the measurements. X.L., Z.W., and J.I.A.L. analyzed the data. O.V. constructed the theoretical model. K.W. and T.T. provided the hBN crystals. The manuscript was written with input from all authors. **Competing interests:** The authors declare no competing financial interests. **Data and materials availability:** Experimental data files are available at the Open Science Framework (*41*)

SUPPLEMENTARY MATERIALS

science.sciencemag.org/content/371/6535/1261/suppl/DC1
Materials and Methods
Supplementary Text
Figs. S1 to S15
References (*42*–*44*)

24 March 2020; accepted 8 February 2021
10.1126/science.abb8754

ASTROCHEMISTRY

Detection of two interstellar polycyclic aromatic hydrocarbons via spectral matched filtering

Brett A. McGuire[1,2,3]*, Ryan A. Loomis[2]†, Andrew M. Burkhardt[3]†, Kin Long Kelvin Lee[1,3], Christopher N. Shingledecker[4,5,6], Steven B. Charnley[7], Ilsa R. Cooke[8], Martin A. Cordiner[7,9], Eric Herbst[10,11], Sergei Kalenskii[12], Mark A. Siebert[11], Eric R. Willis[10], Ci Xue[10], Anthony J. Remijan[2], Michael C. McCarthy[3]

Unidentified infrared emission bands are ubiquitous in many astronomical sources. These bands are widely, if not unanimously, attributed to collective emissions from polycyclic aromatic hydrocarbon (PAH) molecules, yet no single species of this class has been identified in space. Using spectral matched filtering of radio data from the Green Bank Telescope, we detected two nitrile-group–functionalized PAHs, 1- and 2-cyanonaphthalene, in the interstellar medium. Both bicyclic ring molecules were observed in the TMC-1 molecular cloud. In this paper, we discuss potential in situ gas-phase PAH formation pathways from smaller organic precursor molecules.

Aromatic molecules are a ubiquitous structural motif in organic chemistry and the chemical evolution of the Universe. Of all interstellar carbon, 10 to 25% is thought to be incorporated into polycyclic aromatic hydrocarbons (PAHs), which are expected to form primarily (if not exclusively) in the circumstellar envelopes of evolved stars (*1*). The aromatic molecule benzonitrile (BN; *c*-C_6H_5CN) has been detected in TMC-1, located within the interstellar Taurus Molecular Cloud (*2*), far from any evolved star. Motivated by the detection of BN, we have performed a spectral line survey of TMC-1 to investigate its inventory of aromatic molecules.

Most interstellar molecules (>80%) have been discovered using pure rotational spectroscopy at radio frequencies (*3*). We therefore searched for PAHs using observations of TMC-1 in the range of 8 to 33.5 GHz, where rotational emission lines of many aromatic molecules are predicted to be strongest, given the 5 to 10 K temperature of this cloud (*4*). Using the 100-m Robert C. Byrd Green Bank Telescope (GBT), we initiated an observing project entitled GOTHAM (GBT Observations of TMC-1: Hunting Aromatic Molecules) to perform a spectral line survey of TMC-1. The first reduction of the GOTHAM data, comprising observations obtained between February 2018 and May 2019 (hereafter data release 1, or DR1), has near-continuous frequency coverage in the ranges of 8 to 11.6 GHz and 18 to 29.5 GHz, with a few small gaps. Details of these observations have been presented elsewhere (*4*, *5*). Further observations were obtained until June 2020 (hereafter DR2), which allowed us to extend the coverage to higher frequencies and improved the sensitivity in some regions already covered by DR1 (fig. S1) (*4*, *5*). Both datasets have a spectral resolution of 1.4 kHz, equivalent to a velocity resolution of 0.05 to 0.02 km s^{-1} (varying with frequency).

Given the previous detection of BN (*2*), a single benzene ring with an attached CN group, we searched for derivatives of naphthalene (two fused benzene rings; $C_{10}H_8$). Like benzene, naphthalene lacks a permanent dipole moment and therefore has no pure rotational spectrum. However, its CN-substituted derivatives, 1- and 2-cyanonaphthalene (1-CNN and 2-CNN; collectively CNNs), have large permanent dipole moments (Fig. 1) and laboratory-measured rotational spectra (*6*) that peak in the frequency region covered by our observations (fig. S3).

Similarly to BN (*2*), initial searches for the CNNs in our DR1 data showed no individual rotational lines above the noise level of the observations. We therefore calculated a spectral stack by combining the positions of all lines predicted in the dataset. Because the average excitation temperature of molecules (T_{ex} ~ 7 K) and the velocity (5.8 km s^{-1}) of TMC-1 are known from other species (*4*, *7*, *8*), we averaged the signal from all rotational transitions covered by our observations weighted

[1]Department of Chemistry, Massachusetts Institute of Technology, Cambridge, MA 02139, USA. [2]National Radio Astronomy Observatory, Charlottesville, VA 22903, USA. [3]Center for Astrophysics, Harvard & Smithsonian, Cambridge, MA 02138, USA. [4]Department of Physics and Astronomy, Benedictine College, Atchison, KS 66002, USA. [5]Center for Astrochemical Studies, Max Planck Institute for Extraterrestrial Physics, Garching, Germany. [6]Institute for Theoretical Chemistry, University of Stuttgart, Stuttgart, Germany. [7]Astrochemistry Laboratory and the Goddard Center for Astrobiology, NASA Goddard Space Flight Center, Greenbelt, MD 20771, USA. [8]Université de Rennes, Centre National de la Recherche Scientifique, Institut de Physique de Rennes, Unité Mixte de Recherche 6251, F-35000 Rennes, France. [9]Institute for Astrophysics and Computational Sciences, Department of Physics, Catholic University of America, Washington, DC 20064, USA. [10]Department of Chemistry, University of Virginia, Charlottesville, VA 22904, USA. [11]Department of Astronomy, University of Virginia, Charlottesville, VA 22904, USA. [12]Astro Space Center, Lebedev Physical Institute, Russian Academy of Sciences, Moscow, Russia.
***Corresponding author. Email: brettmc@mit.edu**
†These authors contributed equally to this work.

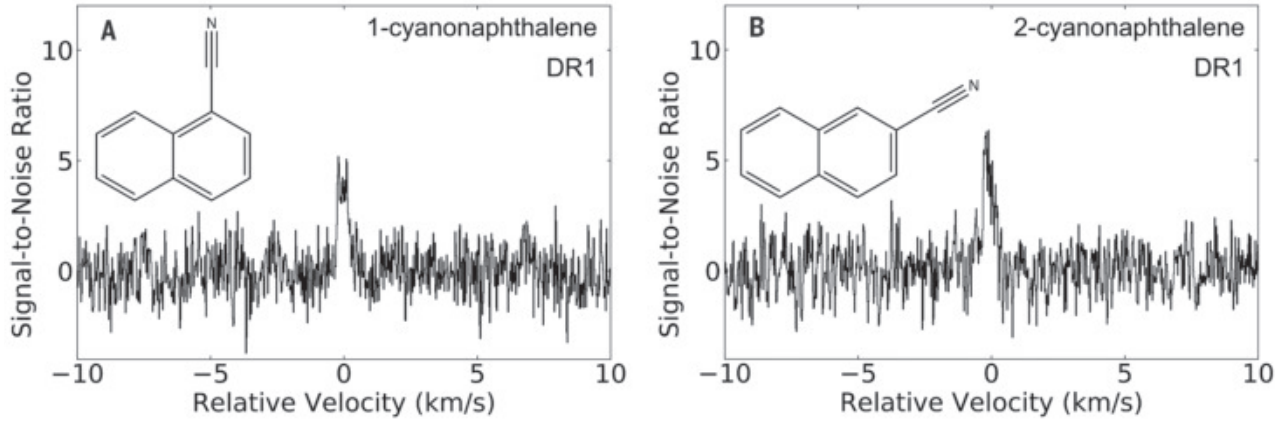

Fig. 1. Molecular structures and spectral stacks of 1-CNN and 2-CNN in the GOTHAM DR1 data. These molecules are derivatives of naphthalene, substituting a nitrile (–CN) group for a hydrogen atom. This substitution produces two distinct isomers, both of which are highly polar, with dipole moments (μ) along the *a* and *b* principal axes: (**A**) 1-CNN: μ_a = 3.6 debye, μ_b = 3.0 debye and (**B**) 2-CNN: μ_a = 5.1 debye, μ_b = 1.0 debye (*6*). The spectral stacks are shown relative to the TMC-1 systemic velocity of 5.8 km s^{-1}. The weighting process assumed an excitation temperature of T_{ex} = 7 K.

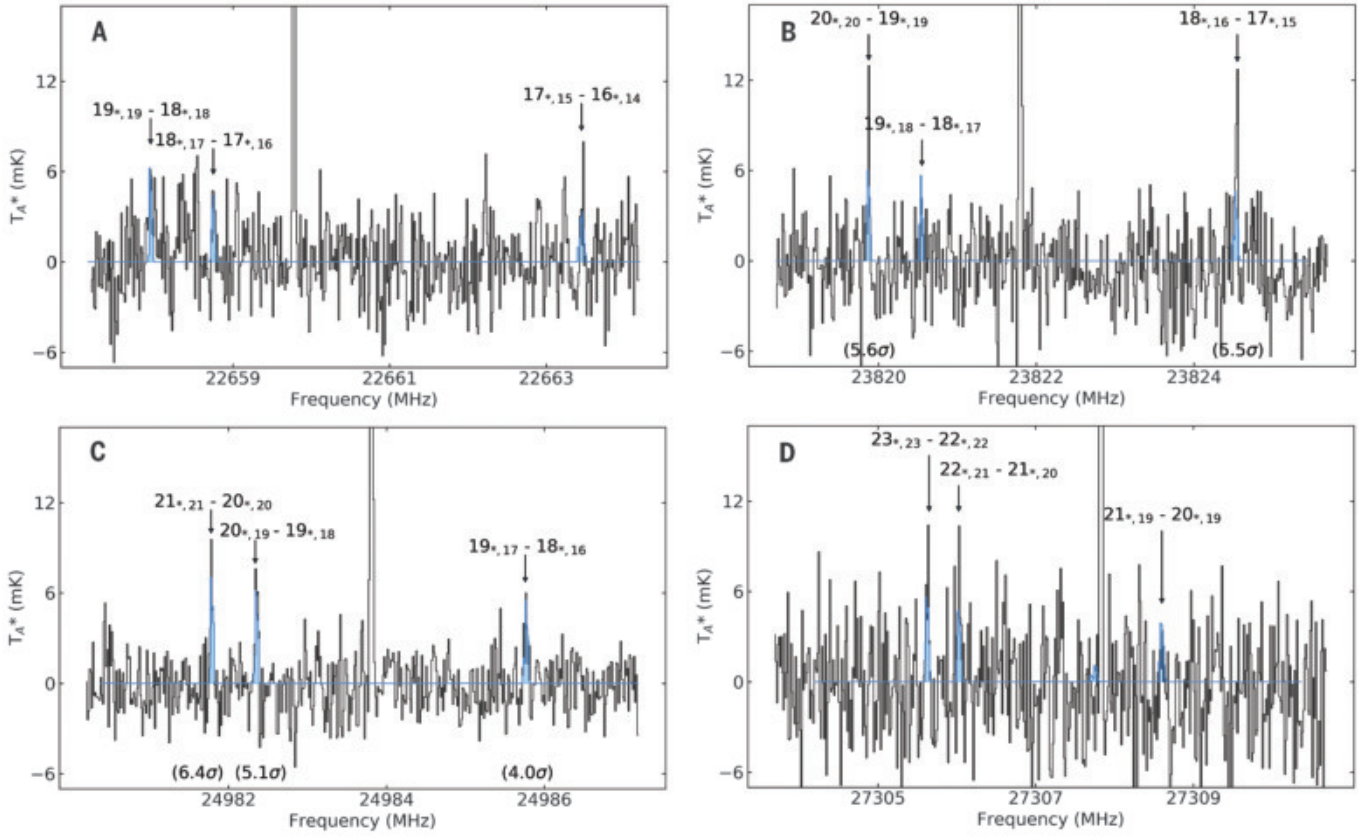

Fig. 2. GOTHAM DR2 spectra in the vicinity of the strongest predicted 1-CNN transitions. (**A** to **D**) Observations are shown in black, with simulated spectra of 1-CNN using the parameters derived from our MCMC analysis (table S5) overlaid in blue. The *y* axis is the atmosphere-corrected antenna temperature scale (T_A*). The observations have not been adjusted for the systemic velocity of TMC-1 (5.8 km s^{-1}). The spectra have been smoothed with a Hanning window to a resolution of 14 kHz for display. The quantum numbers of the transitions, ignoring hyperfine structure, are labeled at the predicted position of each line (arrows). Multiple closely spaced *K*-components of each transition contribute to each line and are denoted by asterisks. Transitions with SNRs ≥4σ are labeled in parentheses beneath the spectra.

by their predicted intensities and by the local noise level of the observations (*5*). The two stacks for 1-CNN and 2-CNN derived from the DR1 data are shown in Fig. 1 and indicate the presence of both molecules.

We used the higher-quality DR2 dataset to determine the physical parameters [T_{ex}, column density (N_T), linewidth (ΔV), source size (θ), and velocity in the local standard of rest (v_{lsr})] that best reproduce the observations. A Markov chain Monte Carlo (MCMC) analysis was used to derive the physical parameters that best reproduce the stacked emission, including radiative transfer corrections for optical depth (*9*), which provides more robust uncertainty

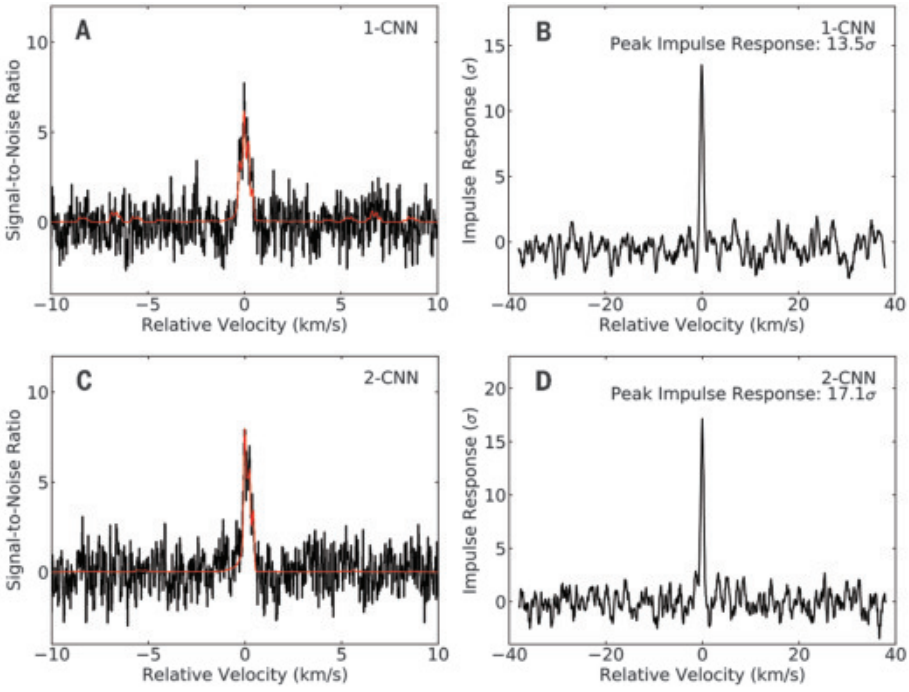

Fig. 3. Stacked spectra and impulse responses for the matched filtering analyses of 1-CNN and 2-CNN. The stacked spectra of (**A**) 1-CNN and (**C**) 2-CNN from the GOTHAM DR2 data are shown in black, overlaid with the line profile in red from the MCMC analysis of the DR2 data. The SNR is shown on a per-channel basis. Impulse response functions of the stacked spectra of (**B**) 1-CNN and (**D**) 2-CNN are shown, using the simulated line profiles as matched filters. The peak of the impulse response functions provides a minimum significance for the detections of 13.5σ and 17.1σ, respectively.

estimates than a least-squares fit. For this more detailed analysis, we assumed four partially overlapping Doppler velocity components with v_{lsr} between 5.5 and 6.1 km s^{-1}, as seen in observations of other species (*10*, *11*), each with their own column density and source size (the latter is poorly constrained in our single-dish observations). A single excitation temperature T_{ex} and linewidth ΔV (*4*, *12*, *13*) are assumed to apply to all four velocity components. We used the physical parameters from the more strongly detected BN (table S4 and fig. S15) as Gaussian priors in this analysis.

The results from the MCMC analysis for 1-CNN (table S5 and fig. S16) and 2-CNN (table S6 and fig. S17) yield total column densities (the sum of all four velocity components) of $7.35^{+3.33}_{-4.63} \times 10^{11}$ cm^{-2} and $7.05^{+3.23}_{-4.50} \times 10^{11}$ cm^{-2}, respectively. At those column densities, we predict that roughly a dozen lines of 1-CNN, and none of 2-CNN, should be above the local noise level in parts of the DR2 data. Figure 2 shows the DR2 data along with simulated profiles of those lines; all others are predicted to be below the noise. There is evidence for at least five lines with peak signal-to-noise ratios (SNRs) >4σ and tentative evidence for several others. Although these individual lines are weak, they provide us with additional confidence in the results of the stacking process.

The information content of the entire spectrum can also be used to assess the presence or absence of each molecule, which has many weak transitions at or below the root mean square (RMS) noise level of the observations. We performed this test using spectral stacking combined with matched filtering (*5*, *13*). Although care must be taken with respect to interloping signals and the noise characteristics of the data, this approach increases the SNR, with the averaged spectrum encapsulating the total information content of all observed lines, rather than examining each (lower-significance) line individually.

The details of this methodology, including analysis of the robustness, are presented elsewhere (*5*, *13*). Briefly, we extracted a small portion of the observations centered on the predicted frequency of each spectral line, discarding any windows with a spectral feature >5σ to avoid interloping signals from other species. A signal-to-noise weighted average of the spectra was then calculated on the basis of the expected intensity of the line (derived from the MCMC parameters) and the RMS noise of the observations, verified to contain no red-noise contamination (fig. S11). The results are shown in Fig. 3, A and C. Calculating the overall significance of any detections required us to consider the peak SNR in the central channel as well as the SNR of all channels that contain molecular emission. To do this, the model spectra were stacked using the same weights as those used for the observations, and the stacked model was then used as a matched filter that was cross-correlated with the stacked observations. The resulting impulse response spectrum provides a lower limit on the statistical significance (Fig. 3, B and D): 13.5σ for 1-CNN and 17.1σ for 2-CNN. We performed additional tests (*5*), including jack-knife tests (fig. S4) and checks for spurious detections (figs. S5 to S8 and S10), to evaluate the robustness of this methodology.

We conclude that both CNNs are detected in TMC-1. The presence of these PAH molecules in the interstellar medium (ISM) supports the hypothesis that PAHs are responsible for the unidentified infrared (UIR) emission bands (*1*). The UIR bands are composed of features at mid-infrared wavelengths characteristic of C–C and C–H stretching and bending motions of aromatic molecules, consistent with PAHs. Although the infrared spectra of different PAH molecules are readily distinguishable in the laboratory at high spectral resolution (*14*), the assignment of individual PAHs as carriers of the UIR features has not been possible because the differences in frequency are smaller than the width of the observed interstellar band profiles. It is therefore likely that many different PAHs contribute to the UIR emission bands (*1*). Although the carriers of the UIRs must have substantial aromatic character and PAHs are likely responsible for a sizable fraction of the overall emission, the specific structures and elemental compositions of the carriers remain a subject of debate (*15*). This uncertainty has limited the detailed analysis of sources that emit UIR bands (*16*).

We now consider the interstellar formation and destruction chemistry of 1-CNN and 2-CNN as individual molecules rather than PAHs in aggregate. Two scenarios have been proposed to explain the formation of PAHs: "top-down" and "bottom-up" formation chemistry. In the top-down scenario, small interstellar carbon clusters, or carbon soot particles in the envelopes of evolved stars, are broken down by ultraviolet (UV) radiation to form a variety of PAHs (*17*). PAHs may also be formed on the surfaces of interstellar dust grains in the envelopes of evolved stars (*18*). These PAHs are then distributed into the ISM, including molecular clouds. In the bottom-up scenario, PAHs are built in situ in molecular clouds from smaller precursors through chemical evolutionary pathways such as gas-phase ion-molecule and neutral-neutral reactions or reactions occurring on grain surfaces (*19*, *20*).

Any population of PAHs inherited by TMC-1 from prior top-down formation must have

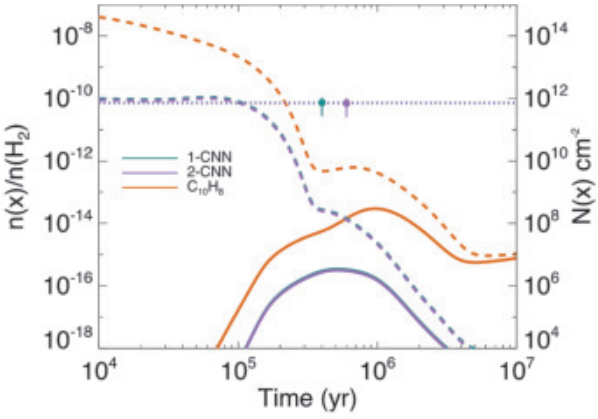

Fig. 4. Results of the astrochemical models. Calculated abundances of naphthalene (orange), 1-CNN (purple), and 2-CNN (teal) under TMC-1 conditions. Data for 1-CNN and 2-CNN overlap. Results are shown for our fiducial model (solid lines) and a model that assumes an initial naphthalene abundance of $n(C_{10}H_8)/n(H_2) = 1.0 \times 10^{-7}$ [where $n(x)$ is the volume density of molecule x] (dashed lines). The right y axis shows equivalent column densities, assuming $n(H_2) = 10^{22}$ cm^{-2}. The circles indicate the values for these species derived from our DR2 observations, with 1σ error bars, at arbitrary times. The dotted horizontal lines show these values extended over the range of the x axis for display.

survived in the diffuse ISM. However, PAHs composed of less than ~20 to 30 atoms cannot radiatively stabilize upon absorption of a UV photon and are therefore destroyed in the diffuse ISM (*21*). The presence of small PAHs (CNNs) in TMC-1 suggests that at least some in situ bottom-up formation has occurred.

Existing astrochemical reaction networks do not include detailed PAH formation and destruction chemistry (*22*, *23*). We have extended a gas-grain chemical network (*24*) to include reactions relevant to naphthalene, 1-CNN, and 2-CNN, along with reactions relevant to other detections from the GOTHAM survey (*4*, *12*, *13*, *25*).

We included two major formation routes for naphthalene. The first is formation of $C_{10}H_8$, directly from the reaction of a phenyl radical with vinylacetylene

$$C_6H_5 + CH_2CHC_2H \rightarrow C_{10}H_8 + H \quad (R1)$$

This barrierless gas-phase reaction is viable under TMC-1–like conditions (*26*). The second route involves a dihydronaphthalene ($C_{10}H_{10}$) precursor that forms via the reaction between a phenyl radical and 1,3-butadiene

$$C_6H_5 + CH_2CHCHCH_2 \rightarrow C_{10}H_{10} + H \quad (R2)$$

This reaction is also expected to occur in the ISM (*27*). Successive abstraction of two hydrogen atoms from $C_{10}H_{10}$, both of which have no energy barrier (*28*), yields $C_{10}H_8$. For all species added to our network, we assume gas-phase depletion via both destructive reaction with ions (with rate coefficients calculated using the Langevin formula) and adsorption onto grains.

For 1-CNN and 2-CNN, we added the formation routes

$$C_{10}H_8 + CN \rightarrow 1\text{-CNN} + H \quad (R3)$$

$$C_{10}H_8 + CN \rightarrow 2\text{-CNN} + H \quad (R4)$$

assuming equal branching fractions. We assume that reactions R3 and R4 occur on every collision, because analogous reactions between CN radicals and unsaturated hydrocarbons such as benzene are known to be both barrierless and exothermic (*29*). We included a process for 1-CNN that is analogous to the one for naphthalene (*26*): This process involves the reaction of phenyl radicals (C_6H_5) with cyanovinylacetylene ($HC_2CHCHCN$), which presumably occurs at the collisional rate. However, we find that the contribution of this reaction to the 1-CNN abundance is small. Our reaction network operates with the assumption that the chemistry of PAHs in molecular clouds such as TMC-1 is predominantly in the gas phase, because the rate of thermal desorption of CNN from dust grains at ~10 K is negligible. Nonthermal desorption mechanisms may allow for the introduction of aromatic molecules into the gas from icy surfaces (*30*) but are not included in our calculations.

The results of our simulations are shown in Fig. 4. In the fiducial model, the abundances of both 1- and 2-CNN are underpredicted by $\gtrsim$6 orders of magnitude. CN is abundant in the model, so naphthalene is the limiting reagent. The large disparity between observations and predictions suggests that (i) additional production pathways for naphthalene may be missing, (ii) the efficiency of existing pathways is substantially underestimated, or (iii) a nontrivial initial abundance of naphthalene is inherited from prior top-down chemistry. To test scenario (iii), we performed a second calculation to ascertain how PAHs inherited from earlier stages of cloud evolution affect the abundances of 1- and 2-CNN under TMC-1 conditions. For this model, we added an initial abundance of naphthalene (representing an inherited population) tuned to reproduce the observational data. We found agreement with the observations for a naphthalene abundance of $n(C_{10}H_8)/n(H_2) = 1.0 \times 10^{-7}$ at early times, where n refers to the volume density. This would correspond to ~1% of the total carbon. However, the calculated abundances of 1-CNN and 2-CNN again deviate from the observational values at times $>10^5$ years, the typical lifetime of sources such as TMC-1.

Our calculations neglect grain-surface formation pathways (*5*). Nevertheless, we regard the required initial abundance of naphthalene as unrealistically large, which in turn implies that a purely top-down formation pathway is also disfavored. Conversely, the pathways we have considered for in situ bottom-up formation are also insufficient to reproduce observations. Other pathways are required, such as ion-neutral reactions. Such processes are generally efficient under interstellar conditions and can lead to $C_{10}H_9^+$ (*31*), which may form naphthalene as a product of its dissociative recombination with electrons in a manner analogous to the benzene formation route from $C_6H_7^+$ (*32*).

We conclude that two PAHs—1-CNN and 2-CNN—are present in the molecular cloud TMC-1. We are unable to explain the derived abundances with either top-down or bottom-up formation scenarios, indicating that other routes may be required or that existing routes may be more efficient than previously thought.

REFERENCES AND NOTES

1. A. G. G. M. Tielens, *Annu. Rev. Astron. Astrophys.* **46**, 289–337 (2008).
2. B. A. McGuire *et al.*, *Science* **359**, 202–205 (2018).
3. B. A. McGuire, *Astrophys. J. Suppl. Ser.* **239**, 17 (2018).
4. B. A. McGuire *et al.*, *Astrophys. J.* **900**, L10 (2020).
5. Materials and methods are available as supplementary materials.
6. D. McNaughton *et al.*, *Mon. Not. R. Astron. Soc.* **476**, 5268–5273 (2018).
7. P. Gratier *et al.*, *Astrophys. J. Suppl. Ser.* **225**, 25 (2016).
8. N. Kaifu *et al.*, *Publ. Astron. Soc. Jpn.* **56**, 69–173 (2004).
9. B. E. Turner, *Astrophys. J. Suppl. Ser.* **76**, 617 (1991).
10. K. Dobashi *et al.*, *Astrophys. J.* **864**, 82 (2018).
11. K. Dobashi *et al.*, *Astrophys. J.* **879**, 88 (2019).
12. C. Xue *et al.*, *Astrophys. J.* **900**, L9 (2020).
13. R. A. Loomis *et al.*, *Nat. Astron.* **5**, 188–196 (2021).
14. D. M. Hudgins, S. A. Sandford, *J. Phys. Chem. A* **102**, 329–343 (1998).
15. S. Kwok, Y. Zhang, *Nature* **479**, 80–83 (2011).
16. C. W. Bauschlicher Jr., A. Ricca, C. Boersma, L. J. Allamandola, *Astrophys. J. Suppl. Ser.* **234**, 32 (2018).
17. O. Berné, J. Montillaud, C. Joblin, *Astron. Astrophys.* **577**, A133 (2015).
18. L. Martínez *et al.*, *Nat. Astron.* **4**, 97–105 (2020).
19. P. M. Woods, T. J. Millar, A. A. Zijlstra, E. Herbst, *Astrophys. J.* **574**, L167–L170 (2002).
20. B. M. Jones *et al.*, *Proc. Natl. Acad. Sci. U.S.A.* **108**, 452–457 (2011).
21. M. Chabot, K. Béroff, E. Dartois, T. Pino, M. Godard, *Astrophys. J.* **888**, 17 (2020).
22. R. P. A. Bettens, E. Herbst, *Astrophys. J.* **468**, 686 (1996).

23. R. Bettens, E. Herbst, *Astrophys. J.* **478**, 585–593 (1997).
24. C. N. Shingledecker, J. Tennis, R. L. Gal, E. Herbst, *Astrophys. J.* **861**, 20 (2018).
25. M. C. McCarthy *et al.*, *Nat. Astron.* **5**, 176–180 (2020).
26. D. S. N. Parker *et al.*, *Proc. Natl. Acad. Sci. U.S.A.* **109**, 53–58 (2012).
27. R. I. Kaiser *et al.*, *J. Phys. Chem. A* **116**, 4248–4258 (2012).
28. P. A. Jensen *et al.*, *Mon. Not. R. Astron. Soc.* **486**, 5492–5498 (2019).
29. I. R. Cooke, D. Gupta, J. P. Messinger, I. R. Sims, *Astrophys. J.* **891**, L41 (2020).
30. D. Marchione, J. D. Thrower, M. R. S. McCoustra, *Phys. Chem. Chem. Phys.* **18**, 4026–4034 (2016).
31. V. G. Anicich, "An index of the literature for bimolecular gas phase cation-molecule reaction kinetics" (JPL Publication 03-19, NASA, 2003); http://hdl.handle.net/2014/7981.
32. M. J. McEwan *et al.*, *Astrophys. J.* **513**, 287–293 (1999).
33. GOTHAM Collaboration, Spectral Stacking Data for Phase 2 Science Release of GOTHAM, Version 3.0, Harvard Dataverse (2020); https://doi.org/10.7910/DVN/K9HRCK.
34. GOTHAM Collaboration, Replication Data for Astrochemical Models in the Detection of 1- and 2-cyanonaphthalene, Version 2.0, Harvard Dataverse (2021); https://doi.org/10.7910/DVN/OMYNAE.

ACKNOWLEDGMENTS

The National Radio Astronomy Observatory is a facility of the National Science Foundation (NSF) operated under cooperative agreement by Associated Universities, Inc. The Green Bank Observatory is a facility of the NSF operated under cooperative agreement by Associated Universities, Inc. **Funding:** B.A.M. was supported by NASA through Hubble Fellowship grant HST-HF2-51396 awarded by the Space Telescope Science Institute, which is operated by the Association of Universities for Research in Astronomy, Inc., for NASA, under contract NAS5-26555. A.M.B. acknowledges support from the Smithsonian Institution as a Submillimeter Array (SMA) Fellow. M.C.M. and K.L.K.L. acknowledge financial support from NSF grants AST-1908576 and AST-1615847 and NASA grant 80NSSC18K0396. C.N.S. thanks the Alexander von Humboldt Stiftung/Foundation for their generous support, as well as V. Wakelam for use of the NAUTILUS v1.1 code. I.R.C. acknowledges funding from the European Union's Horizon 2020 research and innovation program under the Marie Skłodowska-Curie grant agreement 845165-MIRAGE. S.B.C. and M.A.C. were supported by the NASA Astrobiology Institute through the Goddard Center for Astrobiology. E.H. thanks the NSF for support through grant AST 1906489. C.X. is a Grote Reber Fellow, and support for this work was provided by the NSF through the Grote Reber Fellowship Program administered by Associated Universities, Inc./National Radio Astronomy Observatory and the Virginia Space Grant Consortium. **Author contributions:** Conceptualization: B.A.M., A.M.B., A.J.R., and S.K.; Methodology: B.A.M., A.M.B., K.L.K.L., and R.A.L.; Software: R.A.L., K.L.K.L., and B.A.M.; Data curation: B.A.M., R.A.L., A.M.B., K.L.K.L., C.X., M.A.S., A.J.R., and I.R.C.; Modeling: C.N.S., A.M.B., C.X., E.R.W., S.B.C., and E.H.; Writing – original draft: B.A.M., A.M.B., R.A.L., C.N.S., K.L.K.L., and M.C.M.; Writing – review & editing: all authors. **Competing interests:** We declare no competing interests. **Data and materials availability:** All of our GBT and VLA data are available in the NRAO archive at https://archive.nrao.edu/archive/advquery.jsp under project codes AGBT17A_164, AGBT17A_434, AGBT18A_333, AGBT18B_007, AGBT19A_047, and TCAL0003. Observational data windowed around these transitions; the full catalogs, including spectroscopic properties of each transition; and the partition function used in the MCMC analysis are available in the Harvard Dataverse repository (*33*). We obtained the NAUTILUS code from http://perso.astrophy.u-bordeaux.fr/~vwakelam/Nautilus.html. Input and output files for the astrochemical models are also available in Harvard Dataverse (*34*).

SUPPLEMENTARY MATERIALS

science.sciencemag.org/content/371/6535/1265/suppl/DC1
Materials and Methods
Supplementary Text
Figs. S1 to S19
Tables S1 to S6
References (*35*–*59*)

16 March 2020; accepted 4 February 2021
10.1126/science.abb7535

ATMOSPHERIC AEROSOLS

Record-breaking aerosol levels explained by smoke injection into the stratosphere

Eitan Hirsch[1] and Ilan Koren[2]*

The early months of 2020 showed record-breaking levels of aerosol optical depth (AOD) over the Southern Hemisphere (SH). Apart from the tropics, monthly AOD values over most of the SH exceeded the average by more than three standard deviations. This anomalous AOD is attributed to a combination of the intensity and location of the Australian bushfires. The fires took place south enough, where the tropopause altitude is relatively low, within the mid-latitude cyclone belt. This location allowed for deep convection over and downwind of the fires, which transported the smoke to the stratosphere, where its lifetime is an order of magnitude longer than it would have been in the lower atmosphere. The lower bound of the stratospheric smoke mass in January 2020 was ~2.1 ± 1 teragrams, which lead to cooling by more than 1.0 ± 0.6 watts per square meter over cloud-free oceanic areas.

The lifetime of aerosols in the atmosphere ranges from minutes to weeks in the lower atmosphere and months to years if they reach the stratosphere (*1*, *2*). Such differences in the aerosols' lifetimes are manifested in their radiative effect. When aerosols reach the stratosphere, their radiative effect is mostly driven by direct interactions of the particles with solar electromagnetic radiation. Submicrometer particles scatter and absorb light in the shortwave (SW) spectral range, thereby reducing the downward solar radiation. Over a dark background, the overall top-of-the-atmosphere effect will be an increase in the radiation reflected back to space (i.e., an increase in albedo). In the case of absorbing aerosols above reflecting clouds, the upward photon flux can be reduced, and the local albedo can be decreased (*3*). Smoke or a thick aerosol layer with coarse particles can also interact with longwave (LW) radiation and affect fluxes in that regime as well (*4*, *5*).

The troposphere is topped by an inversion layer called the tropopause. The height of the tropopause ranges between an average of >17 km in the tropics to <10 km over the high latitudes (*6*). Energetic volcanic eruptions inject aerosols to the stratosphere, which substantially affect Earth's radiative budget in time scales of months to years (*7*). During the second half of the 20th century, three such major volcanic eruptions have been documented: Fuego (1974) (*8*), El Chichón (1982) (*9*), and Pinatubo (1991) (*10*).

Biomass burning is considered to be among the leading sources for aerosols in the atmosphere. A global 8600 Tg of dry matter is estimated to burn every year (*11*), mainly in tropical America, Africa, and Asia. According to continental-scale analyses, wildfires in Australia are characterized by spatial-seasonal patterns, and the fire activity occurs predominantly in the savanna landscapes of monsoonal northern Australia during the dry Southern Hemisphere (SH) summer (*12*). It has been demonstrated in the past that carbonaceous aerosols from large-scale fire events—such as the Canadian wildfires in 2017—can penetrate the tropopause and enter the lower stratosphere (*13*). The aerosol load emitted into the stratosphere during these wildfires has been shown to be comparable to that of a moderate volcanic eruption (*14*).

The Australian bushfire season of 2019 to 2020 was record-breaking in several ways (*15*–*17*). This bushfire season was distinct not only in its intensity, but also in its spatial and temporal distribution, with an important component over southeastern Australia (Fig. 1). Since 1850, 29 fire events have been documented to cover areas larger than 1 Mha. Five of these events occurred in 2020, and two of them occurred in the southeast region of Australia (*18*). Stratospheric smoke from Australia's bushfires was observed over South America in mid-January 2020 (*19*). It was reported that excessive heat from pyrocumulonimbus (pyroCb) convection caused the smoke to cross the tropopause and later reach a height of 35 km, lifted by solar absorption–induced buoyancy (*20*, *21*).

Aerosol optical depth (AOD) is a common measure to estimate aerosol loading, and it is a key parameter in the calculation of radiative effects. Several space-borne sensors monitor Earth's atmosphere and provide excellent temporal and spatial coverage. In this analysis, we focus on the fate and remote effects of the smoke from the Australian bushfires. Because the lower latitudes of the SH are affected by aerosols from biomass burning in the tropics as well as dust aerosols from the Sahara, we selected a latitude belt between 20°S and

[1]Environmental Sciences Division, Israel Institute for Biological Research, Nes-Ziona 7404801, Israel. [2]Department of Earth and Planetary Sciences, Weizmann Institute, Rehovot 76100, Israel.
***Corresponding author. Email: ilan.koren@weizmann.ac.il**

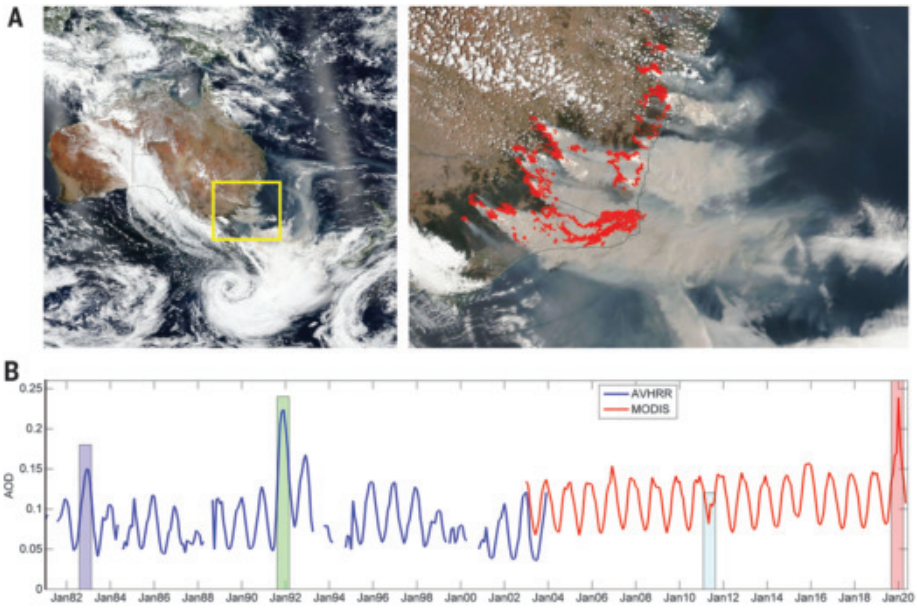

Fig. 1. Southeast Australian smoke emissions and their record-breaking signature on AOD levels over the SH. (**A**) (Left) Smoke emission off the southeast Australian coast on 4 January 2020, shown as a Visible Infrared Imaging Radiometer Suite (VIIRS) true-color image over southeastern Australia. (Right) Red dots mark the locations of fires and areas with thermal anomalies. The emitted smoke density was so high that all of the aerosol algorithms failed to estimate the optical depth over it. (**B**) Average AOD values over the oceans for the mid-southern latitudes (20°S to 70°S) over all longitudes. The blue line was retrieved by AVHRR (wavelength 630 nm), and the red line represents MODIS retrieval (retrieved at 660 nm and scaled to 630 nm). The shaded areas mark the AOD values retrieved during the El Chichón eruption in 1982 (light purple), the Pinatubo and Hudson eruptions in 1991 (light green), the Puyehue-Cordón Caulle eruption in 2011 (light cyan), and the Australian bushfires of 2019 to 2020 (light red).

70°S (referred to here as the belt) in which the Australian smoke is mostly confined and aerosols from northern sources are not likely to contribute (see the clear separation in the global averaged AOD map in fig. S1). We use a combined time series of AOD measurements from two satellite missions [Advanced Very High Resolution Radiometer (AVHRR) from 1981 to 2003 (*22*) and Moderate Resolution Imaging Spectroradiometer (MODIS) instruments aboard the Aqua satellite from 2002 to 2020 (*23*)]. The MODIS AOD wavelength was scaled to match that of the AVHRR (*24*). The overlap of the measurements allowed us to evaluate the consistency of the two systems (*25*). Figure 1B shows the average AOD values over the oceans in the selected belt, demonstrating record-breaking AOD values in early 2020.

Figure 2 shows the spatial extent of this effect. We define the AOD anomalies as the differences between the averages of the previous 17 years (2003 to 2019; Fig. 2A) and the values from January 2020 (Fig. 2B). The figure indicates an AOD increase by >50% over most of the SH. Figure 2C shows net anomalies normalized by the standard deviation, indicating an increase by ~3 standard deviation units over the belt (see the supplementary materials for more details).

As shown in Fig. 2, the record-breaking increase in AOD is distributed quite uniformly around the SH. Therefore, the 2020 anomaly

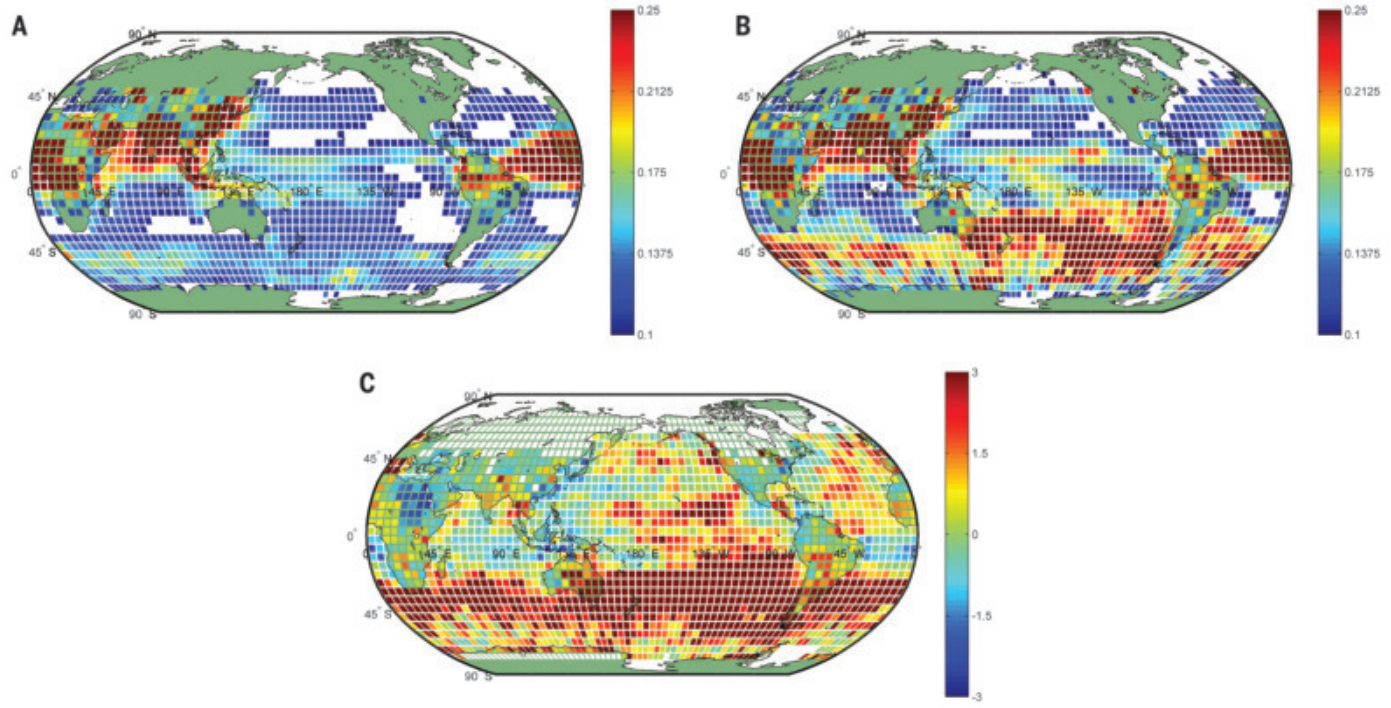

Fig. 2. The SH anomaly for January 2020 (spatial resolution of 5° by 5°). (**A**) Interannual (2003 to 2019) monthly average AOD values for January. (**B**) Monthly AOD values for January 2020. A notable increase in the AOD values over the SH is observed. (**C**) The change in January 2020 AOD values compared with the interannual January average (expressed in standard deviation units).

can be captured by the zonal AOD (land and ocean) averages. Figure 3 shows the monthly mean AOD zonal average as measured by the Aqua MODIS for a period of 18 years. August to December 2019 and January to July 2020 AOD values are depicted in black, and the averages of the previous 17 years are shown in blue (standard deviations are marked in red). These values clearly show that the smoke regime starts at ~20°S and extends until the South Pole (see the separation between the smoke belt and contributions from the tropics in fig. S1). The elevated values are clearly shown from November 2019 until July 2020—after July, the smoke contribution is still evident, but fire smoke originating from South America exacerbates a clear separation of sources. During January 2020, massive aerosol loads were injected into the atmosphere, resulting in a notable change in AOD (as high as 66%) in latitudes 20°S to 70°S. In February, the dominance of the excessive aerosols is still evident over most of the SH; from March to July, the aerosols seem to migrate southward toward Antarctica, but its effect can still be observed over most of the SH.

The Ozone Monitoring Instrument's (OMI) ultraviolet aerosols index (UVAI) is sensitive to aerosol type, concentration, and heights in the atmosphere (*13*, *26*). Moreover, it is sensitive to aerosols over clouds and therefore is an ideal measurement for stratospheric aerosols located above tropospheric clouds (*27*). Analysis of the anomaly in the signal of the UVAI (Fig. 4A and see supplementary materials for details) reveals that the onset of the extreme events occurs around 1 January 2020 at the longitude of the eastern part of Australia. Before this point in longitude and in time, the background anomaly values are relatively low—well within the standard deviation range. However after this point, an elevated value spreads from this longitude eastward and, within ~2 weeks, manages to circulate the entire hemisphere and reach the same longitude again. From this point in time, the entire hemispheric anomaly is elevated to values that are consistently above the standard deviation, decaying slowly and reaching an elevation of 1 standard deviation unit by the end of July 2020. The long-lasting, smooth aerosols index anomaly over the entire hemispheric belt and its slow decay suggest a signature of stratospheric smoke. Tropospheric smoke will not last that long in the atmosphere and would not likely be transported uniformly over longer distances: The few smaller plumes from eastern Australia earlier in 2019 most likely did not reach the stratosphere and therefore decayed fast, leaving a smaller signature as they spread. Moreover, circulating the entire hemisphere in a time range of 15 days suggests an average westerly windspeed of ~22 m/s, which is typical for the lower stratosphere in the higher latitudes (fig. S5) and is by far higher than the typical winds in the troposphere, which also exhibit different directions.

This leads us to consider several questions. What is the mechanism that enabled an excessive amount of smoke to reach the stratosphere? How much smoke was injected into the stratosphere? And what would be the

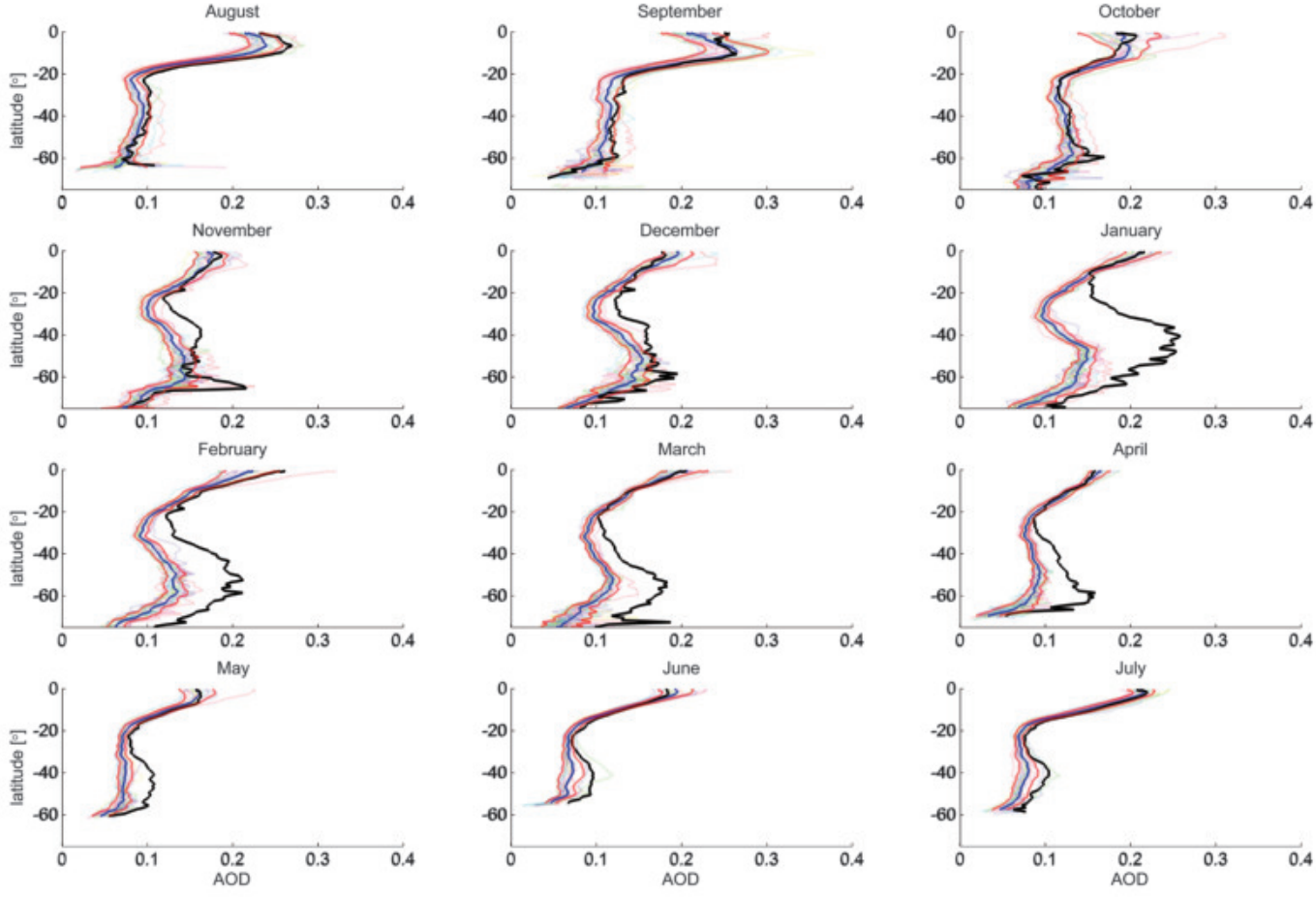

Fig. 3. AOD zonal averages (land and ocean) of the last 18 years in the SH (August to December, years 2002 to 2019; January to July, years 2003 to 2020). Shaded areas represent the previous 17 years of data with averages shown in blue and standard deviations shown in red. August 2019 to July 2020 values are marked in black. As early as November 2019, an increase in the average zonal AOD is noticeable at latitudes 20°S to 40°S. The average zonal AOD increases markedly in January to February and affects latitudes 20°S to 70°S. In March to July, the effect starts to decrease but is still substantial.

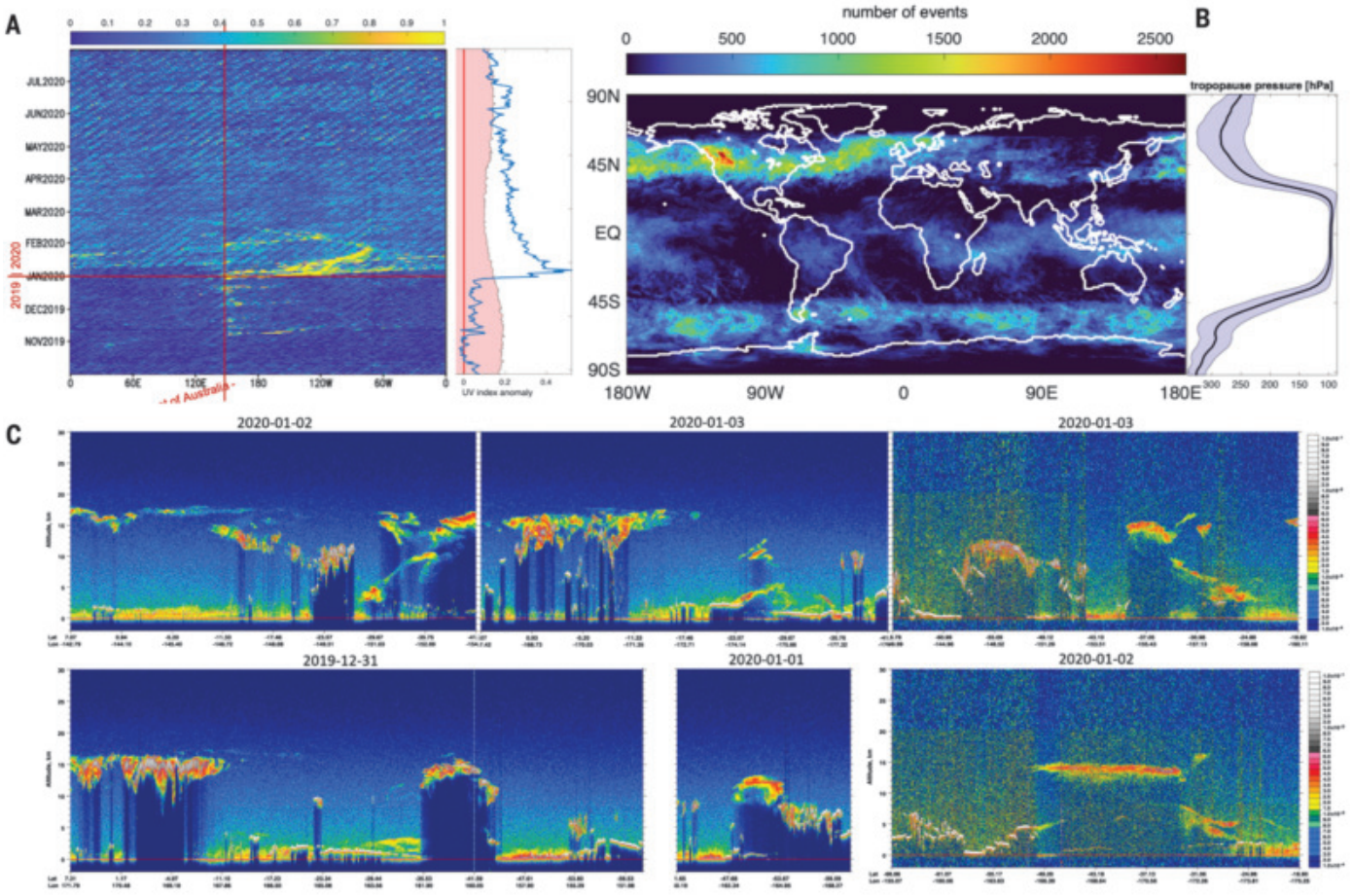

Fig. 4. On the smoke transport to the stratosphere. (**A**) Anomalies of OMI UVAI values averaged over the 20°S-to-70°S belt. (Left) Time-latitude average of the index anomaly. The vertical red line marks the longitude of eastern Australia, and the horizontal red line indicates the beginning of 2020. Note the sharp contrast between the averaged values before the beginning of 2020 (lower part) and after (upper part of the plot). (Right) The anomaly average for the whole belt (blue) and the standard deviation (shaded red). Note the clear increase in the anomaly values around 1 January 2020 and the slow decay later on. (**B**) Statistical map of the number of deep convective cloud events shows that their tops are likely to overshoot the tropopause during January 2020. The average tropopause height profile is shown on the right. (**C**) Six examples of CALIPSO cross sections showing smoke segments (marked in smoother yellow-red areas) lifted by convection. Note the tilted segments on the edge of the lifted ones (see more details in the supplementary materials).

radiative effect of these elevated stratospheric smoke levels?

Few studies have reported smoke transport from biomass burnings over the Amazon and other tropical regions to the upper troposphere and the lower stratosphere (*28*–*30*). However, the most extreme cases were reported in much higher latitudes over Canada and Australia (*31*, *32*). Previous studies have suggested that the Australian smoke was transported to the stratosphere by pyrocumulus clouds that were fueled by the heat from the fires, yielding deep convective clouds that penetrated the tropopause (*20*, *21*). Although some pyrocumulus events were seen over the fires (mostly near Brisbane over the northern fires), geostationary satellite data (*33*) reveal that during most of the fires' duration, the smoke was emitted without pyroconvection above it, thereby reaching the ocean lower in the atmosphere (Fig. 1). Both UVAI data and data from the Cloud-Aerosol Lidar and Infrared Pathfinder Satellite Observation (CALIPSO) light detection and ranging (LIDAR) (supplementary materials) show enhanced smoke signals above convective cells downwind from the fires, which suggests that a large part of the smoke is likely to be transported upward later by convection patterns downwind of the fires' source.

Three factors are interacting to yield this record-breaking smoke transport to the stratosphere: (i) The intensive fire event acts for a long duration over a large area and produces large amounts of smoke; (ii) the fire takes place in higher latitudes, in which the tropopause is shallow; and (iii) the emission area is close to or part of the mid-latitude cyclone belt that is characterized by the steady flux of deep convective clouds that are energetic enough to lift the smoke up into the tropopause (*34*), where the fast and consistent westerly winds then spread it around the hemisphere (fig. S5). Combining the tropopause height and the number of deep convective clouds in the Southern Ocean shows that their tops are likely to exceed the estimated tropopause height for January 2020 (Fig. 4B), which suggests that a substantial contribution of the stratospheric smoke can take place downwind from the fires' source. Backscatter data from the Cloud-Aerosol Lidar with Orthogonal Polarization (CALIOP) LIDAR (*35*) show tropospheric smoke near Australia that is lifted eastward and provide many detailed cases showing smoke that is lifted by convection downwind from the fires (Fig. 4C; detailed examples are shown in figs. S8 to S14).

The AOD anomalies revealed by MODIS can be scaled to estimate the smoke mass [see more details in the supplementary materials,

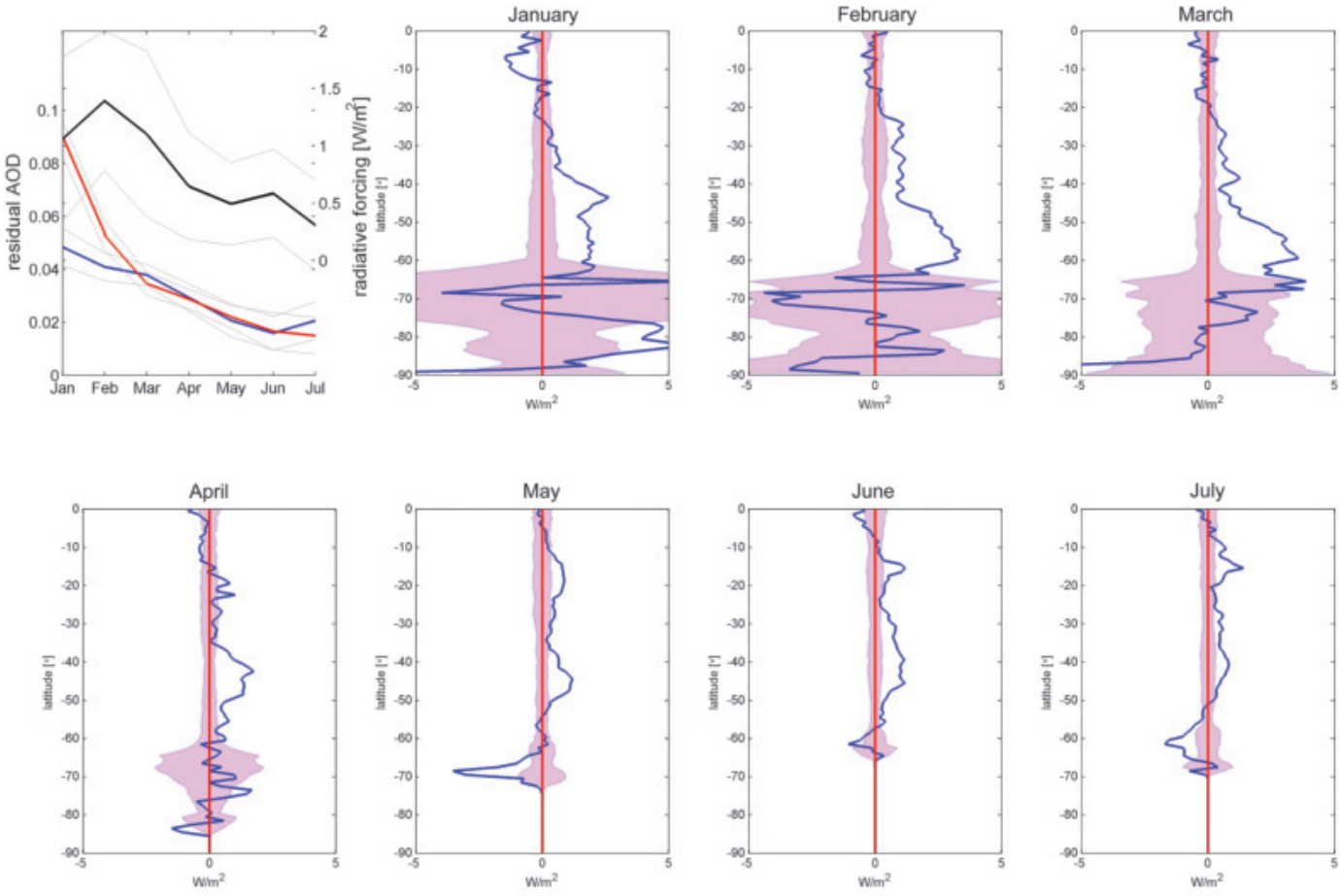

Fig. 5. Stratospheric smoke AOD and forcing estimations. Top left panel shows the AOD anomalies when calculated for all longitudes (red) and when estimated over the far field (blue). The mean smoke forcing is shown in black. The other panels show the zonal far-field SW flux anomalies for January to July 2020. The anomalies are calculated with respect to the 2003 to 2019 measurements, and 1 standard deviation unit is shown on each side of the zero-anomaly red line (red shading).

including a comparison between MODIS and the Ozone Mapping and Profiler Suite (OMPS) Limb Profiler (LP) sensor, which retrieves stratospheric aerosol properties]. To focus on the stratospheric smoke mass, we estimate the residual mass on the basis of the AOD levels as far as possible from the source (far-field), downwind between 1°E and 120°E, mostly over the Indian Ocean, and approaching Australia from the west. The far-field AOD anomalies compared with the total mean anomalies are shown in Fig. 5. The estimated stratospheric smoke mass in the SH during January 2020 is 2.1 ± 1.0 Tg, and it decreases to 1.0 ± 0.5 Tg in July 2020. Notably, when averaging for all smoke anomalies (including the area downwind from and close to the source), the smoke mass estimations are almost doubled in January 2020, but from March onward, the values are approaching the same values as those in the far field, which suggests that the residual is mostly resulting from stratospheric smoke from the entire zonal belt.

The primary measure for radiative effects is fluxes at the top of the atmosphere (TOA). The TOA is the interface between incoming radiation from the Sun and outgoing LW and reflected SW radiative energy. Climate change is measured as the imbalance between these fluxes. The overall direct aerosol effect in the SW depends on the albedo contrast between the aerosol-loaded atmosphere and the baseline atmosphere. Here, we use a direct approach to estimate the stratospheric smoke radiative effect. We use the Clouds and the Earth's Radiant Energy System (CERES) instrument (*36*) on board the Terra and Aqua satellites, which directly measures TOA fluxes. To estimate the stratospheric smoke forcing, similarly to how we approximated the residual mass, we estimate the TOA flux anomalies for the far field. Unlike lower-atmospheric aerosols, stratospheric aerosols are likely to be situated above most clouds. Therefore, they do not interact directly with cloud microphysics and are likely to affect the reflectivity at the top of the cloud. The direct smoke effect in the SW, over cloud-free areas, is the most straightforward measure, as it is proportional to the smoke effect on the albedo.

The anomaly in the SW fluxes compared with those from the previous 17 years is shown in Fig. 5. A clear increase in the flux is shown from 20°S to 60°S. This increase is much larger than three standard deviations from the mean for most latitudes in this range during January to March 2020. The forcing decays but still remains significant until July 2020. The average anomalies for the 20°S-to-60°S belt are >1.1 ± 0.7 W/m^2 for January to March, and they decay to 0.5 ± 0.4 W/m^2 in June 2020. When including Antarctica, the natural variance is larger but the average forcing is similar. Using the measured radiative forcing values leads to an estimation of the single scattering albedo of the smoke aerosols in the range of 0.25 to 0.7 (see supplementary materials for more information).

The SW clear-sky deviation was the only anomaly that was significantly larger than

the standard deviation for all months. The SW all-sky as well as the LW cloud-free and LW all-sky deviations from the mean are not consistent throughout the whole period from January to July and are mostly confined within the standard deviation (supplementary materials). In the SW, the cancellation of the significant flux enhancement in the cloud-free areas is likely caused by a reduction in the albedo of the clouds by the smoke above them (as well as over parts of Antarctica).

A conservative estimation over the far field shows record-breaking AOD levels resulting from smoke from the Australian bushfires that were injected into the stratosphere. Some of the biomass injection occurred by pyroCb activity over the source, but we suggest that the Australian fires are distinct because they took place in the southernmost part of the east coast within the mid-latitude cyclone belt, which allowed for the deep convection over and downwind of the fires to transport the smoke to the stratosphere, where its lifetime is more than an order of magnitude longer than it would be in lower altitudes.

A lower bound of the stratospheric aerosol mass, estimated as far as possible from the source, is assessed to be 2.1 ± 1.0 Tg. Such an amount emitted is comparable to moderate volcanic eruptions, like Kasatochi (1.7 Tg), Sarychev (1.2 Tg), and Nabro (1.5 Tg) (*37*).

The biomass-burning smoke lifetime in the atmosphere increases from a scale of days to months when it reaches the stratosphere, which allows the smoke to spread more uniformly over most of the hemisphere. Moreover, AOD is scaled linearly with the aerosol mass per unit of area and exponentially with the radiative effect. This means that the same aerosol mass will have more collective radiative effect when thinly spread over larger areas.

We note that the effect on climate is not measured only by the overall radiative budget. The stratospheric smoke changes the energy partition in the system. Over cloud-free areas, less solar energy will reach the surface, which can affect the sea temperature, atmospheric temperature and relative humidity profiles, cloud formation, and productivity. On the other hand, smoke absorbs a part of the solar radiation and can warm the stratosphere. This can affect the tropopause inversion strength and change the circulation in the stratosphere. Stratospheric aerosols might modify high (near tropopause) cirrus clouds and possibly affect ozone levels through chemical interactions with pollutants.

REFERENCES AND NOTES

1. F. Raes *et al*., *Atmos. Environ.* **34**, 4215–4240 (2000).
2. P. Hamill, E. J. Jensen, P. Russell, J. J. Bauman, *Bull. Am. Meteorol. Soc.* **78**, 1395–1410 (1997).
3. N. G. Loeb, N. Manalo-Smith, *J. Clim.* **18**, 3506–3526 (2005).
4. Y. Zhou, H. Savijärvi, *Atmos. Res.* **135–136**, 102–111 (2014).
5. V. Ramaswamy, J. T. Kiehl, *J. Geophys. Res.* **90**, 5597–5613 (1985).
6. A. Gettelman *et al*., *Rev. Geophys.* **49**, RG3003 (2011).
7. T. Deshler, *Atmos. Res.* **90**, 223–232 (2008).
8. P. B. Russell, R. D. Hake Jr., *J. Atmos. Sci.* **34**, 163–177 (1977).
9. D. V. Michelangeli, M. Allen, Y. L. Yung, *J. Geophys. Res.* **94**, 18429–18443 (1989).
10. M. P. McCormick, L. W. Thomason, C. R. Trepte, *Nature* **373**, 399–404 (1995).
11. M. O. Andreae, P. Merlet, *Global Biogeochem. Cycles* **15**, 955–966 (2001).
12. J. Russell-Smith *et al*., *Int. J. Wildland Fire* **16**, 361–377 (2007).
13. O. Torres *et al*., *J. Geophys. Res. Atmos.* **125**, e2020JD032579 (2020).
14. D. A. Peterson *et al*., *npj Clim. Atmos. Sci.* **1**, 30 (2018).
15. R. H. Nolan *et al*., *Glob. Change Biol.* **26**, 1039–1041 (2020).
16. M. M. Boer, V. R. de Dios, R. A. Bradstock, *Nat. Clim. Chang.* **10**, 171–172 (2020).
17. N. Borchers Arriagada *et al*., *Med. J. Aust.* **213**, 282–283 (2020).
18. C. Clark, *J. Geosci. Environ. Protection* **8**, 79–94 (2020).
19. K. Ohneiser *et al*., *Atmos. Chem. Phys.* **20**, 8003–8015 (2020).
20. G. P. Kablick III, D. R. Allen, M. D. Fromm, G. E. Nedoluha, *Geophys. Res. Lett.* **47**, e2020GL088101 (2020).
21. S. Khaykin *et al*., *Commun. Earth Environ.* **1**, 22 (2020).
22. A. P. Cracknell, *The Advanced Very High Resolution Radiometer AVHRR* (CRC Press, 1997).
23. A. Lyapustin, Y. Wang, S. Korkin, D. Huang, *Atmos. Meas. Tech.* **11**, 5741–5765 (2018).
24. T. F. Eck *et al*., *J. Geophys. Res.* **104**, 31333–31349 (1999).
25. M. I. Mishchenko *et al*., *Science* **315**, 1543 (2007).
26. H. Guan *et al*., *Atmos. Chem. Phys.* **10**, 6461–6469 (2010).
27. O. Torres, P. K. Bhartia, G. Taha, H. T. Jethva, C. Ahn, Stratospheric Injection of Massive Smoke Plume from Canadian Boreal Fires in 2017 as seen by DSCOVR-EPIC, CALIOP and OMPS-LP Observations, *AGU Fall Meeting*, abstract A41J-3092 (AGU, 2018); https://agu.confex.com/agu/fm18/meetingapp.cgi/Paper/380630.
28. M. O. Andreae *et al*., *Geophys. Res. Lett.* **28**, 951–954 (2001).
29. M. O. Andreae *et al*., *Science* **303**, 1337–1342 (2004).
30. W. J. Randel, E. J. Jensen, *Nat. Geosci.* **6**, 169–176 (2013).
31. A. Ansmann *et al*., *Atmos. Chem. Phys.* **18**, 11831–11845 (2018).
32. J. M. Siddaway, S. V. Petelina, *J. Geophys. Res.* **116**, D06203 (2011).
33. K. Bessho *et al*., *J. Meteorol. Soc. Jpn.* **94**, 151–183 (2016).
34. G. Luderer *et al*., *Atmos. Chem. Phys.* **6**, 5261–5277 (2006).
35. D. M. Winker *et al*., *J. Atmos. Ocean. Technol.* **26**, 2310–2323 (2009).
36. B. A. Wielicki *et al*., *Bull. Am. Meteorol. Soc.* **77**, 853–868 (1996).
37. S. M. Andersson *et al*., *Nat. Commun.* **6**, 7692 (2015).

ACKNOWLEDGMENTS

The Aqua/MODIS Aerosol Cloud Water Vapor Ozone Monthly L3 Global 1 Degree CMG dataset was acquired from the Level-1 and Atmosphere Archive and Distribution System (LAADS) Distributed Active Archive Center (DAAC), located in the Goddard Space Flight Center in Greenbelt, Maryland (https://ladsweb.nascom.nasa.gov/). CALIPSO and CERES data were obtained from the NASA Langley Research Center Atmospheric Science Data Center. AVHRR aerosol products are courtesy of the U.S. Geological Survey. **Funding:** This project has received funding from the European Research Council (ERC) under the European Union's Horizon 2020 research and innovation program (CloudCT, grant agreement no. 810370). **Author contributions:** E.H. and I.K. jointly conceived the principal idea, carried out the analysis, and wrote the paper. **Competing interests:** The authors declare no competing interests. **Data and materials availability:** All of the data used for the analysis of this manuscript are available online at the NASA websites of the different sensors.

SUPPLEMENTARY MATERIALS

science.sciencemag.org/content/371/6535/1269/suppl/DC1
Materials and Methods
Supplementary Text
Figs. S1 to S19
References (*38*–*52*)

3 August 2020; accepted 3 February 2021
10.1126/science.abe1415

Co-Managing Director VIB

VIB is an entrepreneurial Center of Excellence in Life Sciences located in Flanders, Belgium, vib.be. The mission of VIB is to conduct world-leading strategic basic research to unravel life processes and systems and to translate the resulting knowledge proactively into economic and other benefits for society at large. Hence, our motto 'VIB, Science with Impact'.

VIB is managed by a tandem of 2 co-managing directors (MD), reflecting the dual goal of VIB: Excellence in science + Excellence in economic and societal impact. This tandem is the key decision-body on strategy formulation and implementation of VIB.

Due to the retirement of the current Managing Director Science Policy, VIB is seeking an international, dynamic, inspirational, and experienced leader as his successor. The new Co-Managing Director of VIB should ideally start in Q1 2022.

The job

The MD Science Policy shares with the MD Innovation and Business the responsibility for the institutional leadership, strategy, and management of VIB. Key elements are:

- Leading VIB's strategy and implementation of institutional initiatives to advance novel scientific discoveries in basic and translational research;
- Playing a critical role in the recruitment and evaluation of Scientific Directors of VIB Research Centers as well as VIB Principal Investigators;
- Creating a stimulating, collaborative, diverse, and inclusive environment for life sciences research and innovation at VIB;
- Securing strong win-win relations with VIB's local stakeholders such as universities and governmental bodies;
- Representing VIB on the international scientific stage as well as in network organizations and research committees relevant for the visibility and enforcement of research in Flanders and Europe.

Profile of the new MD

- Internationally respected track record in ground-breaking bio-molecular research;
- Vision and a strong drive to develop cutting-edge strategic basic research with opportunities for technology transfer and societal benefits;
- A creative and dynamic mind with an eye for novel opportunities in science and innovation;
- Management experience in leading a multi-disciplinary research center;
- An experienced people manager with excellent mentoring skills as well as being able to take tough decisions when necessary;
- A pragmatic, solution-driven yet diplomatic team-player with a genuine interest in people's well-being and ability to connect people with different goals and priorities;
- An experienced negotiator and flexible interactor with diverse stakeholders;
- Fluent in written and spoken English and willing to acquire basic knowledge of Dutch.

How to apply?

Send your CV with a letter of motivation to Anne.Dentandt@russellreynolds.com and An.Winters@russellreynolds.com not later than **May 1st, 2021.**

For more information, contact the references mentioned above at Russell Reynolds.

VIB

ScienceCareers online @sciencecareers.org

ScienceCareers
FROM THE JOURNAL SCIENCE AAAS

Confused about your next career move?

Download Free Career Advice Booklets!

ScienceCareers.org/booklets

Who's the top employer for 2020?

Science Careers' annual survey reveals the top companies in biotech & pharma voted on by *Science* readers.

Read the article and employer profiles at sciencecareers.org/topemployers

Science 2020
TOP EMPLOYER

By **Taylor Wright**

What sparks joy

"Hot off the press, congratulations!" my Ph.D. supervisor wrote to me back in August. Our paper—which I had written during lockdown based on labwork I completed before the pandemic—had just been accepted for publication. "Great!" I responded. And that was that. I went back to cleaning my apartment and waiting for bread to bake. My city's lockdown made celebrating with co-workers at pub trivia or group drinks impossible. The only person who was going to celebrate this accomplishment with me was me—and I didn't feel like celebrating.

If you had asked me at the beginning of my Ph.D. what I wanted to do after graduating, I would have said that I wanted to hide away at a fume hood and do research. If the pandemic hadn't hit I probably would have blithely remained on that track, carried along by the momentum of my expectations for myself and my future. The cheers of labmates and colleagues when I published that paper would have spurred me forward.

But publishing in isolation, with no celebrations, gave me a chance to reflect on what I truly find rewarding. The paper gave me little sense of personal or professional accomplishment. I realized I don't find satisfaction just from the act of research. In the words of organization expert Marie Kondo, it doesn't "spark joy." Where did that leave me?

"Publishing in isolation ... gave me a chance to reflect on what I truly find rewarding."

I had more than a year of my Ph.D. left. The prospect of working at something I no longer enjoyed, for a goal I was no longer excited about, was discouraging. "Get a Ph.D." had turned out to be less of a career plan and more of a single step toward something unclear. I no longer knew what my career trajectory ought to be. I had been getting emails about university-sponsored graduate student career workshops every week for years. Like most people I knew, I figured I had better ways to use my time. Now, feeling aimless and uncertain about my future, I thought I would give them a try.

When I attended my first (virtual) event in November, I was a little discouraged at first to see it was mostly first-year graduate students who were already thinking about their career plans and how to optimize their grad school experiences accordingly. I felt late to the party, and somewhat regretful I hadn't taken advantage of these resources earlier. But I told myself late is better than never and that there was still lots I could learn.

As part of the workshop we completed an Individual Development Plan (IDP), a sort of quiz that helps you rank your career values and priorities. I had last taken a career quiz in high school. It told me to pursue marketing or vending machine repair, so I was fairly skeptical going in. When I got my results, I was surprised at first to see that "teamwork" and "help society" ended up as my top career essentials. But when I thought more about what I found fulfilling over the previous year, this began to make sense. I realized that I'll remember the people—the graduate students and other researchers I met and got to work with. I'll remember painstakingly going back and forth with my supervisor to craft a manuscript we were both happy with. For me, collaboration sparked joy.

The IDP suggested careers in public policy or administration. The prospect of leaving research was scary. But if the major research milestone of publishing a paper wasn't fulfilling for me, I needed to look elsewhere. So, rather than start new research projects, I've begun to write my thesis earlier than I planned, aiming to apply for a science policy fellowship in the fall. I've started to do something I previously associated only with business students and career professionals: networking with past collaborators and professors.

I wish it hadn't taken a global catastrophe for me to find my way to what I hope will be a rewarding career path. Yet if COVID-19 hadn't happened, I expect I would still be going full-steam ahead on research and would have realized far too late that I was on the wrong path. Going forward, I hope I can make a routine of regularly reflecting on what sparks joy—without waiting for a crisis. ■

Taylor Wright is a graduate student at the University of British Columbia, Vancouver. Send your career story to SciCareerEditor@aaas.org.

ILLUSTRATION: ROBERT NEUBECKER

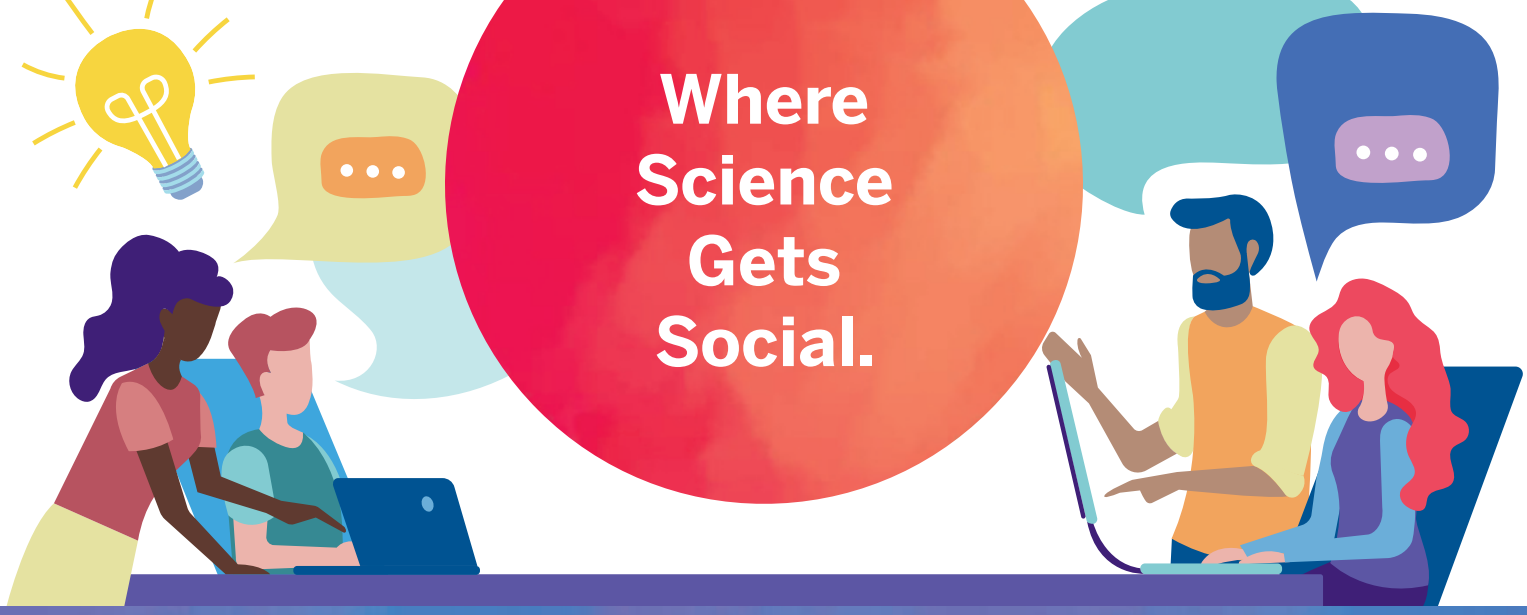

AAAS.ORG/COMMUNITY

AAAS' Member Community is a one-stop destination for scientists and STEM enthusiasts alike. It's "Where Science Gets Social": a community where facts matter, ideas are big and there's always a reason to come hang out, share, discuss and explore.

Member COMMUNITY
AAAS

AMERICAN ASSOCIATION FOR THE ADVANCEMENT OF SCIENCE

ScienceTranslationalMedicine.org

PUT HUMAN HEALTH AT THE HEART OF YOUR RESEARCH

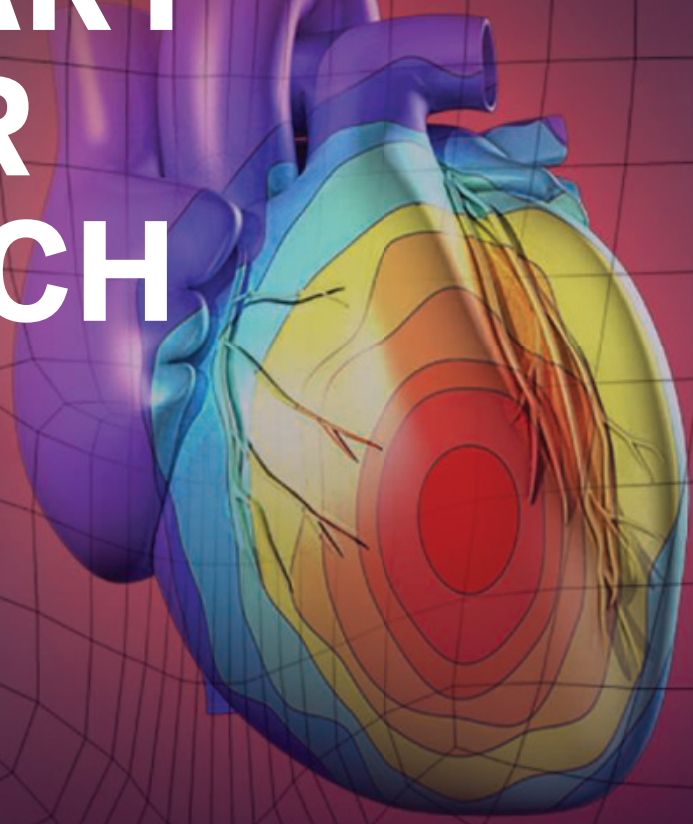

Submit your research:
cts.ScienceMag.org

Science Translational Medicine
AAAS

Twitter: @ScienceTM
Facebook: @ScienceTranslationalMedicine